Development of an energy analyzer for the characterization of the neutral and ionized upper atmosphere

Valentin Steichen

Sorbonne Université

Ecole doctorale d'Astronomie & d'Astrophysique d'Ile-de-France – ED 127

Laboratoire Atmosphères, Milieux, Observations Spatiales (LATMOS)

Développement d'un analyseur en énergie pour la caractérisation des hautes atmosphères neutres et ionisées terrestre et planétaires

Par Valentin Steichen

Thèse de doctorat de planétologie

Présentée et soutenue publiquement le lundi 18 Décembre 2023

Devant un jury composé de :

Laurence REZEAU	Professeure	Présidente
Peter WURZ	Professeur	Rapporteur
Stefano LIVI	Professeur	Rapporteur
Christelle BRIOIS	Maître de Conférence	Examinatrice
Fabrice CIPRIANI	ESA Scientist	Examinateur
François LEBLANC	Directeur de recherche	Directeur de thèse
Jean-Jacques BERTHELIER	Directeur de recherche émérite	Co-encadrant de thèse

REMERCIEMENTS

Tout d'abord, je tiens à exprimer ma profonde gratitude à François LEBLANC, Directeur de recherche CNRS ainsi que Jean-Jacques BERTHELIER, Directeur de recherche émérite, pour avoir encadré mes travaux de thèse. Je leur suis en premier lieu reconnaissant pour la confiance qu'ils m'ont accordée en me permettant de réaliser ce projet.
À François, j'aimerais lui adresser mes remerciements pour son humanité, sa disponibilité tout au long de ces trois années, mais aussi son apport scientifique. Ce fut un réel plaisir et une chance d'avoir pu travailler ensemble et j'espère que nos chemins se croiseront de nouveau à l'avenir.
À Jean-Jacques, en qui je suis reconnaissant pour avoir épaulé le développement de notre instrument au travers de ces multiples idées animées par de nombreuses années d'expertise en instrumentation. Je voudrais également lui exprimer ma gratitude pour la rigueur et la discipline qu'il a su me transmettre.

Mon travail de thèse s'est effectué au sein du LATMOS, je tiens donc à remercier le Directeur d'Unité, François RAVETTA pour son accueil au sein du laboratoire.

Je souhaite également remercier Elisa BALDIT, responsable de ma thèse au CNES, pour avoir suivi mes recherches au cours de ces dernières années et aussi pour le soutien apporté au développement de INEA.

À mon jury, j'adresse ma reconnaissance pour avoir accepté de consacrer un temps précieux à la lecture de ce manuscrit ainsi que de s'être rendu disponible pour ma soutenance.
Merci à Madame Laurence REZEAU d'avoir voulu le présider ; à Messieurs Stefano LIVI et Peter WURZ pour avoir examiné mon travail en tant que rapporteurs de cette thèse, pour l'intérêt qu'ils ont manifesté à l'égard de ce travail et pour leurs appréciations ; à Madame Christelle BRIOIS et Monsieur Fabrice CIPRIANI qui ont eu la gentillesse d'accepter d'en être membres.

Je suis particulièrement reconnaissant à Matthieu BERTHOMIER et Frédéric LEBLANC du Laboratoire de Physique des Plasmas (LPP) pour leur expertise et les bons conseils concernant la réalisation de l'instrument.

Cette thèse n'aurait pas pu aboutir sans le soutien et le travail des ingénieurs et techniciens du LATMOS. En particulier, je tiens à remercier Frédéric FERREIRA et Fabrice QUENAULT du Service Mécanique et notamment pour leur patience lors de mes venues incessantes et non planifiées. Merci également à Christophe MONTARON, Rafik HASSEN-KHODJA et Laurent LAPAUW pour m'avoir appris un petit peu d'électronique et pour avoir pris le temps de vérifier mes bidouillages quelquefois hasardeux.

Merci aux doctorants et post-docs de Jussieu et de Guyancourt notamment Sébastien VERKERCKE, Thomas LESIGNE, Nicolas STREEL, Adrien FINANCE, Maxence LEFEVRE et Florent TENCÉ pour les très bons moments passés ensemble autour d'un café, au Buisson Ardent ou durant nos diverses discussions.

J'adresse un merci particulier aux membres de l'ATC qui m'ont très gentiment accueilli à leur table de tarot et avec qui j'ai pu passer de très bons moments.

Merci notamment à Jean-Luc et Delphine pour les traditionnels cafés/croissants du matin en arrivant à Guyancourt. J’en profite également pour laisser un message à Christophe : promis, je ne te volerais plus ton oscillo !

Je ne saurais oublier mes amis et proches pour leur présence et leur soutien depuis toutes ces années : Alexandre, Victor, Mathilde, Constance, Laurie et Hugo.

Je remercie ma famille et tout particulièrement mon père pour m'avoir toujours soutenu et sans qui je ne serai pas là aujourd’hui.

Le dernier paragraphe de mes remerciements s'adresse à ma compagne : Eloïse. Merci de m'avoir soutenu durant ces années. Merci de m’avoir supporté même dans les moments difficiles de ma thèse et d’avoir su rester toujours à mon écoute.

ABSTRACT

English

Studying the dynamic of particles in the thermosphere – ionosphere and in the exosphere of bodies in the Solar System allows to deepen our understanding of these critical regions that are the bridge between a planet and space.

The aim of my thesis was to develop, build and test a neutral particles energy analyser for studying the upper planetary atmospheres: INEA (Ion and Neutral Energy Analyser). The instrument aims to measure the energy structure of the neutral and ion constituents present in the upper atmosphere. To achieve this challenging task, INEA relies on two concepts: an innovative ion source that is based on a carbon nanotube array as an electron emitter and an electrostatic energy analyser that is able to image directly the energy distribution of the particles.

During these three years of thesis, a numerical model of INEA was developed to meet the instrument objectives imposed by the measurements needed to characterize the upper atmospheres. At the same time, I have been working on the development of an ion source, also necessary for the optimal operation of INEA, and based on the use of carbon nanotubes as electron emitters. The development of the detector, another important part of the instrument has also been conducted. Following the numerical modelling and the work achieved on the different parts of the instrument, a first prototype of INEA has been designed and assembled. This prototype being currently tested.

With the work achieved during this thesis, we have been able to propose two instruments for future space missions: M-INEA on the M-MATISSE mission proposed for the ESA M7 call for project, recently selected for a phase A study up to mid-2026, and PSEE, an electron emitter dedicated to the control of PRELUDE SAT, a 6U CubeSat developed by two Japanese universities and scheduled to be launched mid-2025.

Français

L'étude de la dynamique des particules dans la thermosphère - ionosphère et dans l'exosphère des corps du système solaire permet d'approfondir notre compréhension de ces régions critiques qui sont l'interface entre une planète et l'espace.

Le but de ma thèse était de développer, construire et tester un analyseur en énergie pour l'étude des hautes atmosphères planétaires : INEA (Ion and Neutral Energy Analyser). L'instrument vise à mesurer la structure énergétique des constituants neutres et ioniques présents dans cette région. Pour réaliser cette tâche difficile, INEA s'appuie sur deux concepts : une source d'ions innovante, basée sur l'utilisation de nanotubes de carbone comme émetteur d'électrons et un analyseur en énergie électrostatique, capable d'imager directement la distribution en énergie des particules.

Au cours de ces trois années de thèse, un modèle numérique de INEA a été développé afin de répondre aux objectifs instrumentaux imposés par les mesures nécessaires à la caractérisation des hautes atmosphères. Parallèlement, j'ai travaillé au développement d'une source d'ionisation, également nécessaire au fonctionnement optimal de INEA, et basée sur l'utilisation de nanotubes de carbone comme émetteurs d'électrons. Le développement du détecteur, une autre partie importante de l'instrument, a également été réalisé. Suite à la modélisation numérique et aux travaux réalisés sur les différentes parties de l'instrument, un premier prototype d'INEA a été conçu et assemblé, ce prototype étant actuellement testé.

Avec le travail réalisé au cours de cette thèse, nous avons pu proposer deux instruments pour de futures missions spatiales : M-INEA sur la mission M-MATISSE proposé pour l'appel à projet M7 de l'ESA, récemment sélectionnée pour une phase A jusqu'en 2026, et PSEE, un émetteur d'électrons dédié au contrôle de PRELUDE SAT ; un CubeSat de 6U développé par deux universités japonaises devant être lancé mi-2025.

RESUME EN FRANCAIS

Dans une exosphère, la couche la plus externe d'une atmosphère, les collisions entre particules sont négligeables. Sur Mars, cette région est peuplée de particules thermiques et non thermiques, ces dernières étant produites dans la haute atmosphère martienne et potentiellement une signature de la perte de l'atmosphère de Mars au cours des 4 derniers milliards d'années. Parmi ces populations exosphériques non thermiques, l'oxygène atomique est particulièrement pertinent pour reconstruire l'histoire de l'eau sur Mars. Les missions précédentes, ayant étudié la planète rouge, ont fourni une assez bonne image des processus d'échappement. Cependant, aucune mesure directe de la structure énergétique de la couronne neutre de Mars n'a été effectuée à ce jour, ce qui limite notre capacité à extrapoler avec précision et dans le temps l'efficacité de ces processus pour éroder l'atmosphère de Mars. Les mécanismes décrits ici sont essentiellement contrôlés par notre Soleil. Il est donc essentiel de comprendre comment le forçage solaire influe au travers du vent solaire et de son flux radiatif, mais aussi, quelle est la contribution de la basse atmosphère.

De la même manière, sur Terre, dans la basse ionosphère-thermosphère, 'low thermosphere-ionosphere' (LTI), située entre ~100 et 200 km, des processus d'interaction couplent l'atmosphère neutre aux populations chargées. Avec ses propriétés uniques, la LTI est couplée au vent solaire et à la magnétosphère terrestre, et à divers types d'ondes atmosphériques produites dans les couches plus profondes de l'atmosphère, en dessous de 100 km. Jusqu'à présent, la plupart des informations sur cette région proviennent de la télédétection, y compris la télédétection par satellite, et d'observations au sol combinées à quelques mesures in situ sporadiques effectuées à partir de fusées sondes. Pourtant, seules des études in situ permettront d'obtenir les mesures souhaitées à ces altitudes critiques. Une image complète de la thermosphère et de l'ionosphère est cruciale en raison de son impact direct sur les activités technologiques modernes. Cette connaissance est essentielle pour prédire avec précision l'orbite des satellites et leur désorbitation, pour assurer un fonctionnement fiable des réseaux électriques et pour maintenir la stabilité des systèmes de communication.

Ce qui ressort d'une brève analyse du besoin de mesures dans ces régions de Mars ou de la Terre est qu'il n'existe pas encore d'instrument capable de couvrir le domaine en énergie allant du domaine thermique à quelques eV. Pour cela, un instrument doit pouvoir mesurer les caractéristiques atmosphériques sur une gamme allant de quelques dixièmes d'eV à environ 10 eV avec une résolution supérieure à 0.1 eV, une gamme de masse de 1 à 60 amu avec une résolution de ~20, et avec une sensibilité capable de mesurer des densités entre 10^8 et $10^2\ cm^{-3}$. La caractérisation de la thermosphère – ionosphère nécessite également des instruments capables de mesurer les vents et la température avec des résolutions respectives d'environ 5 m/s et 10 K. La spectrométrie de masse, couplée à des techniques d'analyse en énergie est la seule méthode adaptée à ces objectifs.

INEA (Ion and Neutral Energy Analyser) s'appuie sur un nouveau concept qui associe un émetteur d'électrons à cathode froide utilisant des nanotubes de carbone et un spectrographe en énergie capable de mesurer instantanément la distribution en énergie des particules neutres, ainsi que leur masse.

Les travaux réalisés au cours de ma thèse et détaillés dans ce manuscrit commencent en décrivant le fonctionnement théorique de l'analyseur en énergie à plaques parallèles qui est le cœur de INEA. A partir du modèle théorique, une version mécanique de laboratoire de l'analyseur d'énergie a été construite et assemblée, y compris l'électronique associée qui contrôle les tensions des électrodes de l'analyseur en énergie. Les dimensions de l'analyseur ont été obtenues en utilisant les équations théoriques de Green et Proca (1970), et en choisissant des paramètres appropriés afin que les dimensions totales de l'analyseur restent raisonnables pour un instrument spatial dont la masse ne doit pas dépasser quelques kgs. Un modèle numérique de l'analyseur a également été développé. Le modèle a permis d'estimer les performances "idéales" de notre prototype, et de prendre en compte les défauts électrostatiques inhérents à un modèle mécanique de l'instrument.

La section suivante détaille le fonctionnement du détecteur de INEA et les enjeux liés à l'utilisation de galettes à micro canaux (MCP). Pour obtenir une efficacité de détection suffisante, les ions doivent être accélérés avant d'impacter la face avant de la MCP. Il faut donc y appliquer un potentiel négatif de l'ordre de quelques centaines de volts. Un tel potentiel perturbe une région supposée sans champ électrique, ce qui entraîne une diminution du pouvoir de focalisation de l'analyseur à l'entrée du détecteur. Un modèle numérique du sous-ensemble EA/détecteur a donc été développé dans le but de trouver une solution limitant cette perturbation. Le modèle suggère qu'une grille relativement épaisse (transparente à seulement ~50%) doit être placée à l'entrée du détecteur afin que le potentiel appliqué à l'entrée de la MCP soit suffisamment écranté. De plus, la structure à petite échelle du champ électrique entre les grilles du détecteur modifie les trajectoires des particules et élargit la distribution des impacts, un effet que nous avons cherché à limiter également.

Suite à la modélisation numérique, un prototype de détecteur a été construit en tenant compte des principales conclusions tirées de la simulation. Afin de détecter la position d'impact des particules, un collecteur pixelisé est utilisé avec son électronique associée. La sortie des pixels est reliée à un ASIC qui a été initialement conçu par le Laboratoire de Physique des Plasmas (LPP). L'ASIC permet de détecter les impulsions de charge de chaque pixel indépendamment et simultanément. L'ASIC convertit ensuite les impulsions détectées en sorties numériques qui sont finalement lues à l'aide d'un DPU dédié. Comme le détecteur avec ASIC a nécessité un long temps de développement, une électronique du détecteur plus simple a été également conçue. Cette dernière ne comprend qu'un amplificateur de charge (CSA) qui convertit l'impulsion de charge provenant de la MCP en impulsions de tension lisibles par un oscilloscope. L'amplificateur de charge peut être branché à la sortie du pixel désiré.

Nous avons réalisé une série de simulations permettant de comprendre le fonctionnement de la source d'ion. Ces simulations ont mis en évidence l'effet de la grille d'extraction sur le champ électrique et l'émission d'électrons au sommet du réseau de nanotubes de carbone. Les résultats de ces simulations ont mis en évidence l'importance de la géométrie de la grille afin d'obtenir un champ d'émission homogène. Les simulations sur l'ensemble de la source d'ionisation ont montré que pour un fonctionnement en laboratoire de INEA, il est possible d'extraire des ions du volume grâce à leur vitesse thermique et à l'effet de la bulle de potentiel à proximité de la grille de sortie. Des tests expérimentaux effectués avant la thèse ont montré la présence d'électrons primaires dans l'espace entre le volume et la lentille d'ion. Pour réduire

le nombre de ces électrons, il a été décidé d'étendre le volume d'ionisation le long de l'axe de visée de l'instrument.

Un modèle mécanique de la source d'ions a été construit et testé. Une électronique de mesure dédiée a été conçue afin de réaliser les expériences sur la source d'ion seule. Les tests réalisés sur la source d'ions nous ont permis de mieux comprendre son fonctionnement et de mesurer une sensibilité de $1.6 \times 10^{-4}\ count/s/cm^{-3}$ dans une configuration de laboratoire. En utilisant SIMION, cette valeur a pu être interpolée à une sensibilité en vol de $1.1 \times 10^{-3}\ count/s/cm^{-3}$.

La dernière section décrit le modèle numérique complet de INEA, comment il a été construit et les modules développés pour simuler les différents types de fonctionnement de l'instrument. Le modèle numérique a permis d'estimer ses performances, c'est à dire : une résolution en énergie meilleure que 0.1 eV et une résolution en masse de ~22 ainsi qu'une capacité de mesure de la température et de la vitesse avec des résolutions supérieures à 50K et 20 m/s respectivement.

Dans le même temps, le prototype de INEA a été assemblé et placé dans sa chambre à vide. Les premières mises en fonctionnement ont été réalisées mais faute de temps et en l'absence des deux circuits nécessaires à l'utilisation de l'ASIC, seuls des tests préliminaires de INEA ont pu être réalisés pour l'instant.

INEA est proposé dans le cadre d'une mission spatiale dédiée aux mesures multipoints de la thermosphère et de l'ionosphère martiennes. La mission Mars - Magnetosphere Atmosphere Ionosphere and Space Weather Science (M - MATISSE), actuellement proposée à l'Agence Spatiale Européenne dans le cadre de l'appel à projets M7, fournira pour la première fois, des observations continues et simultanées du système martien. Deux orbiteurs, l'un principalement dans la magnétosphère et l'autre principalement dans le vent solaire, assureront une couverture simultanée de la haute et de la basse ionosphère et de l'atmosphère neutre (grâce à INEA). Notre instrument est proposé dans le contexte de M-MATISSE comme une suite de trois instruments, dont un analyseur d'électrons et un détecteur de particules solaires, partageant un DPU commun. M-MATISSE a été selectionné par l'ESA pour une phase A compétitive en Octobre 2023. Cette phase durera jusqu'à mi-2026.

En plus de la mission M-MATISSE, les progrès sur l'émetteur d'électrons ont permis de proposer un système de contrôle du potentiel d'un microsatellite japonais. Les universités Shizuako - Ken et Nihon construisent un CubeSat de 6U, PRELUDE-SAT, pour caractériser les perturbations du champ électrique ionosphérique, précurseurs potentiels des tremblements de terre. En raison de la petite surface totale du satellite, la collecte d'ions dans l'environnement est beaucoup moins efficace que la collecte d'électrons pendant le fonctionnement de l'instrument. Par conséquent, le potentiel du satellite serait amené à des valeurs négatives importantes et variables. La solution proposée consiste à assurer l'équilibre global du CubeSat, en émettant un courant d'électrons dans l'espace. Ce dispositif, appelé Prelude-Sat Electron Emitter (PSEE), repose sur l'utilisation d'une cathode à émission de champ utilisant des nanotubes de carbone, similaire à la source d'ions de INEA. PSEE est une version améliorée du prototype d'émetteur d'électrons utilisé dans cette thèse. Il se compose d'un réseau circulaire de nanotubes de carbone et de deux grilles, qui permettent respectivement l'extraction des électrons et le blindage du potentiel électrique. À la fin de ma thèse, j'ai eu l'occasion de travailler sur la

conception de ce système et de participer aux premiers tests. PRELUDE-SAT doit être lancée à la mi-2025.

TABLE OF CONTENTS

INTRODUCTION

The exploration of celestial bodies within our Solar System is a compelling endeavour, driven by the quest for scientific knowledge and the potential for profound insights into the origins, evolution and future of both Earth and the wider Universe. This multidisciplinary enterprise offers a unique opportunity to unravel the mysteries of planetary formation, planetary dynamics and, ultimately, the potential for life beyond our home planet. It also promises to advance technology and foster international collaboration to expand our understanding of the Universe.

The study of planets and celestial bodies provides a window into the dynamic processes that have shaped our Solar System. Comparative planetology, a cornerstone of modern astronomy, allows researchers to trace the divergent paths of planetary evolution, shedding light on the mechanisms that governed their formation, differentiation and geological activity. For example, the starkly contrasting surfaces of Venus, Earth and Mars provide invaluable insights into the influence of tectonic activity, magnetic activity and atmospheric dynamics on planetary evolution.

In addition, a crucial aspect of planetary exploration is the study of the upper atmospheres, an often overlooked but important region. This frontier acts as a bridge between a planet's core dynamics, surface conditions, and the wider celestial environment. On Mars, where the atmosphere is particularly thin, a comprehensive understanding of the upper atmosphere is crucial to unravel the planet's historical climate and the presence of water in its distant past. The complex interplay between Mars and the Sun exerts a profound influence on the Martian upper atmosphere. This interaction shapes the planet's current atmospheric conditions and has probably played a key role in its climatic evolution over geological epochs (Jakosky & Jones, 1997).

While the scientific attraction of distant celestial bodies is undeniable, it is important not to overlook the importance of Earth's near-space environment. The study of the regions adjacent to our planet, its upper atmosphere, remains essential to protect our technological infrastructure and to understand the complex interactions between Earth and the surrounding space environment. The study of phenomena such as solar radiation, geomagnetic storms and cosmic rays in these near-space regions is essential to mitigate the potentially damaging effects on satellite operations, GPS systems and even power grids (Sarris et al., 2023). Furthermore, the knowledge gained from studying Earth's near-space environment not only strengthens our resilience to space weather events, but also provides invaluable insights into the broader astrophysical processes that govern planetary atmospheres and magnetic fields. As we venture outwards, it is imperative that we continue to prioritise the exploration of Earth's immediate neighbourhood, as it underpins not only our scientific endeavours, but also our societal well-being.

In the vast field of planetary exploration, the importance of in-situ measurements for characterising the upper atmospheres cannot be overstated (Benkhoff et al., 2010; Jakosky et al., 2015; Taylor et al., 2017; Sanchez-Cano et al., 2022). This methodology involves direct observations and data collection in the target environment. Unlike remote sensing, which provides valuable but sometimes limited perspectives, in situ measurements provide access to measurements that would be inaccessible otherwise.

Among the instruments used for in-situ characterisation, one category is particularly well suited to measuring the gas envelopes (neutral or ionised) of planetary objects. Mass spectrometry makes it possible to identify the constituents of a medium over a wide range of masses and resolutions. Embedded mass spectrometers on board orbiters provide crucial insights into the composition and dynamics of the space environment, including the exosphere and ionosphere (Barabash et al., 2009; Berthelier et al., 2006; Young et al., 2004)

Successful mass spectrometers have already demonstrated the importance of such instruments for characterising the upper atmosphere. For example, the ROSINA (Rosetta Orbiter Spectrometer for Ion and Neutral Analysis) instrument onboard the European Space Agency's Rosetta spacecraft has made several pioneering discoveries about the activity, dynamics and solar interaction of comets (Balsiger et al., 2007).

The aim of this thesis is to contribute to the development of a new type of spectrometer dedicated to the analysis of the neutral and ionised constituents of the upper atmosphere. While most spectrometers on board spacecraft are dedicated to mass analysis, the Ion and Neutral Energy Analyser (INEA) aims to analyse the energetic structure of particles. With its unique differential analysis capability, the instrument could provide significant insight into the processes acting on neutral and ionised particles in the upper atmospheres of Solar System bodies.

This manuscript begins with a presentation of the issues involved in studying the upper atmospheres using two examples, the Earth's lower thermosphere and ionosphere and the atmospheric escape occurring in the Martian exosphere; two very different objects but yet with much similarities when focusing on the missing observations. In the second chapter, which is a review of the technique to analyse neutral particles in terms of mass and energy and an overview of the existing instruments, we will highlight the need for an instrument, like INEA, to characterise the neutral constituents. This chapter also emphasis on the performances required for such measurements. The third and last chapter describes the work carried out on the different parts of INEA in order to produce a first prototype. The last part of this manuscript concludes with the possible improvements of the instrument and gives an insight into its future.

CHAPTER 1
NEUTRAL AND IONISED PLANETARY ENVIRONMENTS

The interest in studying Mars' upper atmosphere and the Earth's lower thermosphere – ionosphere lies in the fact that they are two atmospheres associated with radically different magnetic and electric environments. However, as explained below, the composition of the upper atmosphere of these two bodies is relatively similar, allowing their observations to be made with a comparable instrument approach.

1. MARS

1.1. Mars' atmosphere

The Martian atmosphere is dominated by carbon dioxide, which makes up 95% of its total volume. In addition to CO_2 , there are traces of other gases such as molecular nitrogen (2.7%), argon (1.6%), and small amounts of oxygen and water vapour (Montmessin et al., 2007). The average surface pressure is about 7 millibars and is subject to seasonal variations. The Martian atmosphere can be divided into several distinct layers, each characterised by unique thermal and compositional properties. The troposphere, between the surface and 50 km, experiences a temperature decrease with altitude at a rate of $2-3\ K.km^{-1}$ and is the layer where weather phenomena such as dust storms occur. The next layer, the mesosphere, has the lowest temperature. CO_2 in the mesosphere acts as a cooling agent by efficiently radiating heat into space. From 100 km, the thermosphere extends to the outer limits of the atmosphere. In this region, the temperature gradient is positive due to the absorption of EUV/UV solar radiation. Another characteristic of the thermosphere is the homopause (typically around 110 km), which marks the boundary below which the atmosphere is turbulent and well mixed, and above which the different components of the atmosphere are structured in density with altitude as a function of their mass (Fig. 1.1)

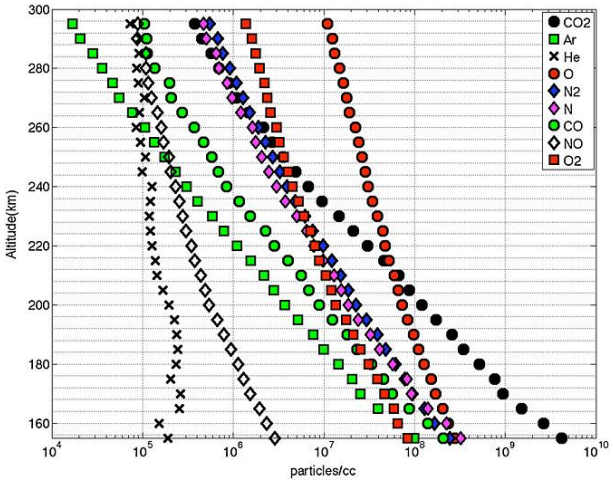

***Figure 1.1**:Density profiles of nine neutral species in the upper Martian atmosphere measured by NGIMS/MAVEN* (Mahaffy et al., 2015)

In the absence of a global magnetic field (Acuna et al., 1999) the solar wind, interacts at high altitudes within Mars' upper atmosphere and generates an induced magnetosphere (Fig. 1.2). The region where solar wind energy dissipates, which occurs at altitudes of ~100 – 500 km is the ionized counterpart of the thermosphere: the ionosphere. As a medium made of charged particles, the ionosphere is sensitive to magnetic and electrodynamics. A particular feature of Mars is that the ionosphere-solar wind interaction is more complex over a region of the southern hemisphere where highly non-uniform crustal magnetic fields are located (Acuna et al., 1999). These fields, which are of the order of a few tens to hundreds nT at ~400 km (Langlais et al., 2019), can interact directly with the solar wind producing a "hybrid magnetosphere" (Dubinin et al., 2023). A myriad of interactions exists in the Martian thermosphere – ionosphere among which current systems, forcing from atmospheric waves, or the effect of precipitating particles can be cited. Reviewing the processes that occurs in this region is not within the scope of this paragraph. (Section 2 of this chapter will give a detailed description of similar processes that occurs on Earth). However, Fig. 1.2 gives an overview of the mechanisms present in the thermosphere – ionosphere system.

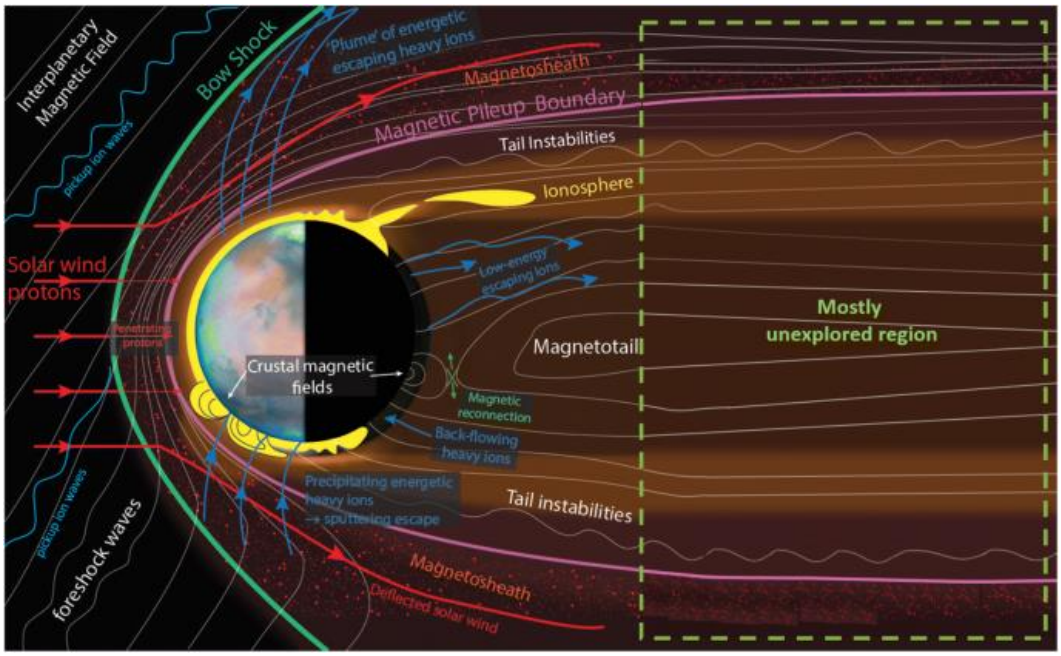

***Figure 1.2**: Schematic of Mars' plasma system with the main physical processes known to occur at Mars (Sanchez – Cano et al., 2021).*

The ion composition measured on Mars' ionosphere revealed the presence of 22 ion species (Fig. 1.3) with major constituents being O^+, O_2^+. At low altitudes (below 220 km) CO_2^+ is the second most abundant species after O_2^+ (Benna et al., 2015).

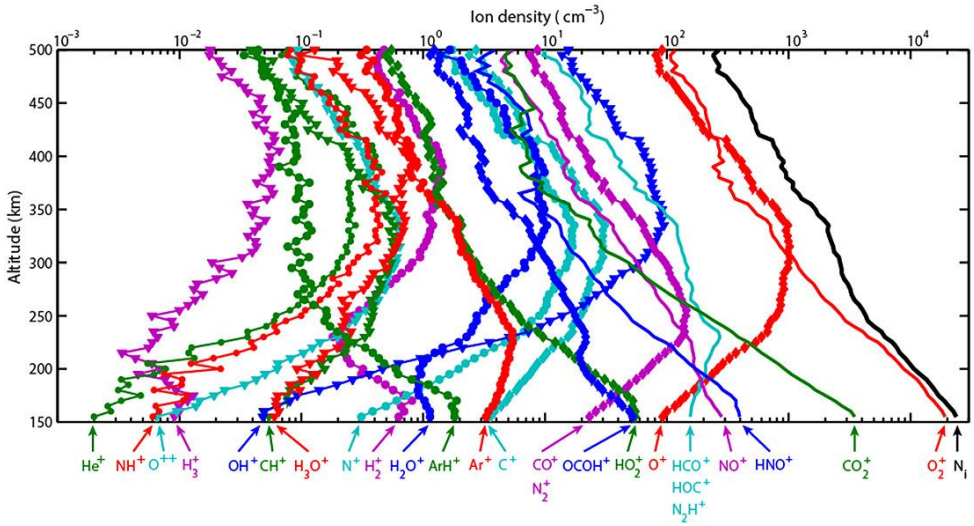

***Figure 1.3**: Altitude profiles of the averaged density of ionospheric ions measured by NGIMS between altitudes of 150 km and 500 km (Benna et al., 2015).*

About water on Mars

The geological record on Mars suggests that the planet had an abundant amount of liquid water on its surface early in its history (Carr, 2007). The presence of an active hydrosphere would in turn have required a thick (~ 1bar) wet atmosphere (Wordsworth et al., 2017), which would have provided sufficient greenhouse warming to maintain atmospheric temperatures that allowed for liquid water reservoirs on the surface. Over time, Mars appears to have lost this thick early atmosphere and now has a CO_2 - dominated atmosphere with pressures of only a few mbars. To quantify the early water loss from the planet, we need to understand the mechanisms by which atmospheric constituents can be lost and how these scale over time. Atmospheric mass can be lost in two directions: upwards into space and downwards into the subsurface. For the downward direction, at most an equivalent 12 mbar of sequestered CO has been identified in exposed carbonate mineral deposits (Edwards & Ehlmann, 2015).

On the upward side, for atmospheric particles to escape into space, they must reach the non-collisional region of the upper atmosphere (150-200 km): the exosphere. At these altitudes, the temperature varies between ~200 - 300K (Stone et al., 2018), which allows a fraction of the hydrogen atoms to thermally escape, thus removing a component of the water molecules. However, oxygen is too heavy to thermally escape from the planet. Thus, non-thermal mechanisms need to provide sufficient energy to overcome the relatively low gravitational pull of Mars. Quantifying these escape processes, which occur in the upper Martian atmosphere and particularly in the outermost region: the exosphere, and their drivers is fundamental to understand the evolutionary history of the Martian atmosphere (Jakosky et al., 2018). In particular, the lack of an Earth-like global magnetic field is often thought to make the Martian atmosphere susceptible to intense escape due to the close interaction between the ionosphere and the solar wind (Ramstad & Barabash, 2021).

1.2. The Martian exosphere

The exosphere is the outermost layer of the atmosphere. It is defined as the region where the particle density is low enough to allow neutral particles to move without colliding with each other. As a result, particles are only bound to the planet by gravity. The lower boundary of the exosphere is called the exobase. It can be defined as the height at which the mean free path of a particle is equal to the height scale of the species to which it belongs. Above the exobase, a particle has a probability to make less than one collision. For Mars, the exobase is between 180 and 230 km, depending on the species, local time and solar activity (Fu et al., 2020). In principle, the exosphere covers distances where particles are still gravitationally bound to Mars, i.e. particles still follow ballistic orbits that return them to the planet. The upper boundary of the exosphere has been defined for atomic hydrogen as the distance at which the influence of the solar radiation pressure on atomic hydrogen exceeds that of the gravitational pull of Mars, which has been observed beyond 10 R_m (Chaffin et al., 2015). In theory, an exosphere extends to infinity.

The exospheric population is usually divided into a population at the temperature of the exosphere T_{ex} (of the order of 200K (Stone et al., 2018) at minimum solar activity on Mars), the thermal population, and a so-called suprathermal population composed of particles whose kinetic energy is larger than 5 to 10 times T_{ex}. Unlike Earth or Venus, whose gravitational constant is sufficient to restrain the suprathermal population, a significant fraction of the particles in the Martian corona have a velocity larger than the escape velocity ($\sqrt{\frac{2GM}{r}}$, where G is the gravitational constant, M is the mass of the planet and r is the distance of the particle from the centre of the planet). This results in a significant atmospheric escape, which has important consequences for the long-term evolution of the atmospheric content.

1.3. The atmospheric escape

The theory of planetary exospheres and atmospheric escape was developed in the 1960s (Chamberlain, 1963). According to this theory, three classes of particles populate the region above the exobase, corresponding to three types of trajectory: ballistic trajectories, satellite trajectories (particles that are gravitationally bound to the planet and whose trajectories never cross the exobase) and escape trajectories. The density profiles of these populations above the exobase were calculated using Liouville's equation. This theory applies to the component of an atmosphere that is thermalized at the temperature of the atmosphere.

1.3.1. Neutral thermal escape

If an atmospheric particle, above the exobase, has a velocity larger than the escape velocity, it is likely to escape into the interplanetary medium. Using the Chamberlain model, it is possible to determine the flux escaping from the atmosphere as a function of density and temperature at the exobase; this is the Jeans escape. The tail of the velocity distribution at the exobase is then slowly emptied of energetic particles and repopulated by collisions. In the asymptotic behaviour of the Jeans escape, it can also happen that the flow of light gas is so large that it drags heavier particles to escape. This effect is known as hydrodynamic escape. However, such an escape requires strong solar activity (e.g. primitive solar conditions). Today, only the lightest particles

(H and He) in the Martian atmosphere escape to any significant extent via the Jeans escape (Chaufray et al., 2007). Estimates from MAVEN observations suggest that the current loss rate of H varies in the range $\sim 1 - 11 \times 10^{26}\ H\ atoms.s^{-1}$ (Jakosky et al., 2018), a rate strong enough for all the atomic hydrogen in Mars' atmosphere to be lost in 3,000 to 30,000 years. Hydrogen atoms form a very extended exosphere as observed by MAVEN (Fig. 1.4).

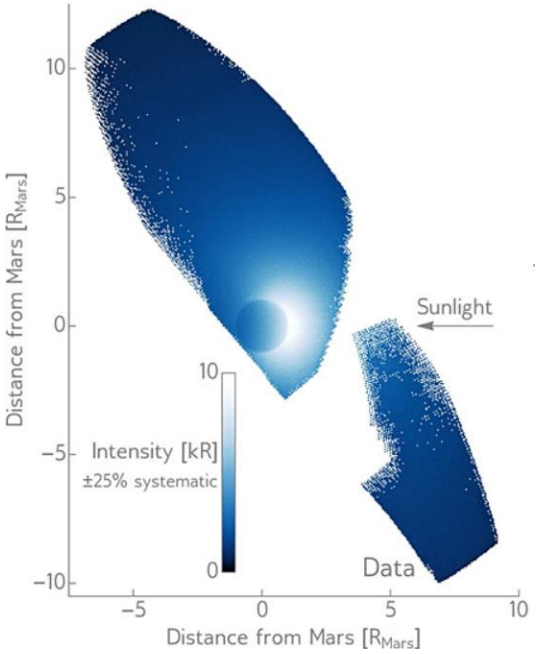

***Figure 1.4** : Observations of the Martian H corona during IUVS/MAVEN insertion orbits* (Chaffin et al., 2015).

1.3.2. Neutral suprathermal escape

The Martian exospheric suprathermal population is thought to be formed by two main processes, atmospheric sputtering of planetary ions and photochemical reactions in the ionosphere. This suprathermal population is particularly interesting because it represents a significant portion of the oxygen atomic population present in the Martian corona, a key tracer of Mars' past water atmospheric escape.

Atmospheric Sputtering consists of the ejection of neutral atmospheric particles into the exosphere by collisions with energetic ions impacting the atmosphere. Pickup planetary ion formation occurs after solar EUV and photoelectron ionisation in the Martian corona. In the absence of a large permanent magnetic field, these newly ionised particles can be accelerated by the partially deflected fields frozen in the solar wind. They move along gyroscopic radial trajectories in the direction of the Martian tail, but a fraction re-enter the atmosphere and collide with neutral particles with sufficient energy to eject atoms and molecules. Since these collisions occur mainly near the exobase, the species that are able to reach this altitude are most affected by atmospheric sputtering. Sputtering is a collisional process. For this reason, Johnson, (1990) proposed two possible scenarios. Either the particle collides with another particle near the exobase and the recoiled particle may be ejected into the exosphere (case 1 in Fig. 1.5), or the incident particle generates a cascade of collisions, some of which are likely to produce recoiled particles that may escape (case 2 in Fig. 1.5).

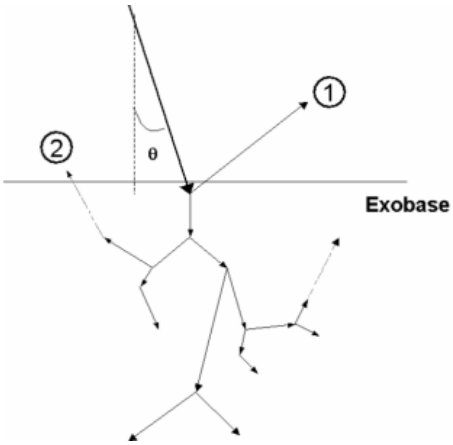

***Figure 1.5**: Typical scenario induced by an impacting particle in the atmosphere* (Johnson, 1994).

A planetary pick-up ion will impact the atmosphere at high speeds, up to twice the solar wind speed (or nearly 1000 km/s), and can transfer its momentum to atoms in the vicinity of the exobase via collisions and eject them into space. This sputtering process can be very effective at removing heavy neutral atoms (Luhmann et al., 1992), and is expected to be the most important mechanism for removing inert gases such as argon (Jakosky et al., 1994; Jakosky et al., 2017). Measurements from MAVEN/STATIC (McFadden et al., 2015) and MAVEN/SWIA (Halekas et al., 2015), through observations of the properties of precipitating ions (Leblanc et al., 2015, 2018; Fig. 1.6), and combined with a 3D atmospheric model (Leblanc et al., 2017), have been used to estimate the efficiency of sputtering to eject atmospheric species. At present day, the inferred mean loss rate of neutral O due to sputtering is $\sim 3 \times 10^{24}\ O\ atoms.s^{-1}$ (Jakosky et al., 2018).

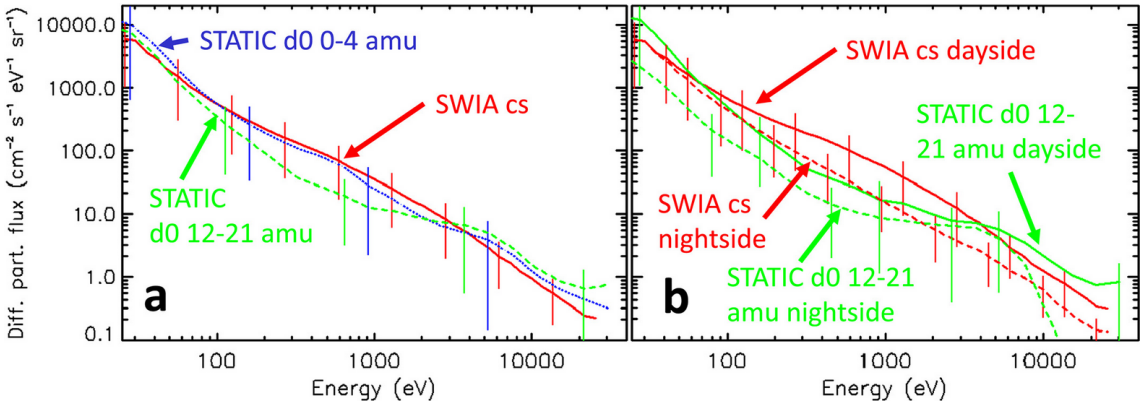

***Figure 1.6**: Differential particle flux of the precipitating ion as measured by MAVEN between 200 and 350 km and over almost 2 years of measurements (Leblanc et al., 2018), averaged over Mars (a) and over the dayside and nightside (b)*

Dissociative recombination (DR) is a chemical reaction that takes place in the thermosphere – ionosphere in which a molecular ion AB^+ present in the atmosphere recombines with an ambient electron to form a metastable neutral AB**, which quickly separates into two neutral species A* and B*. The escape probability of an atom produced by DR depends on three main factors: the initial energy of the atom, the column density and the composition of the gas above the height at which it is "born". As the most abundant molecular ion in the thermosphere

is O_2^+ (Benna et al, 2015), DR is particularly relevant to the escape of O atoms. There are four channels leading to the production of neutral oxygen from the DR of O_2^+, which are given in Table 1.1 (Fox & Hać, 2010).

***Table 1.1**: The four branches of the O_2^+ Dissociative Recombination reaction and their likelihoods.*

Initial State	Final State	Likelihood
$O_2^+ + e \rightarrow$	$O(^3P) + O(^3P) + 6.99\ eV$	26.5%
	$O(^1D) + O(^3P) + 5.02\ eV$	47.3%
	$O(^1D) + O(^1D) + 3.06\ eV$	20.4%
	$O(^1D) + O(^1S) + 0.83\ eV$	5.8%

In the case of the DR of O_2^+, for 74% of the recombination the energy is sufficient to give each of the resulting neutral O atoms an amount of energy (as kinetic energy) larger than the escape energy of Mars (1.98 eV at the exobase). If the recombination occurs close to the exobase, so that the ascending atom is unlikely to be backscattered or slowed below the escape velocity by subsequent collisions, it will escape.

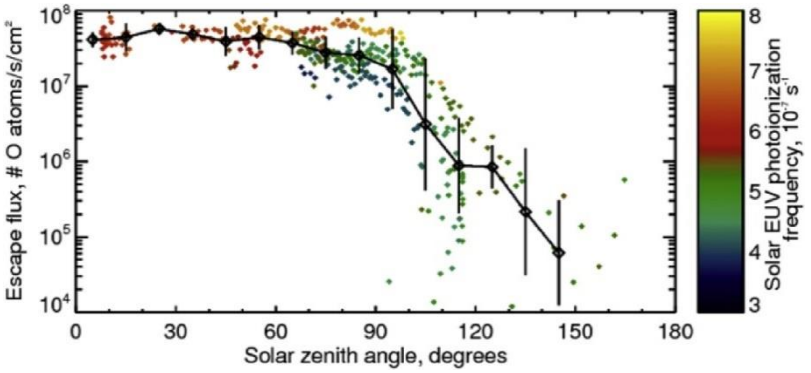

Figure 1.7: O loss rates due to dissociative recombination, derived by *MAVEN* over most of a Mars year (Lillis et al., 2017).

Similar to the sputtering estimates, MAVEN is not able to directly measure these escaping neutral atoms. However, it does measure the ion composition and electron abundance in the upper Martian atmosphere, from which the rate of DR that can occur can be inferred and, by modelling the fate of such atoms through the atmosphere, the escape flux can be derived (Fig. 1.7). The yield loss of DR is estimated to be between in the range $3.5 - 7 \times 10^{25}\ O.s^{-1}$ (Cravens et al., 2017; Lee et al., 2017; Lillis et al., 2017; Rahmati et al., 2017).

1.3.3. Ion loss

Ion loss occurs via the acceleration of ions by the solar wind electric field. The electric field can be generated around Mars by many different processes, including the moving magnetic field of the solar wind (Luhmann & Kozyra, 1991), plasma pressure gradients in the ionosphere (Collinson et al., 2015), plasma flow shear near the strong crustal magnetic fields (Dubinin et al., 2008) movement of ions and electrons around the magnetic field in magnetic cusp regions (Ergun et al., 2016) or acceleration due to magnetic tension forces associated with the draping of the external fields around the Martian solar wind "obstacle" and with magnetic reconnection involving the crustal magnetic fields (Ma et al., 2018). These processes may start in the lower

ionosphere (Ergun et al., 2016; Riousset et al., 2013). MAVEN observations (Fig 1.8) estimate the net global loss rate of both O^+ and O_2^+ ions to be $5 \times 10^{24}. s^{-1}$ (Jakosky et al., 2018).

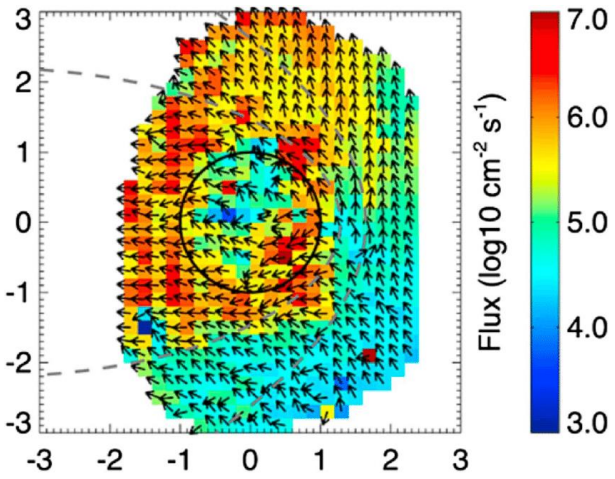

Figure 1.8*:MAVEN observations of escaping oxygen ions from Mars (Dong et al., 2015).*

1.3.4. Total escape at present day

As we have seen in the last paragraphs, the most recent measurements related to atmospheric escape were obtained thanks to a year of observation of the Martian corona with instruments on board the Mars Atmosphere and Volatile EvolutioN (MAVEN) mission (Jakosky et al., 2015). The loss rate for Jeans escape obtained during this year of observation is similar to that of previous missions (i.e. Mariner 6,7 & 9, Mars Express), with a mean loss rate of $5 \times 10^{26}\ H. s^{-1}$. (Fig. 1.9)

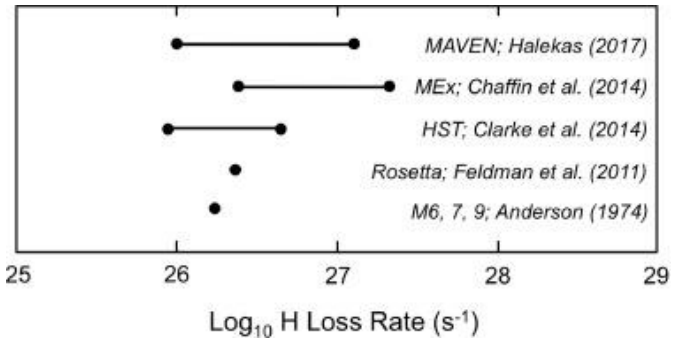

Figure 1.9*: H loss rate derived from observations made from different spacecraft. (Jakosky et al., 2018).*

For O losses, the loss rate derived from MAVEN and combining all the different processes has been estimated to be about $\sim 6 \times 10^{25}\ O. s^{-1}$. As shown in Fig. 1.10, the majority of O losses identified today (either as neutrals or ions) are due to photochemical losses (dissociative recombination).

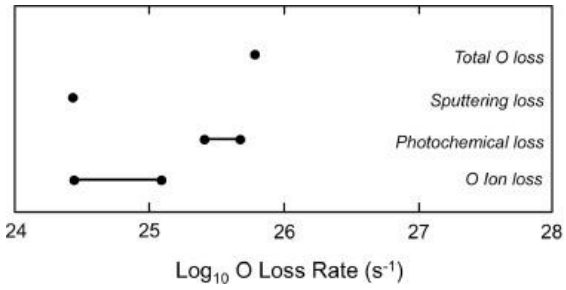

Figure 1.10*:O loss rate as determined from* MAVEN *observations for each of the loss processes (Jakosky et al. 2018).*

1.4. Next needed measurements

Although direct measurements of ion loss have been conducted during previous and current missions to Mars (i.e., Mars Express, MAVEN) (Brain et al., 2015; Jakosky et al., 2018), there are currently no dedicated in-situ measurements of the suprathermal neutral atoms in the exosphere. Currently, only indirect estimations have been made of the rate at which dissociative recombination (DR) and sputtering contribute to atmospheric escape, utilizing proxy indicators and modelling. Atmospheric loss due to DR is far more efficient when compared to present sputtering (Jakosky et al., 2018; Lillis et al., 2015) However, sputtering is considered to have been potentially dominant during the early stages of solar conditions (Jakosky et al., 2018). Therefore, to confirm or refute MAVEN's main conclusions, it would be highly beneficial to directly measure a signature of these two non-thermal processes, in particular their dependencies with solar activities, a key information to extrapolate back in time.

It is well known that escape mechanisms vary in intensity along Mars' seasons and the solar cycle, which control the ion – neutral chemistry in the thermosphere – ionosphere but also the rate of ionization in the exosphere and therefore the intensity of the reimpacting flux of planetary pickup ions. Recently, it has been shown that, as on Earth, the lower atmosphere also controls the state of the thermosphere and therefore the escape efficiency (Chaffin et al., 2022). As on Earth, understanding Mars' interactions with our Sun passes therefore through the characterization of the thermosphere – ionosphere system.

A direct measurement of the low-energy distribution of the neutral particles in the Martian corona will enable, for the first time, a direct identification of processes behind Mars' atmospheric erosion and their relation to solar conditions. This is one of the key scientific and measurement objectives of the mission M-MATISSE, in competition in the frame of the M7 ESA call for project (Sanchez-Cano, 2023).

2. THE EARTH

2.1. The Earth's atmosphere

The Earth's atmosphere is made up of different layers, which are distinguished by their temperature profile (Fig. 1.11). At the bottom of the atmosphere is the troposphere, where we live. This part of the atmosphere has an average temperature of 288K and gets colder with altitude, by about 6.5K per kilometre. The troposphere contains about 75% of the total air in the atmosphere and almost all of the water vapour (which forms clouds and rain). The top of the troposphere is called the tropopause. It is lowest at the poles, where it is about 7-10 km above the Earth's surface. It is highest (about 17-18 km) near the equator. From the tropopause up to about 50 km is the stratosphere. It contains most of the ozone in the atmosphere. In this region, the temperature increases with height due to the absorption of ultraviolet (UV) radiation from the Sun by the ozone, with a maximum temperature of about 300K. The ozone layer is formed by the photodissociation of O_2 molecules. Between 50 and 80 km, the temperature drops again to 130-190 K. In this part of the atmosphere, the density is low and the atmospheric constituents lose some of their energy by emitting infrared radiation without heating the medium. This transitional region is called the mesosphere (which does not exist on Mars). Above 80 km, the temperature rises rapidly due to the absorption of solar ultraviolet and extreme ultraviolet radiation by atmospheric constituents. The temperature in this region depends on solar activity and electrodynamic processes in the magnetosphere. It varies from 750 K at low solar activity to over 5000 K at high solar activity. This region is known as the thermosphere. It typically extends up to 600 km, above which the exosphere begins.

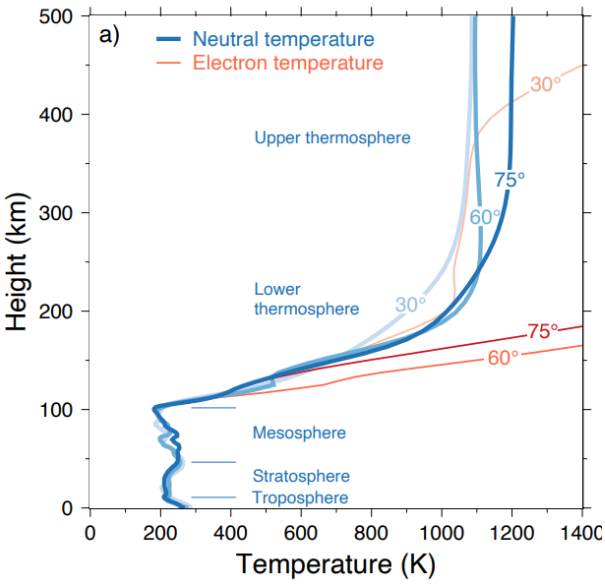

***Figure 1.11**:Temperature profiles from the WACCM-X model at three different geographic latitudes (30, 60 and 75° N).* (Palmroth et al., 2021).

2.2. The thermosphere – Ionosphere on Earth

Above the stratosphere, i.e. above an altitude of 50 km, the atmosphere is characterised by a high density of free electrons and free ions, produced mainly by the energetic photo-ionisation of UV and X-rays from the Sun, and to a lesser extent at high latitudes by corpuscular ionisation. This region of the atmosphere, from the mesosphere to the exosphere (above 600 km), is called the ionosphere. There are three main layers in the ionosphere, called the D, E and F layers. The heights at which they occur vary throughout the day and from season to season. The D region is the lowest, starting at about 60 or 70 km and rising to about 90 km. This is followed by the E region, which begins at about 90 km and extends to 120 or 150 km. The uppermost part of the ionosphere, the F region, starts at about 150 km and extends well upwards. The upper limit of the ionosphere is more difficult to define, but a compromise would be up to 1000 km, where the ionosphere is identified as a transition region to the plasmasphere (Fig. 1.12).

During the day, the solar X-rays and UV light increase the ionisation of the ionosphere, creating the D and E layers, and splitting the F region into 2 layers, F_1 and F_2. On the night side, due to the lack of ionising photons, the D layer disappears completely and the E layer is greatly weakened. The F layer, on the other hand, still exists on the night side thanks to cosmic rays. Because the ionosphere is made up of charged particles, it also reacts to the changing magnetic and electrical conditions in space. These events, such as solar flares, coronal mass ejections or geomagnetic storms, are called space weather and are usually related to solar and geomagnetic activity. Apart from the regular weather here on Earth, space weather is the other major factor affecting the ionosphere.

The neutral component of the D region consists mainly of N_2, O_2, Ar, CO_2, He (Fig1.12) and a highly variable amount of O_3 and H_2O. The ionised component of the D region consists mainly of NO^+ as the major positive charge carrier, with electrons, O_2^- and possibly other negative ions as the negative charge carriers.

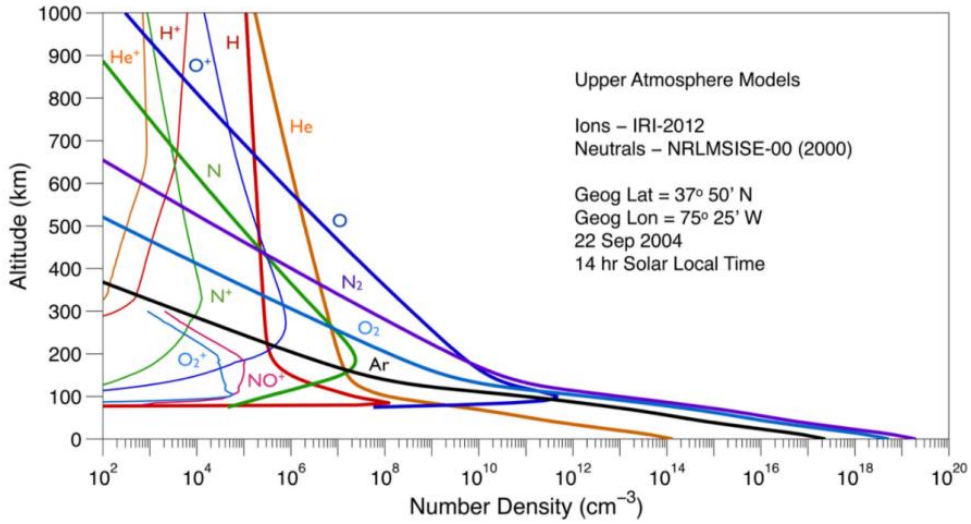

***Figure 1.12**: Typical example of the density altitude profiles of the major ion and neutral species obtained from the NRLMSISE-00 and IRI-2012 models* (Palmroth et al., 2021).

2.3. The Lower Thermosphere and Ionosphere

The lower thermosphere/ionosphere (LTI), located between 100-200 km above the Earth, is a region where the interaction between neutral and ionised gases is a key driver. In this region, the energy and momentum of charged particles, driven by solar wind and magnetospheric interactions, is converted into heat and motion of the neutral atmosphere by plasma-neutral interactions. Geomagnetic disturbances in this region can be sudden, caused by solar phenomena such as flares or coronal mass ejections.

Terrestrial activity plays also an important role in shaping LTI properties. This involves the emission of variable wave fluxes from the lower atmosphere that converge in the LTI. Terrestrial events can range from short-lived, episodic events such as those caused by hurricanes, earthquakes and volcanic eruptions, to more periodic disturbances associated with tides and the cycle of day and night.

The diverse and dynamic energy sources lead to significant changes in the characteristics of the LTI (Fig. 1.13). This includes its vertical and horizontal structure, which are shaped by physical processes that often exhibit irregular and turbulent behaviour (Sarris et al., 2020) (see Fig. 1.14).

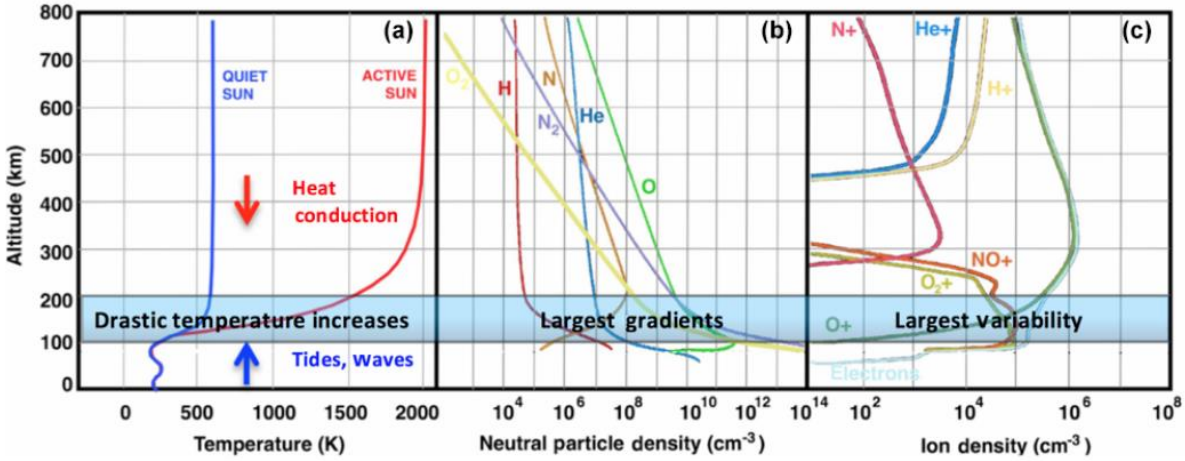

***Figure 1.13**:Simulated key variables in the LTI as a function of altitude: temperature at quiet and active solar conditions: (a) neutral (b) and ion (c) constituents. The altitude range from 100 to 200 km shows the largest rates of change in most variables (Sarris et al., 2020).*

The lower thermosphere and ionosphere are characterised by a complex set of different physical processes, some of which are unique to this region. To achieve a comprehensive understanding of the LTI, it is important to understand how these processes work together as a coherent system. This knowledge is essential to gain critical insight into the Earth's atmosphere-space interface. Interestingly, most of these processes occur in different ways and intensities on Mars, as they also determine the fate of the Martian thermosphere – ionosphere. A more detailed overview of the various processes occurring in the LTI is given in the following sections (see also Fig. 1.14). These physical processes are divided into three groups:

Energetics: This includes all processes and interactions between the charged particles and the neutral constituents that lead to heating and/or energy exchange between species. This

category includes the precipitation of energetic particles and the dissipation of electromagnetic energy by Joule heating.

Electrodynamics is the set of processes associated with the motion of charged particles in the presence of neutral species. Reference is made to Pedersen conductivity, ionospheric Hall currents, auroral and equatorial electrojets, and field-aligned currents.

Dynamics refers to the processes associated with the motion of neutral gases within the LTI. The processes in this category include the effects of plasma-neutral interactions such as ion drag, but also the various forcings from the lower atmosphere (i.e. gravity waves, planetary waves, thermal tides, ...) that dissipate energy on the LTI.

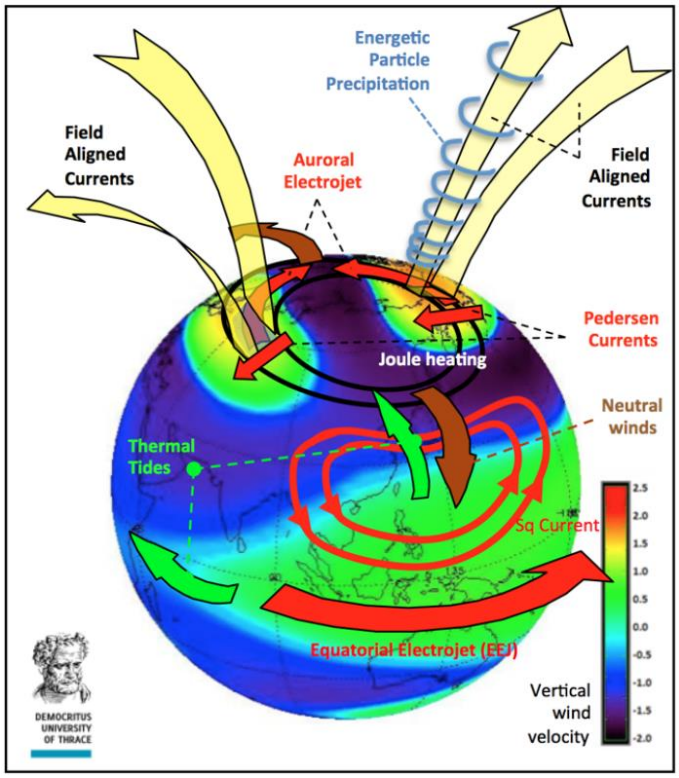

***Figure 1.14**:Overview of the energy deposition pathways in the LTI. (Sarris et al., 2020).*

2.3.1. Heating processes

Within the LTI, there are three primary mechanisms for depositing energy into the thermosphere – ionosphere system: Joule heating (JH), particle (electron and proton) precipitation, and atmospheric forcing. Current understanding suggests that Joule heating is the dominant sink for this energy (Lu, 2016). The effects of this energy deposition on local transport, thermal structure and composition within the LTI altitudes are not well understood at present.

Joule heating occurs in a normal conductor when an electric current is passed through the material with finite resistance. As a result of collisions within the materials, some of the electromagnetic energy is converted to thermal energy, i.e. heat. In the LTI, the same process takes place, but on a planetary scale. Within the LTI, charged particles are transported horizontally through the ionosphere along the geomagnetic field lines. These particles collide

with the neutral constituents, causing a heating of the region. The energy deposition process peaks in the LTI and has a global effect on the structure of the upper atmosphere (Richmond & Lu, 2000), as can be seen in Figs 1.15.

Current estimates of Joule heatinf are mainly based on ground-based measurements associated to global models (Baloukidis et al., 2023), which provide only a subset of the measurements needed to resolve the Joule heating in the LTI (i.e. lack of neutral wind measurements), with limited spatial resolution and lower accuracy compared to in situ measurements.

Precipitating energetic particles are another important source of heat in the 100-200 km region. High energy particles, such as solar energetic particles, have the ability to ionise the lower thermosphere, extending into the lower mesosphere and even the upper stratosphere in the case of solar particles. This ionisation process is crucial as it generates a significant excess of electron density in the LTI.

The effects of energetic particles on the electrodynamics of the LTI are localised, but vary considerably with altitude. The heating of the neutral gas by direct absorption of the kinetic energy of incoming particles represents a heat source estimated by Lu et al., (1995) to be on average about a quarter of the typical Joule heating, although it can be more significant during large auroral events (Thayer & Semeter, 2004).

Energetic particle precipitation also ionises and dissociates neutral molecules through collisions (Sinnhuber et al., 2012). These particle collisions have a direct effect on the chemical composition of the atmosphere via ion chemistry, leading to the production of hydrogen (HOx) and nitrogen oxide (NOx) (Codrescu et al., 1995; Seppälä et al., 2007).

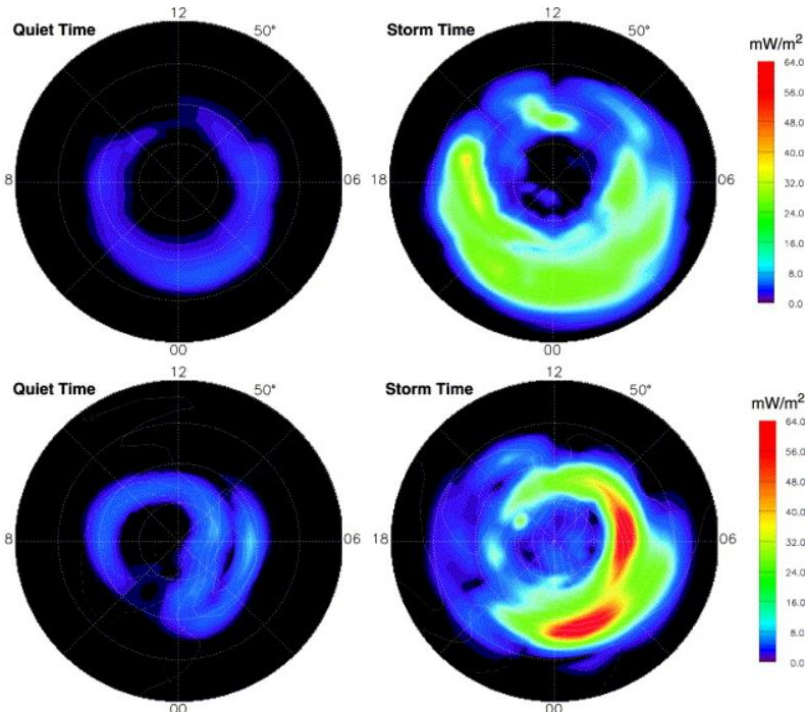

Figure 1.15*: Height integrated joule heating (bottom) and Particle heating (top), during two times on 1997 January 10th: 0255 UT (left), a quiet period, and 1105 UT (right), an active time.*

2.3.2. Dynamic mechanisms

LTI dynamics refers to the motion of plasma and neutral gases in relation to the forces that drive and affect them. In the LTI, external influences from the magnetosphere, atmosphere and solar effect have a significant and far – reaching effect. These influences are closely linked to the exchange of momentum between charged and neutral elements, resulting in vertical and horizontal momentum transport.

Atmospheric waves emanating from the lower atmosphere are considered to be the main driver of LTI neutral particle dynamics. The excitation of such waves can take the form of thermal tides synchronised with the regular solar differential heating, with periods corresponding to the 24h diurnal periods (and harmonics, i.e. 12h semi-diurnal). Atmospheric waves also result from the gravitational interaction of the Earth-Moon system with a period of 12.4h. The wind amplitude due to the lunar tidal effect is about 0.03 $m.s^{-1}$ at the surface and increases with altitude up to about 110 km, where it reaches an amplitude of the order of 10 $m.s^{-1}$ (Hagan et al., 2003).

Small-scale gravity waves, induced either by topography or by meteorological (and geological) events (Fritts & Alexander, 2003) are at the origin of momentum deposition in the LTI. Their amplitudes increase exponentially with altitude due to the decrease in atmospheric density (Andrews et al., 1987). These large wave amplitudes lead to wave breaking, which causes a change in temperature in the LTI region. As a result of this forcing, LTI transport is known to be affected, for example by the formation of vertical wind shears above the mesopause (Fig. 1.16) (Liu, 2007) and by the triggering of plasma instabilities in the equatorial ionosphere (Hysell & Kudeki, 2004; Kelley, 1989).

Thus, gravity waves have a significant impact on the momentum budget of the LTI. Understanding their influence depends on quantifying their power at different spatial scales. While current high-resolution models consider larger scales (200 km and above), the intermediate scales (20-200 km) play a crucial role in the global momentum budget. Smaller scale gravity waves (2-20 km) may also be important, as suggested by regional simulations (Becker, 2004). There are no comprehensive and systematic observations of the neutral-ion coupling in the LTI.

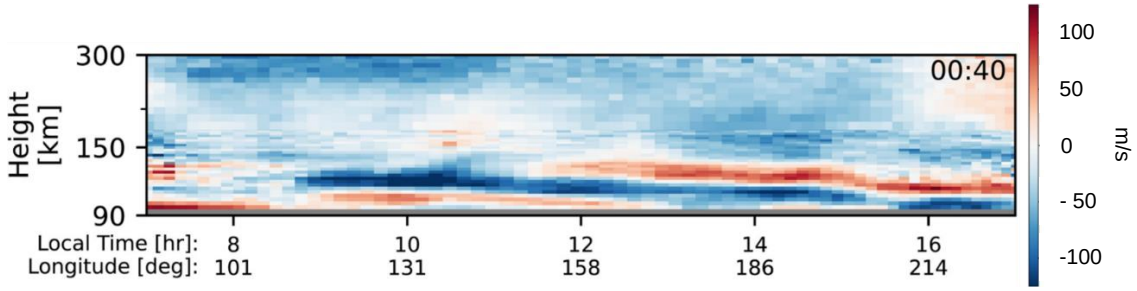

***Figure 1.16**: Daytime zonal winds observed with ICON/MIGHTI during one orbit on Mars 20th 2020.* (England et al., 2022). *The latitudes of observations are in the 30°N - 40°N range. The alternating positive and negative wind direction highlights the significance of the vertical shears present in the 100 -150 km region.*

The atmospheric dynamo is a pattern of electrical currents created in the Earth's ionosphere by a variety of effects, most the solar wind, but also the Moon's and Sun's tides. Atmospheric currents are generated by the motion of neutral gases, or winds (Fig. 1.17). These winds, through collisions with ions, drag the ionospheric plasma along the surrounding magnetic field. This process leads to the creation of a current density. In the lower ionosphere (at altitudes of 90-140 km), the behaviour of ambient ions is mainly determined by collisions. Electrons, on the other hand, are influenced by the magnetic field. Tidally driven neutral winds form a fundamental system of global dynamo currents in the LTI region between 100-140 km altitude (Richmond, 1979). However, due to a lack of measurements, their properties are not understood, including how their associated polarising electric fields and field-aligned currents influence the plasma motions at higher altitudes.

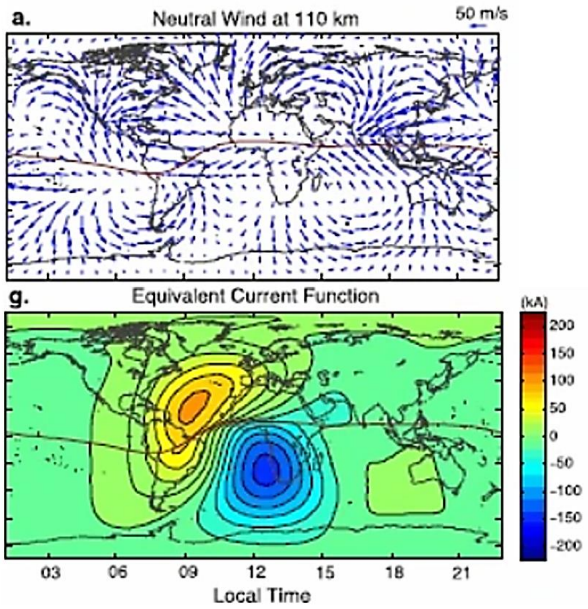

***Figure 1.17**: TIE-GCM simulation results for magnetically quiet equinox conditions (Kp=0), at 12:00 UT. The Top panel is the neutral winds at 110km while the bottom panel gives the current distribution at the same altitude. Adapted from* (Yamazaki & Maute, 2017).

The magnetospheric forcing in the LTI is due to the interaction of the geomagnetic field with ionospheric charged particles. There is a diverse and complex landscape of these interactions, which are detailed in Fig. 1.18. These include the auroral electrojet (a system of horizontal electric currents at high latitudes), the field-aligned currents that electrodynamically link the magnetopause, the inner magnetosphere and the ionosphere. Another broad category of magnetospheric effects includes various waves (e.g. Alfven waves, electromagnetic cyclotron, ...) that are driven by the solar wind-magnetosphere interaction and drive energetic particle precipitation.

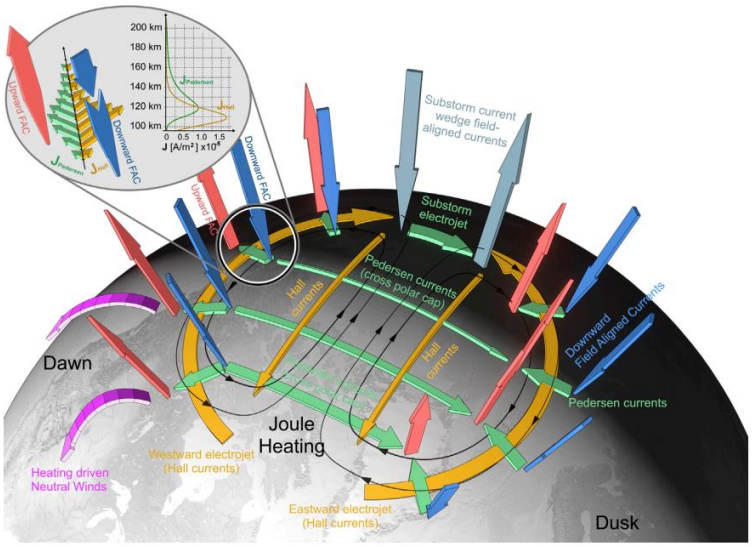

***Figure 1.18**: The magnetospheric driven current system in the ionosphere polar regions* (Sarris et al., 2023).

Solar flares and **coronal mass ejections** are also known to enhance the electron density and hence the JH in the LTI (see Fig. 1.18). The modification of the auroral electrojets by solar flares can be of an extreme enhancement. The European Incoherent Scatter (EISCAT) radar observations suggest that even the height of the JH can be modified by these events (Forme et al., 1998). It is quite possible that the height of the ionospheric current also changes, but no measurement method has been proposed to prove this.

2.4. Measurement gaps in the LTI

Scientific studies of the lower thermosphere-ionosphere (LTI) have faced challenges due to the limited in situ data available. In the 1970s, the Atmosphere Explorer (AE) satellites made some of the first measurements in this region, reaching altitudes as low as 140 km (Spencer et al., 1973). However, interpretation of measurements at these altitudes was complicated by the measurement conditions, particularly for composition. Since then, in situ measurements within the LTI have been sporadic, mainly from sounding rockets (Abe et al., 2006; Cohen et al., 2020; Earle et al., 2013), and have provided only snapshots at specific locations. Density measurements down to 130 km have been estimated from the decay of low-altitude sounding satellites (Ching & Rugge, 1975), providing insights into the lower thermosphere. However, details of the electrodynamics and composition of the transition region between 100 and 200 km remain unclear. At higher altitudes, spacecraft such as CHAMP (Alken & Maus, 2010), DEMETER (Berthelier et al., 2006), GRACE (Tapley et al., 2006) and C/NOFS have provided data on electric fields and density (Fejer et al., 2013).

Consequently, much of our information about this region comes from remote sensing, including satellite-based observations and ground-based experiments such as lidars (Chen & Chu, 2023). While these techniques have contributed significantly to the LTI science, they have limitations. For example, **measurements of neutral density, composition and temperature are currently difficult or inaccurate at 100-200 km** due to weak radiance and non-thermal effects. Determination of the major species composition relies on a combination of ultraviolet, infrared (Mlynczak et al., 2018) and Fabry-Pérot interferometer measurements (Nakamura et al., 2017),

but there's a gap in the profiles available at about 100-200 km due to a lack of suitable emissions to observe. In addition, different observational methods can give significantly different estimates of key parameters in the LTI, such as conductivity, ion drifts and neutral winds, without a standard dataset for comparison.

Three main questions remain to be answered to gain a better understanding of the Earth's lower thermosphere and ionosphere:

1. What is the mechanism and extent of energy deposition by Joule heating in the LTI? How does this heating affect and interact with the thermal structure, local transport and composition within the LTI heights? Furthermore, how does the magnitude, extent and how the evolution of this heating affect the neutral density?

2. How does energetic particle precipitation (EPP) affect the ionisation and composition of the LTI? To what extent does EPP extend its influence into the lower atmospheric layers?

3. What factors contribute to the momentum balance within the LTI, considering the different contributions of magnetospheric, solar and atmospheric forcing? How do these external forcing affect the fluid and electrodynamics at high, middle and low latitudes? How do collisions between charged particles and neutral gases in the LTI influence the density, composition, winds and drifts in this region?

SUMMARY

In an exosphere, the outermost layer of an atmosphere, collisions between particles no longer have a significant effect on the fate of the particles. At Mars this region is populated by thermal and non – thermal particles, the latter being produced by the mechanisms potentially at the origin of Mars' past evolution. Among these non – thermal exospheric populations, the atomic oxygen is particularly relevant to reconstruct the past fate of Mars' water. Previous missions to Mars have provided a fairly good picture of the escape processes acting at Mars. However, no direct measurements of the energetic structure of the suprathermal neutral corona of Mars have been made to date, limiting our capacity to accurately extrapolate back in time the efficiency of these processes to erode Mars' atmosphere. The atmospheric escape mechanisms are indeed essentially controlled by our Sun and occurs in Mars' thermosphere – ionosphere. Understanding how the solar forcing, but also the lower atmosphere, influences this region is essential to reconstruct Mars' present and past climate.

At the Earth, we have highlighted the importance of a similar key region, the lower ionosphere-thermosphere. In this region, located between ~100 – 200 km, interaction processes couple the neutral atmosphere to the charged populations. As at Mars, the LTI is forcibly coupled from above by interactions with the solar wind and the Earth's magnetosphere, and from below by energy transport from various types of atmospheric waves. Until now, much of our information about this region has come from remote sensing, including satellite remote sensing, and ground observations combined with some sporadic in-situ measurements from scientific rockets. However, only in-situ investigations will provide the desired measurements at these critical altitudes, with the necessary range of spatial and temporal scales. A complete picture of the Lower Thermosphere and Ionosphere (LTI) is crucial because of its direct impact on modern technology-based activities.

Overall, the characterisation of thermospheres – ionospheres and exospheres appear fundamental to both space science and practical applications, with implications for various aspects of space exploration (not only at Mars and the Earth), and on our broader understanding of the Solar System.

CHAPTER 2
MASS SPECTROMETRY FOR SPACE EXPLORATION

1. INSTRUMENT OBJECTIVES

1.1. At Mars

In the previous chapter we described the environment of two planetary bodies with very different interaction with the solar wind: The Earth and Mars. In the case of Mars, the erosion of its atmosphere remains a fundamental question for understanding the evolution of the planet. One of the first difficulties in reconstructing atmospheric escape is to be able to determine the physical mechanisms behind them. In the region's most suitable for observing these phenomena (the exosphere and the upper atmopshere), particles of different types coexist: supra-thermal and thermal. Using Argon as a tracer to determine the density profile induced by either the thermal contribution or the suprathermal populations, it has been showed using MAVEN/NGIMS (Mahaffy, Benna, et al., 2014) that below 350 km, the thermal component dominates while at higher altitude, as illustrated in Fig. 2.1, the measured Ar is mainly due to non-thermal populations (Leblanc et al., 2019).

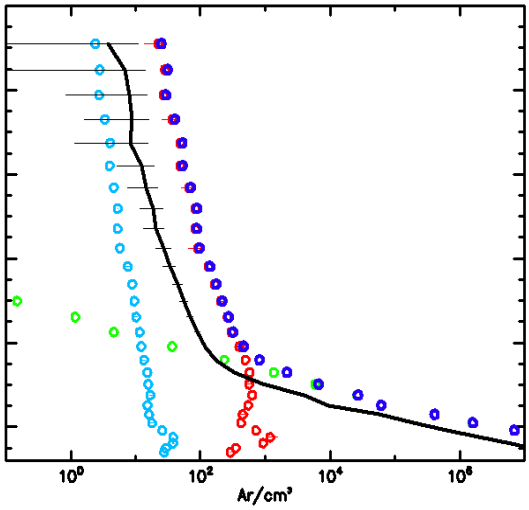

Figure 2.1*: Comparison between a density profile measured by NGIMS (black line) and the Exospheric Global Model (EGM) simulated density profiles. The green, light blue, and red symbols depicts the thermal, pickup sputtering, and induced dissociative recombination simulated components of Ar respectively. The darker blue symbols are the sum of the three populations. (Adapted from Leblanc et al., 2019).*

Moreover, simulations with the Exospheric Global Model (EGM) suggest that atomic oxygen in the exosphere due to sputtering (see Section 3.2 of Chapter 1) is difficult to identify on the dayside. With the dissociative recombination (see Section 3.2 of Chapter 1) being the main driver of hot O escape by at least 2 orders of magnitude compare to sputtering, it remains difficult to detangle the two processes. However, in the night side, DR efficiency is strongly reduced. The ionospheric density being much smaller, the rate of DR and the flux of escaping O atoms due to DR is much reduced with respect to the dayside. As a consequence, EGM simulations showed that the exosphere might be dominantly populated by sputtering at high Solar Zenith Angle (SZA) where nonthermal processes are less efficient (Fig 2.2) (Leblanc et al., 2017).

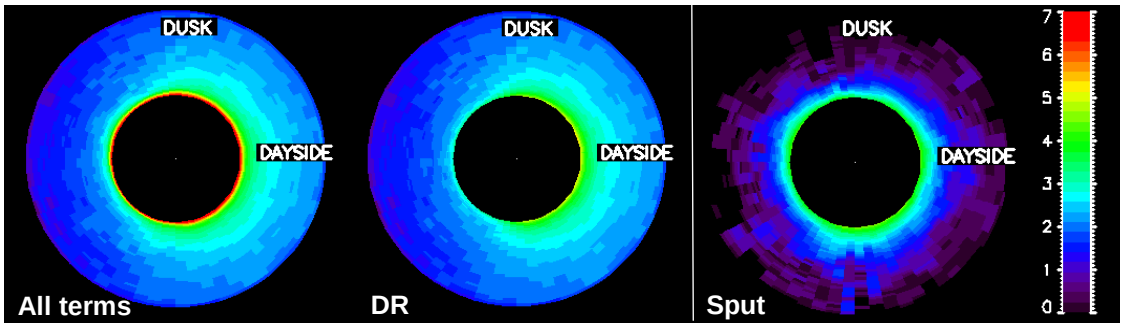

***Figure 2.2**: Equatorial density of O atoms simulated by the EGM with the sum (left) of dissociative recombination (middle), sputtering (right) and thermal populations (not showed). Adapted from Leblanc et al., 2017.*

The simplest approach to observe these supra-thermal particles is therefore to carry out a high-altitude measurement. This however, corresponds to altitudes where the densities become very low (between 10 and $10^5\ cm^{-3}$, see Fig. 2.2). The only way to be sure of measuring suprathermal particles is to be able to achieve a differential measurement that distinguish the energy signature of the non-thermal particles from the thermal population.

Moreover, it is possible to disentangle the contribution of each escape process by looking at their energy distribution. According to Cipriani et al., (2007), dissociative recombination's energy distribution is limited to 5eV while sputtering reaches beyond 15eV (see Fig 2.3). By measuring particle energy levels ranging from 0.1-10 eV, distinction between the two processes and their corresponding contributions can be made.

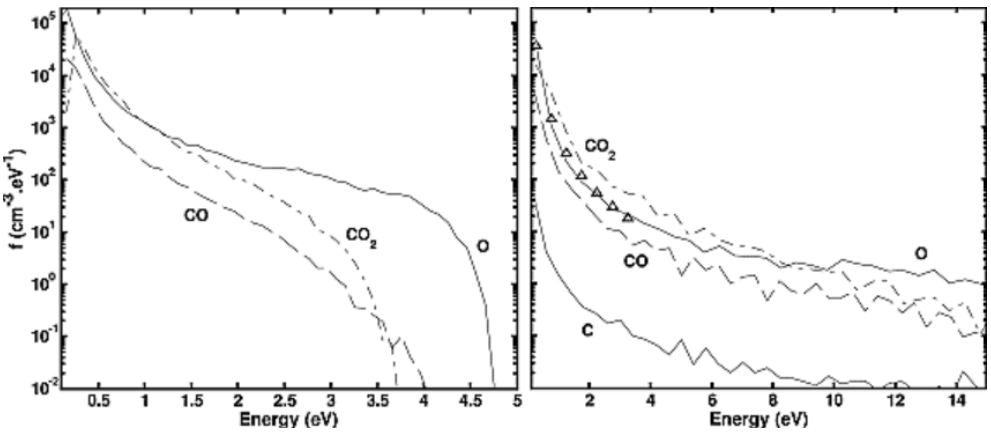

***Figure 2.3**: Energy distribution of hot atoms and molecules created by sputtering (right side) and dissociative recombination (left side) at 200 km at high solar activity (Cipriani et al., 2007).*

Thus, to directly characterize the neutral hot population in the Martian upper atmosphere and exosphere we need an instrument able to:

- Determine the nature of the majority constituents in the upper atmosphere and exosphere, i.e. their mass, with a resolution of the order of 20.
- Measure energies over a range from 0.1 to ~10 eV to differentiate between thermal and suprathermal particles. A resolution better than 0.1 eV is required to reconstruct the distributions as suggested by Cipriani et al. (2007).
- Measure in environments with low densities (from 10^8 to $10^2 cm^{-3}$).

1.2. At the Earth

Measurements required to characterise the Earth's LTI (Section 2, Chapter 1) requires a broad range of different instruments. Ground-based remote sensing facilities have been providing continuous measurements of key LTI parameters as a function of altitude and local time, and are currently the main source of information on the ion-neutral interactions across the LTI (Günzkofer et al., 2022; Tesema et al., 2022). There are however limitations of remote sensing methods in addressing the science questions outlined in Chapter I. Table 2.1 outlines the geophysical observables needed to address the science questions listed previously (Pfaff et al., 2009).

Table 2.1 *: Observables needed to address the LTI science questions. The orange box corresponds to the quantities targeted for our applications.*

Observable	Range	Resolution
Electric field	0 – 500 mV/m	0.1 mV/m
Magnetic field	0 – 65000 nT	10 nT
Energetic electrons		
0 – 20 eV	10^8 – 10^{12} eV/cm^2/s/st/eV	ΔE/E = 0.15
20 eV – 30 keV	10^6 – 10^{10} eV/cm^2/s/st/eV	ΔE/E = 0.15
30 keV – 300 keV	10^4 – 10^8 eV/cm^2/s/st/eV	ΔE/E = 0.25
Energetic ions		
20 eV – 20 keV	10^5 – 10^9 eV/cm^2/s/st/eV	ΔE/E = 0.15
20 keV – 1 MeV	10^3 – 10^7 eV/cm^2/s/st/eV	ΔE/E = 0.25
Plasma density	10^2 – 10^7 cm^{-3}	± 1%
Ion & Electron temperature	300 -10000 K	± 5%
Neutral Density	10^6 – 10^{12} cm^{-3}	± 10%
Neutral temperature	300 – 5000 K	± 5%
Neutral & Ion composition	Relative concentration	± 1%
Ion velocity	0 – 3 km/s	3 m/s
Neutral velocity	0 – 5 km/s	5 m/s

The distribution and magnitude of the neutral winds is a key parameter in accurately estimating the energy budget and determining the dynamics in the LTI: for example, Joule heating has a neutral wind contribution which can be either positive or negative (Lu et al., 1995), and which can be significant. As some rare co-located in situ rocket and trail-gas measurements indicate (Sangalli et al., 2009), the effects of the neutral winds can be significant but can only be evaluated by temporal and spatial measurements of all the relevant parameters, which cannot be provided by ground-based remote sensing measurements. Furthermore, an in-situ platform allows to examine neutral density structuring and compositional changes and, importantly, to determine the causes of these variations, which cannot be determined remotely.

Summarizing the requirements described at Mars and at the Earth, such instrument should ideally achieve the performances listed in Table 2.2:

***Table 2.2**: Instrumental objectives to achieve for the characterization of both the Earth and Martian thermosphere – ionosphere.*

Observable	Range	Resolution
Density	$10^2 - 10^{12}\ cm^{-3}$	10%
Temperature	150 – 2000 K	~10K
Velocity	0 – 3 km/s	~5 m/s
Composition	0 – 60 amu	~20

As we shall see in the following, these are very challenging instrument performances to achieve with the existing space instruments. We can classify into two categories such instruments, remote sensing ones, which do not answer the need to combine several observations as highlighted for the Earth, or in-situ instruments. We will therefore focus on this latter category and in particular on mass and energy spectrometry, the only measurement technic able to address the measurement objectives listed in Table 2.2.

2. EXISTING MASS AND ENERGY SPECTROMETRY TECHNICS

A mass spectrometer dedicated to the measurements of neutral atmosphere consists of two parts: the ionisation source and the analyser. The source is used to ionise the compound so that it can then be analysed. The analyser part determines the mass and/or energy of the particles entering the instrument using various methods.

2.1. Mass analyser

2.1.1. Magnetic sector mass spectrometer

A magnetic sector mass spectrometer is a type of mass spectrometer that uses magnetic fields to separate and analyse ions based on their mass-to-charge ratio (m/z). It is called a "sector" mass spectrometer because it employs magnetic (B) sectors to achieve this separation.

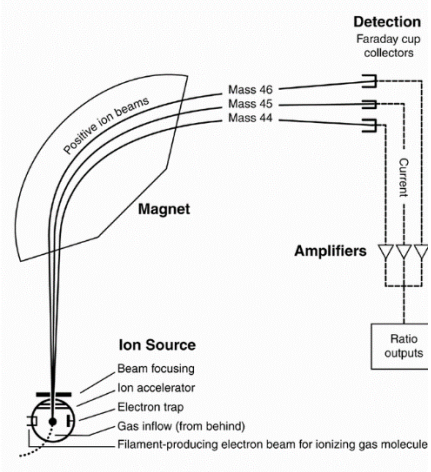

***Figure 2.4**: operating principle of a magnetic sector mass spectrometer (Clark and Fritz; 1997).*

The motion of particles in the instrument is ruled by the Lorentz force law:

$$\vec{F} = q_c(\vec{v} \times \vec{B}) \qquad 2.2.1$$

with q_c the particle charge, $\vec{v}$ its velocity and $\vec{B}$ the magnetic field in the magnetic sector. Thus, the magnetic field bends the ion beam in an arc where its radius *r* depends upon the momentum of the ions $m_c\vec{v}$ (m_c being the ion mass).

$$r = \frac{m_c v}{q_c B} \qquad 2.2.2$$

As a consequence, ions with larger momentum will follow an arc with a larger radius. The inconvenient of such instrument is that its resolution is strongly affected by the energy distribution at the entrance of the magnetic sector. Thus, usually this type of instruments is coupled with a narrow band electrostatic filter and an acceleration optic which homogenize the ion beam velocity. The other con of such concept, that is specific to space application, is the extensive size and mass of the instrument (i.e. DFMS with dimensions of 63 x 63 x 26 cm and

a mass of 16.2 kg, excluding the DPU, see also Section 3.2.1) (Balsiger et al., 2007). However, such architecture of mass spectrometers allows to reach very high resolution (>3000 for DFMS) on a broad mass range (0 – 150 amu for DFMS).

2.1.2. The quadrupole

A quadrupole is made of 4 rods with a cylindrical or hyperbolic cross-section placed symmetrically and that are positioned equidistant from a centre axis. Each pair of opposite rods is connected to each other. Between the two pairs of rods, an electrical voltage consisting of a DC component U and an AC portion with amplitude V at frequency $f = \frac{\omega}{2\pi}$ is applied.

$$U_{quad}(t) = U + V.\cos \omega t \qquad 2.2.3$$

The variation $-U_{quad}(t)$ is applied to the other pair. The ions are introduced at one end of the analyser along the axis of the quadrupole. The high-frequency continuous fields, whose directions are perpendicular to the filter axis, impart an oscillatory lateral movement to the ions. The movement of the ions is described by the so-called Mathieu equations (March, 1997), being in a certain m/z ratio band having a stable trajectory and reaching the other end of the analyser, the other ions being intercepted by the electrodes. This m/z ratio depends on the distance between the electrodes, the frequency f and the voltages U and V.

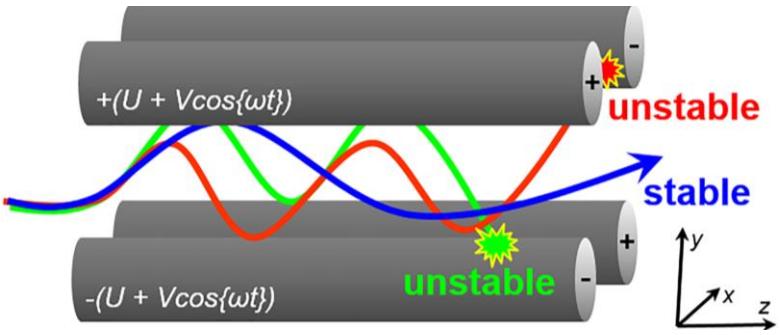

***Figure 2.5**: Trajectories of stable (blue) and unstable ions in a quadrupole mass spectrometer* (Arevalo Jr et al., 2020).

In practice, since d and f are constant, only the voltages U and V vary. By sweeping the amplitudes of the DC and high-frequency voltages applied to the electrodes, the ions are detected successively in ascending order of the values of the m/z ratio, with constant resolution. The disadvantage of this instrument, is that it has to scan in voltage to be able to cover a range in mass. The resolution R of quadrupole mass analysers is directly proportional to the number of RF cycles (n) that an ion undergoes. Increasing the RF frequency is a means by which quadrupole resolution can be optimized. R is defined as follow:

$$R = \ n^2 = \frac{m_c f^2 L^2}{q v_c} \qquad 2.2.4$$

Where m_c is the ion mass, V_c its velocity and L the rod length.

For space applications, typical resolution is the unit mass resolution over the full measurement range that is ~1 – 150 amu; i.e. CASSINI/INMS (Waite et al., 2004), MAVEN/NGIMS

(Mahaffy, et al., 2014a), LADEE/NMS (Mahaffy, et al., 2014b). The main advantages of this type of instrument are its high reliability and relatively small size.

2.1.3. Time of flight analyser

A Time-of-flight (TOF) analyser operates on the simple principle that ions accelerated to the same kinetic energy ($E = ½mv^2$) will separate according to their respective *m/z ratio* in a field-free drift region. The speed of the particle after being accelerated is linked to the acceleration voltage. The particle's potential energy is transformed into kinetic energy:

$$U \times q = \frac{1}{2} m_c v_c^2 \qquad 2.2.5$$

Where U is the acceleration potential, q the particle charge, m_c its mass and v_c its velocity.

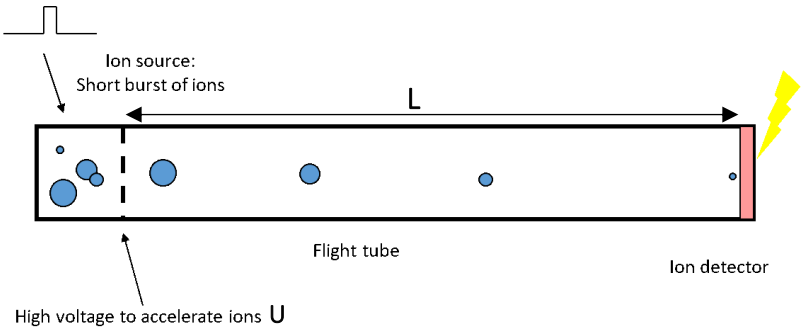

***Figure 2.6**: A simplified diagram of a time-of-flight mass spectrometer (Credit: JEOL USA).*

Lower m/z ions travel at larger velocities than higher m/z ions, resulting in separation based on the time it takes for each species to reach the detector (Fig. 2.6). Unlike quadrupole and sector field instruments, TOF mass spectrometers do not scan across a mass range to collect a mass spectrum but rather collect an entire spectrum via pulsed operations. Knowing the distance between the analyser input where a stopwatch is started when the particles enter the analyser and the arrival at the detector where the stopwatch is stopped, the m/z ratio can be determined, as:

$$\frac{m}{z} = \frac{2Ut^2}{L^2} \qquad 2.2.6$$

Where t is the elapsed time between the entrance of the particle in the analyser and its arrival on the detector, L is the length travelled by the particle and U the acceleration voltage (see Fig 2.6).

Ideally, given the same extraction or acceleration potential U and a fixed length of field-free drift path L, ions of different *m/z* derived from the same pulsed source will arrive at the detector at distinct but predictable times. However, in reality, ion arrival times at the detector also contain variances stemming from the exact timing and positioning of individual ion formation, as well as divergent initial velocity vectors (direction and magnitude) with respect to the detector, i.e, nonuniform temporal, spatial, and initial kinetic energy distributions, respectively (Wiley and McLaren, 1955). The influence of each of these deviations may be minimized

through specific combinations of hardware but the cumulative effect of these delays contributes to the width of spectral peaks, thereby controlling the mass resolution, which is defined as:

$$R = \frac{\Delta m}{m} = \frac{t}{2\Delta t} \qquad 2.2.7$$

where Δt is the peak width measured at FWHM (Satoh et al., 2005).

To improve the resolution, an ion optic device called a reflectron (or ion mirror) can be used. It makes use of an electrostatic field to reflect ions through a small angle towards a detector. On one hand, the particles travel a larger distance than in the case of a linear time of flight analyser, which makes it possible to better separate the arrival times at the detector. On the other hand, ions with the same m/z ratio but with a slightly higher kinetic energy penetrate deeper into the reflector, delaying their time of arrival at the detector relative to the slower low-energy ions (see Fig. 2.7). This results in improved resolution and increased mass accuracy.

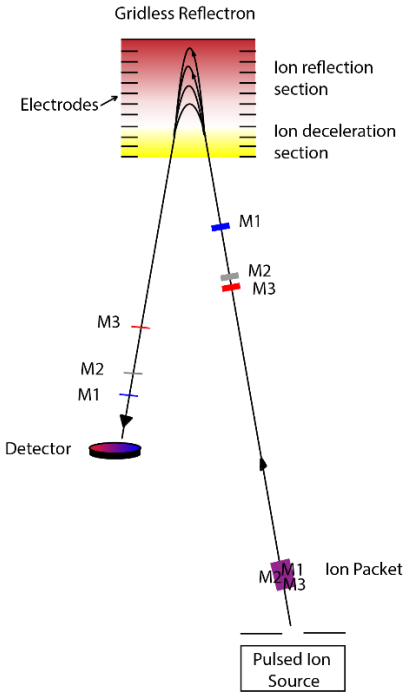

Figure 2.7*: Trajectories of ions through a reflectron analyser. The temporal distribution of the ions with different m/z ratio is represented by the width of the coloured box. We can observe that after passing through the reflectron, ions TOF are more separated and the boxes' width are smaller. (Credit: Auburn University).*

The team of MASPEX/Europa Clipper (Brockwell et al., 2016) has pushed the concept of the reflectron time of flight to its extreme by developing an instrument capable of modulating the number of backs and forth using a dual reflectron. In the highest resolution mode, they have achieved resolution slightly lower than 24000 with ~60 bounces. More classical RTOF instruments achieved resolution varying between 40 and – 500 depending on the scientific objectives (Scherer et al., 2006).

2.1.4. The ion trap

Ion trap mass spectrometers use a combination of electric or magnetic fields to capture or "trap" ions. There are multiple configurations of ion traps including 3D ion traps (the Paul ion trap), and electrostatic trap (Orbitrap), or a magnetic field-based trap (ion cyclotron resonance).

The 3D ion trap basically works on the same principle as a quadrupole mass analyser, using static DC and RF oscillating electric fields, but the hardware is configured differently, where the parallel rods are replaced with two hyperbolic metal electrodes (end caps) facing each other, and a ring electrode placed halfway between the end cap electrodes; ions are trapped in a circular flight path based on the applied electric field.

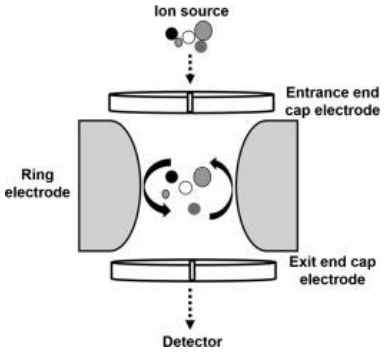

***Figure 2.8**: Schematics of 3D ion trap (Credit: Stefani N. Thomas)*

An orbitrap mass spectrometer consists of an inner spindle-like electrode and an outer barrel-like electrode. The orbitrap stores ions in a stable flight path (orbiting around the inner spindle) by balancing their electrostatic attraction by their inertia coming from an RF only trap. The frequency of the axial motion (*z* axis in Fig. 2.9) around the inner electrode is related to the m/z ratio of the ion. This technique is highly efficient since mass resolution up to 1 000 000 where achieved (Denisov et al., 2012)

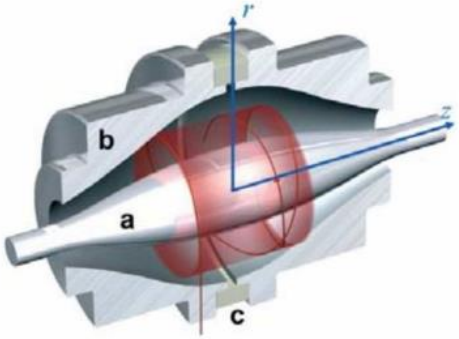

***Figure 2.9**: Sectional view of an orbitrap analyser, consisting of an internal electrode (a), an external electrode (b) split in two and held together by a ceramic ring (c). (Credit: American laboratory).*

Since 2009, a series of R&T programs has been undertaken by a consortium of five French laboratories (LPC2E, LISA, LATMOS IPAG, and CSNSM) to evaluate the potential of in situ

planetary investigation using an Orbitrap. A mass resolution of about 474,000 has been achieved with the laboratory model LAB-Cosmorbitrap (Briois et al., 2016).

The last ion trap, the **ion cyclotron resonance** (ICR) traps use a strong magnetic field to induce a radial orbit of ions, where the frequency of orbit in the magnetic field is a function of the m/z ratio. For both orbitrap and ICR traps, their strength is the ability to trap all ions at once and detect them on the basis of their detected frequencies—a Fourier transform algorithm is required for this signal processing. Mass spectrometers that include an ion trap analyser are most commonly used for qualitative work (identification of the composition).

2.2. Energy analyser

Different methods are used to measure the kinetic energy distribution in a charged particle beam onboard satellites. The first involves applying a retarding electrostatic field along the beam. Then, only particles with kinetic energies larger than the retarding potential difference multiplied by the particle charge will pass through this field. By changing the retarding potential difference and measuring the current at the detector placed behind the field region, one can analyse the distribution of the kinetic energy in the beam. At present, most charge particle energy analysers, for space applications, use the second method: deflecting particles in electrostatic fields. Electrostatic fields are most suitable to cover large ranges of energy from eV to keV, retarding potential analyser targeting ionospheric plasma at low energies. Magnetic energy analysers are used only for measuring kinetic energy distributions in high-energy beams, in which case achieving the necessary electrostatic field strengths is technically difficult.

2.2.1. Retarding potential Analyser

Retarding Potential Analysers (RPA) are built using three to four mesh grids (Fig 2.10). These grids are arranged in alignment within a conductive housing, and with a collector positioned behind them to serve as a detector.

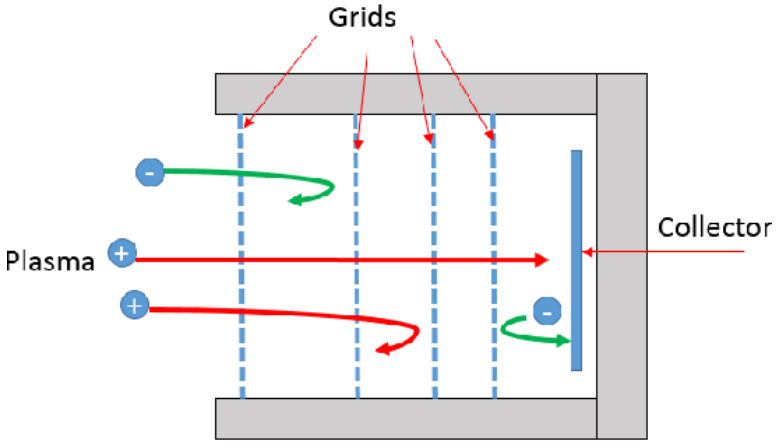

Figure 2.10:Schematic of a 4 grids RPA (Ferda, 2015).

The first grid is grounded. The second grid in the RPA is held at a negative potential, which repels the electrons while allowing ions to pass through. The third grid of the RPA has a variable voltage applied, starting from zero volts and increasing to a high positive voltage. This voltage sweep discriminates between ions of different energies. Initially, at low potential, all ions pass

through. However, as the potential increases, lower energy ions are gradually blocked, resulting in fewer ions passing through all four grids. The fourth grid in the RPA is considered optional. It serves as a secondary electron repulsion grid, stopping any electrons that may have been created by the particle bombardment within the RPA and repelling any secondary electrons produced on the collector. This fourth grid push back secondary electrons to the collector elecctrode and thus provide an accurate current. Finally, after passing through all the grids, the ions encounter a detector and generate a current on the collector. This current is measured in relation to the voltage of the discriminator grid (third grid).

The relationship between the energy distribution function $f(E)$ and the measured current as a function of the discriminator voltage $I_c(V_d)$ is given by:

$$I_c(V_d) = -\frac{q_c^2 n_i A_{probe}}{m_i} \int_{q_c V_d}^{\infty} f(E)\, dE \qquad 2.2.8$$

where n_i is the ion density, m_i the ion mass and A_{probe} the RPA aperture.

By differentiating Eq. 2.2.8, the energy distribution can be reconstructed (see Fig. 2.11).

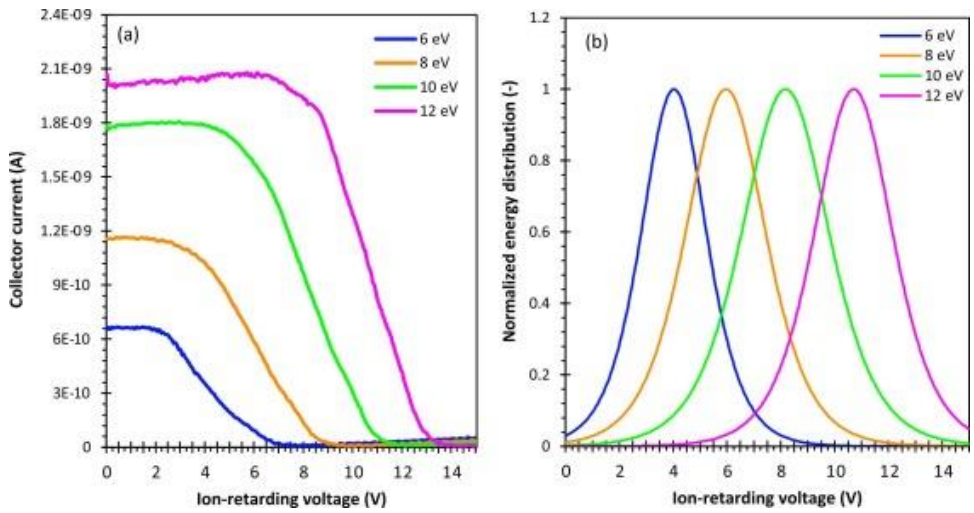

***Figure 2.11**: Examples of different IV curves and the estimated ion energy distributions using an RPA (Izquierdo-Reyes et al., 2022).*

Retarding potential analysers have been used for space mission such as the instrument IAP on board DEMETER (Berthelier et al., 2006) which was designed to measure the characteristics of the thermal ions in the Earth ionosphere (i.e. ram velocity and temperature).

2.2.2. Cylindrical energy analyser

Electrostatic optics are generally used to deflect the ion beam for energy scanning (same process as for magnetic analysers, expect that the deflection is based on energy rather than momentum). The simplest geometry is the circular electrostatic analyser (CEA), which allows energy selection with a certain bandwidth. The analyser consists in two curved parallel plates with the outer shell being at a higher potential than the inner one. The resulting E – field is then radially oriented toward the axis of symmetry of the cylinder (see Fig. 2.13). Ions enter the analyser at one end and either reach the other end or collide with the walls of the analyser, depending on their initial energy. In this type of analyser, only the radial velocity component of the charged particle is affected since the potentials between the plates only varies in the radial direction.

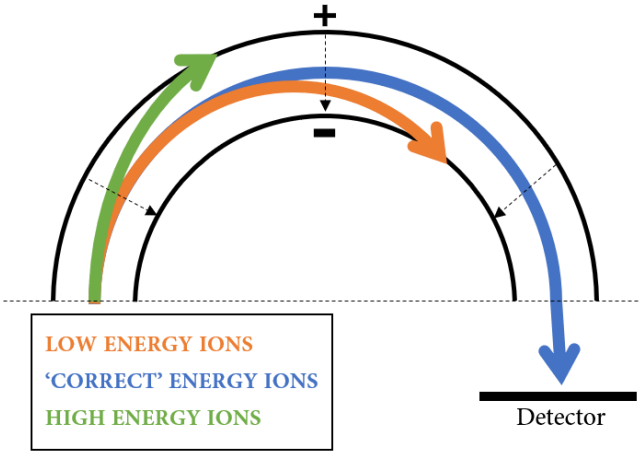

***Figure 2.12**: Operating principle of a cylindrical energy analyser. The dotted arrows illustrate the direction of the electric field.*

This type of analyser is more often used in its 3D version: the hemispherical energy analyser in the top-hat configuration. This geometry, illustrated in Fig 2.13, was designed by Carlson et al. (1983). The "top hat" consists of two spherical electrodes where the particles enter the instrument and are deflected according to their energy. It is based on the same principle as the cylindrical energy analyser, but offers a field of view of 360° around the axis of revolution and a few degrees of angular aperture. At the output of the analyser, a detector is placed to define the direction of arrival of the particles in the plane perpendicular to the axis of symmetry. It is also possible to complete the top hat analyser by adding a mass spectrometer after the energy anlyser (i.e. Mars 96/DYMIO (Berthelier et al., 1998); MSA/BepiColombo (Delcourt et al., 2016); CASSINI/CAPS (Young et al., 2004)).

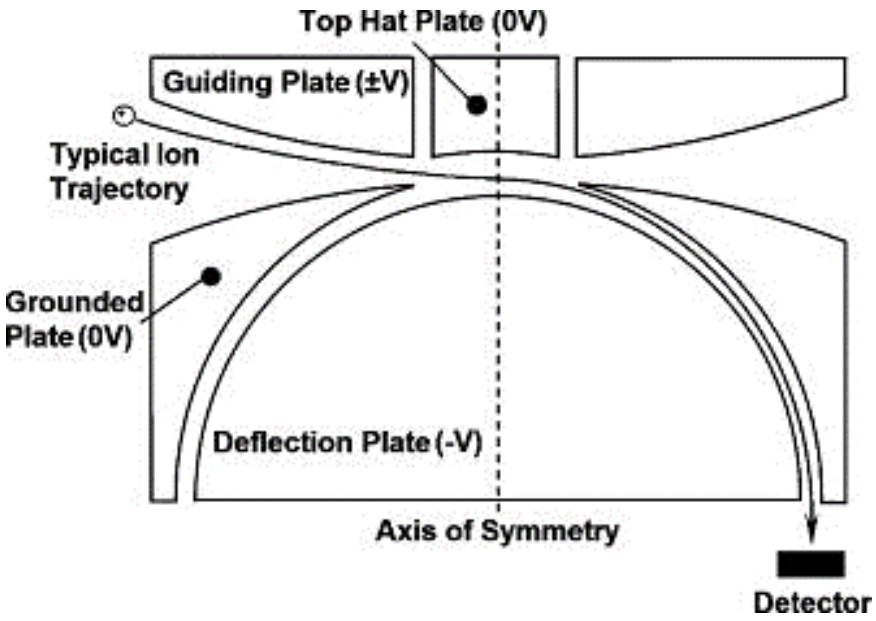

Figure 2.13*: Major components and a typical ion trajectory for a top hat electrostatic analyser (Victor et al., 2006).*

The most important criterion of the 'top hat' analyser is the ratio of the mean channel radius R_c of the spherical electrodes to the gap distance between the two electrodes ΔR, which defines the so-called analyser constant K (Victor et al., 2006):

$$K = \frac{R_c}{\Delta R} \qquad 2.2.9$$

This constant K determines few parameters of the analyser among which its energy resolution. The relationship between the deflection voltage V_d, the analyser constant and the measured E/z ratio is (Victor et al., 2006):

$$\frac{E}{z} = -\frac{KV_d}{2} \qquad 2.2.10$$

Usually, the top hat instruments are designed to let enter only a narrow energy bandwidth to achieve the highest energy resolution. As a counterpart, the instrument has to sweep along the entire desired energy range to reconstruct the energy distribution.

2.2.3. Parallel plates energy analyser

The parallel plates energy analyser is the only type of electrostatic analyser that gives an instantaneous image of the energy distribution of the charged particle beam. Its operation is simple. Two parallel plates are separated by a distance *d* and a potential difference is applied between the two plates. Ions entering the analyser at a precision source point travels in the deflecting region along a parabolic path. Thus, the particles are discriminated depending on their energy (Fig. 2.14). A complete description of the parallel plate analyser is given in the next chapter since it is the type of spectrograph that we developed during this thesis.

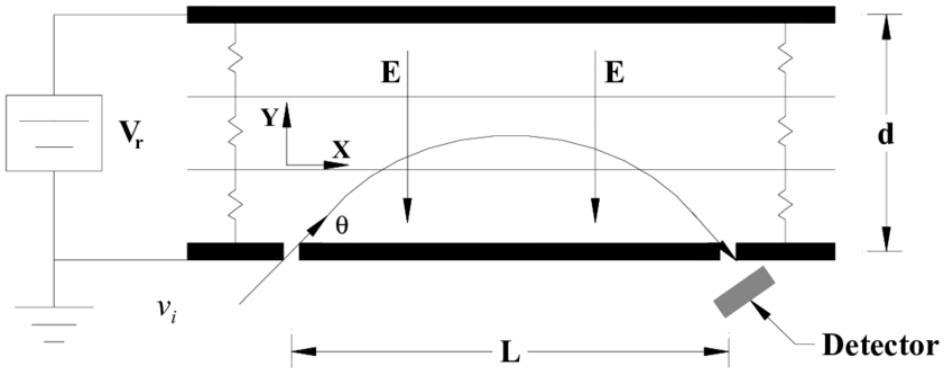

***Figure 2.14**: Schematic of a parallel plate energy analyser (Thesis of M. Walter, 2005).*

3. MASS AND ENERGY SPECTROMETERS FOR PLANETARY EXPLORATION

In the following, we present few examples of recent mass and energy spectrometers operating on board various planetary space missions.

3.1. A wide field-of-view ion mass spectrometer: MSA

MSA (Mass Spectrum Analyzer) is a time-of-flight mass spectrometer coupled to a top hat spherical electrostatic analyser. Its design is inherited from the Cassini/CAPS instrument (Young et al. 2004). Installed on the Mercury Magnetospheric Orbiter (MMO) module of the BepiColombo mission, MSA will provide, with a spinning spacecraft, a 3D view of the ion magnetosphere (Delcourt et al., 2016). MSA's energy analyser features 32 windows each defining a 11.25° azimuth angle. 4 are obstructed for mechanical support and 7 sectors cannot be used due to the presence of another instrument located at the vicinity of MSA. Thus, 21 windows are useful for measurements. Since MMO spin axis is in the same direction as the spin axis of Mercury, measurements of the full 3D ion distribution function are obtained after one spacecraft spin.

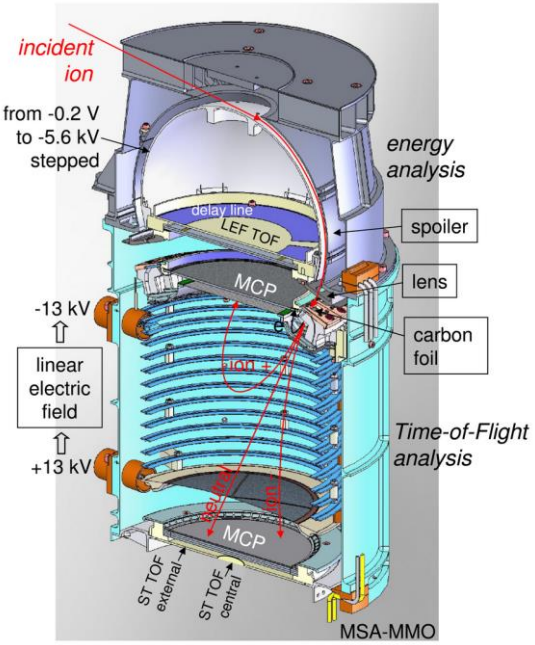

***Figure 2.15**: Schematic illustration of MSA principle of operation (Delcourt at al., 2016)*

After entering the instrument, ions travel in a spherical top-hat electrostatic analyser (ESA) which allows to select specific energy per charge ratio from a few eV/q up to ~38 keV/q. At the exit of the ESA, ions are accelerated towards a TOF linear field mass spectrometer. At the entrance of the TOF analyser, ions impact a thin carbon foil that is used as the start time for the TOF measurement but also gives indication of the azimuthal sector from the incoming ion (association of a microchannel plate and a delay line is used to retrieve the azimuthal sector).

As a result of charge exchange, ions may exit the carbon foils as neutrals, positive, or negative ions. An electric field is applied inside the TOF chamber that varies nearly linearly along the

instrument main axis from -13kV (at the carbon foil), up to +13 kV. Under the action of this electric field, positive ions are reflected back towards the top of the TOF chamber, while the largest fraction (~80%) of incoming particles exits the carbon foil as neutrals or negative ions. These particles have straight trajectories toward the bottom end of MSA TOF chamber, where their STOP signal is measured. Using this instrumental concept, MSA performances achieved an energy resolution of 8% and a mass resolution of 40 with respective ranges of 1eV/q – 38 keV and 1 – 60 amu. The angular resolution of the instrument is $5° \times 11.25°$ with a $5° \times 260°$ field of view.

3.2. Neutral particle analysers

Neutral mass spectrometers differ from ion mass spectrometers in that neutral particles must first be ionised before they can be manipulated and thus separated by mass (and/or by energy). There are several technics for achieving ionisation, depending on the energy range of the particles to be measured. The ion source is the device that transforms the neutral particles of the environment into measurable ions. It relies on two technics to ionize the particles:

- Ejection or capture of an electron by electronic, photonic, ionic or atomic impact (E <10 eV)
- exchange an electron with a particle or group of particles. (E > 10-15eV)

Examples of instruments using both technics are described in the following.

3.2.1. ROSINA: An instrumental suite for cometary exploration

ROSINA (Rosetta Orbiter Spectrometer for Ion and Neutral Analysis), on board the ROSETTA mission is an instrument suite composed of 3 instruments along which two spectrometers.

DFMS (double focusing magnetic mass spectrometer) is a neutral mass spectrometer consisting of a filament ionisation source and a mass analyser using a double electrostatic and magnetic focusing, according to the Mattauch – Herzog geometry (Fig. 2.16). It is a combination of a 90° electrostatic analyser and a 60° magnetic deflector. In the neutral mode, the neutral particles are firstly ionized in the ion source using energetic electrons (in the range 10 – 90 eV). The newly formed ions are then extracted from the ionization volume and accelerated towards a transfer optics with a potential of 1kV. The transfer lens has the objective of focusing the ion beam onto the entrance slit of an electrostatic sector which determines the high- or low-resolution mode (14µm in high resolution and 200µm for low resolution). Following a corrective lens element accomplished by a pair of biased plates, the ions fly through the electrostatic sector which allows to select specific energies to be mass focused on the detector. Then, charged particles pass through the magnetic sector and a system of zoom lens (only active in high resolution mode) to finally reach the detector.

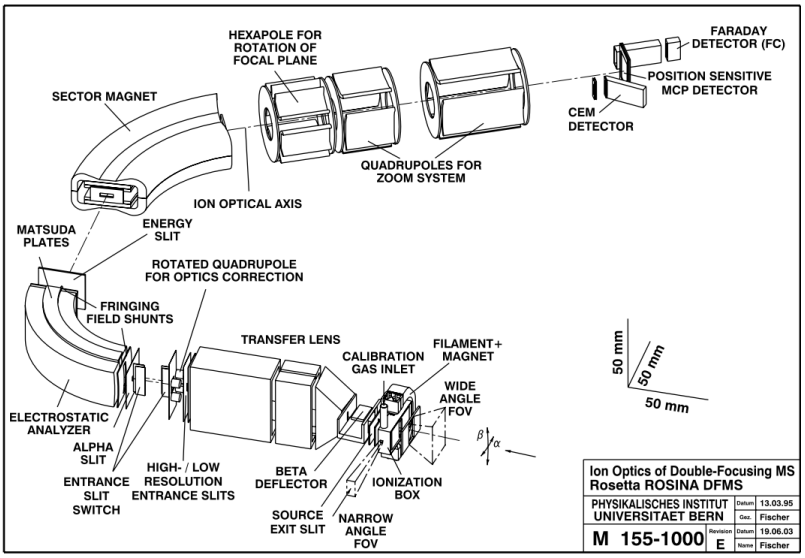

Figure 2.16 *:Three-dimensional view of the main ion optical elements of DFMS. The ion path is the dotted line along the instrument main axis (Bälsiger et al., 2007).*

DFMS in high resolution mode achieves a mass resolution as high as 3000 at 1% peak height in the range 12 – 150 amu. Moreover, its $20° \times 20°$ field of view allows cometary gas with wide angular spread in the flow direction to enter the ionization region. With the adequate potentials, DFMS can be tuned to a narrow field of view of $\pm$ 2° for determination of the gas flow direction.

To complement DFMS, the ROSINA package includes a second mass spectrometer based on **the reflectron time-of-flight (RTOF)** technique. This instrument has the advantage of recording the entire mass spectra at once. The instrument has been designed to extend the mass range of the DFMS and to provide higher sensitivity, allowing measurements in less dense regions. The RTOF ion source consists of a high transmission storage ion source. As the electron beam continuously produces new ions, these are trapped in the ionisation volume until an extraction voltage is applied. After extraction, the ions are accelerated and focused to form a beam at the exit of the ion source. The next optical element is the reflectron analyser with triple ion reflection. The first reflector uses a gridless reflectron to narrow the width of the time-of-flight distribution, while the second reflector (called hard mirror) is used to increase the time of flight of the particles before they reach the detector. In this way, the ions fly first towards the gridless reflectron and are reflected towards the hard mirror, which reflects a second time towards the reflectron. The ions are finally directed to the detector after passing again through the reflectron (Fig. 2.17).

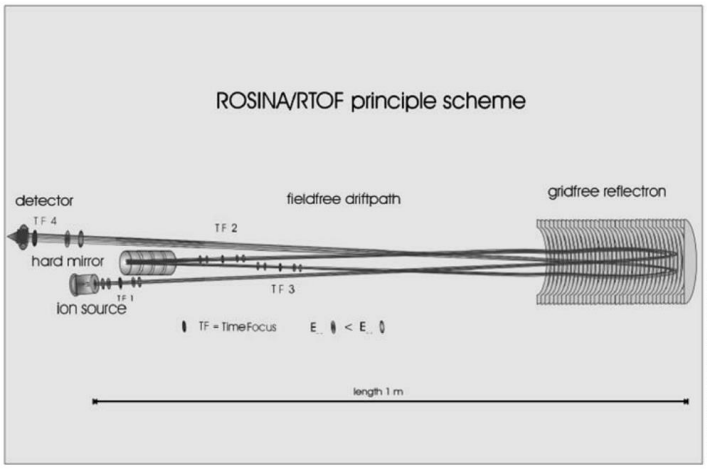

***Figure 2.17**: Ion optical principle of ROSINA/RTOF (Bälsiger et al., 2007; Scherer et al., 2006)*

With the combination of both DFMS and RTOF, the ROSINA package reached measurement capabilities in a wide mass range between 1 amu and 300 amu with a high mass resolution exceeding 3000 (giving the ability to resolve CO from N_2 and ^{13}C from ^{12}CH). The high sensitivity of the instruments also provided measurement capability in ultra-high vacuum condition with pressure as low as 10^{-17}mbar (10^{-15} for DFMS).

3.2.2. NGIMS: Neutral Gas and Ion Mass Spectrometer

NGIMS is a mass spectrometer dedicated to the observation of the Martian upper atmosphere on board the MAVEN mission. Its operating principle relies on the quadrupole mass analyser. NGIMS has its direct heritage from previous planetary mass spectrometer such as Cassini/INMS (Waite et al., 2006). The key part of the instrument lies on its double ion source (Fig. 2.18). The closed ion source, developed specifically for upper atmosphere investigations (Spencer & Carignan, 1988), is composed of a spherical antechamber with an off-axis exit. This configuration avoids the particle to have a direct line of sight with the ionizing electron beam, thus when neutrals enter the antechamber, they undergo a series of collision with its walls which thermalize the particles resulting in a mass dependent ram density enhancement in the source. The resulting interesting features of the closed ion source is its 2π steradian field of view as well as the 50% measurement duty cycle. The open source, in turn, is dedicated to the measurement of reactive species such as O and N which otherwise would be destroyed or transformed by the collisions in the closed source. The open source accommodates a repeller grid to reject the lower energy thermalized ions from the surrounding environment. The last electrostatic part of the instrument, located at the exit of the quadrupole rods is a set of 4 ion focusing lens which direct the ion beam into the detector.

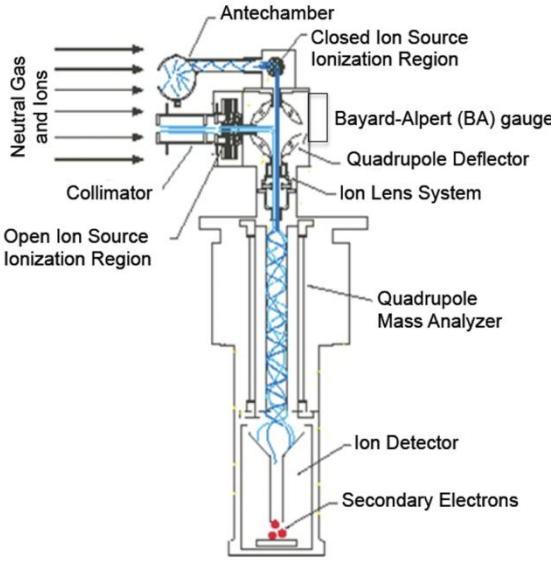

***Figure 2.18** : A schematic of the ion and gas flow into and through the NGIMS (Mahaffy et al., 2014).*

During measurement sequences, NGIMS alternate between a set of closed and open ion source measurements with integration period of 30 ms so that the sample of a full range of species is completed in about 1 second. The mass range is between 1 and 150 amu with a unit mass resolution over the full range. Finally, NGIMS is mounted on an articulated pointing platform (APP) which allows pointing of the instrument independent of the solar array attitude. The APP allows the ion source to operate in its nominal condition; with its axis of sight aligned with the spacecraft ram velocity. Furthermore, even though NGIMS was initially dedicated to mass analysis, the articulated pointing platform allowed wind velocities measurement from the observed modulations of neutral and ion fluxes as the instrument pointing direction changed. A typical uncertainty of $\pm 20\ m/s$ has been achieved with this mode of measurement (Roeten et al., 2019).

3.2.3. STROFIO: STarting FRom a ROtating Field mass spectrOmeter

STROFIO (Orsini et al., 2021) is a neutral particles mass spectrometer which investigates the exospheric gas composition of Mercury on board the MPO module of the BepiColombo mission. The instrument measures the m/z ratio by a time of flight technique. STROFIO consists of two 180° apertures, each with an angular opening of 20° (Fig. 2.19). Neutral particles are ionised by electron impact, electrons being produced by a heated filament and then accelerated toward an ionization volume. The ions are then directed into the time of flight analyser after passing through an acceleration and focusing optics. To achieve time of flight measurements, STROFIO uses an unprecedented technique for the START signal. At the entrance of the TOF analyser, a rotating electric field imprint the START time to the particle trajectory by bending the trajectory in a specific plane. Thus, the time difference between the instant when the particle arrives at the detector and the time when the field was pointing in the appropriate direction is equal to the travel time through the field free region of the Time of Flight analyser. This unique

technique allows to remove any dead time and the instrument is therefore able to analyse every ion that enters the analyser increasing consequently its sensitivity.

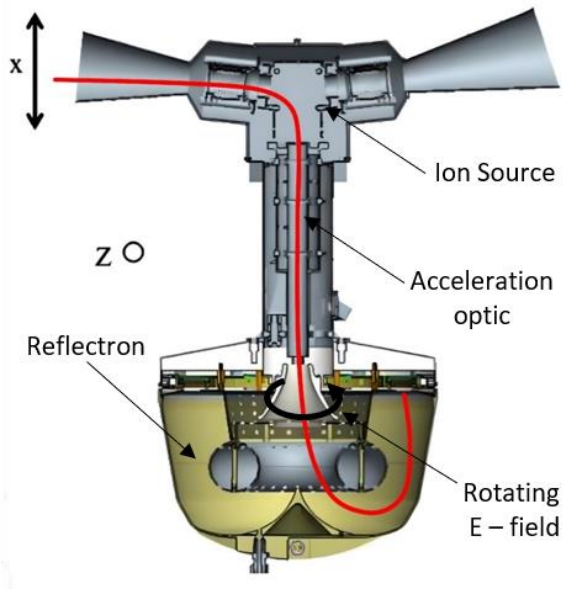

***Figure 2.19**: Cross-sectional view of STROFIO with the ion path inside the instrument (red line) (Adapted from Orsini et al., 2021).*

3.2.4. CENA: Chandrayaan – 1 Energetic Neutral Atoms imager

CENA is a neutral atom mass spectrometer on board the Chandrayaan-1 lunar probe (Barabash et al., 2009; Kazama et al., 2007). Particle detection is based on the conversion of incoming neutrals into ions by surface interaction with charge exchange. At the entrance to the instrument, the electrostatic deflector rejects the charged particles from the environment, allowing only the neutral particles to enter the instrument. After passing through the deflector, the neutrals impact an ionising surface of highly polished silicon, which converts the neutrals into positive ions. The newly created ions then pass through a wave-shaped electrostatic analyser. The electric field is such that the charged particles have to follow wave-like trajectories to pass through the analyser. The aim of this electrostatic optics is to reject all uncharged particles (mainly photons) from the measurement part. The 'wave' analyser also provides a coarse energy analysis capability. The ions leaving the analyser are then accelerated at a potential of 1.5 kV to reduce the energy spread caused by interaction with the conversion surface and finally enter a TOF mass spectrometer (Fig. 2.20). CENA does not use a carbon foil as a START reference for the time of flight measurement, but rather a so-called 'START surface' at a grazing angle of 15°. When the accelerated ions hit the surface, secondary electron emission occurs. These electrons are then deflected towards an MCP for the START time, but

also for the determination of incoming azimuth angle. The ions are reflected towards an MCP, where they are detected and produce a STOP pulse for electronic timing.

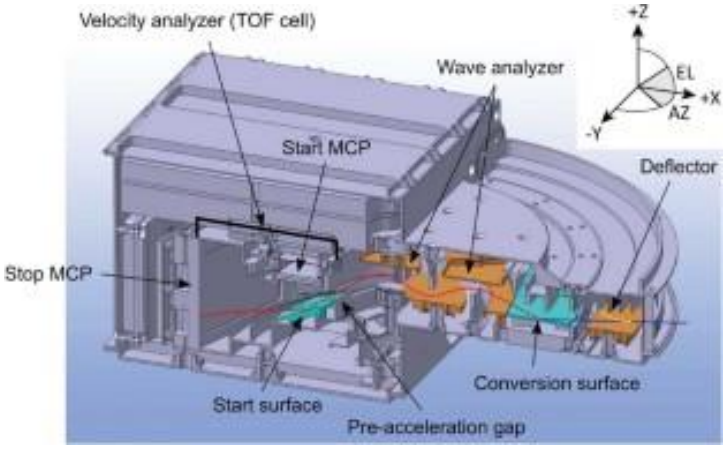

***Figure 2.20** : Cross-sectional 3D view of CENA with typical particle trajectory shown as solid line (Barabash et al., 2009).*

The CENA instrument is thus capable of measuring neutral particles in the energy range 10 eV - 3.2 keV with a resolution of 50%. However, Futaana et al., (2012) showed that there are large systematic uncertainties when the energy of the neutral particles is below 25 eV. The mass analysis capability of the instrument is between 1 and 56 amu. Furthermore, with its 7 azimuthal sectors, CENA has a field of view of 15°×160° and an angular resolution of 9°×25° for neutral particles with energy larger than 50 eV.

3.2.5. C/NOFS ram wind sensor

The Ram Wind Sensor (RWS) is an instrument flown on board the C/NOFS mission dedicated to the characterisation of the Earth ionospheric F region (Fig 2.21). The instrument, mounted on the front face of the instrument and with its aperture perpendicular to the satellite ram velocity, was designed to measure the neutral flow along the track of the satellite. The instrument concept of the RWS is based on the Retarding potential analyser technique (classically used for plasma diagnostic) coupled to an electron impact ion source. Thus, the neutral beam enters the ionisation chamber where it intersects an electron beam and are turned into positive ions. The newly formed ions directly pass through the grid stack of the RPA and are detected with a channeltron. The number of counts on the detector is therefore directly proportional to the retarding voltage applied to the filtering grid. Using a RPA analysis technique, the neutral wind velocity incident to the spacecraft can be inferred. As the ram velocity is precisely known at all time, the wind drift velocity can be determined.

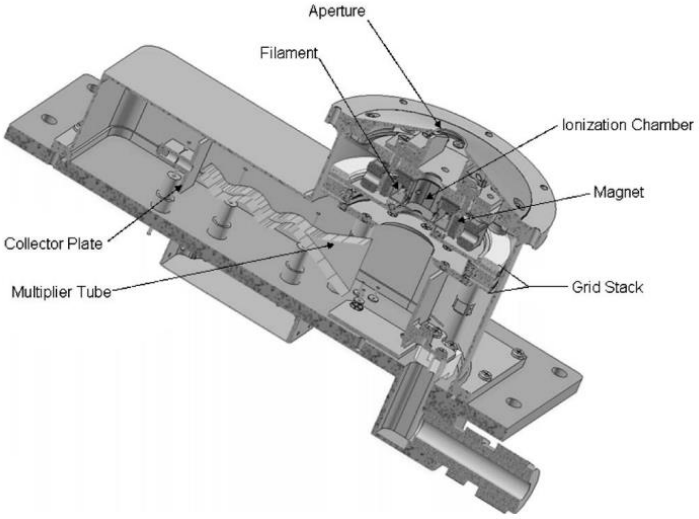

Figure 2.21*:Cross sectional view of the ram wind sensor showing the main functional elements* (Earle et al., 2007).

According to Earle et al. (2007), using a concept of ionization source and Retarding Potential Analyzer (RPA), it is possible to reach an accuracy of ±60 m/s on the determination of the neutral ram velocity (in the case of a pure atmosphere).

4. LESSONS FROM PREVIOUS OBSERVATIONS ON BOARD SPACE MISSIONS

In the previous section we outlined the principle of operation of several instrument concepts capable of characterising the neutral and ion constituents of upper planetary atmospheres. These instruments represent the state of the art for such measurements. Many information related to the challenges that an instrument has to face to perform the measurements of low energy particles in very low-density regions can be derived from these instruments and their measurements.

The ROSINA instrument has highlighted the fact that the spacecraft in space emits gases continuously over time scales of several years. The ROSINA team has shown that any variation of the spacecraft temperature leads to the release of volatile molecules, especially water molecules, from the outer walls of the spacecraft (Schläppi et al., 2010). The spacecraft then retains a residual atmosphere with densities of H_2O up to $10^7\ cm^{-3}$. The significance of the densities measured even after 6 years of cruise is surprising and remains poorly explained. Such a detrimental effect has also been observed by (Mahaffy et al., 2015) aboard the MAVEN Mars probe with a strong background in the egress part of the orbit, due to atmospheric gases trapped on the instrument walls at periapsis. A third example is the result of very recent observations onboard BepiColombo showing clear signatures of the local atmosphere in the measurements made by the mass and ion energy ion spectrometers (Fränz et al., submitted, 2023)

The STROFIO instrument showed another limitation associated with the use of hot filament. When strong currents are emitted from the hot filament, space charge effect limit the ion source efficiency (Orisini et al., 2021). This effect ultimately blocks the newly created ions but also potentially changes their energy in the ion source limiting not only the efficiency of the ion source but also the capability to measure the energy of low energetic neutral particles.

Instruments such as CENA, measured the energy of incoming neutral atoms. However, this type of instrument, which uses conversion surface to convert the neutral particles into ions, is dedicated to energetic neutral atoms (ENA). Albeit, the instrument is able to measure neutral with an energy as low as 10eV, it has been shown that the efficiency of this technique induces large uncertainties at energies lower than 25 eV (Futaana et al., 2012). Other instruments dedicated to neutral energy measurements, i.e. RWS on C/NOFS succeeded to measure the neutral wind velocity. However, on a satellite, the imperfection of the RPA grids might lead to significant uncertainties as large as 180 m/s (Chao et al., 2003; Davidson et al., 2010; Klenzing et al., 2008, 2009). Finally, original techniques were used to measure thermospheric neutral wind in the Martian atmosphere using NGIMS. The instrument was not initially designed to achieved this type of measurement but achieved remarkable velocity resolution as low as 20 m/s. The counterpart lies in the long 30s integration time (Roeten et al., 2019).

SUMMARY

Several characteristics of the upper atmosphere of Mars and the Earth remains unobservable with the existing instruments. We believe that an instrument able to measure low energies ranging from a few tenths of an eV to ~10eV with a resolution better than 0.1eV, masses in the range 1 – 60 with a resolution of ~20, and a sensitivity capable of measuring low densities would achieve unprecedented observations of these regions. The characterization of the upper atmospheres also needs instruments with wind and temperature measurements capability with respective resolutions around 5 m/s and 10K. Moreover, the instrument must be able to differentiate the contribution of the thermal contribution from the non-thermal one. Mass spectrometry and in particular the energy analysis technics are the only analysis method suited to these objectives. A review of the state-of-the-art space planetary instrument available in the last section of the chapter as well as the solutions that have been proposed over the last few decades highlighted a number of limitations making the measurement of low energy neutral particles a challenging task.

CHAPTER 3
ION AND NEUTRAL ENERGY ANALYSER: INEA

1. Instrument objectives

As we saw in Chapter 2, there is currently no space instrument capable of imaging the neutral particles energetic structure from thermal to few eVs in low density environment with enough energy resolution to solve key open questions related to Mars and the Earth upper atmospheres. This is the main motivation for the design of the instrument called Ion and Neutral Energy Analyzer (INEA). This instrument can be described as an energy spectrograph. Indeed, thanks to its electrostatic design, INEA has the capability to instantaneously image the distribution of the particle's energy.

Classically, instruments use heated filaments that thermally emit electrons to ionise the neutral atmospheric particles. The density and average energy of the electrons are to increase the probability of ionisation of neutral particles. The main drawback of these cathodes is that they consume a lot of current to emit electrons. The second problem is the heating of the filament environment, which can induce the outgassing of a neutral population, from the vicinity of the filament, at the risk of polluting the measurement, in particular at low energy.

INEA is being designed to measure particle with energies in the range 0.1-10 eV. One of the challenges to image the differential energy distribution of the local atmospheric species with an energy resolution better than 0.1 eV, in such range, is to suppress any source that could change the energy distribution from the entrance of the instrument up to the detector. To avoid altering the energy of the particles inside the instrument, 2 aspects needed to be overcome. First one is the extraction of newly formed ions from the ion source towards the measurement optics. Classical approaches for the ion source are usually not compatible with this requirement. In INEA, particles entering the ion source are extracted thanks to the relative speed of the spacecraft with respect to the planet's atmosphere, so that their energy remains unchanged. Beside the extraction of newly formed ions, space charge would also change the energy of the ions formed from atmospheric particles limiting the accuracy of the measurement of their energy distribution. As explained in Section 4 of this chapter, INEA uses a cold cathode based on a carbon nanotube (CNT) array. The advantage of using CNT is the large emitting surface which reduces space charge. Moreover, using a cold cathode reduces significantly the outgassing from the instrument's walls as it does not produce heat.

In the following sections of this chapter, we will first investigate the principle used to measure instantaneously the energy spectrum and how we moved from a theoretical model of energy analyser to a prototyped mechanical model. Then we will investigate the operation of the detector. Thirdly, we will detail the operation of the ion source, its associated numerical analysis and its measured performances. Finally, we will discuss about INEA's expected performances and first experimental results.

2. Energy Measurement

2.1. Theory

2.1.1. Motion of the particles

The core of the instrument, which allows to discriminate the particle's energies is called a parallel plate energy analyser or spectrograph. A parallel plate energy analyser consists of two parallel metal plates (respectively base plate and top plate) with an electric potential difference applied between them. When charged particles enter the analyser, they experience an electric field between the plates. The electric field causes the charged particles to deflect, and their trajectory depends on their kinetic energy and charge. By varying the potential difference between the plates, the analyser can be tuned to detect particles within a specific energy range.

The theoretical arrangement of this type of analyser is described in Fig. 3.1 and was detail by Green & Proca, (1970). Here, we consider a distance d between the base plate and the top plate. The base plate is at $y = 0$ and the top plate at $y = -d$. The source point is located below the base plate at $x = 0, y = h$. The mean ray direction, at the source point, is taken to be at angle $-\theta$ to the x axis.

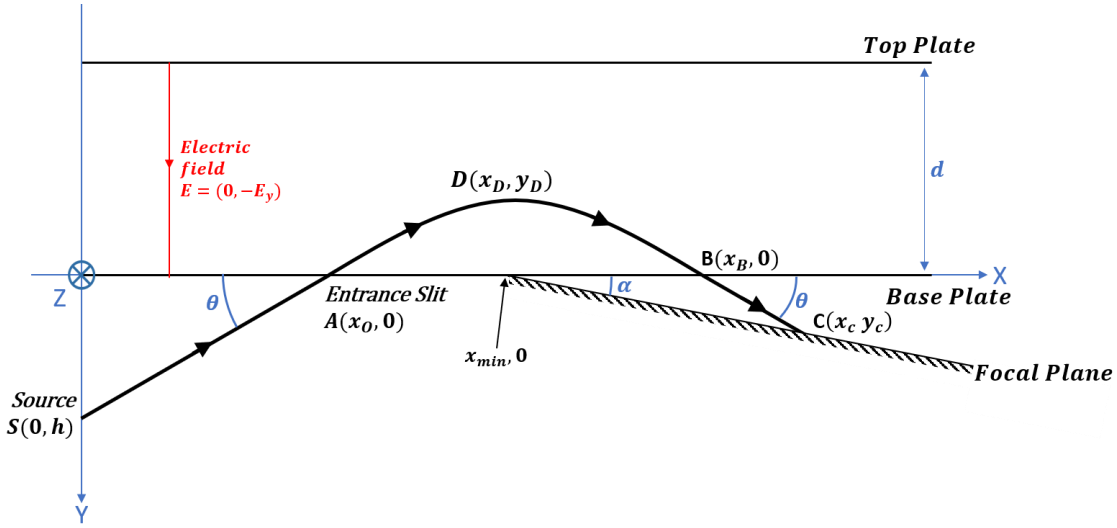

***Figure 3.1**: Theoretical arrangement of the parallel plate energy analyser and the trajectory of a particle from the source point up ot the focal plane.*

In the configuration displayed in Fig. 3.1, the charged particle moves along a straight line from the source point *S* to the entrance slit (point *A*) in a field free region. After crossing the entrance slit, the particle is deflected along a parabolic trajectory due to the electric field *E* between the two plates and return to the base plate at a displacement along *x* at point *B*. After exiting the deflecting area, the particle travel in a straight line back in a field free region.

As particles travels in a straight line from *S* to *A*, we have:

$$\begin{cases} x_1(t) = U_c \cos\theta\, t \\ y_1(t) = h - U_c \sin\theta\ t \end{cases} \quad 3.2.1$$

With t the time, $U_c = \sqrt{\frac{2E_c}{m_c}}$ (E_c being the particle energy and m_c its mass), the particle's velocity. At point *A*, we have $y_1(t_O) = 0$, giving

$$x_A = h \cot\theta \quad 3.2.2$$

From Newton's 2nd law, the trajectory of particles between the two plates (between point *A* and *B* in Fig. 3.1) is described as:

$$\begin{cases} \frac{d^2x_2}{dt} = 0 \\ \frac{d^2y_2}{dt} = \frac{q_c E}{m_c} \end{cases} \quad 3.2.3$$

With q_c the charge of the particle. Thus, the particle trajectory is written:

$$\begin{cases} x_2(t) = U_c \cos\theta\ t + x_A \\ y_2(t) = \frac{q_c E}{2m_c} t^2 - U_c \sin\theta\, t + y_A \end{cases} \quad 3.2.4$$

With $(x_A, y_A) = (h \cot\theta, 0)$. We can now determine the coordinates of point *D*, which is the vertex of the parabola. At point *D*, we have:

$$\dot{y}(t_D) = \frac{q_c E}{2m_c} t_D - U_c \sin\theta = 0$$
$$\rightarrow t_D = \frac{m_c}{q_c E} U_C \sin\theta \quad 3.2.5$$

Therefore,

$$\begin{cases} x_D = \frac{m_C}{q_C}\frac{U_C^2}{E}\sin\theta\cos\theta\ +\ x_A = \frac{E_c}{q_c E}\sin 2\theta \\ y_D = -\frac{m_C}{2q_C}\frac{U_C^2}{E}\sin^2\theta + y_A = -\frac{E_c}{q_c E}\sin^2\theta \end{cases} \quad 3.2.6$$

Now looking at point *B*, we have:

$$\begin{cases} x_B = 2(x_D - x_A) + x_A = 2\frac{E_c}{q_c E}\sin 2\theta + x_A \\ y_B = 0 \end{cases} \quad 3.2.7$$

Finally, after exiting the energy analyser, particles travel again (between points *B* and *C*) in a straight line with the same speed as they entered the energy analyser so similarly as Eq. 3.2.2:

$$x_C = y_C \cot\theta \qquad 3.2.8$$

As a result, the total displacement of a particle entering at the source point *S* and arriving at point *C* is the sum of Eq. 3.2.2, 3.2.7 & 3.2.8:

$$x_{Total} = (h + y_c)\cot\theta + 2\frac{E_c}{q_c E}\sin 2\theta \qquad 3.2.9$$

2.1.2. Focusing condition

Minimizing the angular aberration ($\frac{dx_{Total}}{d\theta} = 0$) particles are focused along a straight line (called focal plane in Fig. 3.1). Using equation 3.2.9, we find that $\frac{dx}{d\theta} = 0$ when

$$(h + y_c) = \left(\frac{4E_c}{q_c E}\right)\cos 2\theta \sin^2\theta \qquad 3.2.10$$

The equation of the foci for various initial energy E_c is therefore

$$x_c = \frac{h + y_c}{\tan\theta} \times \left[1 + \frac{1}{\cos 2\theta}\right] \qquad 3.2.11$$

Thus, the intersection between the focal plane sits at the coordinates $(x_{min}, 0)$ and is found using Eq. 3.2.11 for $y = 0$. This point $(x_{min}, 0)$ corresponds to the minimum detectable energy. From Eq. 3.2.10, we can also derive the angle α between the focal plane and the base plate which is:

$$\tan\alpha = \frac{\tan\theta \cos 2\theta}{1 + \cos 2\theta} \qquad 3.2.12$$

One can see with Eq 3.2.11 that the upper limit of θ is 45°. For values of θ larger than 45°, the focal line is in the space between the two plates.

2.1.3. Correction of the angular aberration

While first order focusing is satisfied, second, third, etc. order focusing are not. This leads to an angular aberration on the focal plane. The latter can be estimated using two rays with the same energy but entering the energy analyser with respective angles of θ and $\theta + \Delta\theta$. Green & Proca (1970) showed that the angular aberration $\frac{\Delta x}{x}$ depends on the angular opening $\Delta\theta$ but more importantly on the angle θ. As we can see in Fig. 3.2, for both $\Delta\theta = 2.5°$ and $\Delta\theta = 5°$, the angular aberration is minimized for a value of θ equals to 30°.

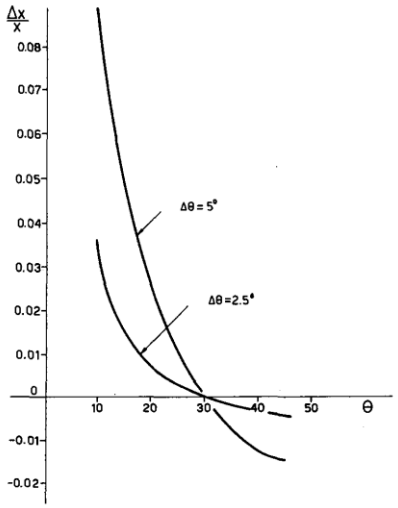

Figure 3.2*: Variation of the angular aberration with respect to the mean angle θ for angular dispersion $\Delta\theta$ of 2.5° and 5° (Green and Proca,1970).*

As illustrated in Fig. 3.2, Green and Proca (1970) also demonstrated that the angular aberration also depends on the angular range being accepted. One can see that for a mean angle θ = 30°, the angular aberration remains very low compare to $\theta = 45°$ (which is in agreement with the previous observation). Following the results described by Green & Proca, 1970, we chose to use a mean angle $\theta = 30°$ associated to an angular dispersion $\Delta\theta = \pm 3°$. The mechanical design that allows to recreate these conditions is described in Section 2.2.2. Thus, using Eq. 3.2.12, the focal plane of our energy analyser sits at an angle α = 10.9° relative to the base plate.

2.1.4. Magnification

In theory, the source point of the energy analyser is a perfect point (in the mathematical sense) without any width. In reality, such a configuration is impossible. Because of the steep rays with respect to the focal plane, there is a magnification of the spot on the focal plane and that is induced by the width of the source 'slit' along the *y* axis. Hence, Green & Proca, (1970) showed that the magnification M only depends on the mean angle θ with the following relation:

$$\mathrm{M} = (1 + cos\, 2\theta) \qquad 3.2.13$$

For $\theta = 30°$, one finds a value of *M* equals to 1.5

2.1.5. Transverse image

In the context of a parallel plate analyser, the transverse image refers to the spatial distribution of the particles on the focal plane in a direction perpendicular to the mean direction of the particle flow (z direction on the reference frame detailed on Fig. 3.1). To fully describe the transverse motion and the resulting image on the focal plane, we need to consider 3 cases.

1- The particles are emitted at a distance z_0 but parallel to the main plane [X, Y, 0]:
In this configuration, the trajectories can be deduced simply by translating into [X, Y, 0] plane, so the impact point *x* is preserved.

$$\frac{\Delta x}{x} = 0$$
$$z = z_0 \qquad 3.2.14$$

2- The particles are emitted from z = 0 at an angle ϕ relative to the plane [X, Y]:
Here, we can define the velocity of the particle to be $V' = V_0 \cos\phi$, which is the particle's velocity in the [X, Y] plane and $V_z = V_0 \sin\phi$. For small angles ϕ, we can approximate $V' = V_0\left(1 - \frac{\phi^2}{2}\right)$ and $V_z = V_0\,\phi$. From there, we have the energy $E' = E(1 - \phi^2)$, because $E' \propto V'^2$. Thus, we have:

$$\frac{\Delta x}{x} = \frac{\Delta E}{E} = -\phi^2$$
$$z = \phi x \qquad 3.2.15$$

3- The particles are emitted at a distance z0 and in the direction of the point of impact of the central trajectories in the plane [X, Y, 0].
We can write (using a small angle approximation) $\phi = \frac{z_0}{x}$. From the results in case 2, we have:

$$\frac{\Delta x}{x} = -\left(\frac{z_0}{x}\right)^2$$
$$z = z_0 - \frac{z_0}{x}x \approx 0 \qquad 3.2.16$$

From the three possible cases studied, theoretically, the transverse image on the focal plane should not affect the energy analyser resolution for small angular dispersion in the $[X, Z]$ plane.

2.1.6. Energy range

As we chose θ to be 30°, Eq. 3.2.11 of the focal line becomes $x = 3\sqrt{3}(h + y_c)$. Thus, the minimum measurable energy is for $y = 0$ and the corresponding focus at $x_{min} = 3\sqrt{3}\,h$. In the frame of INEA, we arbitrarily set $x_{min} = 35$ mm (keeping the total size of INEA within reasonable dimensions), which gives $h = 6.74\,mm$. The maximum energy will correspond to a focus at x_{max} which is the maximum physical dimension allowable for the spectrograph. In our mechanical model $x_{max} = x_{min} + 45\,mm$. The range of energies R observable is therefore given by:

$$\mathrm{R} = \frac{\mathrm{E_{c_{max}}}}{\mathrm{E_{c_{min}}}} = \frac{\mathrm{x_{max}}}{3\sqrt{3}\,\mathrm{h}} \approx 2.3 \qquad 3.2.17$$

2.2. From theory to physical model

2.2.1. Mechanical design

The energy analyser of INEA is directly adapted from the theoretical model of Green & Proca (1970) but including the mechanical constraints. All the dimensions of the energy analyser are determined by the choice of the focal plane starting point x_{min} and the maximum physical dimension that allows particle detection x_{max}, respectively 35mm and 80mm. From this information, we directly have $h = 6.74$ mm.

To reproduce the geometry of the theoretical energy analyser, we chose to use the base plate as an analogy of an optical bench. This means that this mechanical piece must be sufficiently rigid to accommodate all the other parts without deforming while giving exact positioning of the electrostatic parameters ($h = 6.74$, $\theta = 30°$, $x_{min} = 35mm$, $and\ \alpha = 10.9°$). As a result, the base plate is a 1 mm aluminium plate that will directly accommodate 2 mechanical interfaces. One is for the positioning of h and θ while the other one defines x_{min} and α, respectively called 'Interface 60' and 'Interface détecteur' in Fig. 3.3. To allow particles to exit the energy analyser, the base plate's exit window includes an electrostatic mesh where the wire's cross section is 30 x 30µm² and the spacing between the wires is 300 µm.

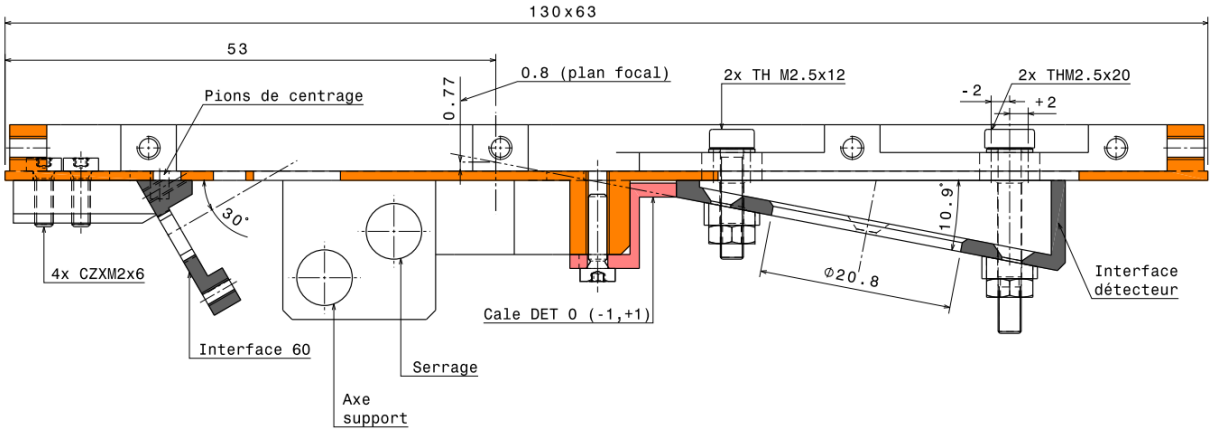

***Figure 3.3**: Mechanical drawing of the energy analyser's baseplate and of its interface parts*

As for the EA's height, it was determined using Eq. 3.2.7 for $x_B = x_{max}$, which allows to write:

$$\frac{E_{c_{max}}}{E} = \frac{x_{max} - h\,cot\,\theta}{2\,sin\,2\theta} \qquad 3.2.18$$

Thus, using Eq. 3.2.6, we have:

$$y_{D_{max}} = \frac{1}{2}(x_{max} - h\cot\theta)\tan\theta = 19.7\ mm \qquad 3.2.19$$

Taking an extra 30% margin to avoid edge effects, we found that the distance between the top and base plates must be around 25.6 mm.

Moreover, the mechanical model has to define clear boundary conditions of the electric field. It was achieved by means of a set of electrodes called guard plates. Those plates have a thickness of 100µm, which represents the best compromise between acceptable mechanical strength while limiting the deformation of the electric field compared with a theoretical model. We found that 20 electrodes of 100µm width and spaced by 1.1mm give a total distance of 25.1mm between the base and top plates which is close enough of the calculated value of 25.6mm.

Finally, the top plate is 0.5mm thick and acts as flange allowing a proper clamping of the electrodes stack. The top plate is also equipped with a square hole covered with an electrostatic grid.

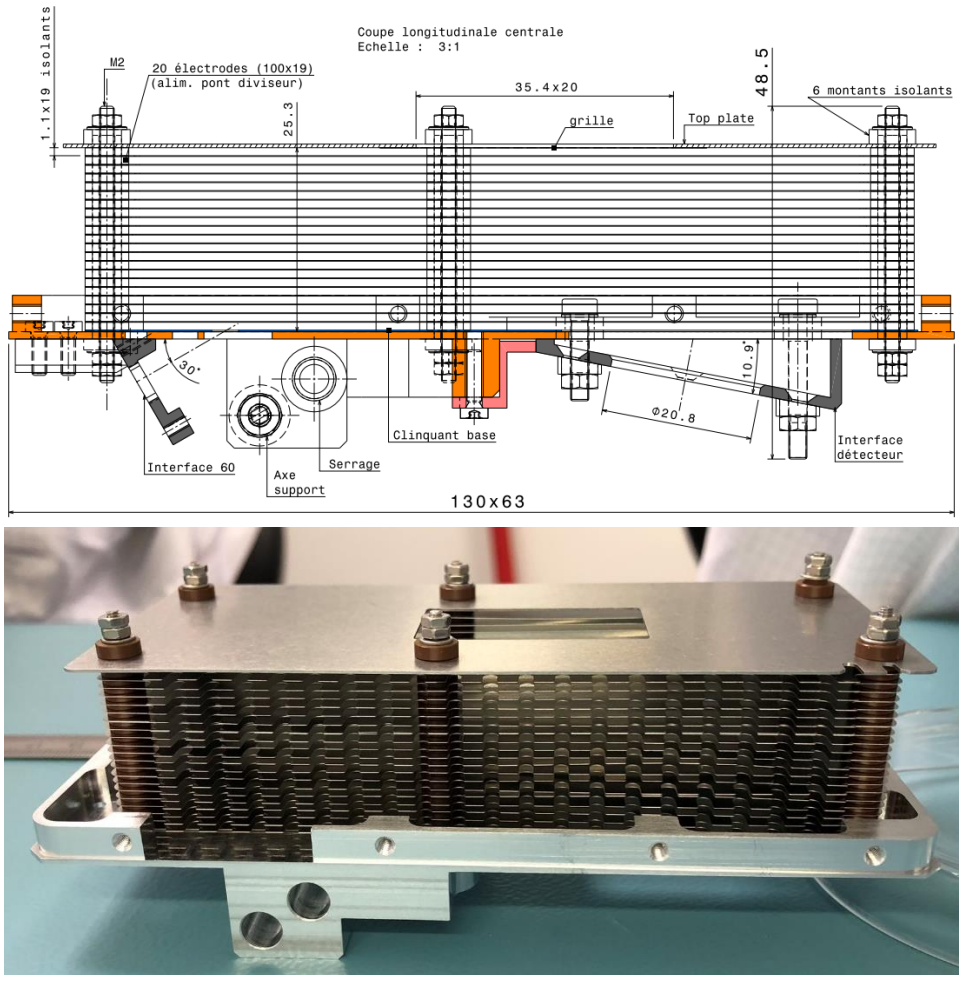

***Figure 3.4**: Top panel is a mechanical drawing of the energy analyser assembly. Bottom panel is the corresponding photograph of the EA prototype.*

2.2.2. Controlling the angular distribution

As explained in Section 2.1.3, we chose an angular acceptance $\Delta\theta$ of $\pm 3°$. To avoid particles with larger angles to enter the energy analyser, we designed a mechanical part placed between the source slit (point S) and the entrance window of the EA (point A). This part acts as a mechanical filter that stops the particle with an angle larger than 3° in both [X, Y] and [X, Z] planes. It is composed of a casing which hosts a stack of 17 electrodes with square 0.5x0.5

mm² holes. These 17 electrodes alternate between 2 types of geometry forming a comb shape in the [X, Y] and [X, Z] planes. The opening of the slit is 0.5mm along the Y axis and 5 mm long on the Z-axis. The length of the filter was designed so that particles entering by the source slit cannot exit the filter if their angle is larger than 3°. The geometrical configuration is detailed In Fig. 3.5.

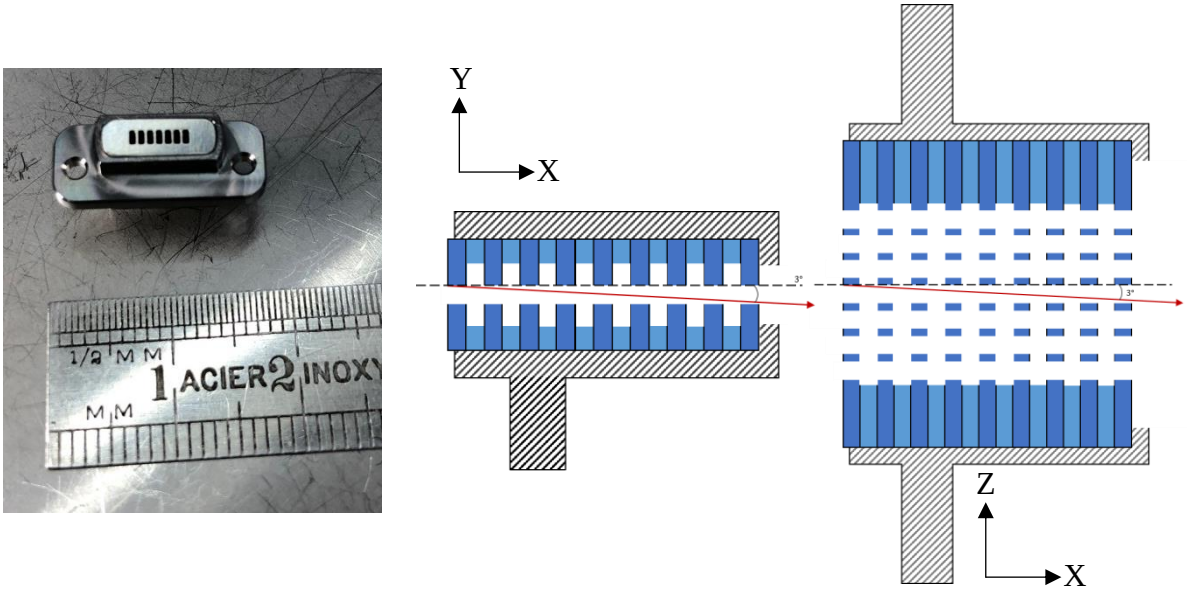

***Figure 3.5**: Left panel: Photograph of the ±3° mechanical filter. Middle and right panels are schematics of the filter in the [X, Y] and [X, Z] planes.*

Considering openings of 0.5mm along the Y axis, the length L of the filter is defined as $L = 0.5 \cot 3° = 9.54$ mm. However, the available room between source slit and the energy analyser window only allows a filter with L = 8.5 mm (plus the casing's dimensions) which slightly increases the angular acceptance to $\Delta\theta = 3.4°$.

2.2.3. Associated electronics

The energy analyser electronics is composed of a simple PCB that operates as a voltage divider allowing to generate the 21 potentials corresponding to the EA's guard plates. The circuit allows two voltages V_{base} and V_{top} as inputs. As described in Fig. 3.6, the circuit is first composed of two power line filters which filters the two input signals, preventing from spikes and noise on the circuit. The core of the circuit is a series of 21 resistors with a value of $1k\Omega$.

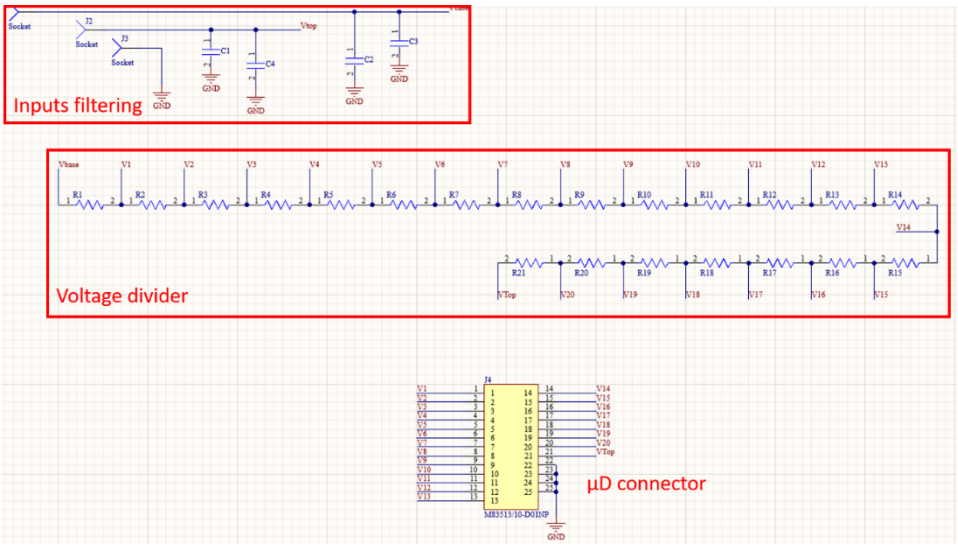

***Figure 3.6**: Electrical schematic of the energy analyser polarisation circuit*

As for the connection between the PCB and the energy analyser, the potential V_{base} is directly applied to the EA's baseplate via the mounting screws. For the 20 other potentials, they are passed to the guard and top plates via a micro-D25 connector, which is a high density, 25-pins connector. The link between the connector and the EA is insured thanks to a cable harness where each cable corresponds to the potential of a specific electrode. As described in section 2.2.1, the guard plates are 100µm stainless steel foils. These are very fragile and therefore really foldable. To link the cable to the electrode we had to use an unusual soldering technique. Since the electrodes are made of stainless steel, it is impossible to solder the cable directly with tin solder. The solution we have found consists in crimping a piece of nickel tube onto the end of the cable and then soldering it electrically to a tab provided for this purpose on the electrode. Figure 3.7 displays the EA's final assembly with the PCB mounted and the cable connected as well as a photography of the soldering technique.

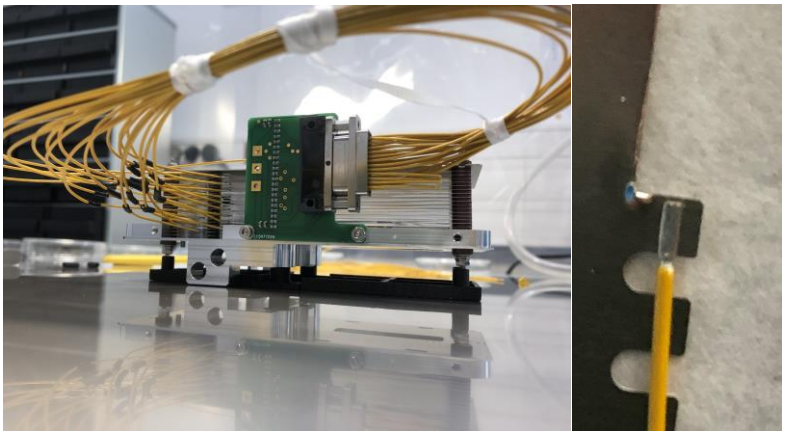

***Figure 3.7**: Left panel: Photograph of the energy analyser assembled with the voltage divider PCB mounted on its side. The photography also shows how the potentials are brought to the EA's guard plates. Right panel: photograph of the electrical soldering using crimped Ni tubes.*

2.3. Numerical model

2.3.1. SIMION: a field and particle trajectory simulator

SIMION® (Dahl, 2000) is a solver for Laplace's equation that calculates the electrostatic potential and the electric field at any point in space for a set of potential values applied to the electrodes of the model. It uses the finite-difference method (Dahl, 2000). SIMION® can be used to compute the trajectories of charged particles moving in the model. All the numerical models studied in this manuscript were produced using SIMION® software. The potential map is composed of a mesh, the size of which is defined according to the model. It is possible to produce 3D models that require a lot of RAM depending on the size of the mesh and the size of the volume to be described. The latest version of the software, SIMION® 2020, enables models to be produced with an unlimited number of points, the limit being given by the computer's RAM. The PC dedicated to INEA's model possesses 64GB of RAM. The typical resolution we've achieved is 25µm which allows to construct electrostatic grids with squared wires of cross section equal to 30x30µm² and a spacing between each wire of 300µm. To calculate the potential inside each volume, SIMION uses a Poisson equation solver with a convergence limit of 10^{-5} V. Finally, a standard fourth order Runge-Kutta method is used for numerical integration of the particle's trajectory in three dimensions. This approach has the advantage of good accuracy and the ability to use continuously adjustable time steps.

2.3.2. Perturbation due to the entrance window

Considering the very low energy range that we want to measure, we need to evaluate, very accurately, the electrostatic default that will alter the electric field within the energy analyser. As suggested by Green & Proca (1970), using a grid mounted on the entrance window of the energy analyser leads to a modification of the curve of the angular aberration. Similarly, we did not put a grid on INEA energy analyser's entrance window. As a consequence, the electric potential created within the deflecting region will leak through the base plate in the field free region between the source slit and the entrance window, as described in Fig. 3.8. This Figure displays a simulation of the mechanical model of INEA where a 1 V/mm electric field is applied in the EA while the filter and the baseplate are grounded.

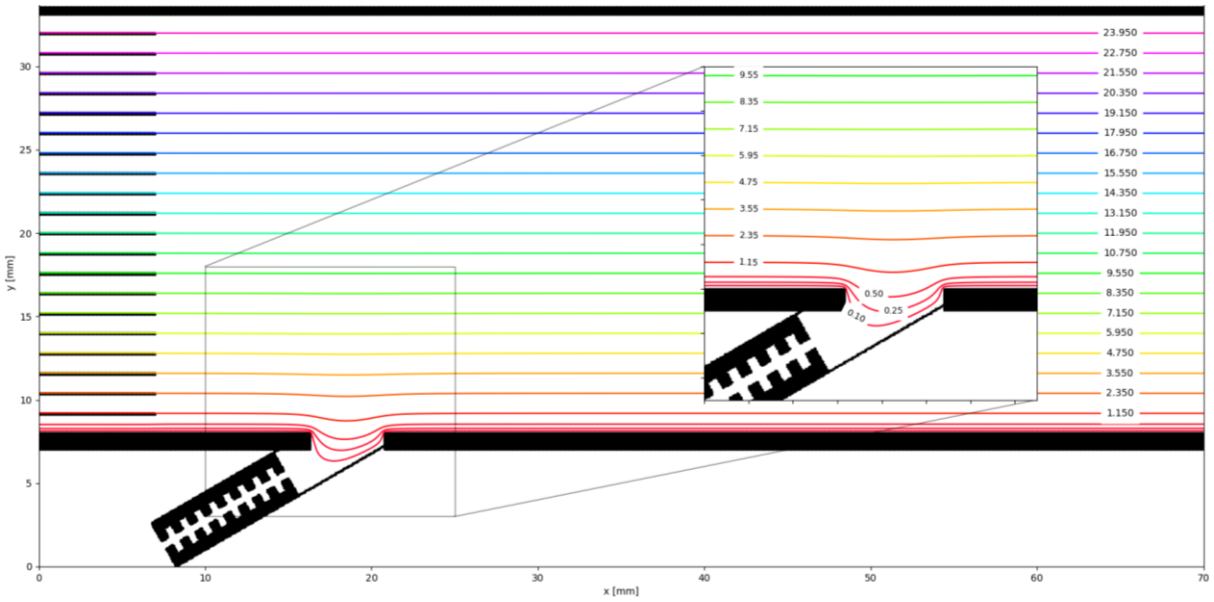

***Figure 3.8**: Simulation of the energy analyser geometry including the electrostatic defaults induced by the entrance window. The top plate is at a potential of 25.1V while the base plate and the filter are grounded.*

This leakage impacts itself the trajectory of the particles. Fig. 3.9 compare the theoretical (black dashed lines) and the simulated (red plain lines) trajectories particles with angles of 0 and $\pm$ 1.5° and an energy of 2.2 eV. The electric field generated between the top and base plate is 0.0837 V/mm. Looking at the zoomed insets, we can see that the particles around the entrance window are deflected more quickly in the case of our mechanical model. This has the direct effect of deteriorating the focus on the focal plane and therefore increasing the angular dispersion.

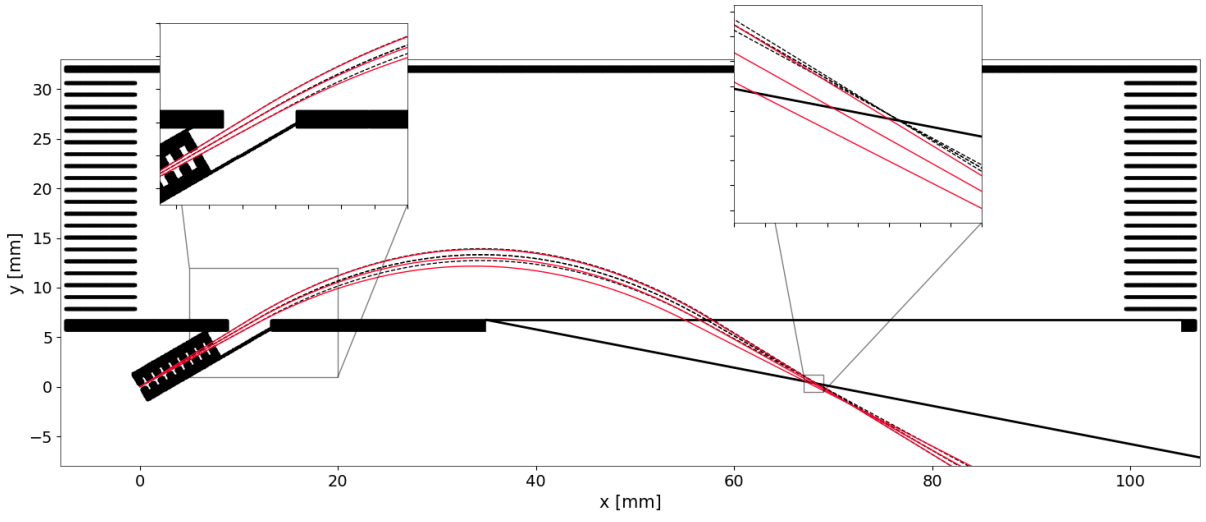

***Figure 3.9**: Trajectories of particles through the energy analyser emitted from the source point and with angles of $0, +1.5°$ and $-1.5°$ with respect to the main axis. The black dotted lines represent the theoretical trajectories as described by Green & Proca (1970) while the plain red lines are the trajectory calculated by SIMION and considering the mechanical geometry of the analyser.*

2.3.3. Simulation of the energy analyser with an 'ideal' detector

To evaluate the performance of INEA the simulations were carried out in 2 successive stages. The first corresponds to the case of an "ideal" detector in which the various potentials are at 0V. The simulation provides the points of impact of the ions on the focal plane for various initial conditions at the source slit. Thus, the images obtained on the focal plane depends solely on the characteristics of the mechanical model of the EA, since the ions are injected from its source slit. The energy spectrum on the focal plane gives us a reference that can then be used to quantify the deformations induced by the detector's potentials detailed in section 3.2.

In this section, we consider the subassembly of the EA and the Detector. The [X, Y, Z] is the global reference and is shown in Fig. 3.10. The X axis corresponds to the direction of the base plate of the EA, the Y axis is perpendicular to this plate and is oriented vertically. The Z axis completes the reference frame. The origin of the reference plane coincides with the source point S of the EA. Thus, the [X, Y, 0] plane corresponds to the median plane of the instrument. The theoretical focal plane is indicated by a blue dotted line. Its intersection with the base plate is at O' $(x_{O'} = 35\ mm, y_{O'} = 6.74\ mm)$ and matches the entrance grid G_{ISO1} of the detector.

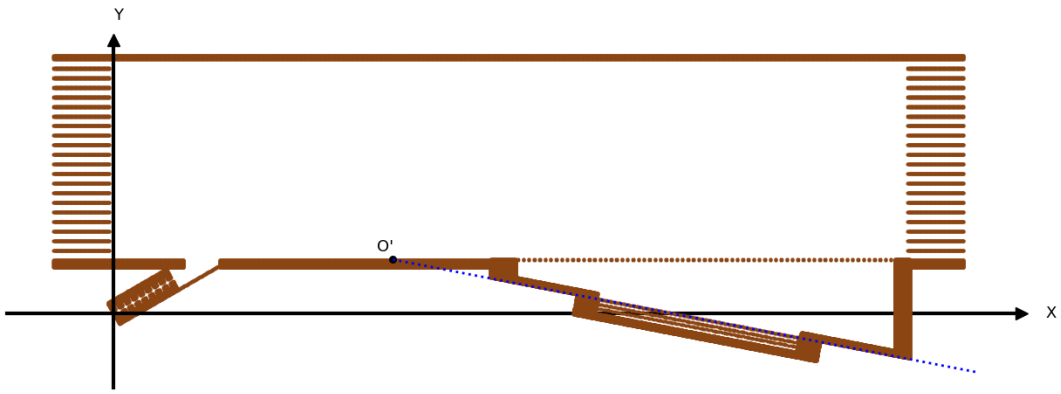

***Figure 3.10**: Geometrical reference frame of the energy analyser. The dotted blue line represents the focal line.*

The ions used for the simulation of the sub-assembly EA/Detector are O_2^+ ions whose energies vary from 2.1 to 2.3 eV with a step of 0.1 eV. For each energy 10, 000 ions are launched. The ions are launched from the source slit centred on the source point S (0, 0) in the XY plane. The source slit is 0.5mm wide along the Y axis and 5mm long along the Z axis. The potential of the EA's base and top plates are respectively $V_{ref} = 0$ & $V_{top} = 2.1$V corresponding to an electric field of 0.0837 V/mm. The deformation of the electric field near the EA entrance window as it was explained in Section 2.3.2 is also considered.

Impact of the angular opening in the [X, Y] plane (angle θ)

In this section, we consider the source slit only in the $[X, Y, 0]$ plane. Therefore, the latter has no dimension along the Z axis. The initial velocities of the particles are inclined at $\theta \pm \Delta\theta = 30° \pm 3°$ relative to the X axis. The initial positions and angles are randomly distributed over the whole source slit. The trajectories corresponding to the different energies are shown in Figure 3.11 left panel. The data used are the positions along the X axis. The distribution of the impact positions is represented in Fig. 3.11 right panel.

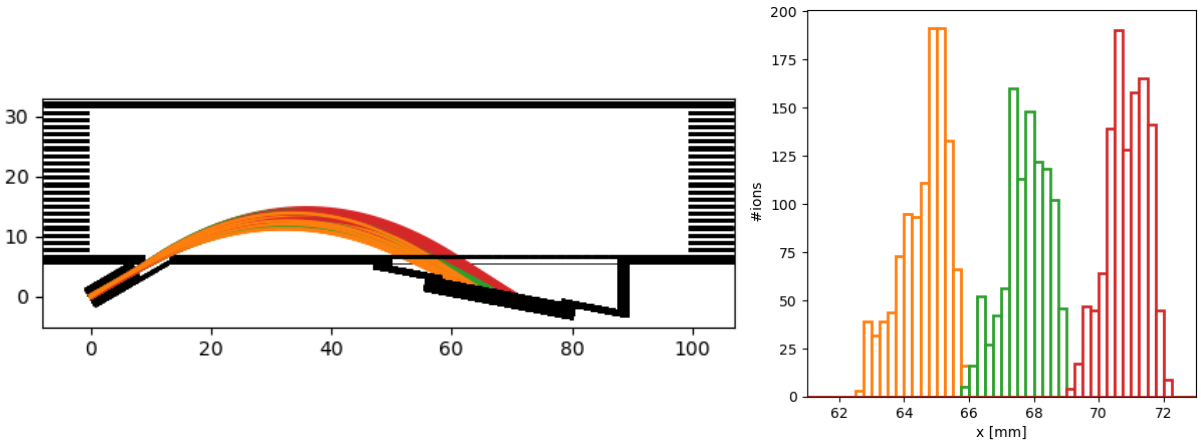

***Figure 3.11**: (a): Trajectory of O_2^+ ions from the centre of the source slit up to the focal plane. Particles only have an angular dispersion of $\pm 3°$ on the [X, Y] plane. The coloured lines represent 3 populations with energies of 2.1 eV (orange), 2.2 eV (green) and 2.3 eV (red). (b): Impact distribution of the 3 populations along the focal plane and in the reference frame of the energy analyser.*

We can already highlight a major point from this simulation: the size of the image along the X-axis is about 2 mm at 3σ, compare to the theoretical 1.5mm estimated from the calculations of Green & Proca (1970). This effect confirms that the entrance window of the EA's baseplate disturbs significantly the trajectories of the particles leading to a degradation of the EA's focussing capapility (see Fig. 3.9).

Effect of the angular aperture in the [X, Z] plane (angle ϕ)

The simulation parameters are identical, but we consider the opening of the ion beam in the [X, Z] plane at the entrance slit by adding an angle ϕ to define the orientation of the initial velocity vector. This angle is in the range $\Delta\phi = \pm 3°$. According to the analytical model, the existence of an angular aperture of ± 3° in the [X, Z] plane should not significantly degrade the resolution of the instrument. This is confirmed by the simulation results. The histograms in Fig. 3.12 show that the results for the $\Delta\phi = \pm 3°$ (coloured lines) are almost identical to the histograms for the ϕ = 0° case (black lines), with the widths of the peaks remaining identical.

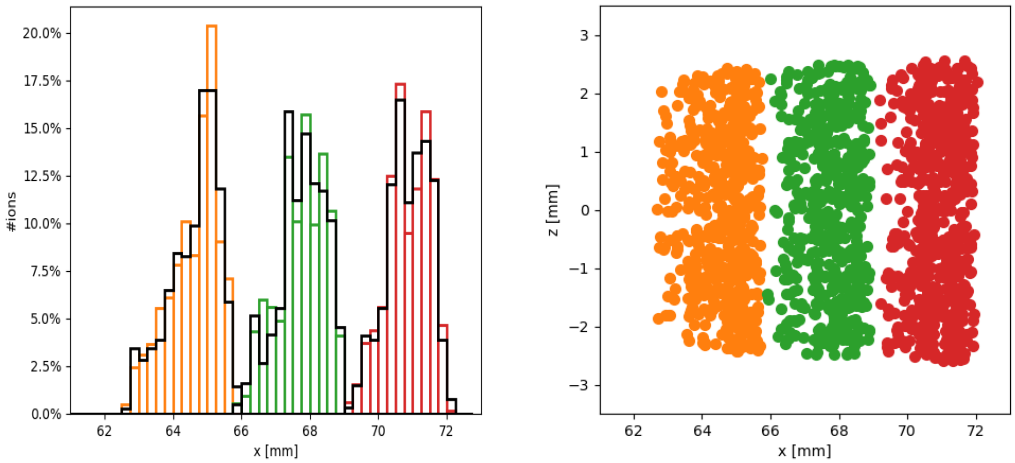

***Figure 3.12**: left panel : distributions of the impact position in the case of particles with an angular dispersion $\Delta\theta = \pm 3°$in the [X, Y] plane and an angular dispersion $\Delta\phi = \pm 3°$ in the [X, Z] plane. The coloured histograms represent the different energies as in Fig. 3.11 while the black lines are the outline of the results from the previous case (Fig. 3.11 right panel). Right panel shows the distribution of the particle's population on the EA [X, Z] plane.*

'Real slit' and combined effect of $\Delta\theta$ and $\Delta\phi$

We then analysed the effect of extending the source slit by 5mm along the Z axis, which is then a rectangle with dimension 0.5 x 5 mm² centred on the source point S (0, 0, 0). This configuration corresponds to the real geometry of the instrument. For each energy, we launch 50 000 particles randomly distributed across the source slit. The angles θ and ϕ are also drawn randomly respectively within the ranges [27°, 33°] and [-3°,3°]. The results obtained in Fig. 3.13 show, for each energy, histograms with the exact same dispersions than in the case of a thin slit with no extension along the Z axis.

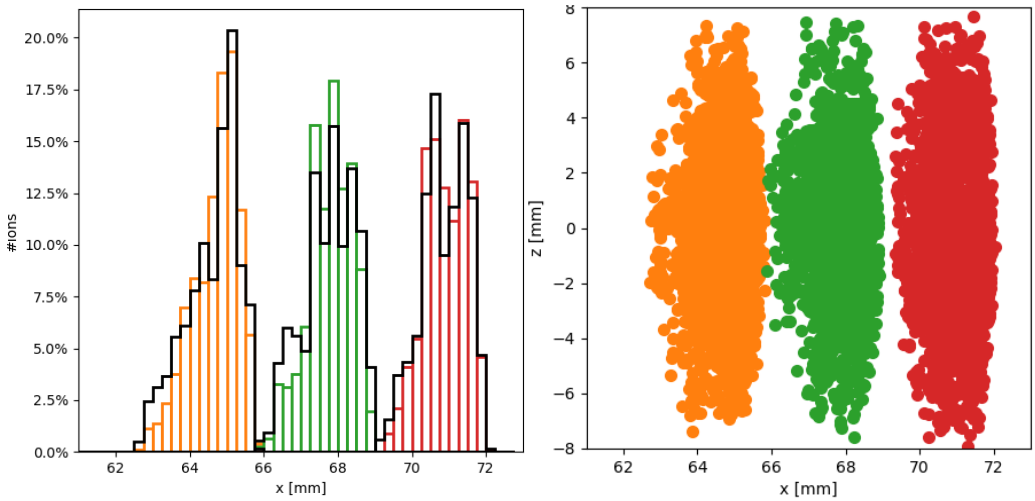

***Figure 3.13**: Left panel: distributions of the impact position in the case of particles randomly launched from the entire source slit, with an angular dispersion $\Delta\theta = \pm 3°$in the [X, Y] plane and an angular dispersion $\Delta\phi = \pm 3°$ in the [X, Z] plane. Black lines are the outline of the distribution from the previous case (Fig. 3.12 left panel). Right panel is the corresponding image on the EA [X, Z] plane.*

3. Detection of particles on the focal plane

3.1. Description

3.1.1. Operation of the detector

The aim of INEA is to measure the energy spectrum of ion particles after they have been dispersed by the electrostatic analyser (EA). The ions are detected individually by means of a Microchannel Plate (MCP) followed by a pixelized collector (see Section 3.3) that allows to retrieve the position of the impact point along the focal plane x_c. As indicated in Section 2.1, x_c is a linear function of the particle energy (Eq. 3.2.9).

A cross-section of the detector is shown in Figure 3.14. At the entrance of the detector, the grid G_{ISO1} is polarised at the potential V_{ref}, which corresponds to the potential of the base plate, so that the potential is constant between the base plate and the detector. As we shall see in Section 3.2.2, the grids do not behave like perfect equipotential planes: the "diffusion" of the electric fields existing on either side of the plane of a grid through the meshes thus leads to disturbances between G_{ISO1} and the base plate, causing aberrations of the image of the energy spectrum as measured by the detector. To reduce the potential disturbances upstream of G_{ISO1}, a second grid G_{ISO2} is placed behind this grid, also at potential V_{ref}. As indicated in Section 3.1.2, to avoid degrading the detection efficiency of the MCP, a third grid G_{repel} is placed in front of the MCP's entrance face, biased at a potential slightly lower (typically -50V) than that of the MCP entrance face V_{front}. The energy of the incident ions must be between 100 and reach a sufficient efficiency of the MCP (see Fig. 3.16), so the potential V_{front} must be between -100V and -500V.

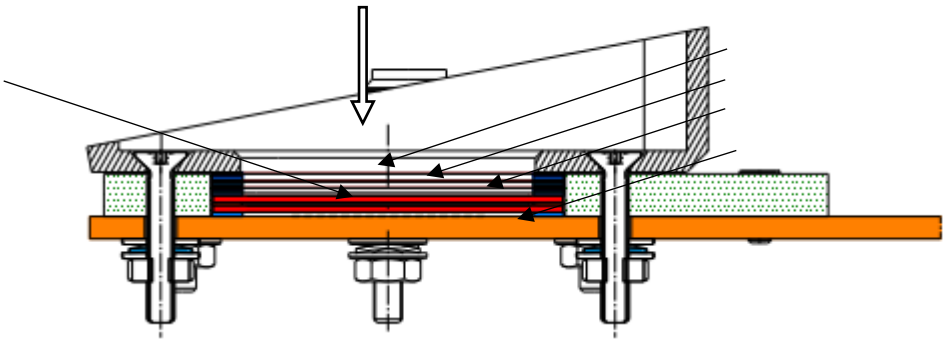

***Figure 3.14**: cross-sectional view of INEA's detector.*

3.1.2. Micro-channel Plates

A MCP is made up of ~1mm-thick glass itself composed of millions of lead oxide-coated tubes ~10µm in diameter polarised by a potential applied between the input and output faces. The potential is of the order of 0.8 to ~1kV (see Fig. 3.15). A particle entering a channel and impacting the wall causes the emission of a few secondary electrons. These electrons, accelerated by the polarisation potential of the MCP, in turn impact the walls and emit new secondary electrons, the number of secondary electrons being amplified by a cascade effect

(Figure 3.15, left-hand image) by a factor depending on the polarisation potential of the microchannel plate (Figure 3.15, right-hand image) and the number of MCPs stacked in series (usually 2 MCPs).

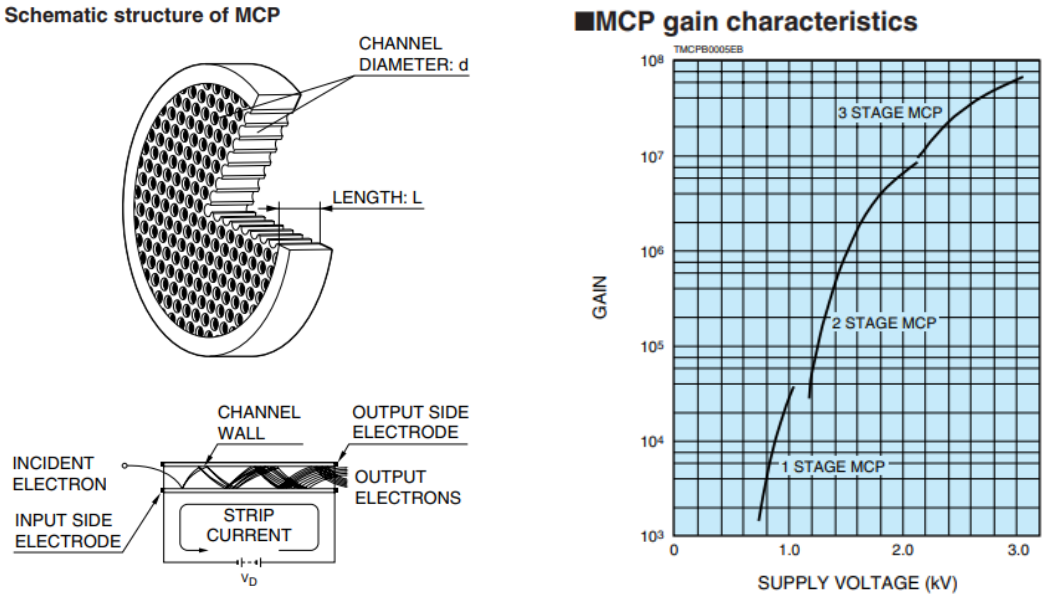

***Figure 3.15**: Left panel: Schematics of a Microchannel plate and schematics of the cascade effect occurring within a MCP channel. Right panel is the typical gain curve of MCPs at different supply voltages and stack configuration (credit: Hamamatsu).*

In our case, 2 MCPs of diameter 20 mm and supplied by Hamamatsu, are associated in a chevron-stack configuration, considered in the following as a single MCP, and operating in "saturated mode" (or "counting mode") with a high bias potential ~ 2 kV. Thus, an incident particle generates a pulse of electrons at the output of the MCP in the form of a current pulse with a total charge equal to G*e (G gain, e electron charge, $1.602 \times 10^{-19} C$). This charge is collected by a collector placed immediately after the output face of the MCP and processed by the associated electronics to provide the position of each individual impact on the focal plane (see next paragraph). Parameters that determine the performance of a MCP are: detection efficiency, gain, maximum flux of incident particles and background noise.

The detection efficiency corresponds to the probability of detection of an incident particle, which is a function of the nature of the particle, its mass and its energy. In INEA, the particles impacting the MCP are ions and Figure 3.16 shows, for different types of MCP, the variation in efficiency as a function of energy for O^+ ions. In our case, the curve to be considered is that corresponding to "uncoated MCPs".

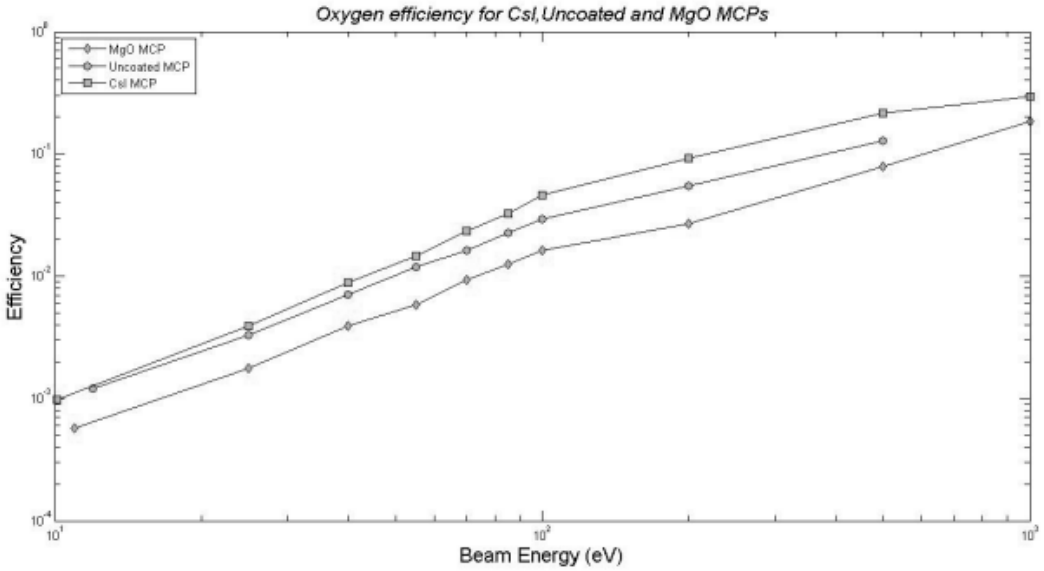

***Figure 3.16**: Comparison between absolute detection efficiency for O^+ for non-coated, MgO and CsI MCPs (Rispoli et al., 2012).*

Rispoli et al., (2012) found that for energies close to 10 eV, the detection efficiency is 10^{-3}. This means that for every 1000 incident particles only 1 will form an electron shower within the MCP and then will be detected. This efficiency is too low. It is therefore necessary to accelerate the ions before they impact on the MCP by imposing an appropriate potential on its input side, of the order of a few hundred volts. Efficiency also depends on the effective surface area of the channels, of the order of ~60% of the total surface area of the entrance face: particles reaching the entrance face over the 40% 'dead zone' do not generate initial secondary electrons inside a channel and therefore cannot be detected. For some specific MCP, the channel assembly has been modified to reduce the dead zone to ~10% and increase the probability of detection to ~90% (see Hamamatsu leaflet). We should also mention another technique for increasing the detection efficiency of ordinary MCP with 40% dead zone. A "repellent grid" placed in front of the MCP's entrance face and biased at a negative potential of -30V to -50V with respect to it, enables a large proportion of the secondary electrons created in the dead zone to be reflected towards the channel entrance. This "repellent grid" is the grid called G_{repel} inside our detector.

The variation in gain as a function of the potential applied to the MCP is shown in Figure 3.15. In saturated mode, the gain with 2 MCPs in series is of the order of 10^6 to 10^7. The corresponding height of the charge pulses at the output of the MCP is therefore around 1pC which is sufficient for the electronics to enable the detection.

The maximum flux of detected particles F_{max} (in $part.cm^{-2}.s^{-1}$) must be such that the current corresponding to the pulses $I_{max} = F_{max} \times \mathrm{G} \times \mathrm{e}$ is lower than 10% of the strip current circulating in the MCP $I_{strip} = \frac{V_{MCP}}{R_{MCP}}$ where R_{MCP} is the resistance of the MCP. From the MCP's datasheet, R_{MCP} is of the order of 100 $M\Omega$, giving a maximum flux of the order of $1.5 \times 10^5\ part.cm^{-2}.s^{-1}$

Finally, the background noise corresponds to the spontaneous emission of secondary electrons generating output pulses in the absence of incident particles. The corresponding N_{bkg} count rate is one of the limiting factors for the overall performance of the detector, both in terms of sensitivity, and in terms of the overall dynamic range of the order of $\frac{F_{max}}{N_{bkg}}$. The typical background count rate under good experimental conditions is of the order of $N_{bkg} = 1\ part.cm^{-2}.s^{-1}$ (Fraser et al., 1987).

3.2. Optimization of the detector's geometry

3.2.1. 'Real' detector

We need now to estimate the effect of a "real" detector in our simulation where the potentials applied to the entrance face of the MCP and to the grids are considered. The real structure of the potential in the space between the base plate and the detector, in the detector itself and the real trajectories of the ions under these conditions are modelled by SIMION. As in the case of the "ideal" detector, the results obtained are the positions of the ion impact on the EA's focal plane. The position on the entrance face of the MCP are registered as well. The simulation also includes the interaction of the leaking electric field outside of the detector and the electric field generated within the EA volume.

3.2.2. Effects of grids as electrostatic screens

The purpose of the G_{ISO1} and G_{ISO2} grids is to electrostatically screen the drift space between the base plate and the detector from the V_{repel} and V_{front} potentials applied to G_{repel} and to the entrance face of the MCP. Two grids have been introduced to improve the efficiency of this screening which is one of the critical points for an instrument designed to analyse low-energy ion populations.

The effect of a grid as an electrostatic screen has been modelled using SIMION and is illustrated in Figure 3.4. The grid simulated are 30x30 µm² wires spaced by 300µm. The grid, polarised at 0V, is placed between 2 polarised planes, one below the grid is also at 0V at a distance d1 = 500µm from the centre of the grid, the other above at potential V = 10V and at a distance d2 = d1. The "theoretical" electric fields are different on either side of the grid: E1=0 in the upper domain, E2=V/d in the lower domain. Fig. 3.17 shows that the grid does not behave like an ideal equipotential plane and that its screening power is not perfect, the electric field "propagating" partially through the grid meshes from the domain where it is strong (E2) to the domain where it is weak (E1=0). The equipotential lines obtained by SIMION show the existence of 2 scales in the potential perturbations:

- On a small scale, i.e. on the scale of the dimensions of the mesh and the wires, "potential bubbles" form in the immediate vicinity of the grid. The size of these bubbles is of the order of the size of the meshes. These irregularities in the local electric field moderately modify the trajectories of the ions because they are small in extent. As these modifications depend on the position of the trajectories relative to the grid bars, the overall effect of the potential bubbles is similar to a diffusion of the ion velocity vectors.

- On a larger scale, at a larger distance from the grid, the bubbles "recombine" to give almost plane equipotential lines, the potential then being variable in the upper domain which was supposed to be equipotential. Given the scale of this disturbance, the effect on the trajectories of the ions will be substantially uniform and potentially important if the potential V is very significant compare to the characteristic energy of the ions. To minimize the effect of the grids on the trajectory of the ions before the detector (in the theoretical field free space between the EA's exit and the detector entrance), the disturbance of the equipotential lines needs to be reduced down to few tenths of eV. We therefore studied several configurations of grids to respect such property.

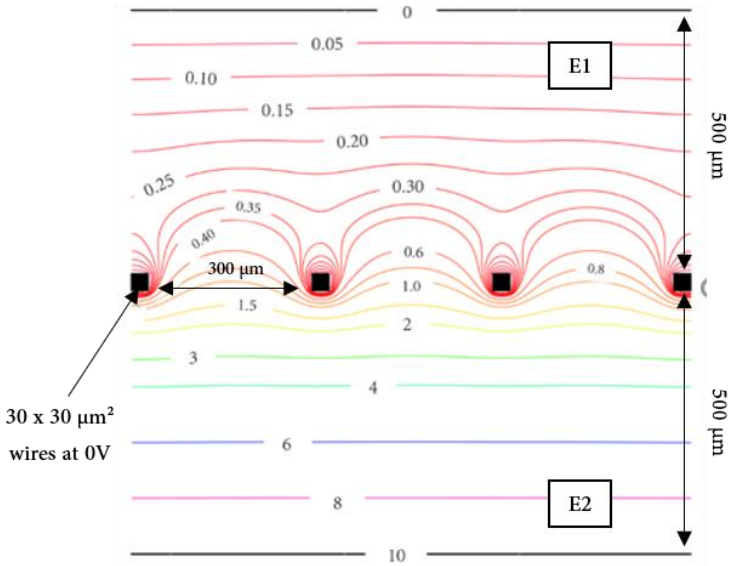

***Figure 3.17**: Simplified model of the penetration of the electric potential through the wire of an electrostatic grid. The coloured lines are the equipotential lines.*

3.2.3. Initial geometry of detector

For the initial geometry, the 3 detector's grids G_{ISO1}, G_{ISO2} and G_{repel} are identical with a ~75% transparency. The wire cross section is a 50 x 50 µm² square and the line spacing is 500µm. To increase the screening of the potential applied to G_{repel}, we chose to shift by half a mesh, in both X & Z directions G_{ISO2} relative to G_{ISO1}. The meshes of G_{repel} are aligned with G_{ISO1} $'s$. Fig. 3.18 gives a top and side view of the grid's geometry.

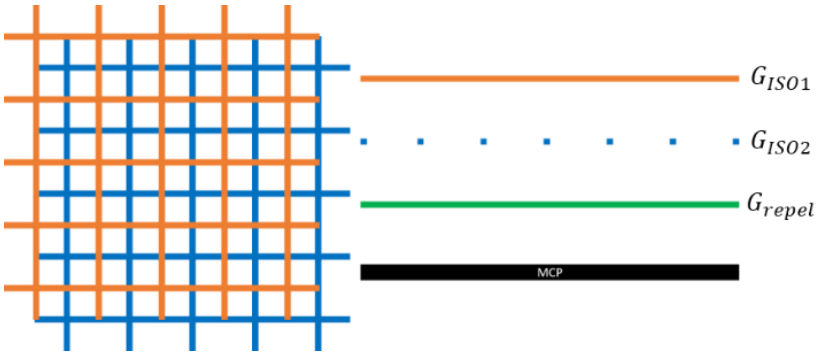

***Figure 3.18**: Left panel is a top view of the grid's arrangement. The orange grid represents G_{ISO1} while the blue one is G_{ISO2}. G_{repel} is not visible on the top view because it is vertically aligned with G_{ISO1}. Right panel is a side view of the grid geometry. The green grid represents G_{repel}.*

The potentials applied to the entrance face of the MCP and on G_{repel} are respectively $V_{front} = -500V$ and $V_{repel} = -550V$. The potential of G_{ISO1} and G_{ISO2} is $V_{ref} = 0V$.

The equipotential lines in the plane of symmetry of the instrument, modelled with SIMION in the free field space between the EA's base plate and the detector's entrance are represented in Fig. 3.19.

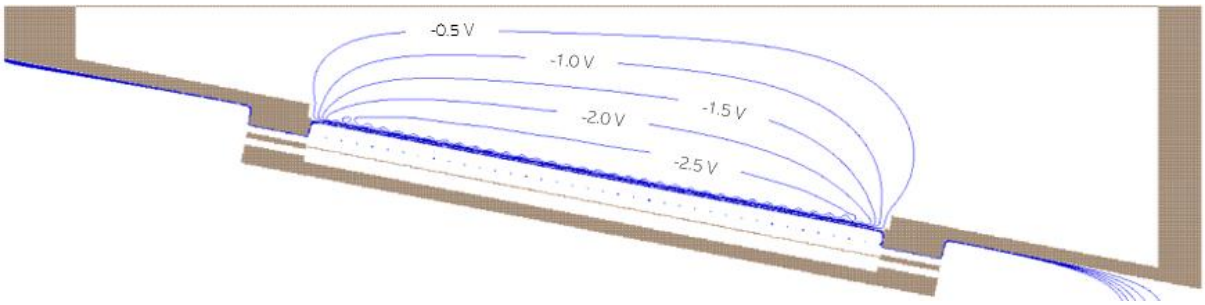

***Figure 3.19**: Extension of the electric potential inside the supposed field free region between the EA's baseplate and the detector entrance in the case where G_{ISO1} is a ~75% transparent grid. The blue lines are the equipotential lines with their corresponding values.*

To compare the goodness of the detector geometry, we compare the impact distribution on the focal plane with the one obtained in Section 2.3.3. The initial conditions of the particles are identical, i.e. 50 000 particles randomly distributed across the EA's source slit with a cone distribution of $\pm 3°$ along both θ and ϕ directions. Hence, Fig. 3.20 gives the 'ideal' distribution (black lines) compare to the one obtained with this detector geometry (coloured lines) for energies of 2.1, 2.2 and 2.3 eV.

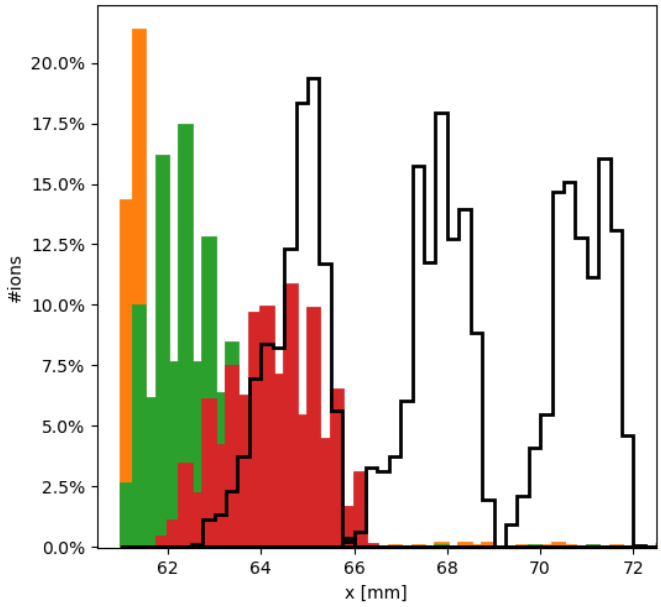

***Figure 3.20**: Impact distribution along the focal line when G_{ISO1} is a ~75% transparent grid. The orange, green and red histograms corresponds to populations with respective energies of 2.1 eV,2.2 eV and 2.3 eV. The black lines show the results from the ideal case displayed in Fig. 3.13.*

Thus, comparing to the ideal detector case, the screening of the potential V_{repel} is not sufficient. We can observe that the distributions for each energy is left-shifted meaning that while particles travel through the space between the EA baseplate and the detector, they are deflected due to the leaking potential in this region. More important, in this case, the 3 populations are not sufficiently separated anymore. The next section describes the geometry's improvement implemented to reduce this effect.

3.2.4. First improvement: Decreasing the transparency of G_{ISO1}

In this second geometry, the grids G_{ISO2} and G_{repel} remains identical as the precedent case. However, G_{ISO1} has now a much lower transparency, down to 50%. The new grid has wires with cross section of 100x50 µm² and a line spacing of 200 µm. Given the very significant deformations of the trajectories observed in the previous case, this choice was essential, even though it reduces the quantity of particles arriving at the detector. As we shall see, in Fig. 3.21, the equipotential lines have the exact same structure as the one depicted in the previous geometry (Fig. 3.20). However, their values are now reduced by a factor 10.

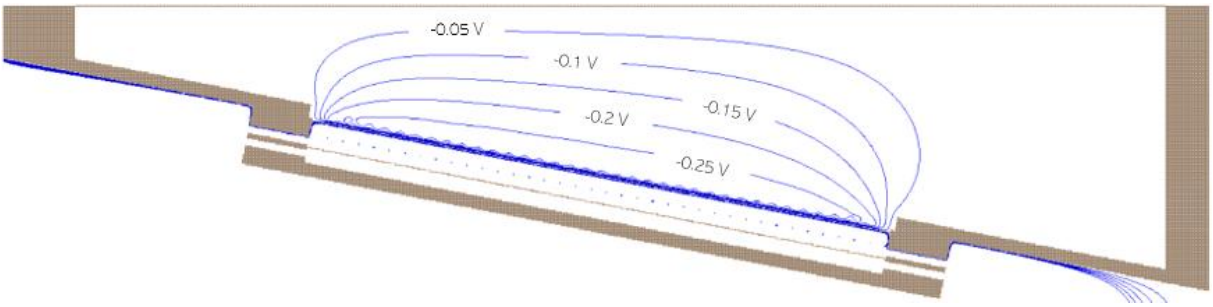

***Figure 3.21**: Extension of the electric potential inside the supposed field free region between the EA's baseplate and the detector entrance in the case where G_{ISO1} is a ~50% transparent grid. The blue lines are the equipotential lines with their corresponding values.*

Now looking at the distribution of the points of impact along the focal line, we can see, as described in Fig. 3.22, that the distribution for every energy has almost returned to the initial positions with respect to the ideal case. This result indicates that decreasing G_{ISO1}'s transparency is a suitable approach in order to correct the effect of the penetrating field in the drift space between the EA's base plate and the detector entrance.

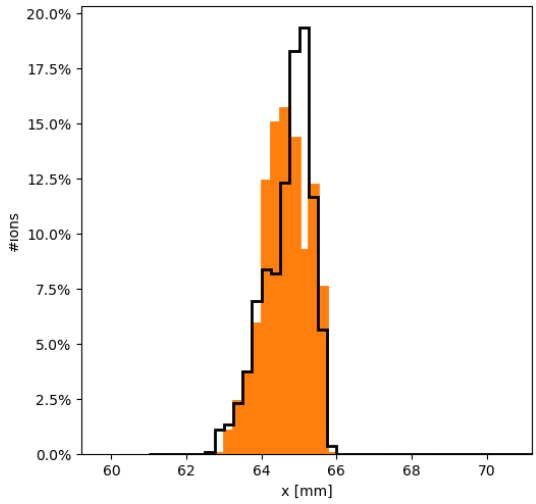

***Figure 3.22**: Comparison of the impact distribution on the focal line between the detector geometry where G_{ISO1} is ~50% transparent (orange histogram) and the ideal case (black line) depicted in Fig 3.13. For a better clarity, only the population at 2.1 eV is displayed.*

Yet, we proved that we can reconstruct the energy dispersion at the focal plane of the detector with respect to the ideal case. However, particles are effectively detected when they impact the entrance face of the MCP. Thus, it is important to compare the impact distribution at this location rather than on the focal plane. Fig. 3.23 left panel displays the histogram of the distribution for the population at 2.1 eV at the focal plane (black dashed lines) compare to the distribution at the entrance face of the MCP. The potentials on each elements of the detector remains the same as the previous section, i.e. V_{ref} = 0V, $V_{repel} = -550V$ and V_{front} = - 500V. It is clearly visible that the particle's trajectories inside the detector are disturbed due to small scale deformation of the electric field at the vicinity of the grid's wires, as depicted in Fig. 3.23 right panel. We can, in particular see that the histogram presents empty spaces which are due to the thickness of G_{ISO1}. Indeed, particles can only enter the detector at specific locations which leads to unreachable position at the entrance of the MCP.

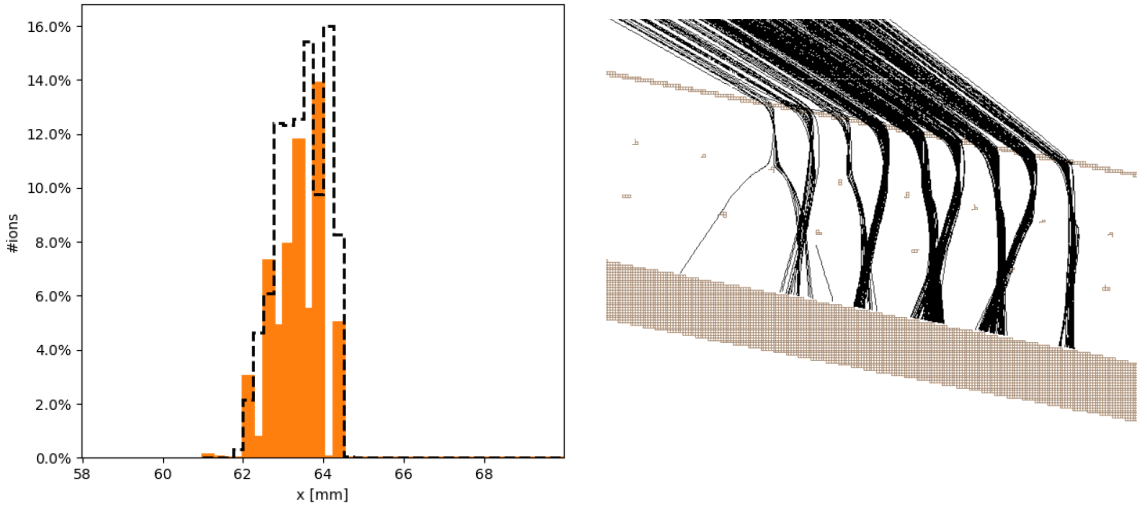

***Figure 3.23**: Left panel: Comparison between the impact distribution on the focal plane (dashed black line) and on the MCP entrance face (orange histogram) when G_{ISO1} is ~50% transparent. Right panel shows example of trajectories of ions inside the detector.*

3.2.5. Second improvement: Orientation of G_{repel}

For this third and last geometry, we decided to rotate G_{ISO2}. As described in Fig. 3.24, the wires of G_{ISO2} are now rotated by an angle of 45° with respect to the wires of G_{repel}. The idea here is to break the electric field structure which forces the particles to reach the MCP at only certain locations.

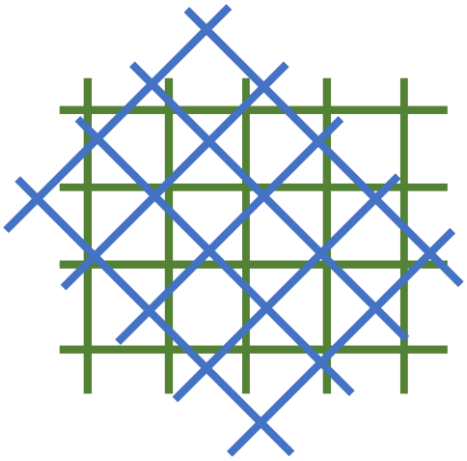

***Figure 3.24**: top view of the grid's arrangement where G_{ISO2} (blue) is rotated by 45° with respect to G_{repel} (green). G_{ISO1} is not represented on this schematic.*

The resulting effect of rotating the grid is displayed in Fig. 3.25 where we can observe that the distribution of particles along the focal plane is now distributed much more evenly. We can however still see the effect of G_{ISO1}'s geometry on the impact distribution at the MCP entrance face.

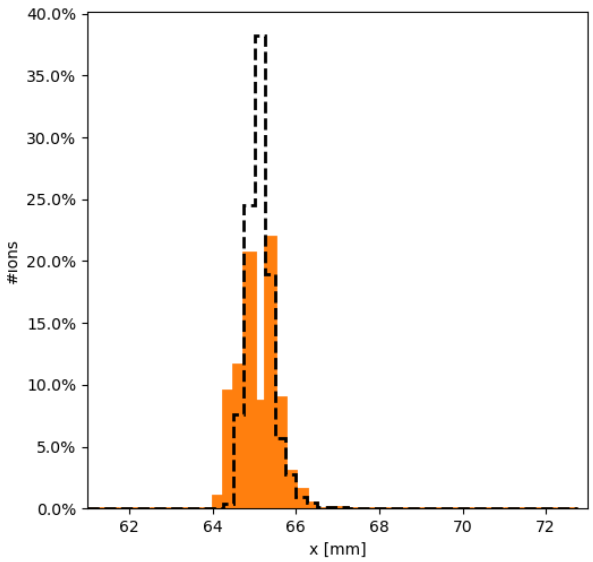

***Figure 3.25**: Comparison between the impact distribution on the focal plane (dashed black line) and on the MCP entrance face (orange histogram) when G_{ISO2} is rotated by 45° with respect to G_{repel}.*

From this study, we showed that the capability of INEA's energy analyser and detector assembly to reconstruct the ideal condition presented by the theory of Green & Proca (1970) strongly depends on the transparency of G_{ISO1}, which significantly controls the leakage of the electric potential in the space between the EA's baseplate and the detector entrance. We can also observe that during the mechanical assembly of the detector we should take care of the grid's placement. However, it is still noticeable that the three detector's grid should not be aligned on the mechanical model. One last improvement to control the width of the impact distribution is to tune the potential V_{front} *and* $V_{repel.}$ As an example, Fig. 3.26 shows a comparison of the impact distribution for a potential $V_{front} = -500V, V_{repel} = -550V$ (blue line), with the impact distribution when the potential are decreased to respective values V_{front} and V_{repel} of -200V and -250V (red line). Even though the width of the peak is unchanged, the distribution is much more uniform indicating a much lower impact of the small-scale structure of the electric field within the detector.

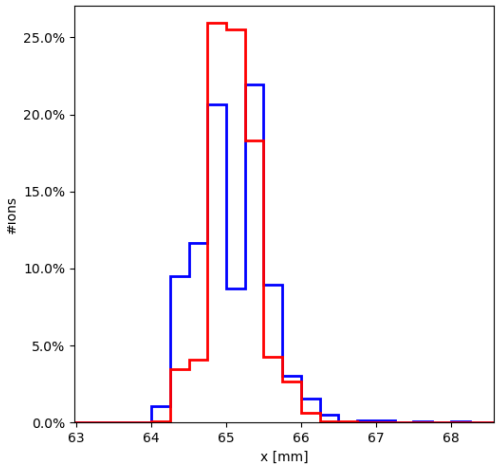

***Figure 3.26**: Comparison of the impact distribution at the entrance of the MCP between Vfront = -500V (blue) and Vfront = -200V (red)*

3.3. Position measurement

3.3.1. Pixelized Collector

To retrieve the impact position of the particles that arrives into the detector, we designed a pixelized collector on a PCB placed right after the output face of the MCP. As we shall see in Fig. 3.27 the collector is composed of 16 independent pixels. Each pixel represents a 0.5 x 12 mm² array and is made of gold-coated copper. The pixels are separated by a distance of 375µm. Also, the pixels are surrounded by a conductive area which allows charges that would otherwise not reach a pixel to be dissipated. The size of the array is a disk with 20 mm diameter which corresponds to the usable area of the MCP.

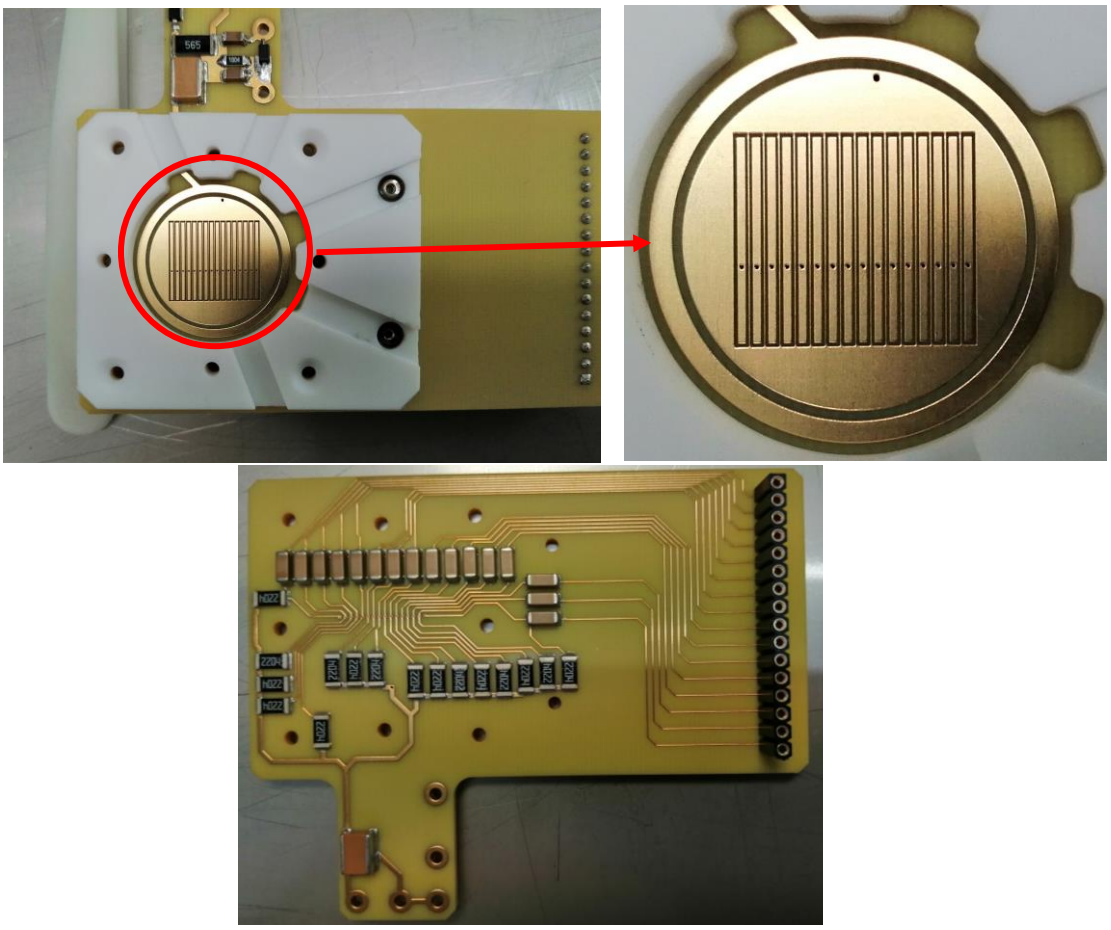

***Figure 3.27**: Top left panel is a top view of the detector PCB. A zoomed image of the 16 pixels used to retrieve the particle impact position is given on the top right panel. We can also see the ring track used to polarize the output face of the MCP (V_{back}). Right panel is a bottom view of the PCB.*

As explained in Section 3.1.1, the potential difference between the front and back of the MCP is ~2kV. Furthermore, as we set the front potential V_{front} in the range -100V – -500V, we are forced to polarise the back of the MCP at a potential V_{back} between 1.5kV and 1.9kV. In addition, the potential of the pixel must be slightly larger than the potential V_{back} to accelerate the electrons leaving the MCP (typically $V_{pixel} = V_{back} + 100V$). This acceleration prevents the spot formed by the electron spray from spreading too widely on the collector. Taking all

this information into account, this means that the pixels have to be brought up to a high voltage, making it impossible to use direct electronics to measure the signals coming out of the pixels. To address this problem, we placed 16 coupling capacitors with a value of 1.5 nF at the output of the pixels. A coupling capacitor, is an electronic component used to enable the transfer of alternating current signals while blocking direct current signals. It acts as a bridge between two parts of a circuit, allowing AC signals to pass through while preventing any DC bias or offset from affecting the connected components. This allows us to disregard the high voltage of the pixel and to use the desired electronics at the output of the coupling capacitors. These capacitors are highlighted in Fig. 3.27 bottom right panel.

3.3.2. Detector polarisation

INEA's detector requires 4 voltages to operate as shown in Figure 3.28. To limit the number of cables inside the vacuum chamber, the voltages V_{front} and V_{repel} as well as V_{back} and V_{pixel} are generated directly on the PCB using the two input voltages, respectively Alim_HT1 and Alim_HT4. Alim_HT1 and Alim_HT4 are laboratory power supplies placed outside the vacuum chamber. The voltages V_{ISO1} and V_{ISO2} are equal and are supplied by mechanical contact with the EA's base plate. The electrical circuit including the polarisation stage, and the pixel coupling is displayed in Fig. 3.28. The potential on the exit face of the MCP V_{back} is created by the mean of a Zener diode with a breakdown voltage $V_z = 100\,V$ (Ref: 1PMT4135, Microsemi). The output of the Zener is directly connected to a conductive ring placed around the collector. This ring is electrically connected to the output face of the MCP via a circular stainless-steel foil 200 µm thick (see Fig. 3.27). For the polarisation of V_{pixel}, 2.2 $M\Omega$ resistors are connected in series with each track between the input voltage Alim_HT4 and the pixels. These resistors force the signals picked up by the pixels to flow towards the coupling capacitors rather than back to the high voltage power supplies.

V_{front} and V_{repel} voltages are polarized in a similar way to $V_{back}\ and\ V_{pixel}$. The only difference is the choice of reference for the Zener diode (Ref: MMSZ51T1G, ON Semiconductor) with a breakdown voltage $V_z = 51V \pm 5\,\%$ at 100 µA. The electrical connection between the PCB and G_{repel} is made using a cable that is electrical soldered to the grid support (similarly as the electrical soldering used for the EA's guard plates) while the connection of the front end of the MCP is achieved thanks to a cable that is fixed on a dedicated slot on a 100 µm thick annular stainless-steel foil.

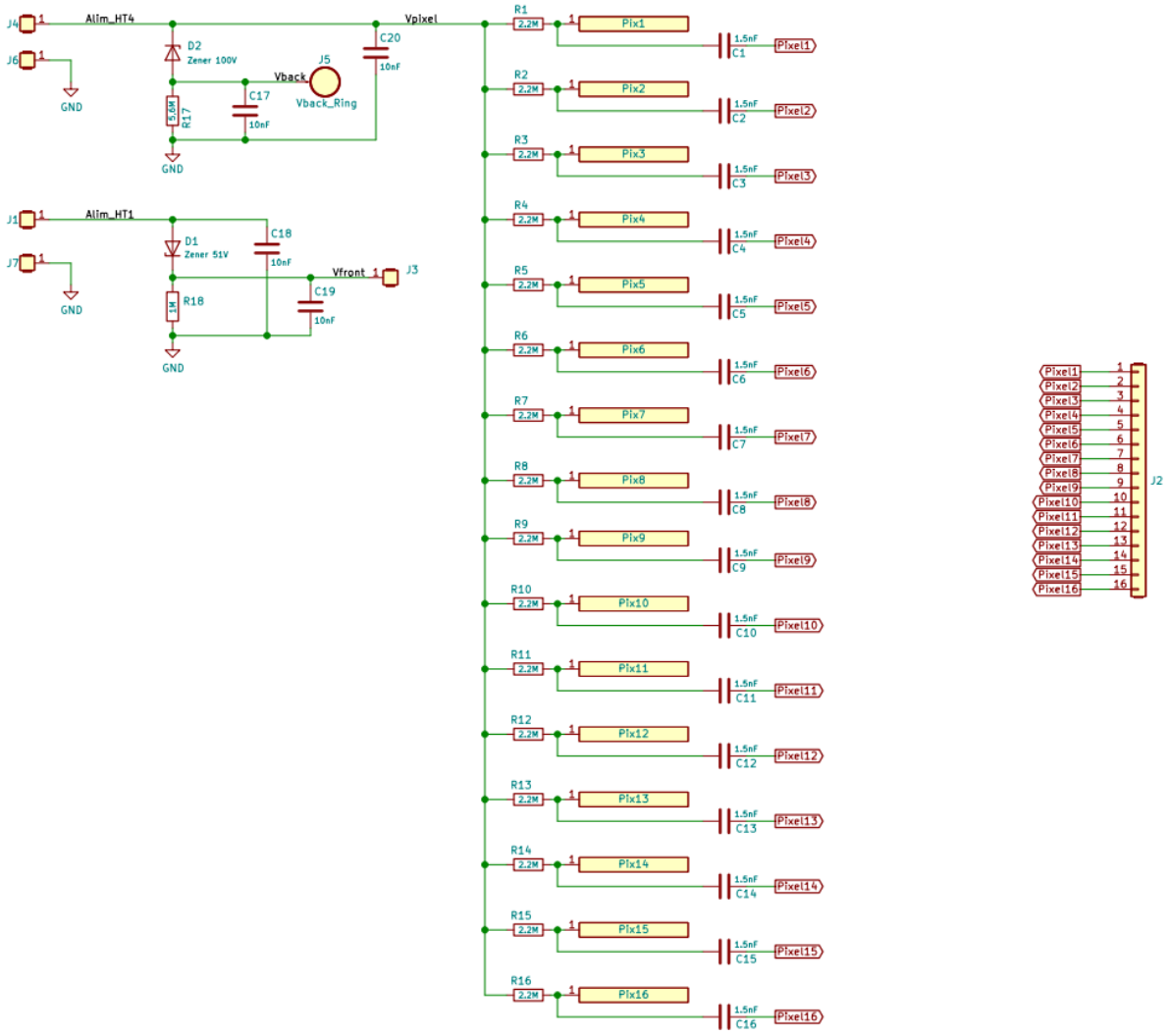

***Figure 3.28**: Electronic scheme of the detector polarisation circuit.*

3.4. Detector V1: 3pix

3.4.1. Description

For this first version of the detector, we choose to mask most of the pixels on the collector leaving only 3 of them visible by the output face of the MCP. The associated electronics are composed of a simple circuit integrating only a charge sensitive amplifier (CSA) that is plugged at the output of the desired pixel. As we shall see in Fig. 3.29, the pixels are masked using a 100µm thick stainless-steel foil with 3 slits aligned with pixels n°3, 8 and 14.

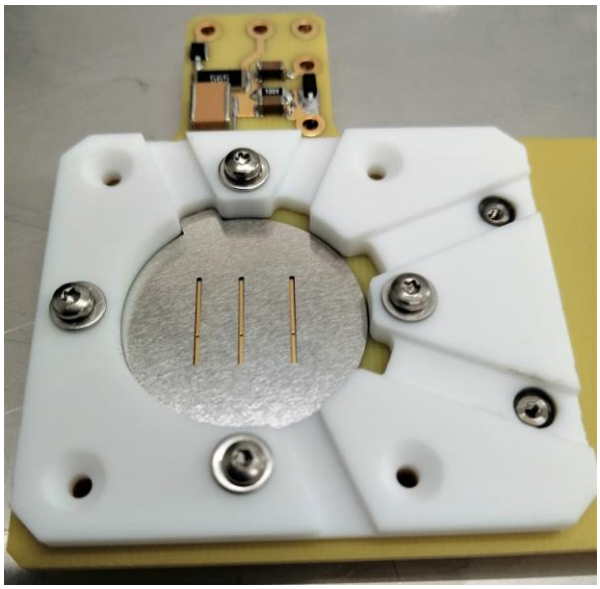

***Figure 3.29**: Photograph of the detector showing the stainless-steel foil used to mask the pixels*

The goal of this set up is to characterize the electron shower coming out of the MCP stack, i.e. estimating the charge pulse amplitude and the dark noise generated by the MCP as well as simple tests of the EA.

3.4.2. Charge Sensitive amplifier

The electron spray collected by a pixel travels in a conductor in a form of a current pulse. This latter has a very amplitude that is difficult to measure in our setup, thus an electronic device such as a charge sensitive amplifier (CSA) must be used. The CSA integrates the current pulse arriving from the pixel and convert it in a voltage pulse with an amplitude proportional to the incoming input charge. The charge sensitive amplifier design in its most basic form is shown in Fig. 3.30 below. A feedback capacitor C_f between the input and output stores the charge from the detector, and the gain of the preamplifier is $1/C_f$. Each pulse of current from the detector causes the output of the charge sensitive preamplifier to step, the output being the time integral of the current pulse. The gain of a CSA is given in units of output volts over input charge (e.g. volts/picocoulomb).

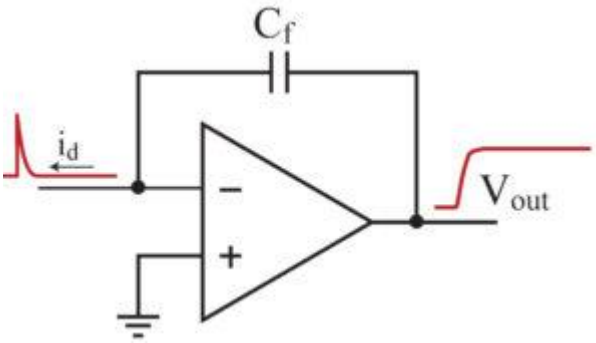

***Figure 3.30**: Simplified circuit of a charge sensitive amplifier*

The CSA circuit in the above schematic has no way to be reset - the output will increase until the charge sensitive preamplifier reaches its maximum output. So, the circuit as drawn above is not practical. The most common method to reset the CSA is to place a resistor R_f in parallel with the feedback capacitor. The pulse response of the amplifier is hence transformed to that of a tail pulse, where the rise time is similar to the pulse's one, but there is now a longer decay time. The decay is exponential and the time constant τ is equal to the $C_f \times R_f$. Thus, the signal charge pulses Q_s are converted into voltage pulses with an amplitude $V_{out} = -\frac{Q_s}{C_f}$ which is damped by the time constant τ.

For our applications, we chose $C_f = 1pF \; and \; R_f = 510 \; k\Omega$ which leads to a time constant of 510 ns. The OpAmp that we used is the AD825 from Analog Device, which is a high-speed amplifier with ultra-low input bias current. The complete electrical circuit of the CSA is displayed in Fig. 3.31 left panel including the power supply filtering. Fig. 3.31 right panel is a photograph of the PCB associated to the circuit.

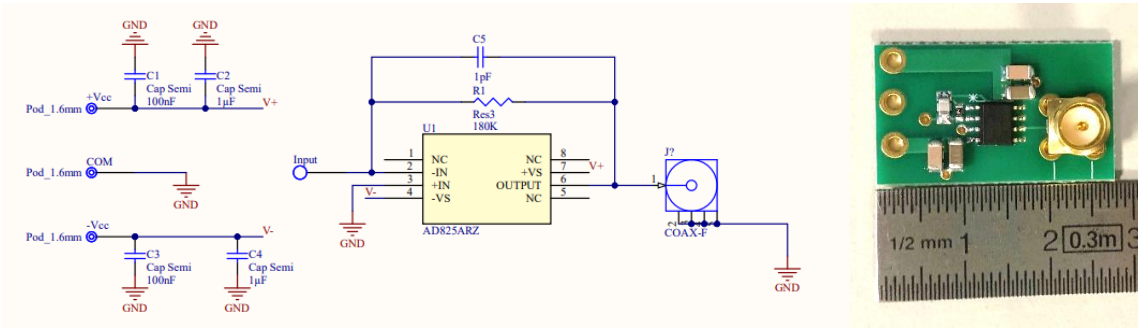

***Figure 3.31**: Left panel: Electronic scheme of the detectors charge sensitive amplifier. Right panel is a photograph of the corresponding PCB.*

3.4.3. Breadboard testing

Before integrating the CSA circuit to INEA's detector, we made a quick test on a breadboard outside the vacuum chamber. It consists in generating a charge pulse at the entry of the CSA that is similar to the one generated by the electron shower coming from the output face of the MCP. This was achieved by using an arbitrary function generator (Tektronix AFG3102) in series with a 2pF capacitor placed at the entrance of the CSA. The AFG3102 generates pulses with an amplitude of 200 mV across the capacitor. Fig. 3.32 show an example of the response obtained with the CSA circuit. The blue trace is the input voltage pulse from the signal generator while the yellow is the output from the CSA. We can therefore estimate the time constant τ. Classically we consider that after 3τ the voltage decay is about 95% which is around 1.6µs on our measurements giving a measured τ of 530 ns. This value is in very good accordance to the theoretical 510 ns. Using the CSA equation, we can determine the charge of such voltage pulses through a 2pF capacitor to be Q_c = 0.4 pC. The charge pulses from the MCP is expected to be ~0.1 pC, which is the same order of magnitude.

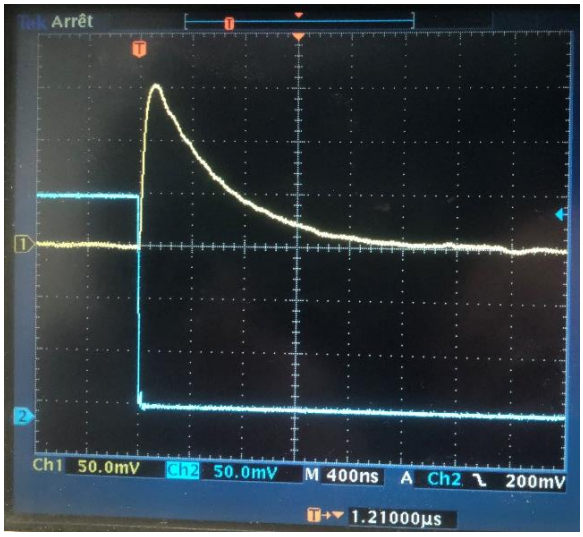

***Figure 3.32**: Yellow line is the output voltage pulse relative to an input charge pulse of 2pC. The blue line is the voltage pulse generated by the pulse signal generator.*

3.5. Detector V2: ASIC

3.5.1. Description

Fig. 3.33 shows the block diagram of the detector, the processing electronics and the signal interface with the PC used to control the experiment and acquire, record and display the data. Also shown are the potentials applied to the various elements of the detector, comprising:

- A set of 3 grids: G_{ISO1}, G_{ISO2} and G_{repel} .
- 2 MCPs.
- A collector with 16 pixels located immediately after the output face of the second MCP.
- An LPP_16 ASIC for detecting charge pulses on 16 channels. The collector and LPP_16 are mounted on PCB1.
- The Data Processing and Acquisition Unit (DPU), electronics used to control and monitor the voltages applied to the detector, and to acquire and display data. The DPU is located on PCB2, which is connected to PCB1.

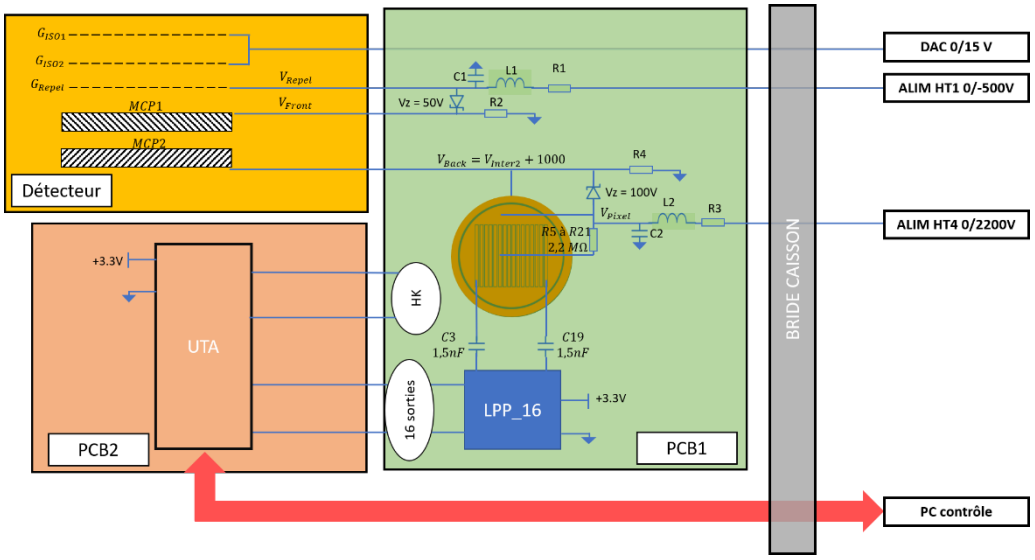

***Figure 3.33**: Block diagram of the detector including the LPP_16 ASIC and its DPU*

3.5.2. Description of the LPP_16 ASIC

The LPP_16 detects charge pulses (electrons) from the MCP whose amplitude is distributed according to a Gaussian with an average gain of the order of ~10^6, i.e. ~ 0.1pC. The ASIC consists of 16 detection chains (Fig. 3.34). Each of the chains is composed of a charge sensitive amplifier (CSA) for amplifying the charge pulses (Iq) from the MCP and converting them into voltage pulses, followed by a discriminator (Discr) to generate a logic pulse for each voltage pulse with an amplitude larger than the threshold applied to the discriminator's reference input (V_{seuil}).

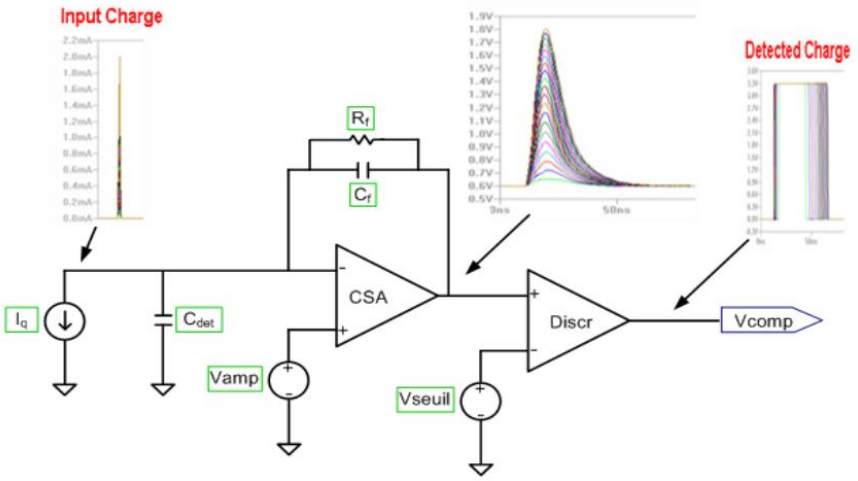

***Figure 3.34**: Detection chain of the LPP_16 ASIC*

The characteristics of the LPP_16 are as follows:

- Power supply: 3.3V ± 100 mV
- V_{seuil}: 0.5V to 2.4V
- Power dissipated per channel: 1.25 mW
- Anode+track capacitance C_{det}: 2pF - 15 pF.
- Min/max loads of detected pulses: 32fC - 3pC

C_{det} represents the capacitance seen at the LPP_16 input, formed by a pixel and the link track with the CSA input.

The signals at the LPP_16 outputs are digital signals with the following characteristics:

- Output voltage (Vout): 0 to 3.3V
- Output Pulse width (Tw): 40 to 250 ns
- Minimum delay between 2 pulses (Td_{min}): 330 ns

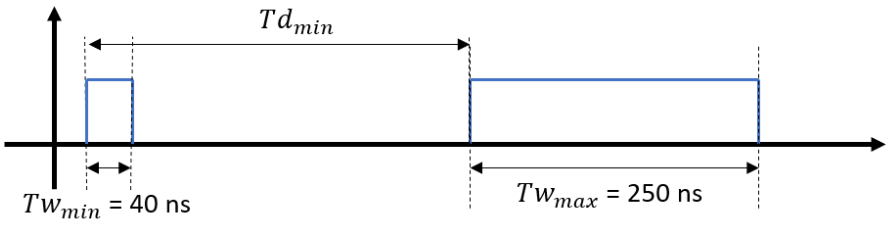

***Figure 3.35**: Chronogram of the logic pulses at the output of an LPP_16 channel*

3.5.3. Operation of the DPU

Fig. 3.36 shows a block diagram of the DPU electronics, located on PCB2 and comprising a processor, a block of 16 counters, a memory, an ADC and a DAC.

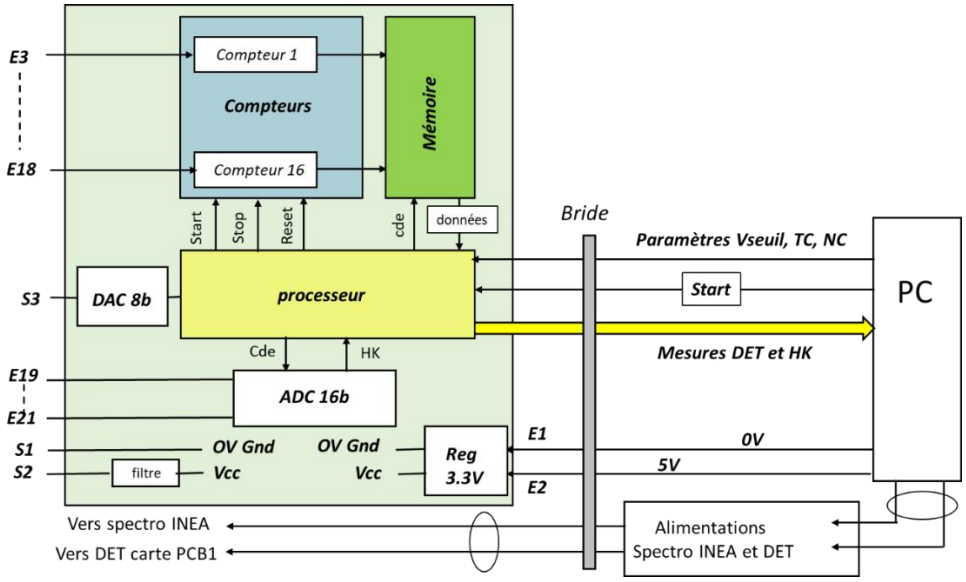

***Figure 3.36**: Block diagram of the DPU used to operate the detector with the LPP_16 ASIC*

The measurement sequence carried out by the DPU is described as follows:

1- The PC opens a "measurements" file listed by its number, date and time. The file number must be stored in the software so that it can be incremented each time a measurement sequence is performed.
2- At the start of a measurement sequence, the PC controls all the power supplies needed to run the experiment. The HV power supplies pass through the vacuum chamber flange and then via cables to the PCB1 board. The LPP_16 ASIC supply voltage V_{cc} is that of PCB2 obtained via the connection between PCB2 and PCB1. The 3.3V Vcc voltage is obtained from the 5V available on the PC followed by a 3.3V regulator on the PCB2 board.
3- The PC transfers to the processor the parameter V_{seuil} required for the detector to operate the measurement sequence TC (integration time of an elementary measurement), NC (number of elementary measurements in a measurement sequence). V_{seuil}, TC and NC are stored in the "measurements" file.
4- The PC send the start signal
5- On receiving this signal, the processor acquires the 5 housekeeping (HK) parameters supplied by PCB1 (inputs E19, ..., E23), resets the 16 counters and then starts the measurement sequence.
6- The 16 counters count the pulses from the 16 channels of the LPP16 ASIC on PCB1 which are connected to inputs E3, …, E18 on PCB2.
7- At the end of each elementary TC duration measurement, the 16 counts are transferred to the memory on the processor's command.
8- These 16 values are transferred to the PC and archived in the "measurements" file.

A summary of all the input/output used to operate both PCB1 and PCB2 is displayed in Fig. 3.37 below.

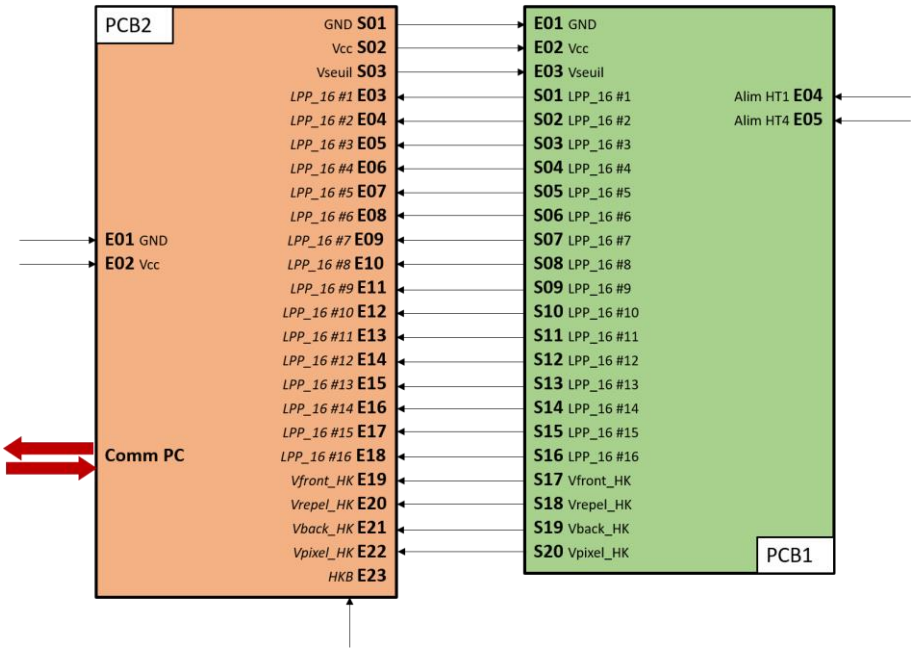

***Figure 3.37**: Block diagram of the I/O between the DPU (PCB2) and the detector's PCB (PCB1).*

PCB1 and PCB2 are being designed, manufactured and tested by REC[1]. Unfortunately, the conception of these two PCBs have been delayed by several months so that no test of the detector using this setup could be done before the submission of this manuscript.

4. The Ion Source

4.1. Objectives

The ion source aim is to convert neutral particles or atoms into charged ions, a necessary initial stage which allows the ionised particles to be manipulated with the electrostatic optics of the instrument.

As it was briefly discussed in chapter 2, several ionisation techniques exist. The two main ones used for embedded instruments are electron bombardment and charge exchange surfaces. Each technique has its advantages and drawbacks. Electron bombardment is capable of ionising particles without consideration of their energy; however, it can dissociate molecules. When using electron bombardment source, the energy of the electrons must be precisely controlled to avoid breaking the molecules. The other ionisation technique relies on charge exchange when the neutral particle is reflected from a surface. This technique is much less destructive for the molecule however its efficiency is significantly decreased at energy lower than 100 eV (Futaana et al., 2012).

Most recent mass spectrometers developed for space exploration of planetary atmospheres used ion sources based on electron bombardment of the neutral constituents. Electron impact ionisation is a technique in which electrons collides with atoms resulting in the formation of positively charged ions. In the frame of space-based mass spectrometer, electrons used to ionize the neutral particles are classically emitted by hot filaments via thermionic emission. Such approach faces several limitations when targeting low density environment or low energy particles. On one hand, the strong heating at the vicinity of the filament leads to the outgassing of the instrument walls during the measurements, in particular water molecules (Mahaffy et al., 2015; Schläppi et al., 2010). On the other hand, electrons emission from a hot filament requires a significant power consumption.

To resolve these two difficulties, we have been working on the development of a new neutral particle ionisation source. It is based on the use of carbon nanotube (CNT) cathodes. This solution offers three major advantages over current techniques:

- a current of ionising electrons of the same order of magnitude as previous ionisation sources emitted over a large surface, which limits space charge inside the ion source,
- much lower power consumption than sources using hot cathodes,
- no heating when electrons are emitted, which significantly reduces the outgassing from the inside of the instrument.

A schematic of the ion source developed in this thesis is given in Fig. 3.38 showing the 3 main parts of the source:

- The electron source which includes the large area CNT cathode, an extracting (G_1) and anode grids as well as an electron lens (EL) with 3 electrodes to reduce the divergence of the extracted electrons and maximize their flux into the ionization volume.
- The ionization volume (IV).
- The ion lens with 6 electrodes at exit of the ionization volume which focuses the newly created ions towards the entrance of the energy analyser.

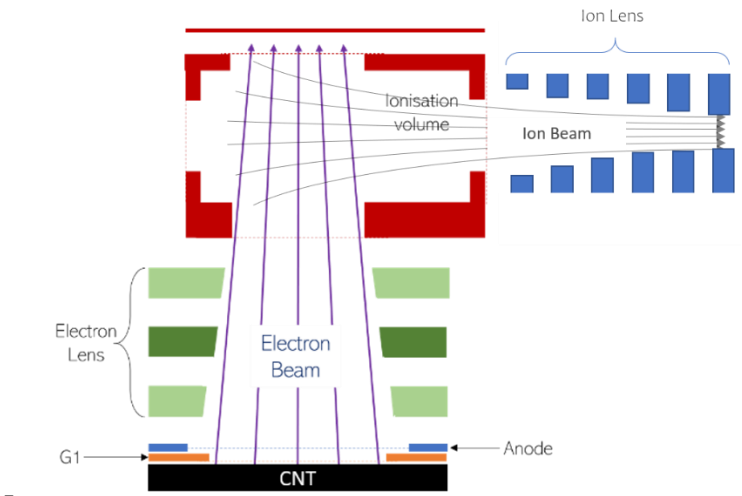

***Figure 3.38**: Schematic of the ion source including the trajectories of electrons and ions.*

4.2. Characteristics of the electron source

4.2.1. Field emission

Field emission comes from a quantum process called tunnel effect. This effect allows the electrons to cross the potential barrier between a solid body and vacuum. One way to lower this potential barrier is to apply a strong electric field to the surface of the material (Fowler & Nordheim, 1928). Fowler – Nordheim (1928) described an exponential relation between the current I and the electric field (Eq. 3.4.1)

$$I = A\frac{1.42 * 10^{-6}}{\varphi}(\beta V)^2 \exp\left(\frac{10.4}{\sqrt{\varphi}}\right)\exp\left(-\frac{B_{FN}\varphi^{1.5}}{\beta V}\right) \qquad 3.4.1$$

where A (m^2) is the effective emitter area, V is the gate potential, β (m^{-1}) is the field factor, φ(eV) is the work function, and B is equal $to\ 6.44 \times 10^9\ V.m^{-1}.eV^{-1.5}$. The product βV is equivalent to the local electric field at the emission sites.

For most of materials, an electric field with a magnitude of the order of $10^9\ V.m^{-1}$ is required to sufficiently lower the barrier and to allow for field emission. However, field emission from cold cathode rely on a second phenomenon: localized enhancement of the electric field. In the vicinity of an object with a high aspect ratio (with a high length to diameter ration or high curvature radius, i.e. tip, wire, cone, …) the equipotential lines tighten at the top of the sharp tip, resulting in a localized amplification of the electric field. By cleverly modifying the geometry of the material it is possible to obtain values of β of the order of several hundreds. It is important to emphasize that field enhancement is extremely local. The amplification of the field is only significant over a distance of a few times the radius of the tip, after which, the field becomes equal to the macroscopic external field. The typical result is a decrease of 95% of the amplification factor at 5 times the apex radius (Filippov et al., 2021).

Since the aspect ratio of a single CNT can reach few thousands, an extremely enhanced electric field can be created and thus, allowing emission of electrons in a macroscopic electric field of less than $10^6\ V.m^{-1}$. These considerations on the amplification factor are valid for an individual nanotube in a planar system, and for a tip/anode distance large compared to the height of the nanotube. In the case of a dense carbon nanotube array, electrostatic shielding occurs and a lower amplification is induced. Typical ideal distance between two adjacent nanotubes has been estimated as being equals to half of the height of an individual CNT (Bonard et al., 2001).

For our applications, we chose to use a cathode with a high density of nanotubes in order to optimize the duration of the emitter . We performed a test of 700 hours of continuous operation of a CNT cathode showing only a 20% decrease of the emission intensity (Gallois, 2018). A dense CNT cathode is also more resistant to vibrations as we also demonstrated it during vibrations tests (Gallois, 2018).

The cathode used for our application is a 15 x 15 mm² surface uniformly filled with vertical CNT's with a few tens of nm diameter and an average height of 210 µm. The extracting grid G1, located ~ 300µm above the CNT's upper surface, is polarized at a positive V_{G1} voltage while the CNT's are polarized at a negative voltage V_{CNT}.

4.2.2. Optimization of the emitter assembly

This section objectives are to understand the influence of the extraction grid G1 on the emission from the CNTs. As a first approach, we decided to simulate the electric field generated by the couple CNT-G1. In this simulation, we consider that the field emission from the CNT is homogenous, which implies that small variations of the CNT's height or orientation are not considered. Thus, the spatial distribution of the electric field is only due to G1's geometry.

Figure 3.38 shows an image of the electric field seen by the electron as they are emitted by the carbon nanotubes. As we considered a homogenous emission, we can limit the analysis to only 4 mesh grids. The wire spacing is 300µm and the wire section is 30 x 30 mm². The numerical resolution is 5µm.

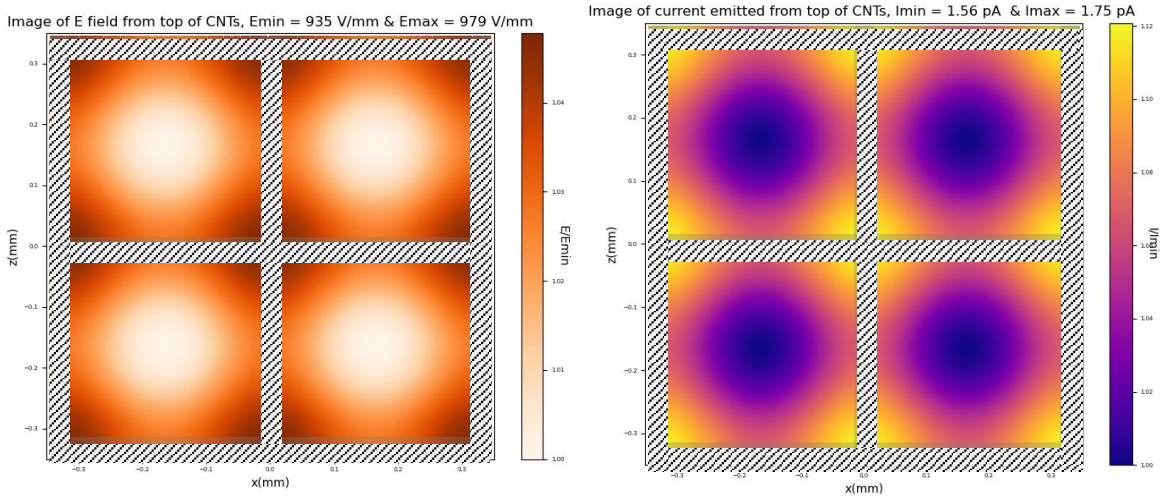

***Figure 3.39**:Left panel: Distribution of the electric field seen from the tip of the CNT array. The position of G_1 is represented with the hatched rectangles. Right panel is the corresponding image of the current emission using the Fowler-Nordheim equation.*

We can therefore see that the grid's wires affect the electric field with an amplitude of $\frac{E_{max}}{E_{min}} = 1.047$. This difference in the amplitude of the electric field therefore induces a difference in the current emitted by the CNTs. The current emitted by the CNTs is estimated using the Fowler-Nordheim emission law:

$$J = aE^2 \exp\left(\frac{-b}{E}\right) \quad 3.4.2$$

Where *J* is the current density, *a* and *b* are parameters dependent on the material and the geometry of the field and *E* is the electric field intensity. The current emitted from the CNT array is obtained with the following method: The emitting surface is split into cells with a surface of 1µm² and we launch *n* particles in each cell. A weight is assigned to each particle representing a proportion of the total emitted current. The weight is calculated with the following formula:

$$I_{particle} = \frac{a \times E_{cell}^2 \times exp\left(-\frac{b}{E_{cell}}\right) \times A_{cell}}{n} \quad 3.4.3$$

Where $A_{cell} = 1\mu m^2$ and E_{cell} is the mean electric field in the cell.

Thus, we also observe a difference in current $\frac{I_{max}}{I_{min}} = 1.12$ between the zone under the bars of the grid and those under a mesh (Figure 3.39 right panel). We can also observe a non-homogenous emission under the grid's wires. As a matter of fact, when two wires cross each other, the current increases under this intersection.

Considering the previous observations, we can estimate the effective transmission of G1 compare to the geometrical one, which is 75%. The current collected on G1 is calculated by:

$$I_{G1} = \sum_{A_{G1}} I_{particle}(x, y) \quad 3.4.4$$

Where A_{G1} is the area of the grid and (x, y) represent the coordinates of a point that is under G1's wires.

We then obtain an effective opacity of G1: $\frac{I_{G1}}{I_{emitted}}$ = 30.3%.

We can also determine the influence of the distance *D* between the CNT tip and G1. Intuitively, as *D* decreases, the electric field difference between a point under the wire's intersections and a point under the centres of the meshes should increase. Figure 3.39 shows the ration $\frac{E_{max}}{E_{min}}$ as a function of *D*. The wire section and line spacing are still 30µm² and 300µm.

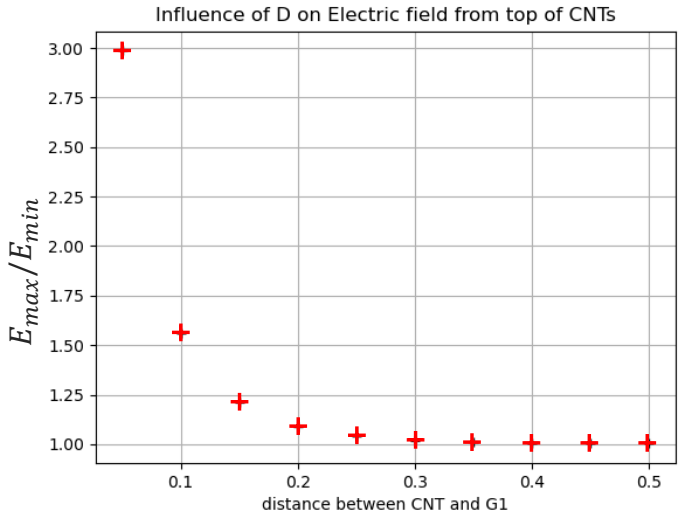

***Figure 3.40**: Difference of electric field seen from the top of the CNT array as a function of the distance D between G1 & CNT*

We observe that at a distance *D = 300µm*, which corresponds to the size of a mesh (Fig. 3.40), the electric field homogenises, leading to neglectable differences due to G1's geometry. Thus, we can define the optimal distance between G1 and CNT at 300 µm, which allows to use an acceptable potential difference between G1 and CNT of ~300V while avoiding significant heterogeneity of electron emission. In the general case, we can extrapolate this result and assume that to minimise the effect of G1's geometry, we must satisfy a configuration where the distance D must be equal to the mesh size.

Finally, the last parameter that can affect the electron emission due to G1's geometry is the size of the meshes. Figure 3.40 gives the ratio $E\frac{max}{E_{min}}$ as a function of the mesh size L_{mesh}. In order to keep a constant transmission of G1, we define the wire width (and height) L_{wire} as $\frac{L_{mesh}}{L_{wire}} = 10$.

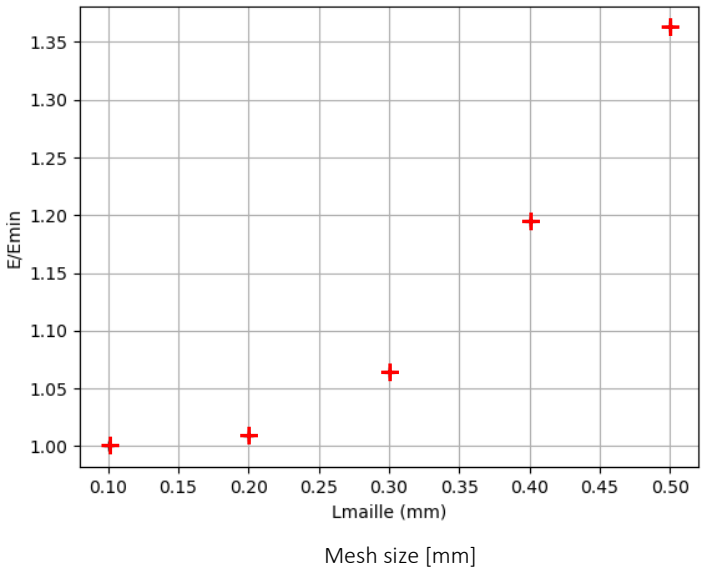

***Figure 3.41**: Influence of G1 mesh size on the electric field at the top of the CNT array*

As L_{mesh} is reduced, the geometry of the grid approaches that of a solid electrode and therefore the electric field between the CNT and G1 approaches an ideal configuration between 2 parallel planes. For meshes < 300µm, the electric field smoothes out. However, such meshes requires very thin wires leading to fragile and very loose grids. Considering an electric field with magnitude ~1000V/mm, this kind of grids could bend and completely modify the geometry in an unpredictable manner.

To optimise and thus reduce the effect of the grid bars on the CNT emission, a G1 grid with the smallest possible mesh size (while maintaining an acceptable mechanical stiffness) should be chosen. This grid must then be placed at a minimum distance from the CNTs such that $D = L_{mesh}$.

4.3. Ions extraction and energy distribution

In this section, using SIMION, we have carried out a study of the extraction efficiency of the ion source. As mentioned earlier, INEA should operate embedded on a spacecraft which will allow the ions created in the ionization volume (IV) to be extracted toward the energy analyser. In the case of laboratory operations, the mean gas velocity is zero so we defined a strategy to extract the ions from the IV while controlling their energy.

4.3.1. Geometrical reference frame

For the following analysis, we will consider the sub-assembly of the ionisation volume and the ion lens. The global reference frame [X, Y, Z] is shown in Fig. 3.42. The X axis corresponds to the line of sight of INEA, the Y axis is perpendicular to X and is oriented vertically. The Z axis completes the reference frame. The origin of the reference frame is located at the centre of the ionization volume.

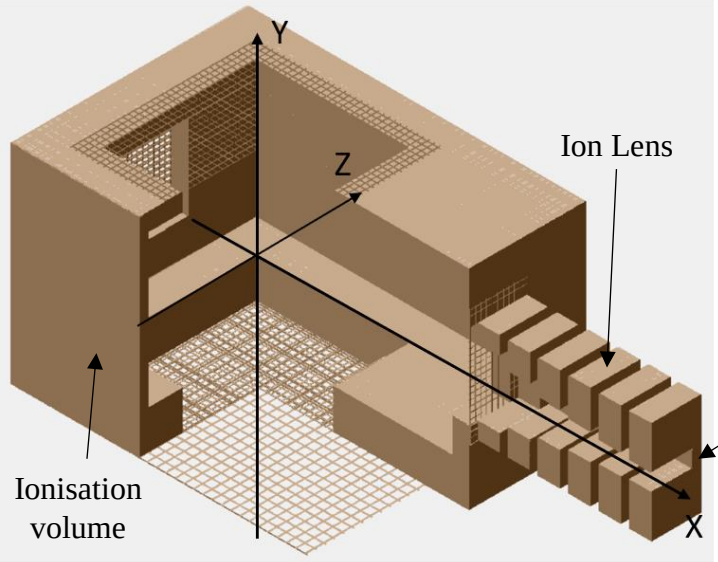

***Figure 3.42**: Simulated geometry of the ionization volume and the ion lens. Neutral particles enter from the left and the formed ions leave on the right*

4.3.2. Particle initial conditions

For each different simulation, we fly 2 million O_2^+ ions with no background speed and a Maxwellian distribution of thermal speed corresponding to a temperature of 293K (room temperature). To create the Maxwellian distribution, 3 numbers are calculated from a gaussian distribution with a standard deviation equals to $\sqrt{\frac{K_b T}{m_{O2}}} = 275.92\, m/s$ at T = 273K. Each number corresponds to the velocity of the particle along one axis.

The mean free path of the particles inside the vacuum chamber is

$$\bar{l} = \frac{k_b . T}{\sqrt{2} . P . \sigma} \qquad 3.4.5$$

Where T is the temperature, P the pressure in the vacuum chamber and σ^2 is the collision cross section. For $O_2^+ ion, \bar{l}$ is equal to 65 meters at 1×10^{-6} mbar. This confirms that the ions created within the IV do not interact with each other and therefore travel in straight lines.

4.3.3. Ions extraction: Ideal Case

As the particles travel in random directions, a fraction of them have the adequate direction that is directed toward the IL exit. We first estimated the geometrical transmission. In this 1st approach, we used a simplified 3D case with a 5mm side square ionization volume with ideal grids (perfect planar equipotential) at the exit of the IV. Then, as we shall see in Fig. 3.43, we mapped the probability, over the entire volume, of an ion to reach the exit of the IL with an angular dispersion within $\pm 3°$. To calculate the probability at every point within the IV, we used the following method: First, we create a cone that is oriented parallel to the X axis and with its top locate at the particle initial position. The cone half-angle is set at 3° and its length is determined by the distance L between the initial position of the particle and the slit located

at the end of the IL. The radius of the cone base (which is in the same plane [Y, Z]) at the IL exit is then defined as:

$$r = L \times \tan 3° \qquad 3.4.6$$

Secondly, using a Monte-Carlo integration method we estimate the overlapping area between the IL slit and the projected cone (if the intersection exists). The obtained area represents all the angular solutions that allows the particle to cross the IL exit with an angular dispersion within $\pm 3°$. Thus, the ratio of the calculated overlapping area over the area of a sphere defined by $4\,\pi L^2$ gives the probability for a particle to reach the slit with the desired acceptance angles lying inside a 3° cone at a specific initial location within the IV.

This method is repeated over the whole IV and then we compute the average probability which gave the geometric transmission.

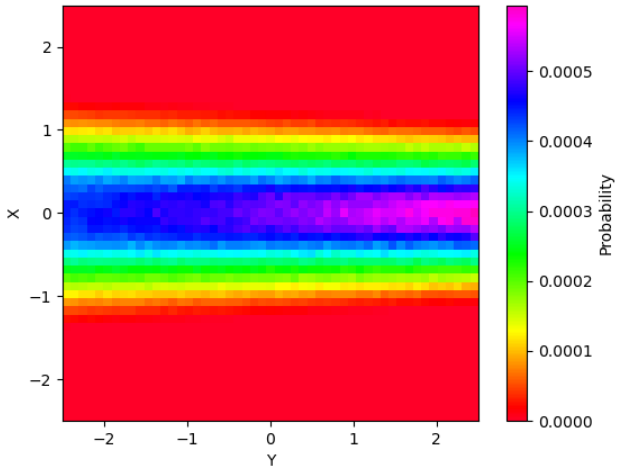

***Figure 3.43**: Probability distribution in the plane of symmetry [X, Y, 0] for particles to reach the end of the ion lens with a velocity vector direction at less than 3° with respect to the X-axis.*

With the previously described method, we find that for this simplified case, the transmission of the setup is $\frac{N_{exit}}{N_{VI}} = 1.26 \times 10^{-4}$.

In the next step to characterize the transmission of the sub assembly, we simulate, with SIMION, the fate of ions created within the IV. We still consider an ideal grid at the exit of the simplified IV. Particles initial conditions are as detailed in Section 4.3.2. Fig. 3.44 displays examples of trajectories reaching the IL with an angular dispersion of $\pm 3°$ in the case of an ideal grid at the exit of the IV. The transmission $\frac{N_{exit}}{N_{IV}}$ of the described setup is estimated to equals to 1.24×10^{-4} according to the simulation which is in very good accordance with our previous calculation.

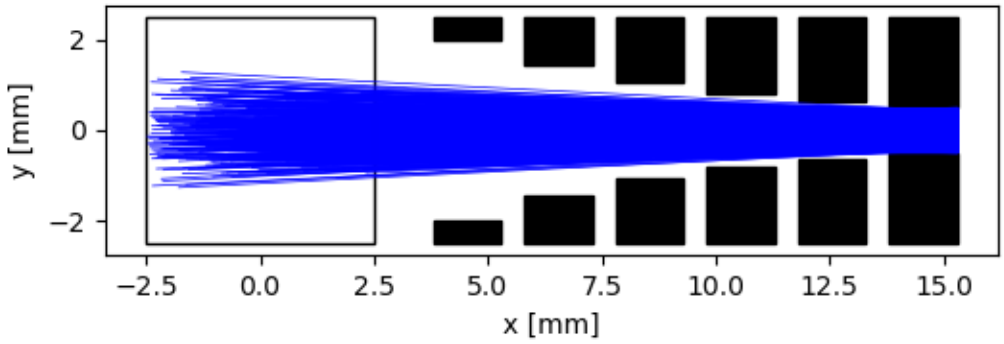

***Figure 3.44**: Trajectories of particles launched from the simplified ionisation volume and reaching the IL with an angular dispersion lower than 3°.*

One solution to control the energy of the extracted ions is to apply to the ionization volume a potential V_{IV} of few volts. Applying such a potential will generate an electric field between the IV and the 1st electrode of the IL. Theoretically, the energy distribution of the particles should not be altered since they will all experience the same acceleration once reaching the end of the IL. In another words, the particles energy distribution should peak at V_{IV} and then have a long tail at higher energies representing the thermal contribution. We then used our simplified model to simulate the fate of ions created inside the IV elevated at a potential of +2V, the IL electrodes being all grounded. In Fig. 3.45 we plotted the trajectories of particles in the XY and XZ plane.

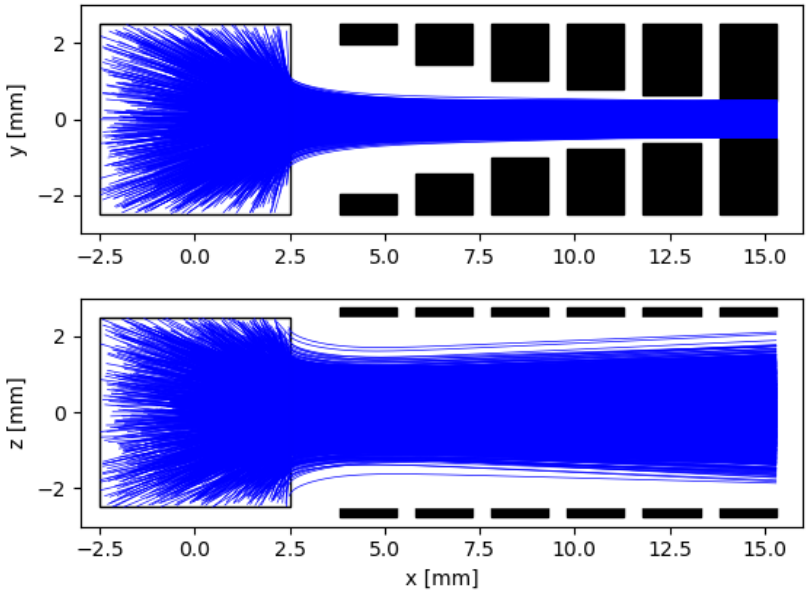

***Figure 3.45**: Trajectories of particles launched from the ionisation volume and reaching the IL within the acceptance cone angle of 3°. In this case, particles are accelerated between the IV and the 1st ion lens electrodes. Top panel illustrates the trajectories in the [X, Y] plane while the bottom is in the [X, Z] plane.*

As expected, the energy distribution peaks at 2.0 eV and has a long tail at higher energies due to the thermal contribution, as illustrated in Fig. 3.46. We can also observe that the shape of the initial distribution is not deformed compare to the energy distribution at the exit of the IL. This is due to the ideal grid at the IV exit.

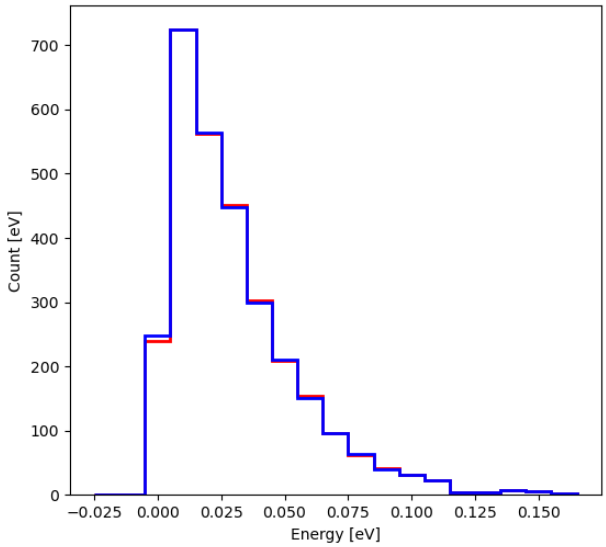

***Figure 3.46**: Comparison of the energy distribution between the particles at the end of the IL (red) and the same particles at their initial positions (blue). The red line distribution has been obtained by subtracting 2 eV to the particle's energy.*

Finally, looking at the transmission of the setup with this potential's configuration, we found that $\frac{N_{exit}}{N_{VI}} \approx 0.15\%$, that is a factor 10 increase compared to the case with potential.

4.3.4. Ions extraction: Real case

We detailed in the previous section a method to extract the newly formed ions inside the IV towards the exit of the Ion Lens. This method was applied in the frame of a simplified geometry where the exit grid of the IV was considered to be ideal, i.e. a perfectly planar equipotential with 100% transparency. We now want to estimate the feasibility of this method using a real geometry. Replacing the grid at the exit of the IV by a real grid formed of meshes and wires will create a potential leakage at the vicinity of the grid as we already saw in Section 3.2.2.

In this section, we consider an ionization volume with the following dimensions: 14mm along X, 10 mm along Y and 14mm along Z. The walls width is 0.5mm and the grids are placed inside the IV. Fig. 3.47 details the mechanical dimensions. The IV exit grid has wires with a cross section of 30 x 30 µm² and the distance between two wires is 300µm.

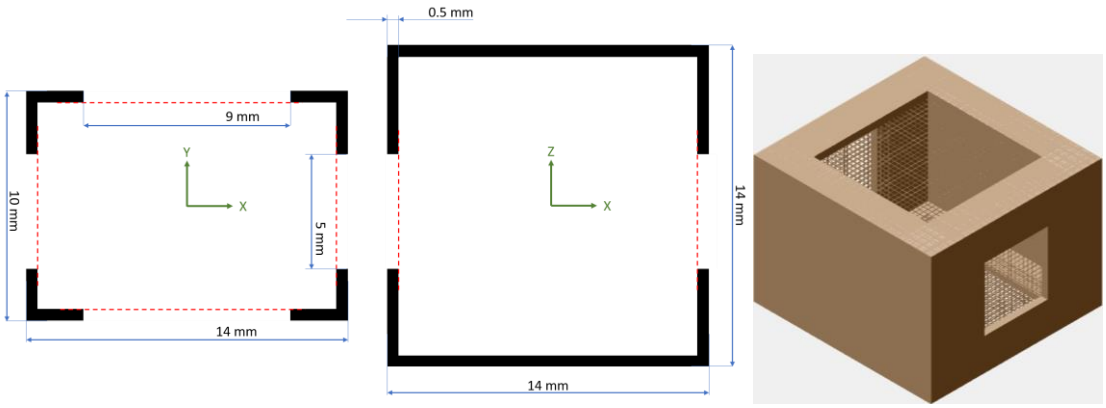

***Figure 3.47**: Left and middle panel are the dimensions of the ionization volume respectively in the $[X, Y]$ and [X, Z] planes. Right panel is a 3D view of the simulated corresponding geometry.*

Using particles initial conditions as described in Section 4.3.2 and applying a potential difference of +2V between the IV and the 1st IL electrodes, we can see, as illustrated in Fig. 3.47 right panel, that there is indeed a potential bubble penetrating inside the ionization volume. Moreover, we can see that this bubble tends to improve the transmission of the setup since it will attract particles inside the IV, allowing them to be accelerated towards the exit grid (see Fig. 3.47 right panel). Using the numerical method detailed previously, we found that the geometric transmittivity of the setup without the extraction potential V_{IV} is $\frac{N_{exit}}{N_{IV}} \approx 3 \times 10^{-5}$.

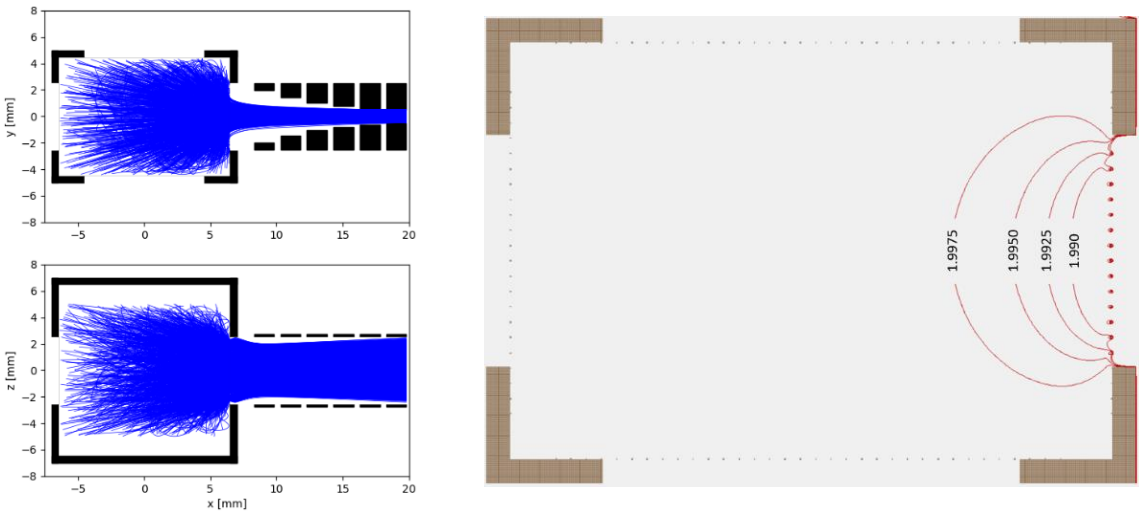

***Figure 3.48**: Left panel top and bottom are the particles trajectories in the [X, Y] and [X, Z] planes. Right panel displays the penetration of the electric potential through the IV exit grid in the case of a real grid. The IL 1st electrode is grounded while the IV is at +2V. The redlines shows the equipotential lines and their corresponding values.*

We then simulated the trajectories of ions with an extraction potential $V_{IV} = 2V$ and the IL electrodes grounded. According to the simulation, the transmission is equal to 0.122%, similar to the ideal case presented in the last section. As we look at the initial energy distribution (Fig. 3.49), the peak energy is almost 0 eV. However, we would expect to find an average energy of 0.012 eV (energy corresponding to 275 m/s for O_2). This difference can be explained when we look at the phase space ($v_y = f(v_x)$ *and* $v_z = f(v_x)$).

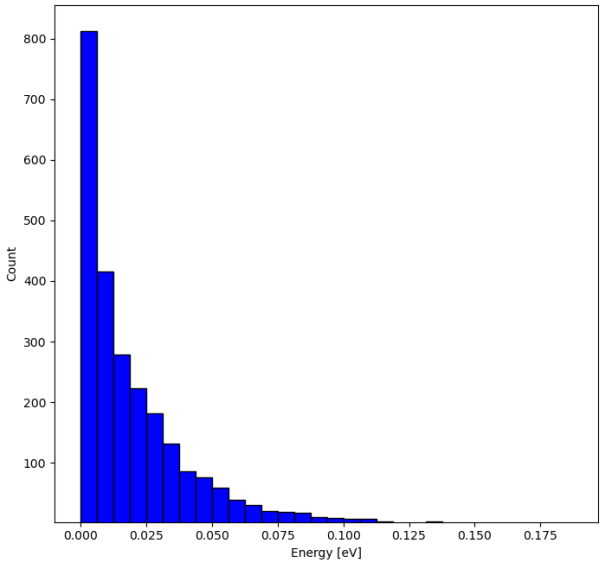

***Figure 3.49**: Initial particles energy distribution that reached the IL exit with an angular dispersion within* $\pm 3°$.

In fact, when we plot these two distributions. We observe a population of particles with negative velocities and small amplitudes along the 3 axes. This velocity distribution convoluted with the effect of the potential bubble contribute to shifting the main peak of the distribution towards 0 eV.

Once they reach the exit of the IL, particles exhibit an energy dispersion as shown in Fig. 3.50 below.

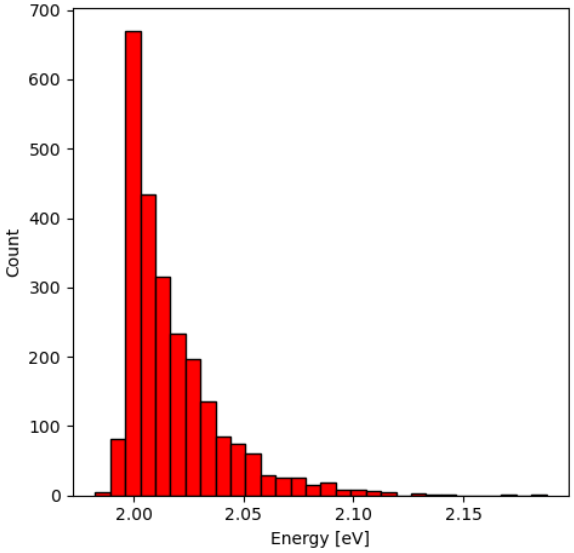

***Figure 3.50**: Particles energy distribution at the IL exit for* $V_{IV} = +2V$ *and the IL at 0V.*

When the IV and the IL are at potentials of +2V and +0V respectively, the potential difference experienced by the particles corresponds to 2.0V, which iss to the energy peak in Fig. 3.50. However, a long tail can be seen towards the highest energies. This corresponds to the thermal velocities, similarly as the ideal case presented before. There is also a tail to the left of the peak,

towards the lowest energies. This part of the histogram is due to the potential bubble induced by the grid separating the IV from the IL. As this grid is not ideal, it allows the potential generated between the IL and the IV to penetrate slightly into the ionisation volume. Thus, the particles generated closer to the grid experience a potential difference slightly lower than 2V (equipotential lines shown in Fig. 3.47).

In addition, it is possible to compare the dispersion obtained by SIMION with the theoretical dispersion obtained if there were no penetration of a potential bubble inside the IV. The theoretical dispersion thus corresponds to the initial dispersion shown in Fig. 3.49, shifted by 2eV (see Fig. 3.51). This corresponds to the theoretical potential difference between the IV and the output of the IL.

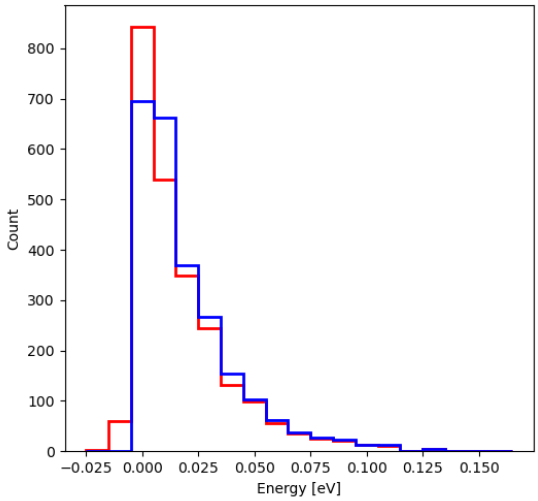

Figure 3.51*: Comparison of the energy distribution at the IL exit (red) and at the initial positions (blue) in the case where the IV exit grid is a real grid. To compare the two distributions, the red distribution has been shifted by 2 eV, corresponding to the acceleration potential seen by the particles when they exit the IV.*

4.3.5. Application to different IV geometries

Here we propose to estimate any differences in the final dispersion of the particle's energy distribution according to 3 different geometries:

- A geometry where the grids are placed inside the IV (case studied in the last section): CASE 1
- A geometry where the grids are placed outside the IV: CASE 2
- A geometry where the VI is extended along the x axis with the grids placed outside: CASE 3

Fig. 3.52 illustrates the 3 different geometries as well as few equipotential lines penetrating the IV, which gives a qualitative insight of the extend of the potential bubble for every geometry.

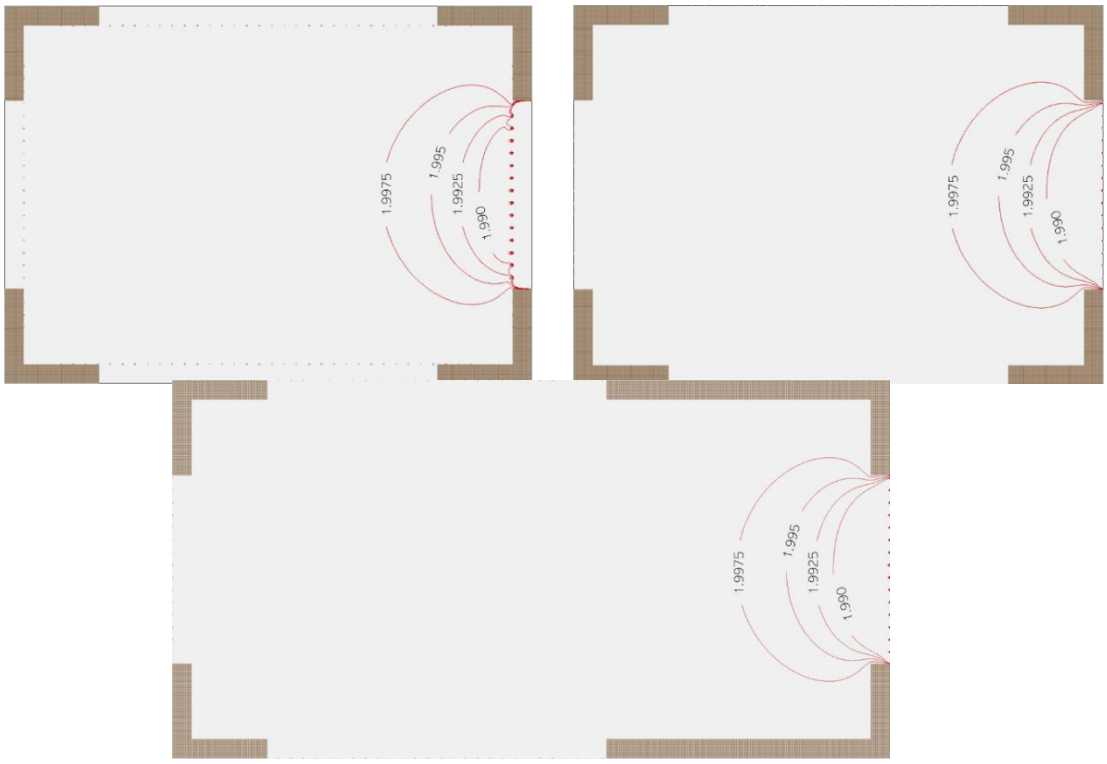

***Figure 3.52**: Structure of the equipotential lines for different IV geometries. Top panel displays case 1 (left) and case 2 (right). Bottom panel shows the equipotential lines for an extended ionization volume (case 3).*

To compare the different geometries, we keep the same initial conditions as detailed in Section 4.3.2. As we shall see in Fig. 3.53, this slight geometry differences do not induce any change of the energy distribution for both cases. This was expected since the extent of the potential bubble remains identical for every case, as displayed in Fig. 3.52.

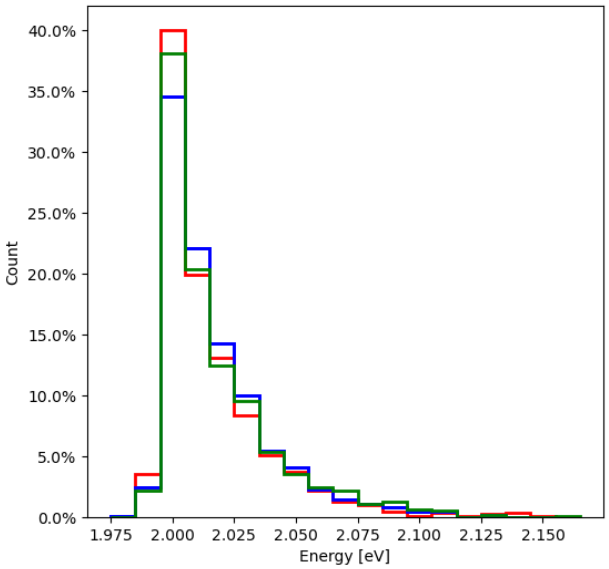

***Figure 3.53**: Comparison of the energy distribution at the IL exit for the 3 IV geometries. Blue corresponds to case 1, red to case 2 and green is case 3, as defined in Fig. 3.52.*

If we now look at the transmission for each case, we find values of 0.122%, 0.06% and 0.05% for respectively cases 1, 2 and 3. Although the transmission looks two times higher when the grids are placed inside the IV, it remains of the same order of magnitude, which does not imply significant differences. To refine these observations, it's worth considering the geometrical volume formed by the IV. For cases 1 and 2, the ionisation volume is 1521 mm^3. For case 3, the geometrical volume is 2106 mm^3. For cases 1 and 2 we therefore obtain a 'density' of 1315 ions/mm^3. For case 3, the density is 950 ions/mm^3. Thus, the simulated particle density is 1.4 higher for case 1 & 2. By correcting this bias, we can thus estimate the transmission at equivalent density, which is 0.07% for case 3. We chose to use case 3 for our mechanical model. The reason is that during experiments achieved with an older version of the ion source (build and tested before the beginning of the thesis), we observed that a fraction of the primary electrons emitted from the CNT array was able to exit the ionization volume towards the Ion Lens (Steichen, 2019). By extending the IV along its X-axis, it should reduce this number by providing a better confinement of the primary electrons within the IV. As it is described in the publication in section 4.6, primary electrons were however still able to reach the IL exit.

4.4. Ion source mechanical assembly

4.4.1. Electron source

For our application, we used CNT developed by NAWA Technologies on Si substrate 0.5 mm thick covered by a layer of 8 to 15 nm of Al on which multiwall carbon nano-tubes (MWCNT) have been synthetized at 600°C with a hot-filament chemical vapor deposition (HFCVD) process. The cathode used for our application is a 15 x 15 mm^2 surface covered by vertical CNTs of 200 µm height. The Si substrate is placed on an aluminium support which is 1mm thick and allows polarisation of the CNT array. Around the CNT array is then placed a set of spacers made of stainless steel and with a thickness slightly higher than the CNT's height. These spacers compensate for the gap between the substrate and the top of the CNT, therefore preventing the CNTs from being crushed. Over the spacers another stainless-steel foil is placed which is 50µm thick with a 10mm hole at its centre. The latter masks the outer part of the CNT array and prevents from edge effects. The distance between the stainless-steel foil and the grid G1 is insured thanks to a Kapton insulator of 230µm, which creates a total distance between the CNT array and G1 of ~300µm. G1 is a 0.5 mm thick titanium plate with a 12 mm bevelled hole at its center. The bevel reduces the lateral surface seen by the electrons and therefore reduces the probability of electrons bouncing off the wall. One side of the Ti plate is covered by a 15 µm Cu + 2 µm Au layers allowing to braze a grid on the Ti plate. We choose to use titanium for G1's support due to its low thermal expansion coefficient. Hence, during the brazing process, the Ti plate does not undergo much deformation compare to grid wires. When the assembly cools down, the grid will thus be uniformly tensioned insuring a good planarity of the grid and resistance to the strong E-field between G1 and the CNT array. A picture of G1 after the brazing process is displayed in Fig. 3.54.

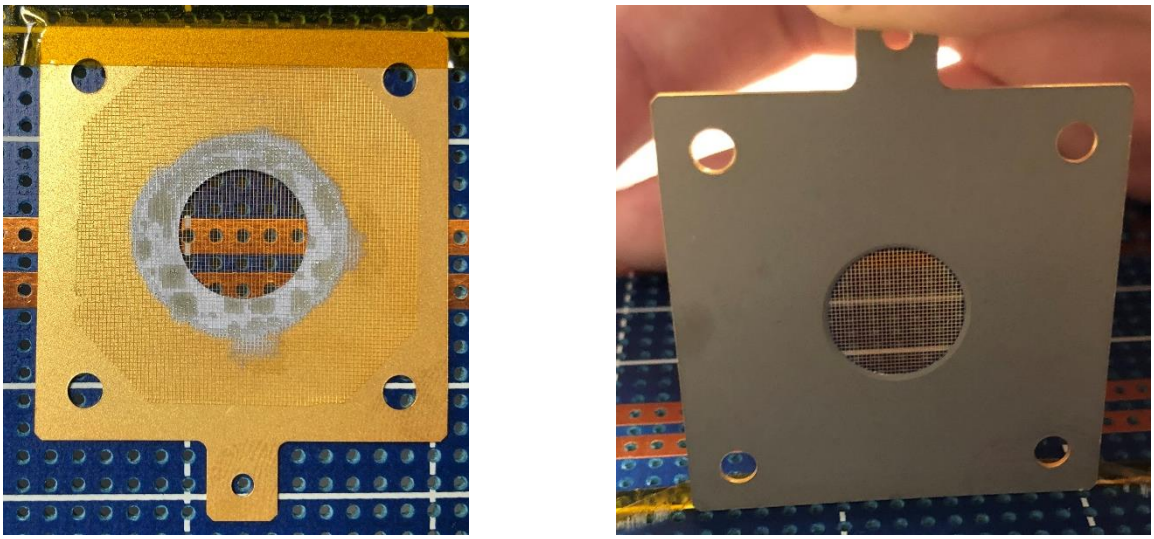

Figure 3.54*: Photograph of G1's titanium support and grid. Left panel is the bottom side of the part where we can see the grid brazed on the support as well as the Au coating. Right panel is the top view where we can see the bevelled hole.*

Finally, the rest of the assembly is made of a 5mm thick Cirlex insulator which separates G1 from a second Grid (Anode). In this case, the grid is electrically soldered between two 100µm stainless steel foils. The electron source assembly is displayed in Fig. 3.55.

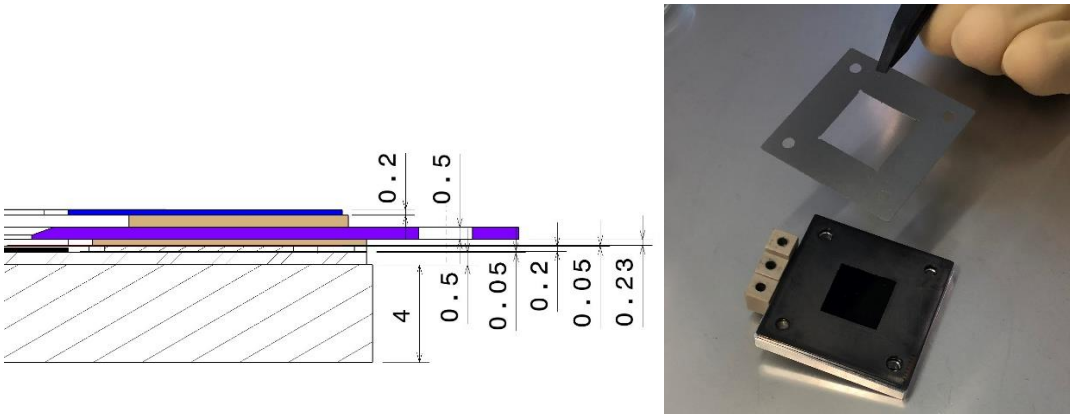

Figure 3.55*: Left panel: Mechanical assembly of the electron source. Right panel: Photograph of the CNT substrate mounted on its support.*

4.4.2. The electron lens

The electron lens EL sits above the electron source and is separated from the Anode grid thanks to a 0.5 mm thick Cirlex insulator. As detailed in Fig. 3.56, each electrode consists of a stack made of 2 types of alternating stainless-steel foils. The first type of foil is 100µm thick and has a 14mm hole in its centre. The second type is 200µm thick and its hole has a diameter of 16mm. Alternating between these two types of foil allows to reduce the lateral area of the electrode and prevents the electron emitted from the CNT array to be reflected by trapping them in this ‘comb shape’. The total thickness for one electrode (which is 6x0.1mm foil and 5x0.2 mm foil) is 1.6mm. Finally, each electrode is separated from the next one by a 1mm insulator.

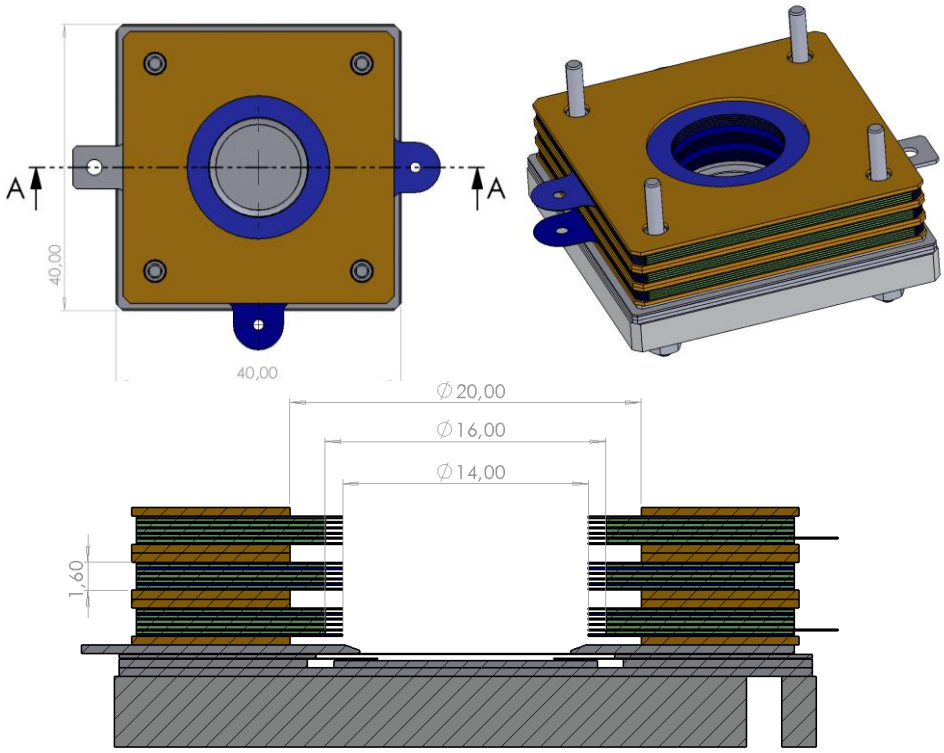

Figure 3.56*: Top left panel is a top view of the electron lens mechanical assembly. Right panel is a 3D view of the assembly and the bottom panel is the longitudinal A-A cut*

4.4.3. Ionization volume

The ionization volume IV is a cuboid with dimensions 21mm along the axis of sight of INEA, 10mm along the electron beam main axis and 14mm for the last axis. The entrance and exit apertures are 5mm x 5mm square while the electron beam apertures located on the top and bottom faces of the ionization volume are 9x9 mm² squares. As we shall see in Fig. 3.57 the top and bottom apertures are not centred on their respective face. We choose to shift those apertures towards the IV entrance in order to minimize the quantity of primary electrons that can reach the rest of the instrument towards the Ion Lens IL (case 3 in Section 4.3.5). Above the IV sits the electron collector separated by a gap of 0.5mm. The ionization volume is screwed to a 2.3mm flange that is itself part of the stack assembly. This flange is also the attachment point for the IL. All the ionization volume's apertures are covered with grids. The bottom one is a spare Anode grid (i.e. a grid electrically soldered between two stainless steel foils) while the three other grids are electrically soldered directly on the IV walls. The IV is separated from the electron lens by a 0.5mm insulator.

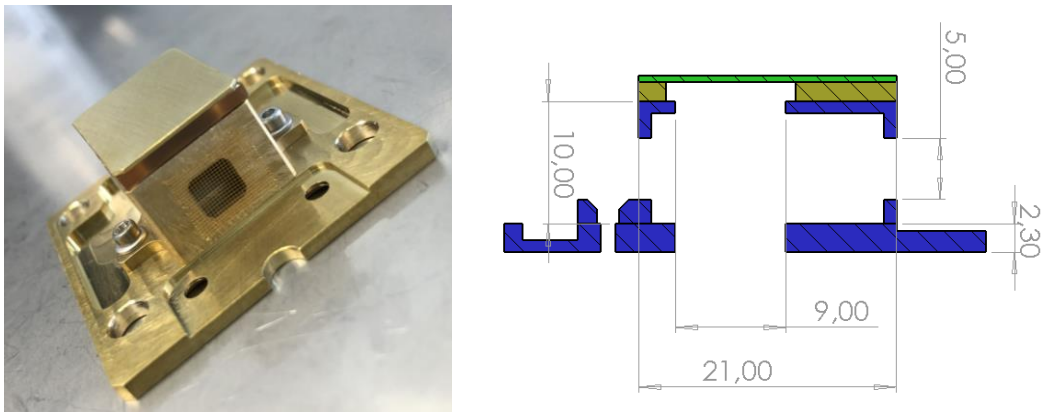

***Figure 3.57**: Left panel is a photograph of the ionisation volume. Right panel is a mechanical drawing of a longitudinal cut.*

4.4.4. The Ion Lens

The Ion Lens is the extraction optics located after the IV. The distance between the IV exit grid and the first IL electrode is 1.3mm. The IL is composed of an insulator casing which hosts 6 electrodes. Similarly, as the EL, each electrode of the IL is formed with a stack of alternating stainless-steel foils. In this case, we want to avoid the extracted ions to bounce off the walls of the electrodes. The stack for a single electrode is composed of five 100µm and four 250µm stainless steel foils. The total length for a single electrode is therefore 1.5mm. The distance between the electrodes is 0.5mm and is insured thanks to vespel insulators. The overall longitudinal shape of the IL is that of a funnel, which focusses the ion beam towards the exit of the IL. In the transverse plane, the electrodes are rectangular. The Ion Lens casing also provides attachment points which allows to mount the entire Ion Source to the Energy Analyser.

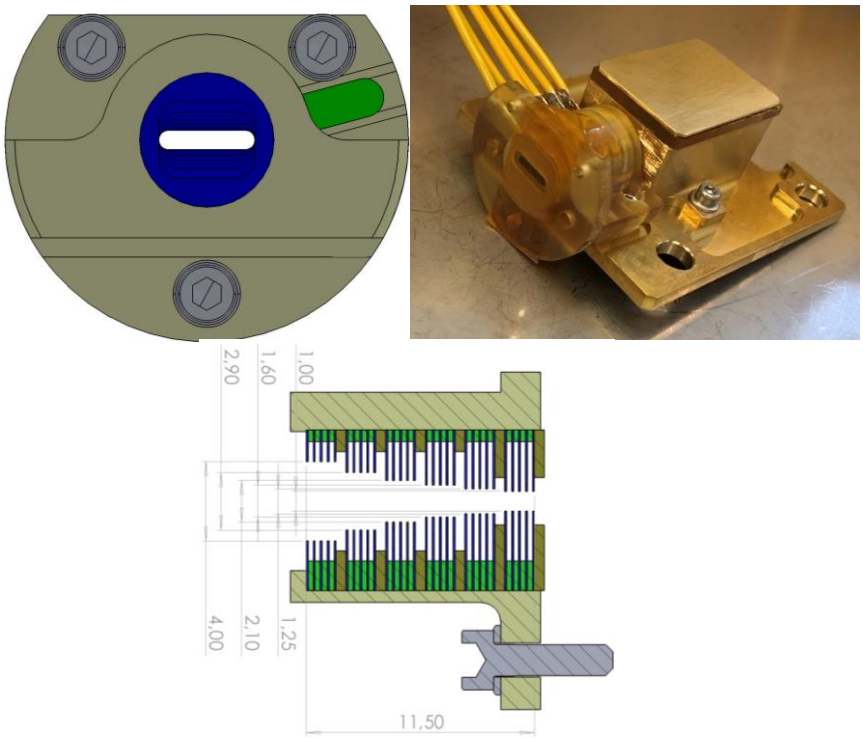

Figure 3.58*:Top left panel: front view of the IL mechanical assembly displaying the IL electrodes geometry. Right panel is a photograph of the ionization volume and the IL while assembled. Bottom panel: cross section of the IL.*

4.5. Associated electronics

4.5.1. Control of electrodes potential

The negative voltages used for the polarisation of the CNT, EL2 and the Ion collector (which is only used to characterize the Ion current at the exit of the ion lens, see Section 4.6) are achieved thanks to 2 elements: programmable high voltages DC-DC converters (CA05-N, XP Power), and a 16 Bits 4 channels Digital-to Analog converter (NI-9263, National Instruments). The CA05-N is a programmable DC-DC converter able to generate a voltage up to -500V. The output voltage can be tuned thanks to an external command that is between 0 and 2.048V. Thus, the DC-DC converter is controlled using the NI-9263 which in turn communicates with a control PC. The transfer function of the converter is defined as:

$$V_{out} = \frac{-500}{2.048} V_{prgm} \qquad 3.4.7$$

Where V_{prgm} is the command voltage coming from the DAC. As the NI-9263 can generate 4 independent voltages, we can control simultaneously the 3 required medium voltages for the CNT, EL2 and the collector. The transmission chain for the 3 negative voltages is shown schematically in Figure 3.59.

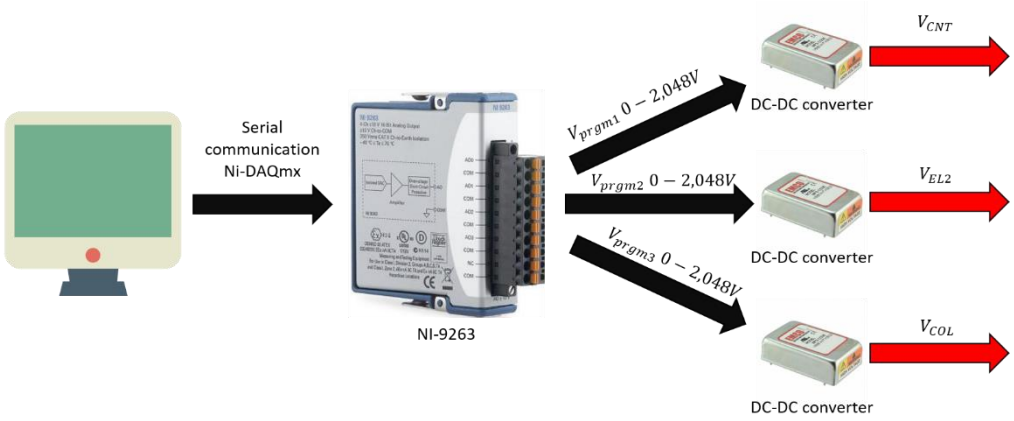

***Figure 3.59**: Communication chain for the control of the ion source medium voltages*

On the other hand, the generation of positive voltages was achieved thanks to the AD5535B from Analog Devices. The AD5535B is a dense 32-channel, 14-bit DAC with a high-voltage output amplifier. The output voltage range is selectable either in the range 0 V to 50 V or 0 V to 200 V. Each amplifier is independent and can deliver up to 550 µA. The AD5535B communicates with an Arduino Mega via an SPI interface. The Arduino itself communicates with the control PC via a serial communication. We chose to use the evaluation board of the AD5535B as it provides a good circuitry for the operation of the DAC. The complete transmission chain is displayed in Fig. 3.60.

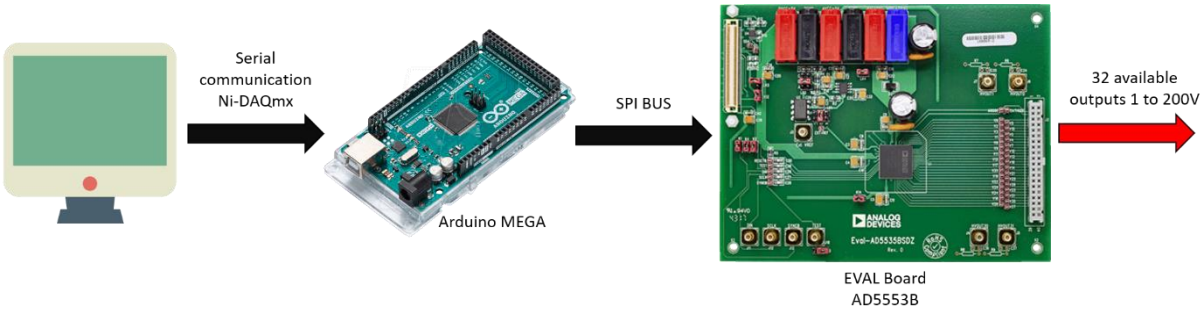

***Figure 3.60**: Communication chain for the control of the ion source low voltages*

We also used a Keithley picoammeter 6487 as a voltage generator thanks to its internal high precision power supply that can be remotely controlled via SCPI commands.

4.5.2. Measurement devices

Originally, only three instruments were available to measure the currents from various electrodes of the ion source. For measuring currents ≥ 0.5µA: two digital multimeters (ref: GWINSTEK GDM-8342) with a resolution of 2% over the 500µA range, which corresponds to their most sensitive range and for measuring low currents < 0.5µA: a pico-ammeter (ref: Keithley Picoammeter/Voltage source model 6487) capable of measuring currents between 20 fA and 20 mA. These 3 instruments were not sufficient to measure simultaneously the currents on all the electrodes of the assembly. Thus, we decided to work with the company ALCIOM to design a device for measuring the current in the various elements of the assembly. In the context of our experiments, the main constraints are as follows:

- High common mode voltage (+/-350V DC)
- Current measurements over ranges of +-120µA and +-10µA
- Acquisition of currents every second
- Data needs to be registered in a control PC

The solution adopted by ALCIOM is made of three sub-assembly:

1- current measurement cards comprising:
- A transimpedance stage to convert the current to be measured into voltage. Each channel is fitted with a low-pass filter via a feedback capacitor that stabilise the measurement as much as possible, and a precision resistor (0.1%). (Ref OpAmp: LTC2064HMS8#PBF, Analog Devices)
- An analog-to-digital converter that allows to convert the analog voltage output of the transimpedance stage into a digital signal.
- A dedicated component that allows to transmit the numerical information over the isolation barrier between common mode voltage and the ground (MAX14850AEE+T, Analog Devices)
- Required auxiliary components (quartz, 5V to 3V3 power supply, Vcc/2 reference, SPI + power supply and filter connector, electrode pads, etc.)

The electronic circuit of the measurement cards is shown in Fig .3.61. The different stages are highlighted in red boxes.

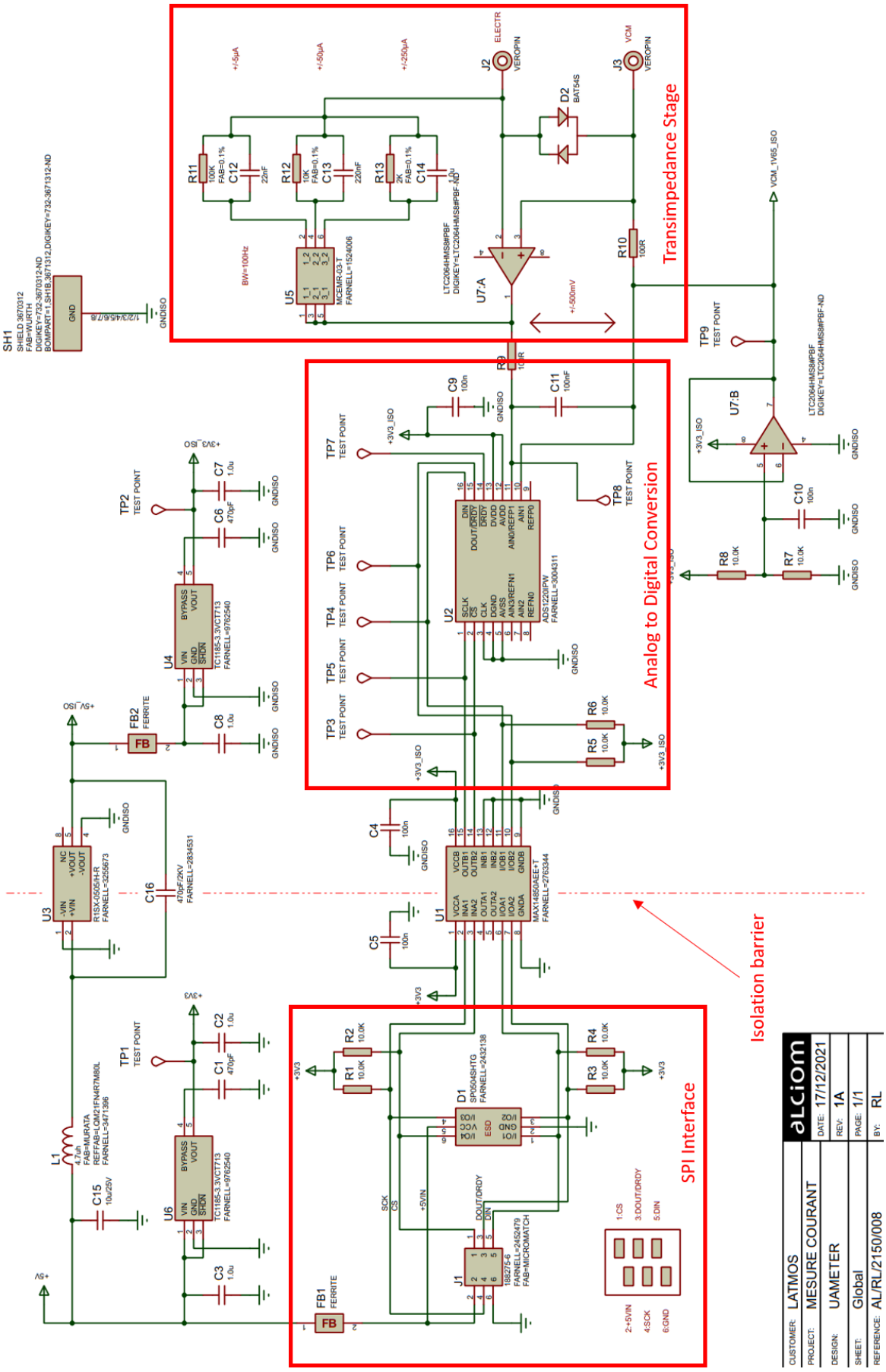

***Figure 3.61**: electronic circuit of the ion source measurement cards.*

2- A hub card with space for 4 dual-channel measurement cards (3 channel with 100µA gauges and 5 with 5 µA gauges). The latter also accommodate a SUB-D25 connector that allows connection with the vacuum chamber flange. The wiring of the hub card is illustrated in Figure 3.62, together with a photograph showing the assembly of the measurement cards on the hub board.

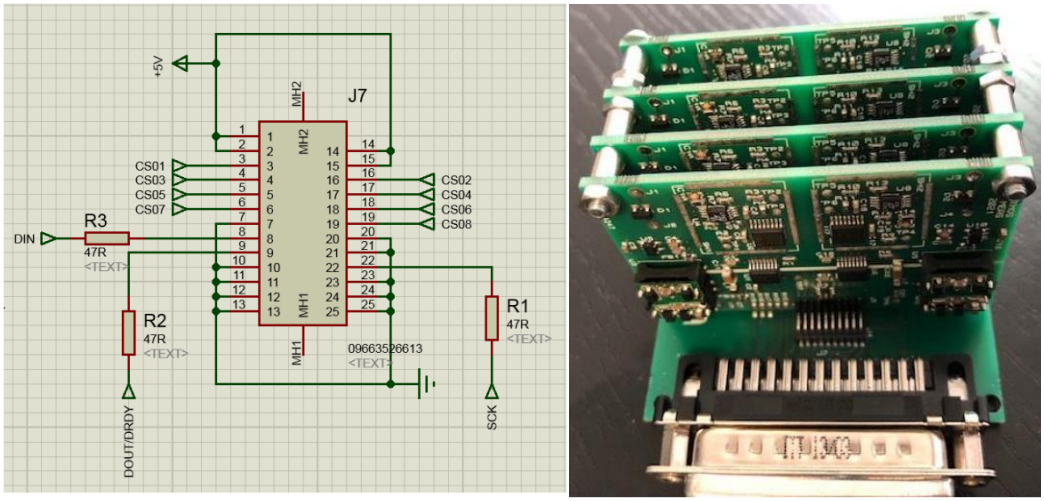

***Figure 3.62**: Left panel: Connection of the hub card. Right panel: photograph of the measurement cards assembled together with the hub card.*

3- A standard evaluation board STM32f0-discovery, associated with specific software developed by ALCIOM ensuring the periodic reading of the values and its transmission on an USB interface in text and CDC profile format (raw ADC value). The wiring of the STM32 card is displayed in Fig. 3.63.

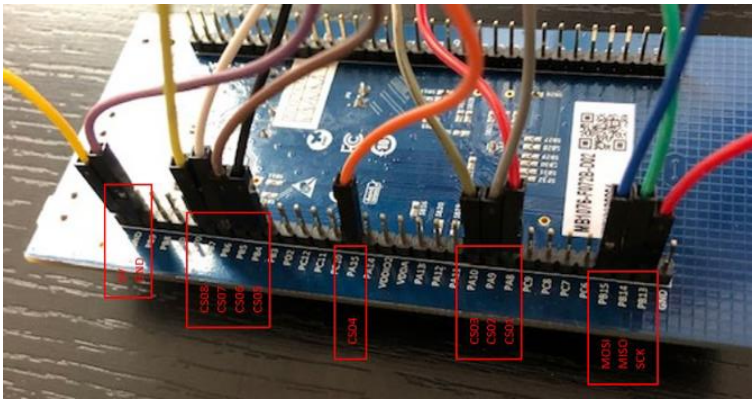

***Figure 3.63**: Connection between the hub card and the STM32*

The measurement sequence consists of taking a burst of 10 successive measurements and calculate the corresponding average value, which takes about 40ms. This sequence is reproduced successively over the 8 channels. The obtained values are finally sent to the computer over the USB bus every second in form of ADC values. Fig.3.64 shows an example of data received by the computer.

```
Passerelle USB/SPI V2.0
test numero 0000001;-4122355;-3845080;0000001;0000049;0000017;0000050;0000073;0000035
test numero 0000002;-4066969;-3853367;0000009;0000026;0000021;0000025;0000035;0000051
test numero 0000003;-4064616;-3863982;0000008;0000034;0000041;0000024;0000044;0000072
test numero 0000004;-4135734;-3848817;0000000;0000059;-000003;0000062;0000058;0000029
test numero 0000005;-4080118;-3840799;0000044;0000022;0000034;0000054;0000004;0000040
test numero 0000006;-4082228;-3885143;0000075;0000096;-000004;0000053;0000071;0000049
test numero 0000007;-4104149;-3888048;0000058;0000040;0000035;0000033;0000047;0000004
test numero 0000008;-4114416;-3900144;0000006;0000053;0000011;0000062;0000047;0000038
test numero 0000009;-4096892;-3880422;0000037;0000041;0000033;0000068;0000020;0000031
test numero 0000010;-4107567;-3853253;0000040;0000023;0000004;0000085;0000111;0000069
test numero 0000011;-4063028;-3851233;0000012;0000058;0000025;0000039;0000068;0000032
```

***Figure 3.64**: example of values returned by the measurement device.*

As the data received by the computer are in the form of ADC values, a calibration of each measurement channel had to be performed. Calibration were performed outside the vacuum chamber and with the following setup: A 1 $M\Omega$ resistor is connected in series with the power supply of the Keithley Picoammeter which allows to generate a positive or negative voltage in the desired range ($\pm$ 10µA *or* $\pm$ 100 µA). We also connect the measurement input of the Keithley picoammeter in series with the resistor which allows to measure with high precision the current injected in the measurement channel. A schematic of the calibration setup is shown in Fig. 3.65 below.

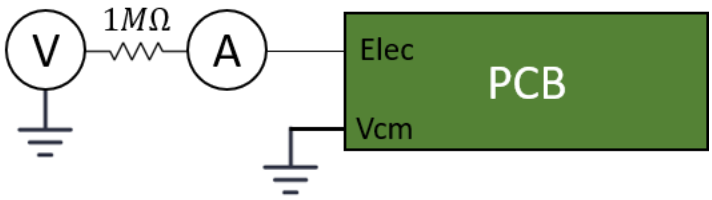

***Figure 3.65**: Electrical scheme of the setup used to calibrate the measurement cards*

The calibration sequence consists, as illustrated in Fig 3.66, in a sweep of current over the entire channel range. A measurement of the ADC value and the current across the resistor is achieved every second. Then, every 30 seconds the voltage across the resistor is incremented by 2V (20V for 100µA gauge) which correspond to an increment of ~2µA (~20µA for 100µA gauge). For every step, the mean value and standard deviation is calculated and thus gives a calibration curve as the one shown in Fig 3.66, right panel. The calibration curve is obtained with a mean square fit giving the transfer function between the ADC values and the measured current.

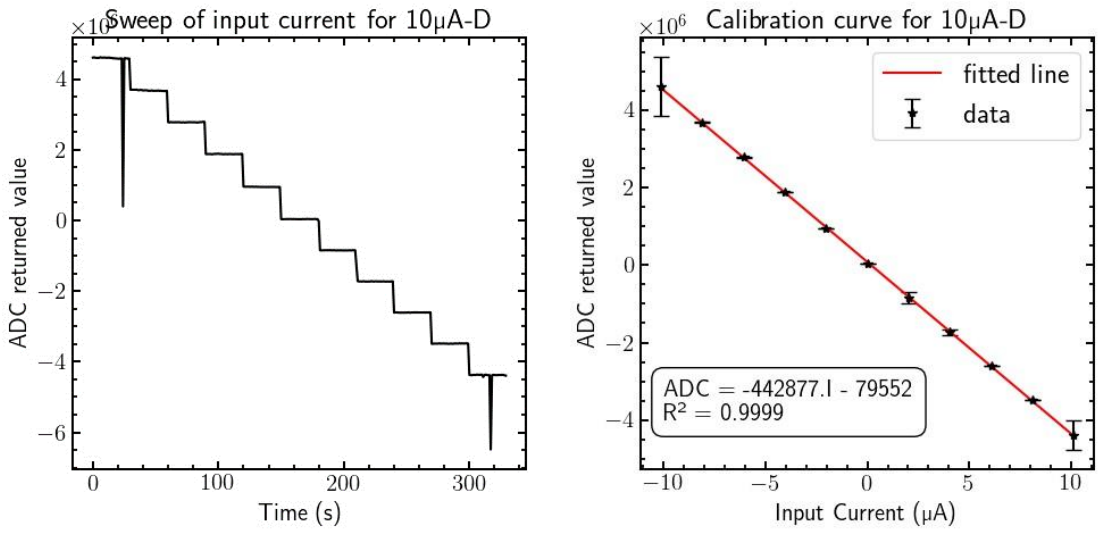

***Figure 3.66**: Left panel: example of a measurement sequence achieved to calibrate the measurement cards. Right panel is the resulting calibration curve.*

4.6. Characteristics of the Ion source

Experiments carried to characterize of the ion source lead to the submission of an article. The latter describes the final ion source assembly as well as the experimental set-up we used. The article describes experimental results regarding INEA's ion source. The article was submitted to the journal Review of Scientific Instruments in October 2023 and published in February 2024.

Review of Scientific Instruments ARTICLE pubs.aip.org/aip/rsi

A carbon nanotube based ion source for planetary space mass spectrometry

Cite as: Rev. Sci. Instrum. 95, 023303 (2024); doi: 10.1063/5.0179530
Submitted: 3 October 2023 • Accepted: 30 January 2024 •
Published Online: 23 February 2024

Valentin Steichen,[1,a)] François Leblanc,[1] Jean-Jacques Berthelier,[1] Nguyen Tuan Hong,[2] Soonil Lee,[3] and Pierre Gilbert[1]

AFFILIATIONS

[1] LATMOS/CNRS, Sorbonne Université, Paris, France
[2] Centre for High Technology Development, Vietnam Academy of Science and Technology (VAST), 18 Hoang Quoc Viet, Hanoi 100000, Vietnam
[3] Department of Physics, Ajou University, Suwon 16499, South Korea

[a)] Author to whom correspondence should be addressed: valentin.steichen@latmos.ipsl.fr

ABSTRACT

Ion sources are used in mass and energy spectrometry to ionize the neutral particles entering the instrument. The most classical technique used in planetary exploration is hot filaments emitting electrons with few tens of eV and impacting the neutral particles. The main limitations of such emitters are power consumption and outgassing due to heating of their local environment. Here, we built, tested, and demonstrated the advantages of using carbon nanotubes to replace hot filaments. Such emitters are based on a cold approach, use a limited amount of power, and achieve essentially the same efficiency as the hot filament-based source of ionization.

I. INTRODUCTION

Characterizing the composition, density, temperature, and dynamics of neutral atmospheres around planets and their moons in the Solar System is a key step to decipher their origin and evolution, and *in situ* measurements using mass spectrometers and energy analyzers are among the most efficient techniques to perform such investigations. When targeting rarefied neutral environments, one of the basic instrument parameters is the sensitivity, which depends on the global efficiency of the ion optics and detector but is mainly controlled by the performances of the ion source.[1,2] Spacecraft and instrument outgassing often appear as limiting factors of the measurement capability, in particular, to detect minor species or neutral constituents that may significantly interact and/or be absorbed on spacecraft structures. Such detrimental effects have been observed by Mahaffy *et al.*[3] on-board the Mars Atmosphere and Volatile Evolution Mission (MAVEN) Martian probe as a strong background on the outbound part of the orbit due to the atmospheric gases trapped on the instrument walls at periapsis. Schläppi *et al.*[4] also put in evidence the existence of a persistent local atmosphere around the Rosetta spacecraft even after a few years of cruise.

Instruments to perform *in situ* measurements must, therefore, be designed to reduce as much as possible outgassing from the instrument walls and allow filtering of the background gas from the rammed neutral constituents. These constraints must be thoroughly taken into consideration when developing new ion sources.

In the most recent neutral mass spectrometers developed for space exploration, ion sources use hot filaments to generate the ionizing electrons due to the well proven reliability and performances of this technics, which offers, in particular, a high sensitivity. In the ROSINA instrument flown on-board Rosetta,[1] the Double Focusing Mass Spectrometer (DFMS) and Reflectron Time of Flight (RTOF) mass spectrometer use two different ion sources, each adapted to the operating principle of the corresponding instrument. In DFMS, a 1 kV acceleration is imposed to the continuously created ions to focus them on the entrance of the electrostatic and magnetic ion optics, leading to an overall sensitivity of 10^{-5} A/mbar (or 2×10^{-3} counts/s/cm^3). The RTOF mass spectrometer uses a different approach, where ions are temporarily stored in the source before being injected during short pulses into the electrostatic optics, which provides a significantly larger sensitivity up to 10^{-4} A/mbar (or 2×10^{-2} counts/s/cm^3).

The Neutral Gas and Ion Mass Spectrometer (NGIMS)[2] on Mars Atmosphere and Volatile Evolution Mission (MAVEN)[5] used two different ion sources, a close source and an open source both equipped with hot filaments. The close source allows a partial thermalization of the entering gas through collisions with its walls, which increases the sensitivity, whereas the open source is designed to minimize the interactions between reactive gases, such as O and N, and their collisions with the walls. The sensitivity of NGIMS operating with the close ion source was estimated to $\sim\times10^{-3}$ counts/s/part/cc for argon.

In the STart from a ROtating FIeld mass spectrOmeter (STROFIO) of the SERENA package[6] on-board the low altitude orbiter of the BepiColombo mission to Mercury, the sensitivity of the ion source has been maximized at 0.14 counts/s/cm^3 (or 1 mA/Torr) by extracting from the hot filament electron currents up to 1.5 mA. Yet, the authors highlighted the influence of the space charge associated with this large current, which leads to a non-linearity between the ion current of the local atmosphere pressure and the ionizing electron current and strongly modifies the ram energy of the newly created ions.

The main problems encountered when using hot filaments are their relatively high-power consumption, the associated heating of the inner walls of the ion source, the resulting outgassing, and the disturbances induced on the ion energy due to the space charge within the emitted electron current. In recent years, other technics to generate the ionizing electrons have thus been investigated, among which Carbon NanoTube (CNT) electron emitters appear to be the most promising since they require a modest power, eliminate any heating and outgassing in the ion source, and offer large enough dimensions of the electron emitting area that may be of interest in several applications. Radauscher *et al.*[7] used vertically aligned multi-walled nanotubes 30 μm high placed in front of a tungsten woven wire grid at 200 μm from the top of the CNT. Electron currents up to 500 μA were obtained applying an extraction potential of 450 V, and successful tests were conducted during 320 h of continuous operation at a steady state pressure of 10^{-4} mbar. Sheridan *et al.*[8] developed an ion source using a CNT and extracted electron currents of 30 ± 1.7 μA for 300 V applied between the CNT and the extraction grid, observing over a 48 h operation a moderate decrease in the emission intensity of few tens of percent, easily corrected by an increase in the extracting potential by several volts. Knapp and Schleußner[9] used a large array carbon buckypaper of 70 μm thick with the extracting grid distant by a few tens of μm to extract up to 1 mA at a potential of 280 V. More recently, Zhang *et al.*[10] developed an ion source using a CNT over an emitting area of 11 × 11 mm^2 and obtained an electron current of up to 100 μA for a 1750 V extracting voltage. The electron current remained stable for various pressures and gas compositions, and the sensitivity of the source for several gas species between 0.088 Pa^{-1} for He and 2.3 Pa^{-1} for CO_2 was measured.

Becker *et al.*[11] used a vertically aligned CNT to extract electron currents up to 420 μA for 350 V on the extracting grid at 120 μm from the CNT upper surface. The authors mentioned that this efficient extraction capability is somehow deteriorated by the low transparency of the device.

In this paper, we present initial results obtained with a novel ionization source using CNTs. This device is described in Sec. II, the main results of the laboratory tests are presented in Sec. III, and the conclusion and improvements foreseen for the next tests are summarized in Sec. IV.

II. THE ION SOURCE

A. Objectives

The ionization source presented in this paper is part of the INEA (Ion and Neutral Energy Analyzer)[12] devoted to the study of the neutral and ionized atmosphere of Mars as well as of other planetary objects. INEA is an energy analyzer with a mass resolving capability, which, in the neutral mode of operation, aims at a high-resolution measurement of the energy distribution of neutral constituents in the range from 0 to ~10 eV. The high energy resolution of INEA, better than 0.1 eV, is required to distinguish the thermal and supra-thermal components of the Martian neutral constituents and understand the physical processes, which are responsible for the evolution of the planet atmosphere. This measurement objective is difficult to target with usual technics, such as the retarding potential analyzer,[13,14] and INEA uses a differential energy analysis of the ionized neutrals and an imaging detector to get the energy distribution of the rammed neutral constituents. A key requirement for the overall instrument design is to suppress any disturbance of the electric potential along the ion trajectories that could modify the original energy distribution of the neutrals when they enter the instrument, thus to have no space charge in the ionization source in particular. As mentioned in the Introduction, this is rather impossible to achieve when using hot filaments to generate the ionizing electrons and maintaining a high enough efficiency of the ion source. This led us to study an ion source based on a large enough electron emitting CNT array.

B. Design of the ion source

A schematic drawing of the ionization source is shown in Fig. 1, which shows the following three main parts of the source:

1. The ionization volume is a rectangular box of 19 mm long along the entrance axis, 9 mm along the electron beam main axis, and 13 mm along the last axis. The ionization volume has been maximized to match the large emission surface allowed by the CNT cathode and also avoid space charge that may affect the ion population.
2. The electron source includes the large area CNT cathode with an active area of ~0.8 cm^2; the extracting grid, G1, 30 μm thick with a 300 × 300 μm^2 mesh size and 30 μm gold plated Ni wires; the anode grid mounted at a distance of 500 μm from G1; and an electrostatic lens with three electrodes to focus the extracted electrons into the ionization volume and maximize their flux. The anode grid is grounded to electrostatically shield the electron lens from the potential applied to the extracting grid. Similarly, a grounded grid at the interface with the ionization volume allows maintaining the ionization volume at ground potential, free from interferences with the potentials applied to the electrostatic lens.
3. The ion lens with six electrodes at the exit of the ionization volume focuses the newly created ions toward the entrance of the INEA. Again, a grounded grid between the ionization

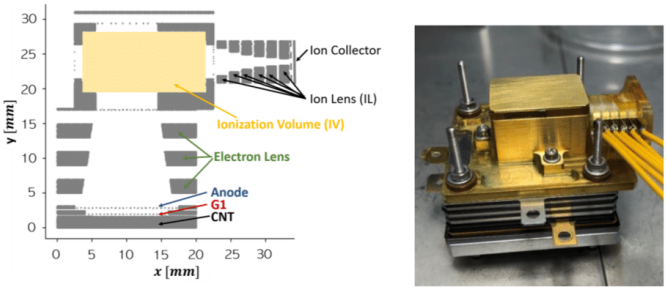

FIG. 1. Ionization source design and picture of the prototype of the source. In the left panel, the neutral particles are entering from the left, get ionized in the volume ionization, and flow through the ionization volume through the ion lens up to the ion collector. The electrons are emitted from the bottom part of the figure.

volume and the ion lens maintains the ionization volume at ground potential free from the potentials applied to the various electrodes of the ion lens. During the tests of the ionization source, the energy analyzer is replaced by a simple collector to measure the current of the exiting ions.

The CNT cathode has been built by Ajou University. A Fe substrate is first covered by an aluminum layer of 8–15 nm thick on which multi-wall carbon nanotubes (MWCNTs) are synthetized at 600 °C using a hot-filament chemical vapor deposition (HFCVD) process. The cathode used for our application is a 15 × 15 mm^2 surface uniformly filled with vertical CNTs with a few tens of nm diameter and an average height of 210 μm. The extracting grid G1, located ~300 μm above the CNTs' upper surface, is polarized at a positive V_{G1} voltage, while the CNT's are polarized at a negative voltage V_{CNT}.

For an extracting voltage $V_{CNT} - V_{G1}$ between −180 and −300 V, the electron current emitted from the active 0.8 cm^2 area varies from 10 to 50 μA (as measured from the substrate). The electron current follows the Fowler–Nordheim law,

$$I = A\frac{1.42 * 10^{-6}}{\varphi}(\beta V)^2 \exp\left(\frac{10.4}{\sqrt{\varphi}}\right)\exp\left(-\frac{B_{FN}\varphi^{1.5}}{\beta V}\right), \quad (1)$$

which provides the relation between the induced current by quantum tunneling and the applied potential gradient at the surface of the CNTs. A (m^2) is the effective emitter area, V (V) = $V_{CNT} - V_{G1}$ is the extracting potential, β (m^{-1}) is the field factor, φ (eV) is the CNT material work function, and the constant B is 6.44 × 10^9 V m^{-1} $eV^{-1.5}$. The product βV is the strength of the local electric field at the emission sites. Our tests were conducted under a vacuum of 10^{-5} mbar, and the electron current, which follows the IV relationship in Eq. (1), was typically ~50 μA cm^{-2} for a potential of −300 V applied to the cathode.

To carry out the tests presented below, a control and measurement system was developed. On the one hand, the device allows the voltages of the different electrodes of the ion source to be controlled independently. On the other hand, it allows the simultaneous acquisition of the current measured on each element of the ion source with an acquisition frequency of 1 Hz.

III. CHARACTERIZATION OF THE IONIZATION SOURCE

In the following, currents are counted positive when they correspond to collected electrons and negative when they correspond to collected ions or electrons emitted from the electrode.

A. Effect of the CNT potential on the electron flux entering the ionization volume

Figure 2 shows the plot of the sum of the electron currents measured on different electrodes of the ionization volume, i.e., the flux of ionizing electrons, as a function of the energy $E_e = V_{CNT}$ of these electrons. Also plotted are the currents measured on the anode grid and on the three electrodes of the electron lens. All these currents are expressed as their ratio with respect to the electron current emitted by the CNTs. In all cases, the extracting potential between the grid G1 and the CNTs, $V_{ext} = V_{G1} - V_{CNT}$, is constant and equal to 300 V.

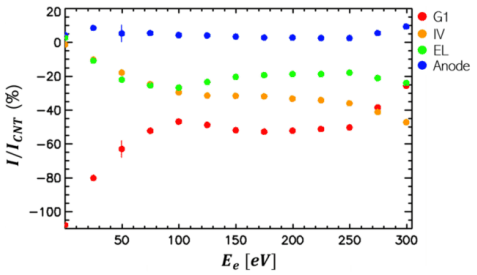

FIG. 2. Currents collected on several elements of the ionization source, expressed by their ratio with respect to the current emitted by the CNTs, as a function of the energy of the primary electrons reaching the ionization volume. $V_{CNT} - V_{G1} = -300$ V. $V_{CNT} = -E_e$ (V). $V_{IV} = V_{Anode} = V_{EL1} = V_{EL2} = V_{EL3} = 0$ V. Red circles: Current measured on the G1 grid. Orange circles: Current measured in the ionization volume. Green circles: Current measured on the electron lenses. Blue circles: Current measured on the anode grid. Each point represents the average current measured during 10 nm, and the error bars represent its one sigma variability.

Several different regimes may be noticed in Fig. 2 depending on the polarization potential of the CNTs, V_{CNT}, thus on the initial energy $E_e = e \cdot V_{CNT}$ also equal to their ionizing energy in the ionizing volume.

- $V_{CNT} = 0$ and thus $E_e = 0$ eV: Most of the electrons are absorbed by the grid G1. The percentage is slightly larger than 100% because secondary electrons produced by the primary electrons on the electron lens and anode get also attracted by the grid G1.
- $-100\ \text{V} < V_{CNT} < 0\ \text{V}$, $0 < E_e < 100$ eV. $+200 < V_{G1} < +300$ V: With larger potentials applied to the CNT and smaller potentials applied to the grid G1, the ratio of the attracting electric field toward grid G1 to the electron energy decreases and less electrons are collected by G1, I_{G1} decreasing, therefore, regularly. Electrons escaping G1 travel further and may be collected by the anode grid, the electron lens electrodes, or even the ionization volume electrodes: I_{IV} and I_{EL} display a regular increase. I_{Anode} is always positive, meaning that this grid emits secondary electrons. I_{Anode}/I_{CNT} shows a moderate increase until $E_e \sim 30$ eV and then decreases slightly to stay nearly constant at ~0.04.
- $-250\ \text{V} < V_{CNT} < -100$ V, 100 eV $< E_e <$ 250 eV. +50 V $< V_{G1} <$ +200 V: For more negative polarization potentials applied to the CNTs, I_{G1}/I_{CNT} increases slightly to stay at a nearly constant value of −0.5 until $E_e = 250$ eV ($V_{CNT} = -250$ V). I_{EL}/I_{CNT} and I_{Anode}/I_{CNT} show nearly symmetrical slight variations with respective plateaus at ~−0.2 and 0.04, while I_{IV}/I_{CNT} increases moderately and regularly from ~−0.3 to ~−0.35.
- $-300\ \text{V} < V_{CNT} < -250$ V, $250 < E_e < 300$ eV. $0 < V_{G1} <$ +50 V: A noticeable variation occurs for more negative CNT potentials with a clear decrease of I_{G1}/I_{CNT} from ~−0.5 to ~−0.25 when V_{CNT} decreases from −250 to −300 V, while all other currents increase linearly of ~−0.1 with respect to I_{CNT}. Such a behavior might be due to the decrease in the efficiency of the G1 grid to keep the secondary electrons emitted from the grid (its potential decreasing from 50 to 0 V). A multiscale simulation will be performed to further investigate this explanation. When the potential applied to the extracting G1 grid is equal to 0 V, I_{G1} reaches the level due to the G1 mechanical transparency.

In the following, the potential of the CNTs was set at $V_{CNT} = -100$ V so that the energy of the ionizing electrons is $E_e = 100$ eV close to the maximum of the ionizing cross section for gases present in our vacuum chamber (H_2O, CO_2, and N_2) during the tests of the ionization source.

B. Role of the electron lens

In a second set of tests, we have tried to increase the flux of electrons in the ionization volume by optimizing the electrode potential in the electron lens. This lens is composed of three circular electrodes, and in these tests, we considered an often-used symmetrical configuration for converging lenses with the first and third electrodes grounded and the potential V_{EL2} of the middle electrode as the only free parameter for optimization. As mentioned above, the CNT potential was set at −100 V corresponding to an electron energy of 100 eV. Figure 3 shows a factor 2 increase in the flux of ionizing electrons in the ionization volume for V_{EL2} between 100 and 200 V compared to $V_{EL2} = 0$, whereas the total current collected by the electron lens decreases, indicating that less electrons are lost by impacting the electrodes. As expected, electrons get focalized for a potential applied to the central electrode close to the electron energy of 100 eV. In the following, the $V_{EL2} = 0$ potential of the central electrode was set at −100 V.

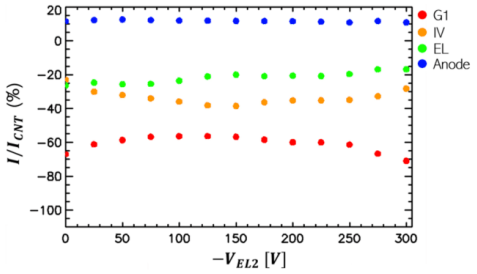

FIG. 3. Measured currents on the same elements of the source as in Fig. 2 (in percentage of the current emitted by the CNT) as a function of the potential of the central electrode V_{EL2} of the electron lens. $V_{CNT} - V_{G1} = -300$ V. $V_{CNT} = -100$ V. $V_{VI} = V_{Anode} = V_{EL1} = V_{EL3} = 0$V. The same legend as for Fig. 2.

C. Efficiency of the ionization source

1. Theoretical model

When reaching the ionization volume, an electron with 100 eV has a probability to ionize the residual gas in the vacuum chamber. The following parameters were used for our experiment:

- $P = 1.1 \times 10^{-5}$ mbar, pressure in the vacuum chamber.
- $T = 293.15$ K, temperature in the vacuum chamber.
- $V = 2.3\ cm^3$, ionization volume.
- $\sigma = 2.0 \times 10^{-16}\ cm^2$, ionization cross section for the electron at 100 eV for the typical molecules inside the vacuum chamber (water molecules, N_2, or CO_2).
- $I = 10\ \mu A\ cm^{-2}$, emitted current from the CNT.
- $S = 0.8\ cm^2$, surface of the CNT (circular area of 10 mm diameter).

The number of neutral molecules in the ionization volume is equal to $N = P/(k_B T) = 2.7 \times 10^{11}$ molecules cm^{-3} with k_B being the Boltzmann constant; this corresponds to an ionization rate of $\tau = N \times \sigma \times V \times I = 7.8 \times 10^9$ ions s^{-1} and, therefore, a total current of ions equal to 1.24 nA. SIMION modeling of the percentage of ions formed in the volume of ionization at a temperature of 20 °C able to reach the collector (Fig. 1) suggested that 0.034% of these ions would impact the collector, that is, a current of 1.0 pA.

2. Measurements of the ion current

To measure the efficiency of the ionization source in the INEA mass spectrometer, the ion current was measured on a collecting plate mounted after the grounded grid at the exit of the ion lens using a Keithley picoammeter 6487 with a background noise level less than

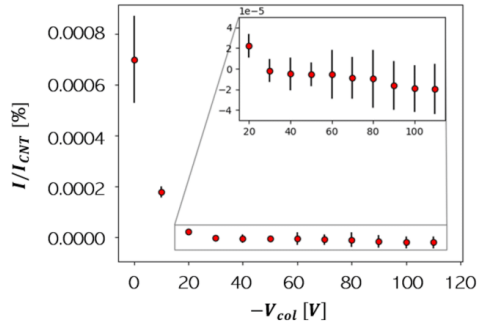

FIG. 4. Current measured on the collector with respect to the potential applied to the collector. The inset is a zoom of the plateau on these measurements as soon as the potential applied on the collector is larger than −20 V. $V_{G1} - V_{CNT} = 300$ V. $V_{CNT} = -100$ V. $V_{IV} = V_{Anode} = V_{EL1} = V_{EL3} = 0$ V. $V_{EL2} = -100$ V.

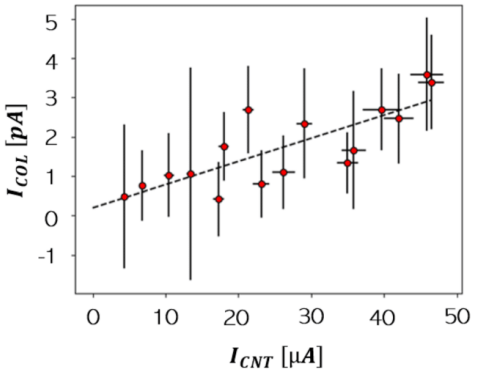

FIG. 5. Measured current on the collector with respect to the CNT current. $V_{CNT} = -100$ V. $V_{IV} = V_{Anode} = V_{EL1} = V_{EL3} = 0$ V. $V_{EL2} = -100$ V. $V_{COL} = -100$ V. $P = 1.1 \times 10^{-5}$ mbar. The dashed line is a best fit of the measurements with a $\chi^2 = 0.64$ and $I_{CNT} = 4.5 \times 10^{-15} + I_{COL} \times 5.9 \times 10^{-8}$.

~0.2 pA. Initial tests showed that a background electron current is still present at the exit of the ion lens due to primary and/or secondary electrons scattered from the end part of the electron lens and from the walls of the ionization volume. The electron current intensity of a few pA, about ~8×10^{-4}, the electron current emitted by the CNTs, is high enough to prevent reliable measurements of the weaker ion currents. This difficulty was solved by applying a negative potential V_{COL} on the collecting plate to repel any scattered primary electron as well as secondary electrons of lower energy. As shown in Fig. 4, the measured electron current decreases rapidly when V_{COL} gets more negative and reverses sign for $V_{COL} <$ ~−50 V, with a clear plateau for $V_{COL} < -80$ V, showing that ions are, indeed, collected and the background electron current is eliminated.

Keeping the CNT potential V_{CNT} and V_{COL} at −100 V, a last set of measurements was performed by varying the potential of the extracting grid V_{G1} to increase the electron current emitted by the CNTs from 4 μA to more than 50 μA. As displayed in Fig. 5, there is a clear linear relation between the electron current emitted by the CNTs and the ion current measured on the collector.

For a CNT electron current of 10 μA, the ion current is ~0.84 pA in excellent agreement with our simple theoretical calculation (Sec. III C 1). For an electron current of 50 μA, the collected ion current increases to 3.0 pA, very close to the value deduced from the linear relation shown in Fig. 5. This indicates that no space charge effect occurs up to at least an electron current of 50 μA emitted by the CNTs.

It is interesting to compare this set of results with those published from previously built ion sources. As mentioned in the Introduction, to keep undisturbed the energy distribution of the ionized neutrals, no extraction potential is applied to the ion source so that the ion flux at the exit of the ion lens is essentially controlled by the neutral ram velocity. In our laboratory tests, there was no ram velocity and the ion flux is considerably reduced since it is only due to the thermal velocity distribution of the stationary neutrals in the vacuum chamber. SIMION simulations show that only 0.034% of the ions created inside the ionization volume would reach the collector, corresponding to part of the energy distribution whose particle velocity vectors allow them to reach the collector, with a corresponding efficiency of 7.6×10^{-4} A/mbar for the source.

If we consider a ram velocity of 5 km/s typical of satellites around Mars, SIMION simulations[12] show that 0.24% of the ions created in the ionization volume reach the collector, practically ten times more than in the case of our laboratory tests. In this case, a much important part of the particle velocity vectors is directed toward the ion lens exit due to the ram velocity that is aligned with the instrument axis of sight. The 3 pA ion current measured in the vacuum chamber at a pressure of 1.1×10^{-5} mbar corresponds to an efficiency of 1.6×10^{-4} counts/s/particle/cm^3. On spacecraft with an orbiting velocity of 5 km/s, the efficiency would thus be 1.1×10^{-3} counts/s/particle/cm^3, a value close to the NGIMS absolute sensitivity.[2] The sensitivity of our source is much less than the 0.14 counts/s/particle/cm^3 of the STROFIO mass spectrometer on Bepi-Colombo,[6] which has been specifically designed to observe the very low-density atmosphere around Mercury. However, such a very high sensitivity is obtained using a very intense ionizing electron current, of the order of 1.5 mA, with the associated drawback of the space charge effect mentioned by the authors.

D. Longevity and stability of CNT emitter

To assess the longevity and stability performances in terms of electronic emission from the CNT cathode, we performed a long-run emission test in 2018 on a similar device but another CNT sample provided by NAWA, a firm based in the south of France. The test run was divided into different sequences in order to perform a wide range of voltage level durations while ensuring the emission to run continuously. Each sequence (see the inset of Fig. 6) represents a voltage cycle with a step by step voltage increase from a minimal value V_{min} (−100 V) to the desired maximum voltage V_{max} (−300 V), where the step size V_{step} (5 V) and step duration T_{step} (5 s) can be tuned. Once V_{max} is reached, the sequence holds this potential for

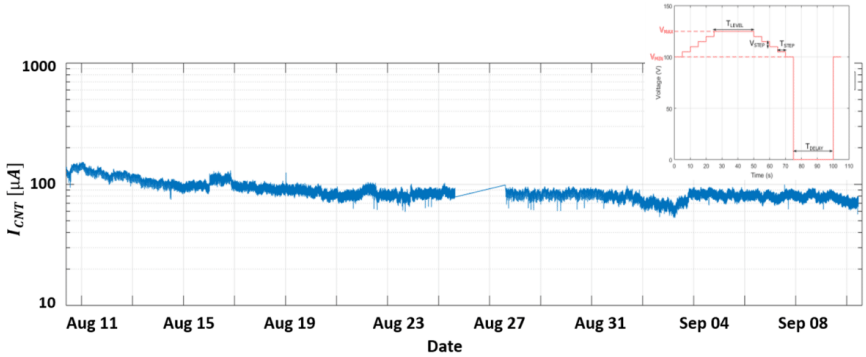

FIG. 6. CNT emitted current evolution over ~700 h of continuous emission. The inset in the top right corner details the different parameters of the cycles achieved during the long-run emission test.

TABLE I. Sequence parameters during long-run emission test.

Duration (Day:h:min:s)	Number of cycles	Duty cycle (%)
07:22:10:10	307	88.7
07:17:27:40	512	79.6
07:03:46:00	852	56.6
06:04:39:10	973	34.3

a duration T_{level} (between 1800 and 120 s) and then steps down to $V_{\min}$ following the T_{step} and V_{step} parameters. The next cycle then starts after a chosen delay T_{delay} (30 s). With such an approach, it has been possible to vary the emission duty cycle, defined as the ratio of T_{level} over the total cycle duration. The total duration of the test lasted 698 h (Table I).

During the test, between August 25 and August 27 (a week end), our measurement devices stopped to register the currents, which explains the lack of data between these dates. Overall, along the entire test set, the maximum emitted current dropped slowly over time from ~130 to ~85 μA, representing a drop of ~20%, a decrease in the emission, which could be corrected by a slight increase in the maximum potential applied as suggested by Eq. (1). Moreover, at $V_{\max}$, the stability of the CNT current is in the order of 10% around a mean value without characteristic frequencies or patterns. We also measured a very stable transparency of the device, showing that I_{CNT}/I_{G1} = 0.23 ± 0.03 during the 698 h of the experiment without showing any long-term evolution.

IV. CONCLUSIONS

In order to characterize the upper atmospheres of planetary objects in the Solar System, we have developed a new type of ion source specifically designed to solve two drawbacks inherent to the usual sources equipped with hot filaments: the background in mass spectra due to the heating and outgassing of the instrument walls, and the detrimental effects of space charge that prevent from measuring the energy distribution of the ambient neutral gases.

The source is based on an electron emitter composed of vertical multi-wall Carbon NanoTubes (CNTs) of 210 μm high and few tens of nm in diameter, followed by an extracting grid of 300 μm from the top of the CNT set at a potential of +150 to +300 V with respect to the CNTs and generating an electric field at the top of the CNTs on the order of 10^6 V/m. An electrostatic lens is used to focus electrons emitted by the CNTs into the large ionization volume of 2.3 cm^3 where neutrals are ionized.

The measured efficiency of this source is comparable to that of sources using hot filaments in mass spectrometers flown on recent space missions, such as ROSINA on Rosetta or NGIMS on MAVEN. Cold emission by CNTs requires much less electrical power than hot filaments and prevents the detrimental instrumental effects due to the outgassing of the heated walls of the ion source and the space charge in high intensity electron beams. The longevity and stability of CNT cathodes are also demonstrated with ~700 h of continuous emission, showing only a drop of about 20% of the emitted current. The source will equip INEA, an energy analyzer with a mass resolving capability followed by an imaging detector to measure the energy distribution of the thermal and supra-thermal low energy, 0.5–10 eV, neutral constituents of planetary atmospheres.

AUTHOR DECLARATIONS

Conflict of Interest

The authors have no conflicts to disclose.

Author Contributions

Valentin Steichen: Formal analysis (equal); Methodology (equal); Writing – original draft (lead). **François Leblanc**: Validation (equal); Writing – original draft (equal); Writing – review & editing

(equal). **Jean-Jacques Berthelier**: Methodology (equal); Supervision (equal); Writing – review & editing (equal). **Nguyen Tuan Hong**: Writing – review & editing (supporting). **Soonil Lee**: Writing – review & editing (supporting). **Pierre Gilbert**: Conceptualization (supporting).

DATA AVAILABILITY

The data that support the findings of this study are available from the correspnding author upon reasonable request.

REFERENCES

[1]H. Balsiger, K. Altwegg, P. Bochsler, P. Eberhardt, J. Fischer, S. Graf, A. Jäckel, E. Kopp, U. Langer, M. Mildner *et al.*, "Rosina—Rosetta orbiter spectrometer for ion and neutral analysis," Space Sci. Rev. **128**, 745–801 (2007).

[2]P. R. Mahaffy, M. Benna, T. King, D. N. Harpold, R. Arvey, M. Barciniak, M. Bendt, D. Carrigan, T. Errigo, V. Holmes *et al.*, "The neutral gas and ion mass spectrometer on the Mars atmosphere and volatile evolution mission," Space Sci. Rev. **195**, 49–73 (2014).

[3]P. R. Mahaffy, M. Benna, M. Elrod, R. V. Yelle, S. W. Bougher, S. W. Stone, and B. M. Jakosky, "Structure and composition of the neutral upper atmosphere of Mars from the MAVEN NGIMS investigation," Geophys. Res. Lett. **42**, 8951–8957, https://doi.org/10.1002/2015gl065329 (2015).

[4]B. Schläppi, K. Altwegg, H. Balsiger, M. Hässig, A. Jäckel, P. Wurz, B. Fiethe, M. Rubin, S. A. Fuselier, J. J. Berthelier *et al.*, "Influence of spacecraft outgassing on the exploration of tenuous atmospheres with in situ mass spectrometry," J. Geophys. Res.: Space Phys. **115**, A12313, https://doi.org/10.1029/2010ja015734 (2010).

[5]B. M. Jakosky, J. M. Grebowsky, J. G. Luhmann, J. Connerney, F. Eparvier, R. Ergun, J. Halekas, D. Larson, P. Mahaffy, J. McFadden *et al.*, "MAVEN observations of the response of Mars to an interplanetary coronal mass ejection," Science **350**, aad0210 (2015).

[6]S. Orsini, S. A. Livi, H. Lichtenegger, S. Barabash, A. Milillo, E. De Angelis, M. Phillips, G. Laky, M. Wieser, A. Olivieri *et al.*, "SERENA: Particle instrument suite for determining the Sun-Mercury interaction from BepiColombo," Space Sci. Rev. **217**, 11 (2021).

[7]E. J. Radauscher, "Design, fabrication, and characterization of carbon nanotube field emission devices for advanced applications," Ph.D. dissertation, Duke University, 2016.

[8]S. Sheridan, M. W. Bardwell, A. D. Morse, and G. H. Morgan, "A carbon nano tube electron impact ionisation source for low-power, compact spacecraft mass spectrometers," Adv. Space Res. **49**, 1245–1252 (2012).

[9]W. Knapp and D. Schleußner, "Special features of electron sources with CNT field emitter and micro grid," Appl. Surf. Sci. **251**, 164–169 (2005).

[10]H. Zhang, D. Li, P. Wurz, A. Etter, Y. Cheng, C. Dong, and W. Huang, "Performance of a low energy ion source with carbon nanotube electron emitters under the influence of various operating gases," Nanomaterials **10**, 354 (2020).

[11]J. Becker, N. T. Hong, J.-J. Berthelier, F. Leblanc, S. Lee, and F. Cipriani, "Multi-scale simulation of electron emission from a triode-type electron source with a carbon-nanotube column array cathode," Nanotechnology **24**, 465303 (2013).

[12]V. Steichen, F. Leblanc, J. J. Berthelier, and P. Gilbert, "An energy and mass analyzer for planetary atmosphere investigations, assessment of performances by a numerical model" (unpublished) (2023).

[13]G. D. Earle, J. H. Klenzing, P. A. Roddy, W. A. Macaulay, M. D. Perdue, and E. L. Patrick, "A new satellite-borne neutral wind instrument for thermospheric diagnostics," Rev. Sci. Instrum. **78**, 114501 (2007).

[14]G. D. Earle, R. L. Davidson, R. A. Heelis, W. R. Coley, D. R. Weimer, J. J. Makela, D. J. Fisher, A. J. Gerrard, and J. Meriwether, "Low latitude thermospheric responses to magnetic storms," J. Geophys. Res.: Space Phys. **118**, 3866–3876, https://doi.org/10.1002/jgra.50212 (2013).

5. INEA final assembly

5.1. Numerical End-to-End model

5.1.1. Description of the model

We used SIMION to model the electrostatic fields through INEA and the ray tracing of the ions inside the instrument. Due to the overall volume of INEA it was not possible to build a global model of the entire instrument, and individual parts were modelled independently with convenient boundary conditions between adjacent ones. Thus, the instrument is split into 4 parts that features the main elements of the instrument: the electron source and electron lens, the ionization volume and ion lens, the energy analyzer (which also includes the angular filter) and the detector. Figure 3.67 shows 3D views of the different simulation box used to construct the numerical model.

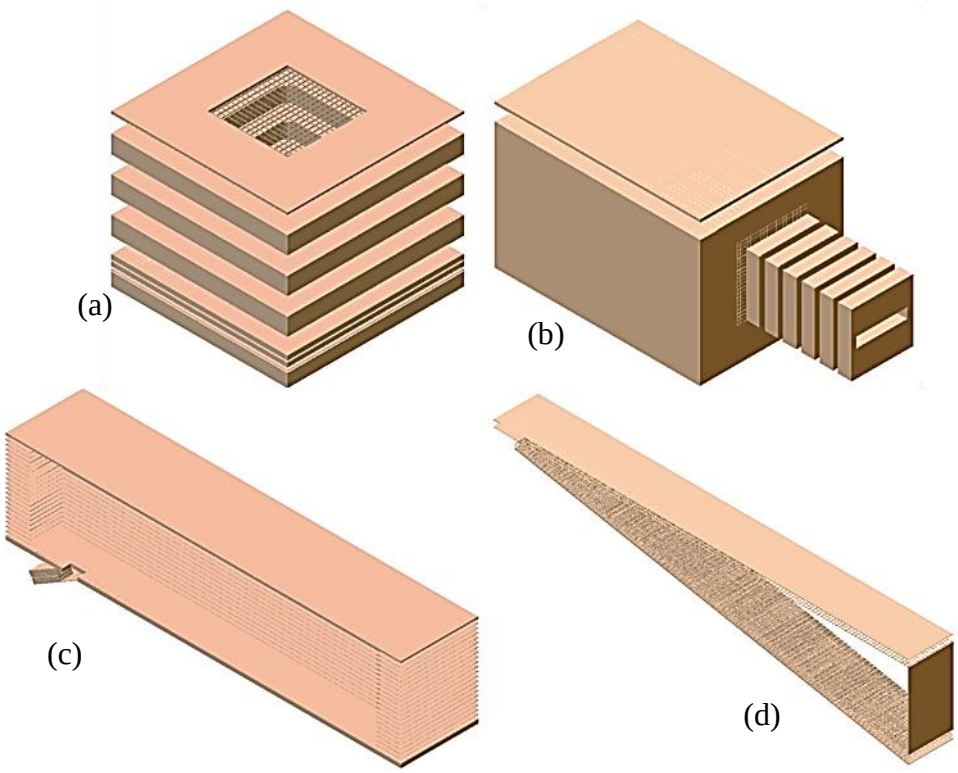

Figure 3.67*: The four ion optical elements used for the numerical end to end model (a) is the electron emitter and electron lens. (b) is the ionisation volume and ion lens. (c) is the Energy analyser and filter. (d) is the detector assembly.*

To reconstruct with high accuracy, the electric field within the different simulations and ultimately the trajectories of the particles throughout the instrument, the boundary layers of the simulation boxes had to be carefully defined. As already discussed, electrostatic grids do not behave as perfect electrostatic shields. The potential applied to G1 will therefore leak through the anode grid and disturb the electron lens. Therefore, the electron source and lens had to be included in a single simulation box to simulate the interaction of the CNT as well as the grid of G1 with the electron lens. A convenient interface to separate the electron source (including the

emitter and the EL) and the ionisation volume is the grid that separates the lower part of the IV from the electron lens. The blue rectangle in Figure 3.68 marks the electron source boundary.

Similarly, as discussed in Section 4.3, when a potential is applied to the ionisation volume, a potential bubble is created within it due to the grounded IL electrodes. The reverse is also true. When simulating in flight operations, the ionisation volume is grounded but the IL electrodes can be biased and a bubble is created within the ionisation volume. The IL and IV are thus simulated in the same numerical array.

The interface between the ion lens and the EA interface at the coincidence plane between the last IL electrode and the angle filter (red rectangle in Figure 3.68). As these two electrodes are electrically connected, they are at the same potential and therefore no electric field exists here.

Furthermore, the simulation box of the energy analyser must include the angular filter to reconstruct the electrostatic defects due to the entrance window of the baseplate and the resulting electric potential leakage. On the exit window side, the simulated geometry is a plain electrode. The effect of the grid and the potentials of the detector are included in the detector box.

Finally, the detector simulation box contains the geometry of the EA exit grid and the detector assembly. The EA exit grid had to be included in this simulation box to accurately reconstruct the electric field induced by G_{repel} between the EA baseplate and the detector entrance. In addition, to fully integrate all the effects of the detector potential, this simulation box also includes a virtual electrode that mimics the equipotential line created by the 1st guard plate above the baseplate. This design of the simulation box allows to take into account the potential interaction between the detector and the EA exit grid. This virtual electrode exists only numerically and serves as a well-defined boundary between the EA and detector simulation boxes (see green box in Figure 3.68).

Another important aspect is the prioritisation of the boxes when they overlap. When assembling several simulation boxes in SIMION, it is possible to apply a priority order. The priorities define which electric field the particle is exposed to when two boxes overlap. For example, the detector and EA simulation boxes overlap, so when calculating the trajectory of the particles, the software first uses the electric field generated by the EA electrode until it reaches the overlapping area, where, as shown in Fig. 3.68, the priority is given to the detector box and the software uses its calculated electric field. The same method is used in the IL, where the EA and IV/IL boxes overlap. Thus, the particles only see the electric field in the EA when they leave the ion lens.

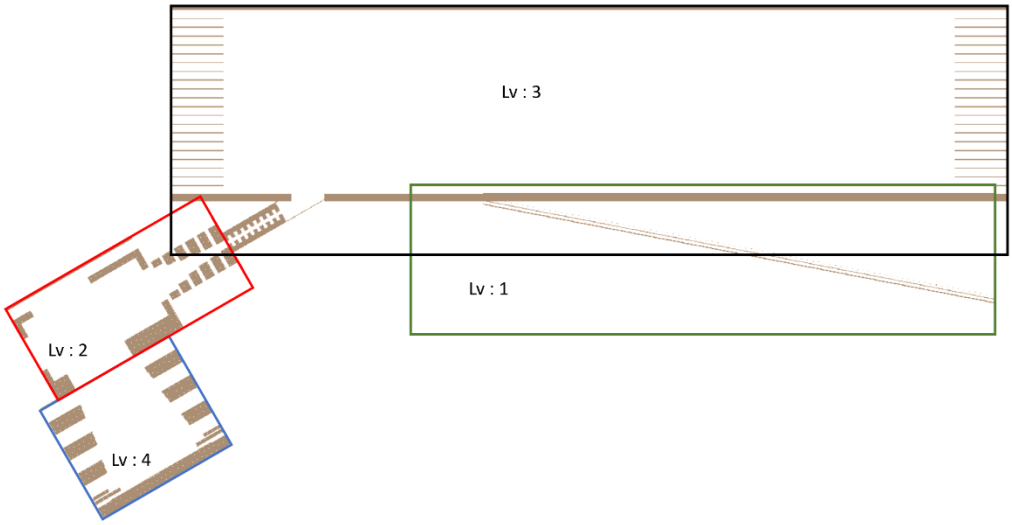

***Figure 3.68**: cross sectional view (in the plane of symmetry) of INEA end-to-end model the coloured rectangles highlight the limit of each simulation box. The labels Lv:1 to Lv: 4 gives the priority order.*

5.1.2. Operation of the model

To operate the model, the user first defines the global simulation parameters in a .txt file, where the following parameters can be defined: the type of particles to fly, the number of particles to simulate, their species, the neutral gas density, the gas temperature and the background neutral velocities along the X, Y and Z axis. Three simulation types can be performed including their own features. They are described in the following.

Electrons simulation type: When operating the model in this mode, electrons are realeased at the CNT. In reality, a strong electric field is generated at the tip of a carbon nanotube due to its high curvature radius, thus the electrons gain much of their energy at the vicinity of the latter and therefore their velocity vector is almost aligned with the electric field at the tip of the nanotube. In the model, electrons are created along a planar equipotential between the top of the CNT array and G1 with an angular cone distribution with 45° half angle (arbitrarily chosen due to the lack of information about the nanotube orientation distribution) and with an initial energy equals to the CNT potential plus the value of the equipotential line along which they are created.

The electrons trajectories are then determined according to the electric field calculated by SIMION in the simulation box. Once the particles reach the second simulation box (i.e. the ionisation volume). An electron – neutral hard sphere collision module becomes active. This module allows to simulate the ionisation of the neutral particles by electron bombardment. Figure 3.69 shows an example of trajectories of electrons (black lines) and ions (green lines) with the ionisation module.

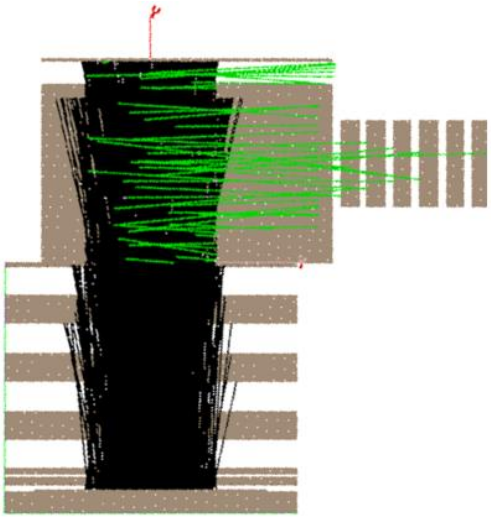

***Figure 3.69**: Example of trajectories of electrons (black) and ions (green) calculated by SIMION and using the electron – neutral hard sphere collision module.*

At each time step, during the electron trajectory calculation, the module computes the electron mean free path defined as:

$$\bar{l} = \frac{1}{n_{neutral} \times \sigma(E)} \qquad 3.5.1$$

Where $n_{neutral}$ is the neutral density and $\sigma(E)$ is the collision cross section which depends on the electron energy. $\bar{l}$ is calculated to limit the next time step (if necessary), as the length travelled during a single step should be a fraction of the mean free path. The next time step is then

$$t_{tstep} = \frac{\bar{l}}{v_e \times \#step\ MFP} \qquad 3.5.2$$

With v_e the electron velocity and $\#step\ MFP$ the number of time step neeeded to travel one mean free path. This value is adjustable but a good empirical estimation is between 10 – 15 which sits as a good compromise between calculation time and accuracy.

To determine if the electron ionize a particle or not, the ionisation probability p is computed with the following equation:

$$p = 1 - \exp\left(v_e \times \frac{t_{step}}{\bar{l}}\right) \qquad 3.5.3$$

A random number r is then generated. If $r > p$ an ion is created with the conditions defined in the parameters.txt (i.e. background velocity, temperature) and at the current electron's position. Otherwise, the code continues to the next time step.

This mode has not been used consequently for modelling the operation of INEA due to its computationally intensive requirements. To achieve a sufficient number of ions reaching the

detector, the number of electrons created needs to in the order of several tens of millions of particles to generate enough ions.

The second developed mode is the **Ions simulation type.** In this mode, the electron source simulation box is not used. Ions are directly created in the ionisation volume according to background velocity, species and temperature defined in the paramters.txt file. The density no longer needs to be defined as it is only involved for the computation of the ionisation module. The initial positions of the ions are defined using two gaussians along the x and z axis. These gaussians simulate a circular electron beam in the [X, Z] plane. The mean values of each gaussian is set at the centre of the IV bottom entrance (i.e. the entrance aperture for the electrons) and the standard deviation can be tuned in order to reproduce different divergence coefficient of the electron beam. A typical value of the standard deviation used is 1.5mm (approaching the size of the electron beam in the electron simulation mode). In the Y direction, ion positions are determined following a uniform random distribution. Both distributions are illustrated in Fig. 3.70.

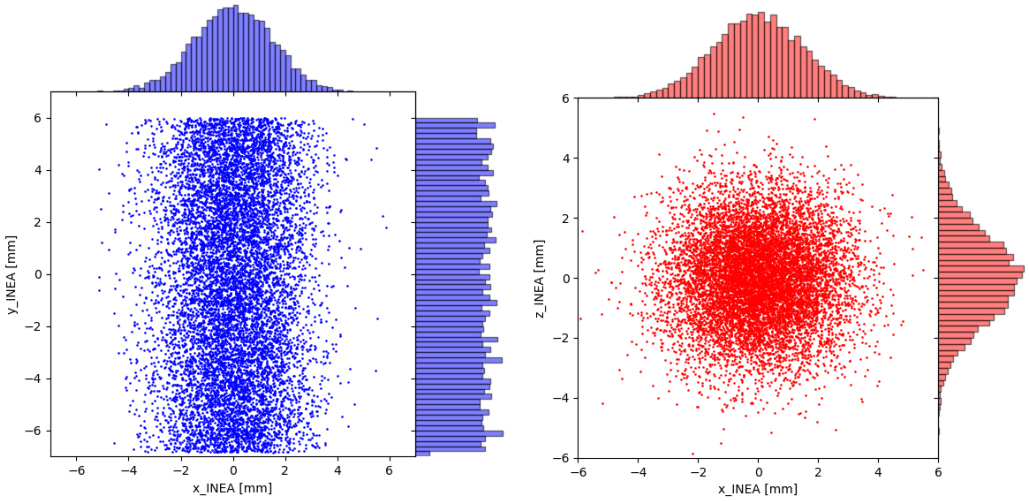

***Figure 3.70**: Distribution of ions initial positions in the [X_{INEA}, Y_{INEA}] (blue) and [X_{INEA}, Z_{INEA}] (red) planes when operating the model in Ions simulation type.*

Finally, the **Ions_from_slit simulation type** is the last possible operating mode. Ions are created at the Energy Analyzer source slit. In this mode, the ions are no longer determined with their velocities and temperature but with their kinetic energy and angular distributions. Their initial positions are distributed uniformly all across the EA source slit.

In the three modes of operation, test planes are placed at different location across the instrument. These plans serve as trigger to register the particle state when it is crossed. The information registered are the ion number, its velocity along the 3 spatial axes, its Time-of-flight and position. Three test planes were defined. The 1st one is at the IL exit. It is mostly used to determine the number of particles that exit the ion source. It is also used to reset the time of flight of the ion. The second test plane sits along the theoretical focal plane and finally, the last one is at the MCP entrance face. The time of flight measurement is thus determined as the elapsed between the IL exit plane and the MCP plane. Each plane is illustrated in Fig 3.71.

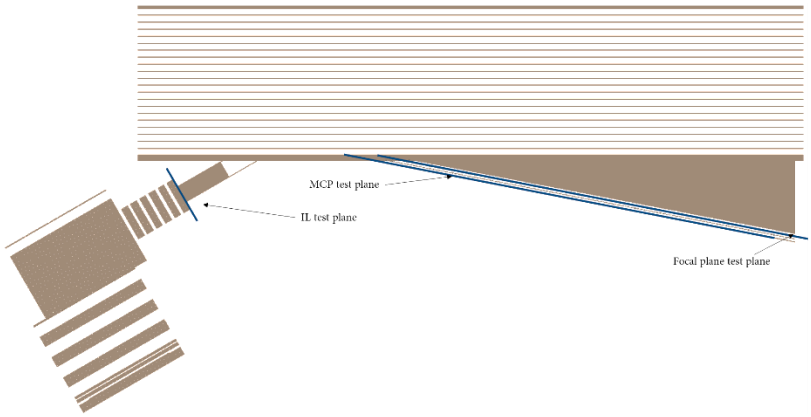

***Figure 3.71**: Position of the end-to-end model test planes*

At the end of each run, the data are registered in a folder including 6 different .txt files. One file 'PosInit.txt' gathers the initial conditions of the particles. 3 files registered the particles state at the IL, MCP and Focal plane test planes and a last file registers the whole ion trajectories. To reduce the amount of produced data, only the information of the particles that reaches the MCP test plane are saved. Finally, a last .txt file is created summarising the parameters used for the simulation

5.1.3. Performances according to the numerical model

Prior to start initial measurements with INEA's mechanical prototype, our main task has been to estimate the expected performances of the instrument. The development of an end-to-end numerical model. The results of this model were used to write an article that is submitted. The article details the modelling of the various components of the instrument and then gives an estimate of the expected performance in terms of energy, mass, temperature and velocity.

Ion and Neutral Energy Analyzer: An Energy and Mass spectrometer for planetary exosphere investigations Numerical model

V. Steichen, F. Leblanc, J.J. Berthelier and P. Gilbert

LATMOS/CNRS, Sorbonne Université, Université Versailles Saint-Quentin, Paris, France

ABSTRACT

We present in this paper a numerical study and modeling of the INEA Ion and Neutral Energy Analyzer designed to study the erosion processes responsible of the long-term evolution of the Martian thermosphere and exosphere and their dependency on solar activity. This instrument performs high resolution measurements of the low energy distribution of neutrals with a mass resolving capability to precisely characterize the thermal and supra-thermal populations and their variations that control the dynamics and evolution of the planet atmosphere. Detailed numerical models were built to optimize the design of the various sections of the instrument from the ion source till the detector and determine their performances. INEA will measure the neutral temperature and drift velocity to better than 50K and 20 m/s respectively associated to an energy resolution of 0.1 eV. Finally, INEA also achieves a mass resolution of ~ 22 allowing to identify all the major thermospheric constituents.

1. INTRODUCTION

Investigating the composition, dynamics and long-term evolution of planetary atmospheres may require neutral and ion spectrometers with significantly higher performances than those already flown on past and current planetary missions. This is, in particular, the case of Mars for which it was recently established (Jakosky et al., 2018) that the current state of its tenuous atmosphere results from the escape of its initial denser atmosphere through photo-chemical processes triggered by the impact of solar radiation and the direct interaction with the solar wind favoured by the lack of a global planetary magnetic field. Among the processes that contributed to the erosion of the atmosphere, dissociative recombination of the major O_2^+ ion species in the ionized atmosphere (Lillis et al., 2015; McElroy & Donahue, 1972) giving rise to supra-thermal $O^{\downarrow}$ ions and sputtering by heavy pick-up ions (Luhmann & Kozyra, 1991) feature two non-thermal processes thought to be the major drivers of the loss of the atmospheric oxygen together with the escape of thermal neutrals and ions during the early stage of Mars (Jakosky et al., 2018).

36 The loss of atmospheric oxygen is currently dominated by dissociative recombination, much
37 more efficient than sputtering (Lillis et al., 2015), while sputtering is thought to have been
38 potentially important for early solar conditions (Jakosky et al., 2015). However, so far, no
39 instrument flown on board past and present missions dedicated to the study of the Martian
40 atmosphere has been specifically designed to directly characterize the neutral particles that
41 escape from Mars. As a consequence, the efficiencies of the various processes that control the
42 atmosphere loss have only been indirectly determined (Jakosky et al., 2018). An accurate
43 measurement of the energy distribution of neutral particles in the thermosphere and exosphere
44 would thus allow for the first-time a quantitative assessment of this process and provide data to
45 characterize the involved mechanisms and their dependency upon solar conditions and Martian
46 seasons, that constitute a key knowledge to determine their efficiency and their contribution to
47 the erosion of the atmosphere under past solar conditions. Thanks to its improved performances
48 in the energy distribution measurement of thermal and supra-thermal neutrals and to its
49 simultaneous mass resolving capability, INEA offers the needed performances for an in-depth
50 study of the Martian atmosphere as well as the upper atmospheres of other planets and of their
51 moons in the Solar System.

52 Based on a high-resolution numerical model of INEA, we have performed an in-depth analysis
53 of the instrument performances to ascertain, in particular, its appropriateness for the challenging
54 conditions met in the tenuous and cold Martian atmosphere and its complex escape processes.
55 Following a summary of the measurement objectives and performance requirements, a detailed
56 description of INEA is given in section 2. Then the numerical model is presented in section 3
57 and we discuss in section 4, the instrument performances derived from the modelled ion
58 trajectories from the ion source to the detector and expressed in terms of energy, mass, ram
59 velocity and temperature measurements. An overall summary and conclusion are given in
60 section 5.

2. MEASUREMENT OBJECTIVES AND INEA DESCRIPTION.

2.1. Measurement objectives

A proper identification of the physical processes that control the dynamics and evolution of the Martian atmosphere asks for the measurement of the energy distribution of the neutral oxygen constituents over a wide enough altitude range from the thermosphere to the exosphere with a good enough resolution allowing to distinguish the thermal and supra-thermal populations.

At the exobase close to 200 km altitude, the thermal population density vary from 10^7 to 10^8 part/cm^3 (Fu et al., 2020) while the density of the supra-thermal population amounts to 10^3 to 10^4 part/cm^3 (Leblanc et al., 2019). Disentangling these two populations with such large density differences requires a differential measurement of the neutral oxygen energy spectrum with a resolution in the order of ~ 0.1 eV. Such a performance, significantly better than a previous evaluation by (Cipriani et al., 2007) will allow determining with no ambiguity the temperature of the low energy thermal population and the spectrum of the supra-thermal particles.

2.2. Description of INEA

INEA is composed of 4 main elements: The Ion Source (IS), inactive during the Ion Modes of operation, the Ion Lens (IL) which focuses the newly created ions on the entrance slit of the Energy Analyzer (EA) which is followed by the Detector (DET). The axis of sight of the instrument, perpendicular to the entrance area of the ion source, is oriented close to the spacecraft orbital velocity. Shown in Figure 1 is a schematic view of the INEA configuration where have been indicated the 3 reference frames that will be used to describe the instrument operation.

- $[X_{INEA}, Y_{INEA}, Z_{INEA}]$ is the main frame of the instrument with X_{INEA} along the average velocity direction of the incoming particles and perpendicular to the IS entrance area. The $[X_{INEA}, Y_{INEA}]$ plane is the plane of symmetry of the instrument and the origin O_{INEA} is at the EA source slit in the plane of symmetry of the instrument.

- $[X_{EA}, Y_{EA}, Z_{EA}]$ is the EA reference frame with the X_{EA} axis in the symmetry plane of the instrument and parallel to the EA base plate inclined at an angle θ with respect to X_{INEA}. The $[X_{EA}, Y_{EA}]$ plane, identical to the $[X_{INEA}, Y_{INEA}]$ plane is the plane of symmetry of the instrument with the origin O_{EA} at the center of the EA source slit.
- $[X_{DET}, Y_{DET}, Z_{DET}]$ is the detector DET reference frame. $[X_{DET}, Z_{DET}]$ is the detector plane and, as for the previous reference frames, $[X_{DET}, Y_{DET}]$ is in the symmetry plane of the instrument. The X_{DET} axis is inclined at an angle α with respect to the base plate and the origin O_{DET} is at the center of the intersect line between the base plate and the detector plane.

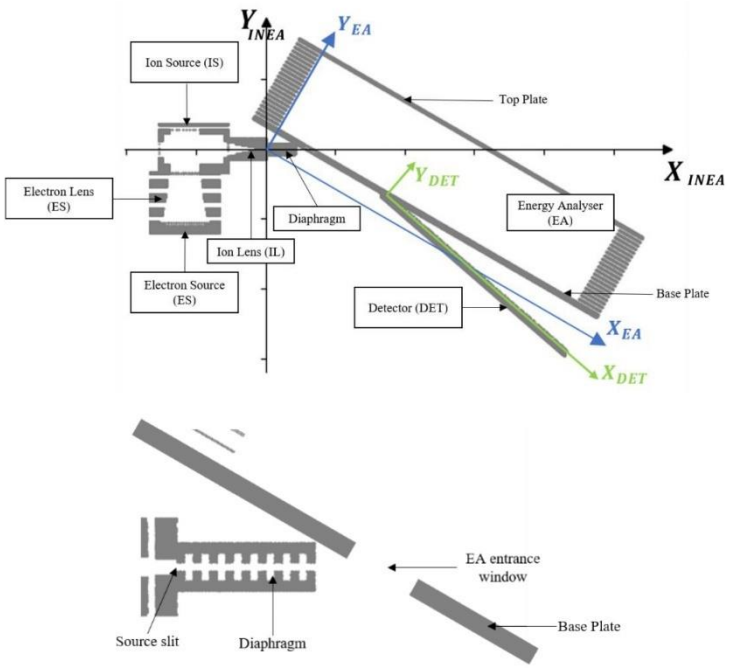

Figure 1 : Top panel is an overview of the different elements constituting INEA. The coloured arrows represent the 3 used reference frames. Bottom panel is a zoom on the energy analyser entrance area.

In the *Neutral mode* neutral atoms and molecules enter the ion source (IS). through a 5x5 mm² entrance grid perpendicular to the X_{INEA} axis. The ionizing electrons are emitted from a Carbon Nano-Tube cold cathode at -100 V through an extracting grid at a potential between +150V and +250V followed by 3 electrodes forming an electron lens EL which reduces the electron beam divergence and maximize the electron flux in the ionizing volume. Heated filaments have been used in mass spectrometers flown on-board previous space missions such as the recent and highly successful ROSINA spectrometer (Balsiger et al., 2007). Thanks to progresses in the fabrication and performances of CNT electron emitters leading to a satisfactory reproducibility and stability over time (Hong et al., 2009), these devices have recently emerged as efficient electron sources in mass spectrometry (Bonard et al., 2001) and have been already selected in the recent JAXA KITE mission (Ohkawa et al., 2020). CNT electron emitters offer two main advantages

1- The ~ 0.5W power consumption associated to the High voltage electronics is much lower than the average 2 to 3W for heated filaments.
2- There is no heated surfaces in the ion source thus no measurement background which may hamper reliable measurements of the low mass constituents in planetary atmospheres (Mahaffy et al., 2015; Schläppi et al., 2010). A more detailed description of the ion source is given in (Steichen et al., 2023)

The newly created ions exiting the ion source are focused by the IL electrostatic Ion Lens onto the source slit of the parallel plate Energy Analyzer (EA), 5 mm long parallel to the Z_{EA} axis and 0.5 mm wide along the Y_{INEA} axis. A diaphragm located between the IL exit and the entrance window in the EA base plate allows maintaining the angular dispersion of the ion velocity vectors parallel to the symmetry plane within $\pm 3°$ along both the Y_{INEA} and Z_{INEA} directions. The EA energy analyzer is identical to the parallel plate energy spectrograph of (Green & Proca, 1970): charged particles entering through the EA source slit with a velocity

close to the X_{INEA} axis are focused along the detector at a distance linearly dependent on their energy E_c. For small variations of the incidence angle with respect to the nominal direction X_{INEA}, second order focusing is obtained for θ = 30° and α = 10.9°, values adopted for INEA. A set of 20 thin metallic guard plates with linearly varying potentials are used to maintain the best possible uniformity of the EA electric field parallel to the Y_{EA} axis. As mentioned in Section 3, only close to the EA entrance window is a small volume where the EA electric field is distorted. Ions follow parabolic trajectories as shown in *Figure 2*, then exit through the EA exit grid of the base plate towards the entrance plane of the detector following straight trajectories in the field free region between the base plate and the detector. The following relation holds for the coordinates x_{ea} and y_{ea} of the impact points of the ion on the detector in the EA reference frame.

$$x_{ea} = (\mathrm{h} - y_{ea}) \cot\theta + \frac{2\mathrm{E_c}}{\mathrm{E}} \sin 2\theta \quad (1)$$

where h is the distance, along Y_{EA}, between the EA source slit and the base plate, h = 6.74 mm, E_c is the energy of the particle in eV and E is the EA deflecting electric field. In the Ion mode the electron source is inactive and the incoming ionospheric ions directly travel through the Ion Lens to be focused onto the source slit of the energy analyzer then following similar trajectories as the ionized neutrals.

According to (Green & Proca, 1970) ions traveling in the symmetry plane are focused at the exit of the EA along the X_{DET} axis inclined by an angle α with respect to the X_{EA} axis and intersecting the base plate at O_{DET} located at x_{min} = 35mm from the position of the EA source slit as shown in Figure 1. The α angle is such that:

$$\tan\alpha = \frac{\tan\theta \cos 2\theta}{1 + \cos 2\theta} \quad (2)$$

thus α = 10.9°

A stopping potential applied at the exit of the Ion Lens IL allows to operate INEA in a Time of Flight mode where the mass of the detected ions is determined from their Time-of-Flight (TOF) between the exit of the IL and the impact on the detector.

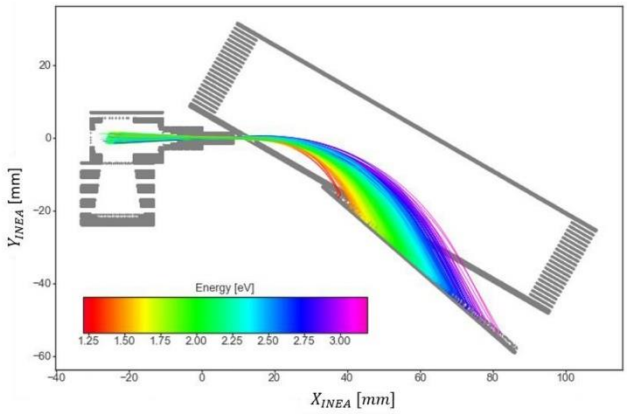

Figure 2: Trajectories of ions created in the Ion Source up to the detector plane.

3. NUMERICAL MODEL

In order to assess the performances of INEA we performed a thorough numerical modeling of the various parts of the instrument. The first two parts are the Ion source and the Ion Lens till the EA source slit, which control the sensitivity of the instrument. The main goal of the numerical modeling was thus to optimize the potentials of the electrodes in the EL Lens, between the CNT and the ionization volume, and, independently, of the IL electrodes in order to maximize the number of ionized neutrals entering the Energy Analyzer. The following 2 parts, the EA Energy Analyzer and the DET Detector control the energy resolution, thus the instrument performances for the drift velocity and temperature measurement of the thermal population, and the mass resolution. The main goal of the numerical modeling was to assess the corresponding performances from an accurate ray tracing of ion trajectories.

The SIMION Software (Dahl, 2000) was used to compute the electric potential maps in the various sections of INEA. Deviations of the electric potential from the ideal case considered by

(Green & Proca, 1970) occur mainly close to the grids used in several parts of the instrument and at a small-scale length commensurate with their mesh size. Since they constitute a major source of disturbances of the ion trajectories they have to be accurately modelled using a fine enough computational mesh. The grids feature a 300µm square mesh with bars of 30x30µm² cross section: this led us to use a computational mesh size of 25µm. Due to the overall volume of INEA it was thus not possible to build a single model for the entire instrument, and the successive individual parts were modelled independently with convenient boundary conditions between adjacent parts. The Poisson solver used by SIMION leads to a convergence limit of 10^{-5} V. A standard fourth order Runge-Kutta method with continuously adjustable time steps provides the necessary accuracy for the numerical integration of the ion trajectories.

3.1 Ion source and Ion Lens

A simplified sketch of the Ion Source is shown in *Figure 3a*. The CNT electron emitter is polarized at -100V so that electrons reaching the grounded ionization volume have an energy corresponding to the maximum of the ionizing cross section. The extracting grid G1 is polarized at ~ +150V to +250 V with respect to the CNT and followed by the 'Anode' grid at 0V just before the EL electron lens after which the electrons enter the ionizing volume through a grid at 0V. The 'Anode' grid aims at preventing the variable potential of the extracting grid to modify the operation of the EL lens. When exiting the 'Anode' grid, the electrons have a wide angular distribution due both to the emission process from the individual CNT's and to the small-scale potential disturbances induced by the G1 and the 'Anode' grids, as illustrated in *Figure 3b*. The EL lens aims at reducing the angular dispersion of the electrons and maximize their flux towards the ionization volume where they ionize the incoming neutral particles. The EL lens is a usual symmetrical electrostatic lens with a negative potential V2 applied to the central electrode EL2 and the end electrodes EL1 and EL2 at 0V. The optimal value of V2 was found to be equal to the 100eV electron energy. The newly formed ions exit the ionization volume and enter the Ion lens IL, an assembly of 6 electrodes, which forms a funnel-like shape along the X_{INEA} axis and shown schematically in Figure 3a. Our optimization algorithm was applied for O^+ ions at 273K and a ram velocity equivalent to 2 eV. The results of these

simulations showed that the number of particles entering the energy analyzer can be increased at least by a factor 2.

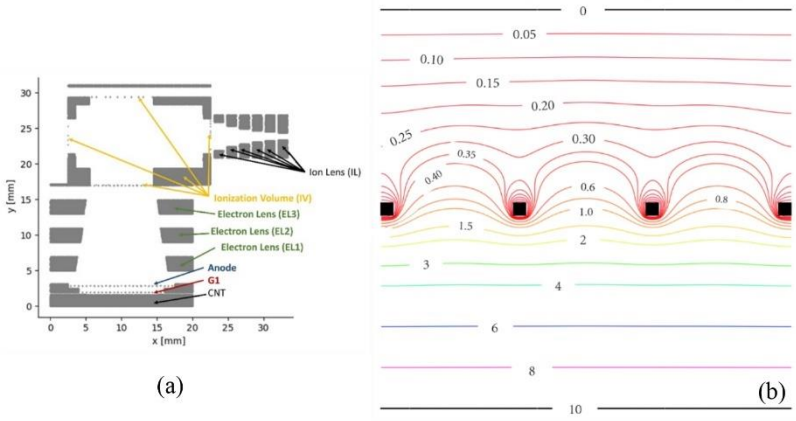

(a) (b)

Figure 3 :(a) Schematics of INEA's Ion Source with a description of every electrostatic parts. (b) Propagation of the electric potential through an electrostatic grid. The grid and top electrodes are at 0V while the base electrode is at 10V. The coloured lines are the equipotential lines.

3.2 Energy Analyser

Between the EA source slit and the EA entrance window in the base plate, ions travel through the diaphragm which aims at limiting the angular dispersion of the components of the velocity vectors in the [X_{INEA}, Y_{INEA}] and [X_{INEA}, Z_{INEA}] planes to less than +/- 3° with respect to their average direction along the X_{INEA} axis.

As shown in *Figure 4*, a set of 20 electrodes polarized by linearly varying potentials is used to generate the EA electric field as close as possible from the ideal uniform electric field of (Green & Proca, 1970). *Figure 4* also shows within the energy analyzer. The top plate is at 25.1V while the base plate is at 0V, leading to a 1V/mm electric field within the EA. From the equipotential lines drawn in *Figure 4* the guard plates clearly generate a very uniform electric field within the energy analyzer except close to the entrance window where the electric potential is distorted and leaks in the supposed field free region between the source slit and the base plate inducing

disturbances in the ion trajectories that increase the aberration of impact points in the detection plane.

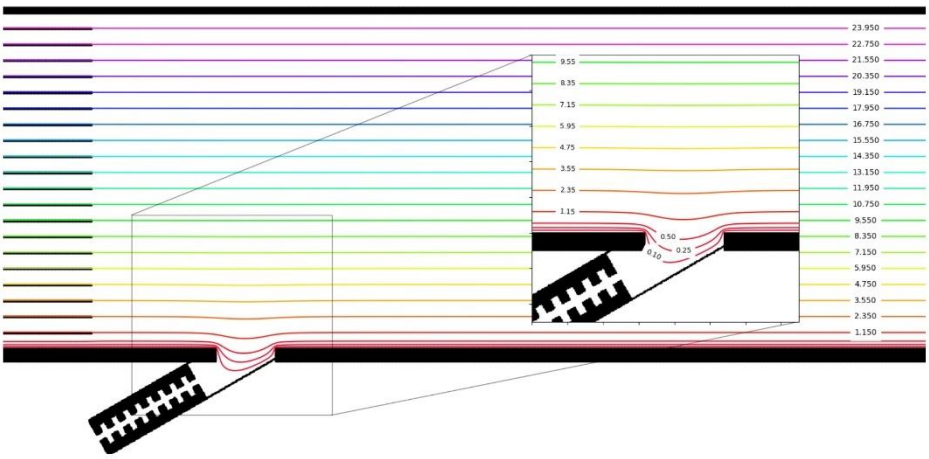

Figure 4: *Geometry of the equipotential lines inside the EA. Top plate is at 25.1V and base plate is at 0V. The coloured lines display the equipotential lines and the associated values in volts.*

3.3 Detector

Ions exiting the Energy Analyzer enter a nominally field free drift space between the EA exit window in the base plate and the detector. The detector consists in an assembly of 2 Micro Channel Plate (MCP) providing, for each ion impact, a pulse of $\sim 10^6$ electrons collected by a pixelized collector with its associated electronics. The MCP detection efficiency depends on the energy of the incident ions, with a typical efficiency of $\sim 10^{-3}$ for O^+ ion with an energy of 10 eV (Rispoli et al., 2012), insufficient to reach the desired sensitivity of INEA. Ions must thus be accelerated before impacting the front face of the MCP by polarizing the MCP front face at a negative potential of ~ -200V that increases the efficiency up to $\sim 10^{-1}$ if the secondary electrons generated by ion impacts on the front face of the MCP assembly are repelled towards the MCP pores by a convenient electric field. This electric field is obtained using a repeller grid G_{Repel} polarized at ~ -250V and at a distance 300µm in front of the MCP. To shield the potential applied on G_{Repel} and maintain, as much as possible, a field free region between the exit of the

base plate and the detector's entrance, a set of 2 grids G_{ISO1} *and* G_{ISO2} polarized at the base plate potential are mounted in front of G_{Repel}. This dual grid set-up is more efficient than a single grid to decrease the leakage, through the grid mesh, of the strong electric field between G_{ISO2} and G_{Repel} in the region in front of G_{ISO1}. The amplitude and extent of the potential disturbances decrease with the grid transparency: this led us to select a 50% transparency for G_{ISO1} (mesh size 180µm, width of the bars 40µm) while G_{ISO2} has a transparency of 80% (mesh size 300 µm, width of the bars 30µm) similar to the grids at the exit window of the base plate. The detector configuration with the 3 grids is shown in *Figure 5a* where have also been indicated the boundaries of the detector volume used to compute the potential. Equipotential lines are displayed in *Figure 5b*. In *Figure 5c* we have illustrated the overall outcome of the DET numerical model by showing several ion trajectories starting a few mm above the EA exit window then through the 3 grids till their impact on the MCP front face. While the G_{Repel} potential is efficiently shielded by the dual set of grids [G_{ISO1}+ G_{ISO2}], significant potential disturbances exist between the 2 grids and, even more, between G_{ISO2} and G_{Repel} leading to a dispersion of the ion impact locations on the front face of the MCP, thus reducing the energy resolution of INEA. This is analyzed in detail in the following section.

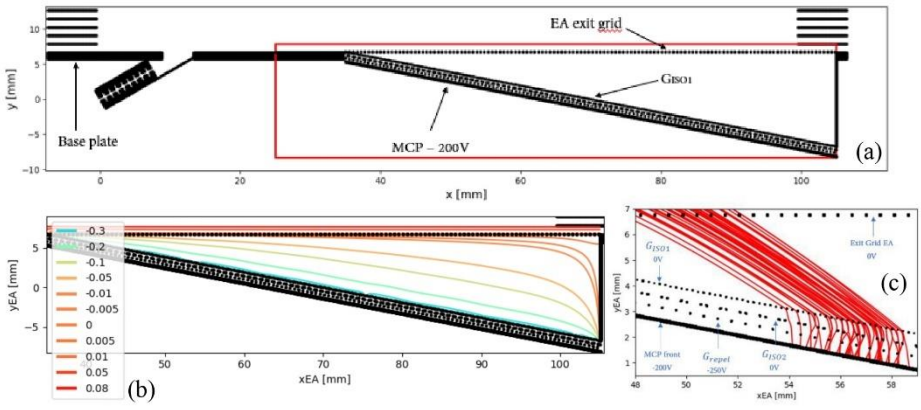

Figure 5: *(a) Geometry of the detector. The red box represents the boundaries of the simulation box relative to the detector. The top boundary condition matches the potential of the 1st EA's guard plate.*

(b) Structure of the equipotential lines in the free space between the base plate and the detector entrance.

(c) Trajectories of few ions from the EA's exit window up to the MCP front face

4. MODELLED PERRFORMANCES OF THE INSTRUMENT

4.1 Energy Resolution

In order to estimate the energy resolution of INEA, we computed the trajectories of 10^6 O^+ ions created randomly within the ionization volume with energies of 2.0 eV and 2.1 eV, representative of the ram energy along a Martian orbit. *Figure 6* displays the dispersion of the impact locations of these ions along X_{DET} together with their time of flight (TOF) from the EA source slit.

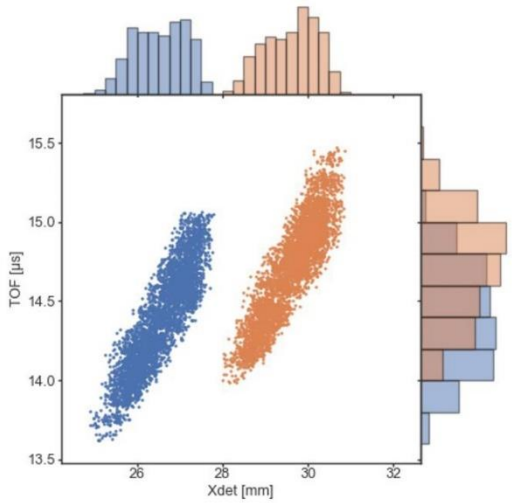

Figure 6: Distribution of the impact points of O^+ ions at 2.00 eV (blue) and 2.10 eV (orange) along X_{DET} with their Time of Flight from the EA source slit.

The width *e* of the EA source slit along the Y_{INEA} axis leads to a magnification Δx_{DET} of the focal line along X_{DET} given theoretically by (Green & Proca, 1970) as:

$$\frac{\Delta x_{Det}}{e} = \frac{1 + \cos(2\theta)}{\sin(\theta)\cos(\alpha)} \qquad (3)$$

With e = 0.5 mm, Δx_{DET}= 1.5 mm. The modelled width of each packet is ~2mm at 3σ. This result is slightly greater than the theoretical value due to the previously mentioned electric field disturbances at the EA entrance window and along the detector grids (see *Figures 4 & 5*).

In order to illustrate the energy resolution of INEA for realistic conditions encountered in flight, we considered the case of two ion populations with largely different densities and 0.1eV energy difference, ions at 2.1 eV being only 10% of ions at 2.0 eV. To retrieve the energy of each population, 2 gaussian functions were applied to the modelled data. As displayed in *Figure 7*, the two populations are clearly distinguished with the peaks of each gaussian functions giving the mean impact position of the two populations respectively at 26.54 mm and 29.61mm corresponding to energies of 1.97 eV and 2.07 eV and the 0.91 and 0.09 weights of the 2 gaussian functions in perfect agreement with their density ratio. Albeit, the retrieved energies are slightly offset by 0.03 eV their difference is 0.1eV, showing the good linearity between position and energy. By varying the mean energy, the two ion populations with an energy difference of 0.1eV, we have checked that they can be distinguished whatever the positions of their impact points along the detector. The 0.03 eV energy bias will be corrected by a calibration of the instrument.

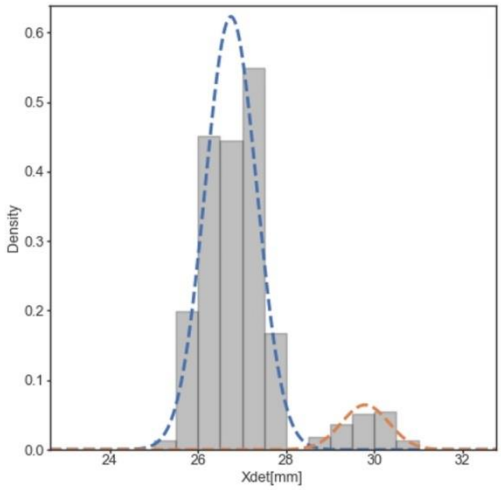

Figure 7: Distribution of two populations of particles with energy of 2.0 and 2.1 eV, respectively launched from the ionization volume with a cone angle of $\pm\ 20°$. The weight of each packet is respectively 90% and 10%. The blue and orange dashed lines represent the result of a fit with two Gaussian functions.

4.2 Mass resolution

The mass resolution is exemplified in *Figure 8* where have been displayed for 10^6 ions of three species O^+, N^+, C^+, all with an energy of 2.0 eV, the impact positions on the detector and the time of flight between the EA source slit and the detector. Ions are launched from the ionization volume with random initial conditions as indicated in the previous paragraph and cross the source slit uniformly over its entire area. Irrespective of the ion species, their impact locations on the detector are identical but the time of flight are different as shown in *Figure 8*. In order to simulate a realistic operation of the instrument in a Time of Flight mode, we added a random value to every TOF value comprise in a range $[-150\ ns, 150\ ns]$. Adding randomly such values mimics the gating operation that can be achieved at the end of the ion lens.

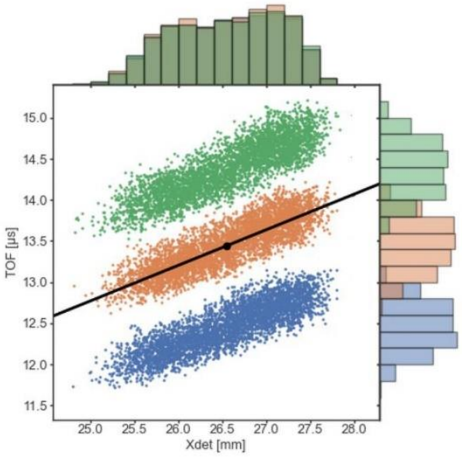

297

298 **Figure 8:** Distribution of particles on the [X_{det},TOF] reference frame for the three species
299 O^+ $(green), N^+(orange)$ and C^+ $(blue)$ at 2.0 eV. The black line and dot represent
300 respectively the average slope of the 3 populations and the centroid of all points.

301 As illustrated in Figure 8, we calculated the centroid C of all the points and the mean slope S
302 (represented by the black dot and line in Fig 8). Then, every point, independently of their
303 species, is rotated around C by an angle $\phi = \arctan S$. Figure 9 shows the distribution of TOF
304 after such rotation. The three species distribution being clearly separated, we can calculate the
305 mass resolution of INEA $\frac{m}{\Delta m} = \frac{\bar{t}}{2\Delta t} = 22$. Here, $\bar{t} = \sum_{i=1}^{n} \frac{TOF_i}{n}$ for every peak and Δt is the
306 FWHM of each peak.

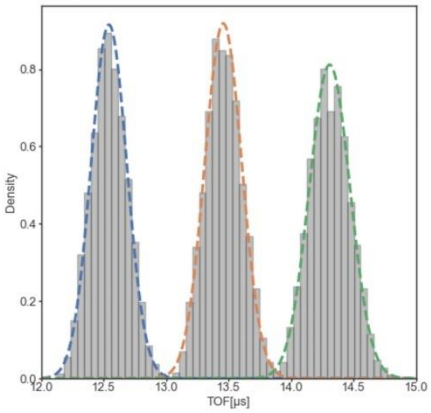

307

308 **Figure 9** : Distribution of TOF for O^+ $(green), N^+(orange)$ and $C^+(blue)$ after a rotation in
309 the plane $[X_{DET}, TOF]$ has been applied as explained the text. The coloured dotted lines are
310 fitted gaussian functions of each peak. Each distribution considers a gate time $dt = 300\ ns$.

311 ### 4.3 Temperature resolution

312 The temperature resolution was studied by sending O^+ ions randomly from the ionizing volume
313 with a velocity distribution typical for an instrument in orbit around Mars, i.e. a ram velocity
314 of 5 km/s and a temperature of 300K or 350K. *Figure 10a* illustrates the distribution of the
315 impact locations and TOF in the [X_{DET}, TOF] coordinate system for a temperature of 300K.

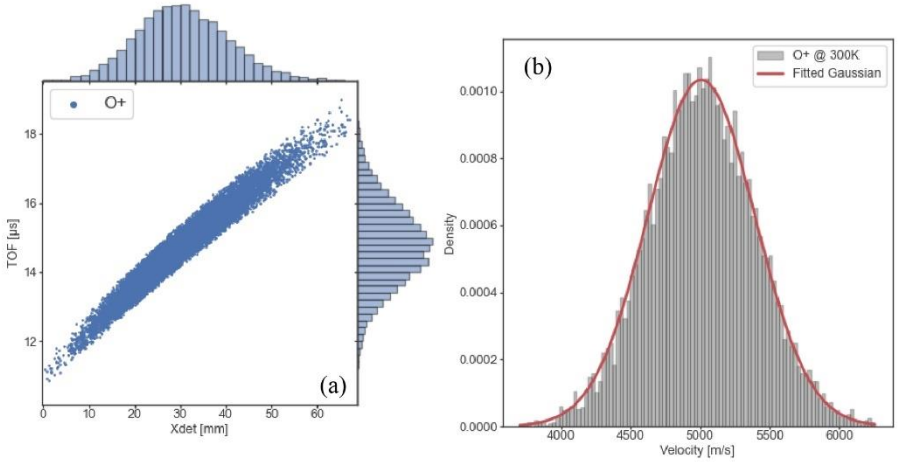

316

317 **Figure 10:** (a) Distribution of particles on the [X_{DET},TOF] reference frame with mean velocity
318 of 5 km/s and a temperature of 300K in the ionization volume. Here the particle impacts are
319 distributed all along the X_{DET} axis. (b)Velocity distribution of the particles with 5km/s and a
320 temperature of 300K obtained from the impact distribution on the detector.

321 Using the data analysis indicated in the previous paragraph to determine the ion mass, one gets
322 the relation between the impact points for O^+ ions along the X_{DET} axis and the energy through
323 Eq. 4.

324 $$E_c\ [eV] = \left[x_{min} - x_0 + x_{det}\left(\cos\alpha - \frac{\sin\alpha}{\tan\theta}\right)\right] \times \frac{Ef}{4\cos\theta\sin\theta} \qquad (4)$$

325 Where $x_{min} = 35\ mm$ and is the intersection between the detector plane and the base plate,
326 $x_0 = h\cot\theta$ and x_{det} the impact position along the X_{DET} axis. From the reconstructed velocity
327 distribution (Figure 10b); the mean velocity $\bar{v}$ as well as the standard deviation $\langle v\rangle$ are estimated
328 with a fit of a gaussian function (red line on figure 10b). From $\langle v\rangle$, the temperature can be
329 derived using the equation $T = \frac{\langle v\rangle^2 m}{k_b}$ where m is the mass of the species (supposed to be known)
330 and k_b the Boltzmann's constant.

The cases of 2 slightly different temperatures of 300K and 350K were studied with respective thermal velocities of 395 $m.s^{-1}$ and 426 $m.s^{-1}$. From the above described analysis, we got $\langle v \rangle_{300K} = 386 \pm 3\, m.s^{-1}$ and $\langle v \rangle_{350K} = 419 \pm 4\, m.s^{-1}$ corresponding to temperatures of $287K$ and $338K$ with a 51K difference practically identical to the 50K imposed on the initial ion distribution launched from the ionizing volume. The deduced absolute temperatures are slightly different from the initial ones but may be corrected from the instrument calibration.

4.4 Velocity resolution

Similar simulation tests were conducted to determine the ram velocity resolution. 10^6 O^+ ions with a temperature of 300K were launched with mean velocities $\langle v \rangle$ of 4080 m/s, 5000 m/s and 5020 m/s respectively with results already illustrated in Figure 10 for a ram velocity of $\langle v \rangle$ = 5000 m/s. The computed mean velocities from the detector data were respectively $4976 \pm 3.9\, m.s^{-1}, 5008 \pm 3.7\, m.s^{-1}$ *and* $5026 \pm 4.1\, m.s$ corresponding to relative errors of less than 5m/s even better than the goal of ~20 m/s specified for the instrument.

CONCLUSION

The Ion and Neutral Energy Analyzer (INEA) presents with its innovative design, including the utilization of carbon nanotubes for electron emission, a powerful tool for characterizing energy distributions of neutral particles in the planetary thermosphere and exosphere. Through numerical modelling and simulations, it has been demonstrated that INEA possesses capabilities, including an energy resolution of 0.1 eV, a mass resolution of 22, and the ability to measure temperature and velocity with resolutions better than 50 K and 20 m/s, respectively. This novel instrument not only opens doors for in-depth studies of Mars' atmosphere but also holds promise for investigating the atmospheres of other celestial bodies within the Solar System.

ACKNOWLEDGMENTS

This work was supported by the the French Space Agency CNES.

5. REFERENCES

Balsiger, H., Altwegg, K., Bochsler, P., Eberhardt, P., Fischer, J., Graf, S., Jäckel, A., Kopp, E., Langer, U., Mildner, M., Müller, J., Riesen, T., Rubin, M., Scherer, S., Wurz, P., Wüthrich, S., Arijs, E., Delanoye, S., Keyser, J. D., … Wollnik, H. (2007). Rosina – Rosetta Orbiter Spectrometer for Ion and Neutral Analysis. *Space Science Reviews*, *128*(1-4), 745-801. https://doi.org/10.1007/s11214-006-8335-3

Bonard, J.-M., Kind, H., Stöckli, T., & Nilsson, L.-O. (2001). Field emission from carbon nanotubes: The first five years. *Solid-State Electronics*, *45*(6), 893-914. https://doi.org/10.1016/s0038-1101(00)00213-6

Cipriani, F., Leblanc, F., & Berthelier, J. J. (2007). Martian corona : Nonthermal sources of hot heavy species. *Journal of Geophysical Research*, *112*(E7). https://doi.org/10.1029/2006je002818

Dahl, D. A. (2000). Simion for the personal computer in reflection. *International Journal of Mass Spectrometry*, *200*(1-3), 3-25. https://doi.org/10.1016/s1387-3806(00)00305-5

Fu, M., Cui, and J., Wu, X., Wu, Z., & Li, J. (2020). The variations of the Martian exobase altitude. *Earth and Planetary Physics*, *4*(1), 1-7. https://doi.org/10.26464/epp2020010

Green, T. S., & Proca, G. A. (1970). A Parallel Plate Electrostatic Spectrograph. *Review of Scientific Instruments*, *41*(10), 1409-1414. https://doi.org/10.1063/1.1684294

Hong, N. T., Koh, K. H., Lee, S., Minh, P. N., Tam, N. T. T., & Khoi, P. H. (2009). Comparison of field-electron emission from different carbon nanotube array structures. *Journal of Vacuum Science &amp\mathsemicolon Technology B: Microelectronics and Nanometer Structures*, *27*(2), 749. https://doi.org/10.1116/1.3097850

Jakosky, B. M., Brain, D., Chaffin, M., Curry, S., Deighan, J., Grebowsky, J., Halekas, J., Leblanc, F., Lillis, R., Luhmann, J. G., Andersson, L., Andre, N., Andrews, D., Baird, D., Baker, D., Bell, J., Benna, M., Bhattacharyya, D., Bougher, S., … Zurek, R. (2018). Loss of the Martian atmosphere to space : Present-day loss rates determined from MAVEN observations and integrated loss through time. *Icarus*, *315*, 146-157. https://doi.org/10.1016/j.icarus.2018.05.030

Jakosky, B. M., Grebowsky, J. M., Luhmann, J. G., Connerney, J., Eparvier, F., Ergun, R., Halekas, J., Larson, D., Mahaffy, P., McFadden, J., Mitchell, D. L., Schneider, N., Zurek, R., Bougher, S., Brain, D., Ma, Y. J., Mazelle, C., Andersson, L., Andrews, D., … Yelle, R. (2015). MAVEN observations of the response of Mars to an interplanetary coronal mass ejection. *Science*, *350*(6261). https://doi.org/10.1126/science.aad0210

Leblanc, F., Benna, M., Chaufray, J. Y., Martinez, A., Lillis, R., Curry, S., Elrod, M. K., Mahaffy, P., Modolo, R., Luhmann, J. G., & Jakosky, B. (2019). First In Situ Evidence of Mars Nonthermal Exosphere. *Geophysical Research Letters*, *46*(8), 4144-4150. https://doi.org/10.1029/2019gl082192

Lillis, R. J., Brain, D. A., Bougher, S. W., Leblanc, F., Luhmann, J. G., Jakosky, B. M., Modolo, R., Fox, J., Deighan, J., Fang, X., Wang, Y. C., Lee, Y., Dong, C., Ma, Y., Cravens, T., Andersson, L., Curry, S. M., Schneider, N., Combi, M., … Lin, R. P. (2015). Characterizing Atmospheric Escape from Mars Today and Through Time, with MAVEN. *Space Science Reviews*, *195*(1-4), 357-422. https://doi.org/10.1007/s11214-015-0165-8

Luhmann, J. G., & Kozyra, J. U. (1991). Dayside pickup oxygen ion precipitation at Venus and Mars: Spatial distributions, energy deposition and consequences. *Journal of Geophysical Research*, *96*(A4), 5457. https://doi.org/10.1029/90ja01753

Mahaffy, P. R., Benna, M., Elrod, M., Yelle, R. V., Bougher, S. W., Stone, S. W., & Jakosky, B. M. (2015). Structure and composition of the neutral upper atmosphere of Mars from the MAVEN NGIMS investigation. *Geophysical Research Letters*, *42*(21), 8951-8957. https://doi.org/10.1002/2015gl065329

McElroy, M. B., & Donahue, T. M. (1972). Stability of the Martian Atmosphere. *Science*, *177*(4053), 986-988. https://doi.org/10.1126/science.177.4053.986

Ohkawa, Y., Kawamoto, S., Okumura, T., Iki, K., Okamoto, H., Inoue, K., Uchiyama, T., & Tsujita, D. (2020). Review of KITE – Electrodynamic tether experiment on the H-II Transfer Vehicle. *Acta Astronautica*, *177*, 750-758. https://doi.org/10.1016/j.actaastro.2020.03.014

Rispoli, R., Angelis, E. D., Colasanti, L., Vertolli, N., Orsini, S., Scheer, J. A., Mura, A., Milillo, A., Wurz, P., Selci, S., Lellis, A. M. D., Leoni, R., D'Alessandro, M., Mattioli, F., & Cibella, S. (2012). ELENA MCP detector : Absolute detection efficiency for low-energy neutral atoms. In R. Navarro, C. R. Cunningham, & E. Prieto (Éds.), *SPIE Proceedings*. SPIE. https://doi.org/10.1117/12.926185

Schläppi, B., Altwegg, K., Balsiger, H., Hässig, M., Jäckel, A., Wurz, P., Fiethe, B., Rubin, M., Fuselier, S. A., Berthelier, J. J., Keyser, J. D., Rème, H., & Mall, U. (2010). Influence of spacecraft outgassing on the exploration of tenuous atmospheres with in situ mass spectrometry. *Journal of Geophysical Research: Space Physics*, *115*(A12). https://doi.org/10.1029/2010ja015734

Steichen, V., Leblanc F., Berthelier J.J., Hong, N.T., Lee, S and Gilbert, P. (2023). A carbon nanotube based ion source for planetary space mass spectrometry. Submitted in Review of Scientific instruments.

5.2. Laboratory model of INEA

Based on the numerical model and experiments described in the previous sections, a complete mechanical prototype has been assembled to validate INEA's operating principle in the laboratory. A cross sectional view in the plane of symmetry of the instrument is displayed in Fig. 3.71a while a photograph of the instrument assembled is shown in Fig. 3.72b.

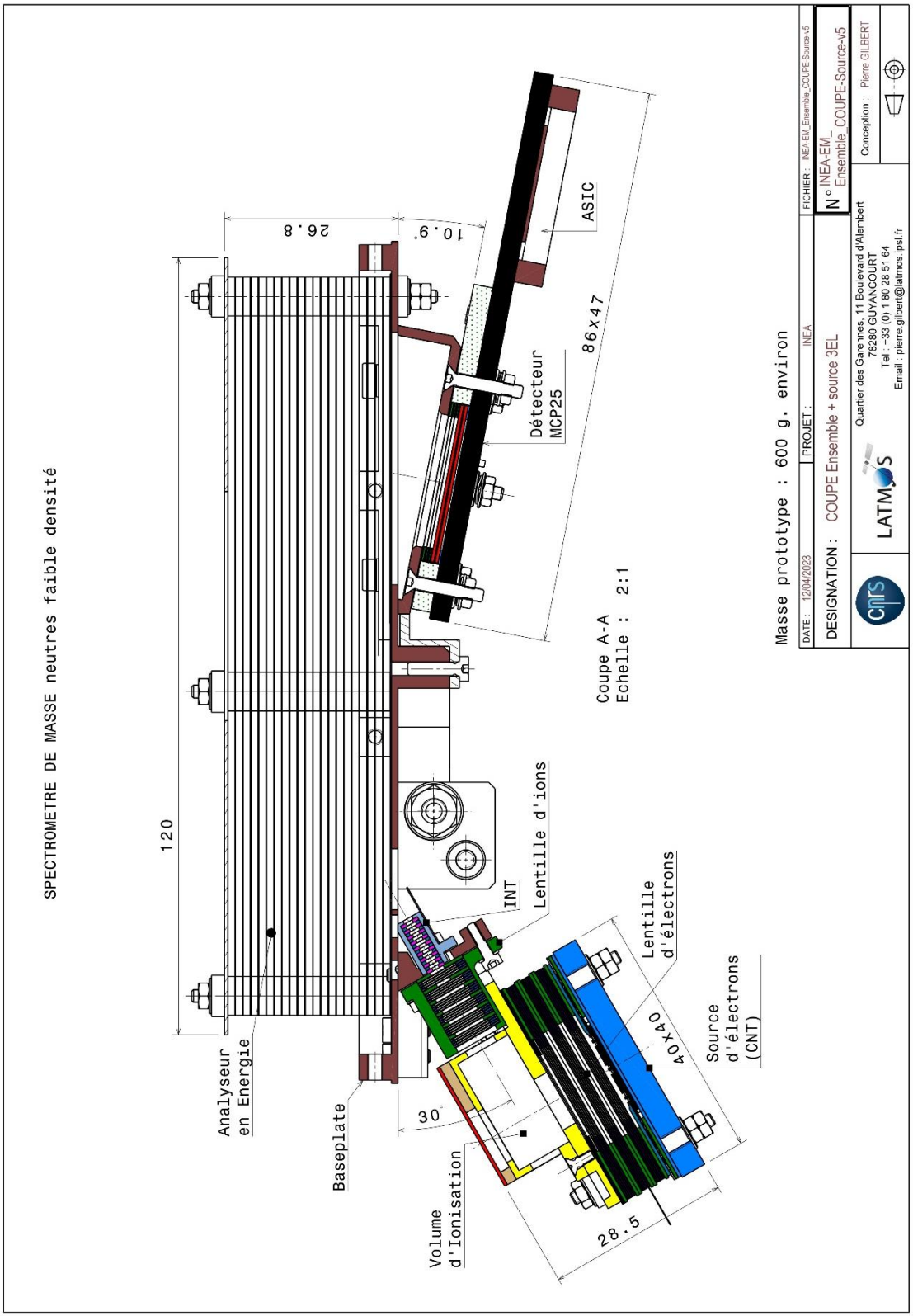

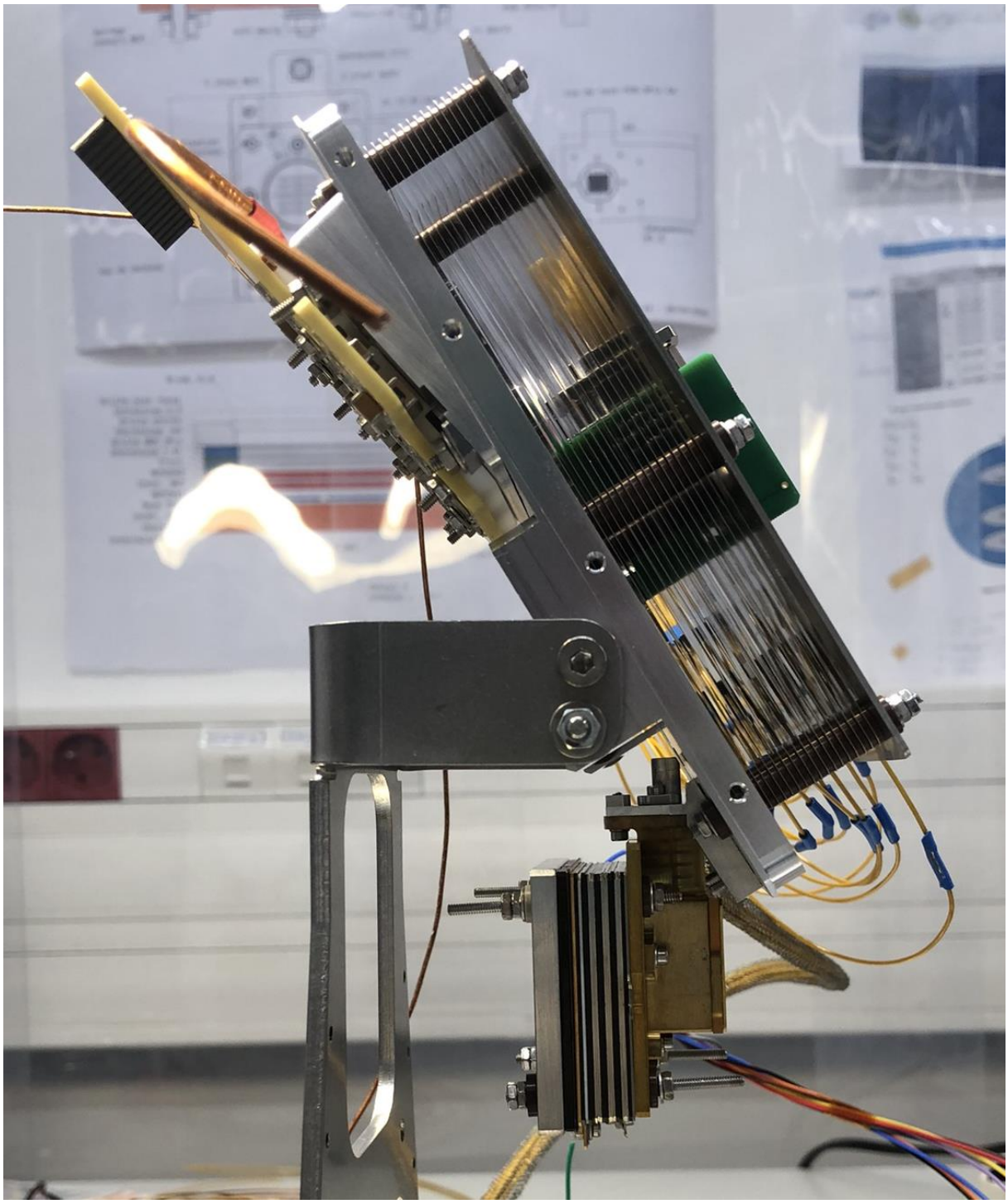

***Figure 3.72**: (a) cross sectional view cut of INEA final assembly. (b) Photograph of INEA mounted on its stand.*

To date, experiments on the prototype are currently being carried out. However, no usable data are yet available. Experiments that will be carried until the end of the PhD are expected to bring data to present at the defence.

SUMMARY

This chapter starts with an **introduction** summarizing the scientific and technical challenged about measurements of low energy neutral atoms in very low dense environment. To answer these questions, INEA relies on a new type of concept which associates a carbon nanotube cold cathode electron emitter and an energy spectrograph able to instantaneously measure the energy distribution of the neutral particles.

In the 2nd section, we started by detailing the theoretical operation of the parallel plate energy analyser which is the core of INEA. From this theoretical model, a laboratory mechanical version of the energy analyser has been built and assembled, including the associated electronics that control the energy analyser's electrode voltages. The dimension of the analyser was obtained using the theoretical equations of Green and Proca (1970) so that the total dimensions of the analyser stays within reasonable size for space applications.

Afterwards, a numerical model of the analyser has been developed including the electrostatic defects due to the mechanical constraints. The model could estimate the 'ideal' performances of our prototype and the effect of the angular distribution in the different planes.

The 3rd section, detailed the operation of INEA's detector and the issues to overcome associated to the efficiency of the MCP assembly when dealing with low energy ions. To obtain a sufficient detection efficiency, the ions must be accelerated before they impact the front face of the MCP. Thus, a negative potential of the order of few hundreds of volts must be applied. Such potential ultimately disturbs the supposed field free region between the energy analyser base plate and the detector entrance leading to a decreased focusing power on the focal plane.

A numerical model of the EA and detector subassembly has been developed in order to optimize the detector's grid geometry. The goal is to reduce the inevitable leaking electric potential in the field free region. The model suggests that using a relatively thick grid (~50% transparency) must be placed at the detector entrance, the electric potential at the MCP entrance will be sufficiently shielded. Furthermore, the small-scale structure of the electric field inside the detector also disturbs the particle trajectories and widen the impact distribution.

Following the numerical modelling, a detector prototype has been built. To detect the particles impact position, a pixelized collector is used with its associated electronics. In the nominal operation of the detector, the pixels' output are linked to an ASIC which was initially designed by the Laboratoire de Physique des Plasmas (LPP). The ASIC allows to detect input pulses from each pixel independently and simultaneously. The ASIC then converts the detected pulses into numerical outputs that are finally read using a dedicated DPU.

As the detector with ASIC underwent a long development time, a simpler detector was designed quickly. It only includes a charge sensitive amplifier (CSA) which converts the charge pulse originating from the MCP into readable voltage pulses. The CSA can be plugged at the output of the desired pixel.

In the **4th section**, we started by a set of simulations. The simulation, highlighted the effect of the extracting grid on the electric field and electron emission at the top of the CNT array. The results of these simulation detailed the importance of the grid geometry to obtain a homogenous field emission.

Furthermore, simulations on the ionisation volume and ion lens assembly showed that during laboratory operations of INEA, it is possible to extract ions from the volume thanks to their thermal velocity and the effect of potential bubble at the vicinity of the exit grid. Thanks, to the previous simulations, a mechanical model of the ion source has been built and tested. A dedicated measurement electronics has been designed and implemented on the experimental setp-up to carry experiments in the best possible conditions. The tests achieved on the ion source allow us to estimate a sensitivity of $1.6 \times 10^{-4}\, count/s/cm^{-3}$. Using SIMION, this value could be interpolated to an in-flight sensitivity of $1.1 \times 10^{-3}\, count/s/cm^{-3}$.

The last section explains the numerical end-to-end model, how it was constructed and the module developed in order to simulate different operations. The numerical model of INEA allows to confirm the targeted performances of INEA: a resolution in energy better than 0.1 eV, a resolution in mass of ~22 associated to a temperature and ram velocity measurement capability with resolutions better than 50K and 20 m/s respectively.

At the same time, INEA's prototype has been assembled and put into its vacuum chamber. First tests where achieved but no usable data has been recorded before the submission of this manuscript.

CONCLUSION

During my thesis I had the opportunity to work on a new generation of energy analysers: The Ion and Neutral Energy Analyser (INEA). This instrument is designed to measure the energy structure and mass distributions of particles in the upper planetary atmospheres of planetary objects of the Solar System. It is an original instrument which goal is to achieve measurements not accessible today with the existing instrumentation of space research. On one hand, INEA should enable in situ measurements in the planetary exospheres, providing crucial information on the surface and atmospheric erosion mechanisms acting in the Solar System. On the other hand, with its ability to measure wind, temperature and mass, the instrument is also suitable for studying thermospheres and ionospheres. Such measurements provide key information about the interplay between the Sun and the atmospheres or surfaces of celestial bodies.

The electrostatic parts of INEA were defined from a numerical model using SIMION®. The innovative concept of this optic consists in the use of an energy analyser capable of instantaneously imaging the energy spectrum of the particles entering the instrument. In addition, a time-of-flight mass analysis is performed between the end of the ion source optics (the ion lens) and the impact on the detector, allowing the mass to be determined simultaneously with its energy. The numerical End-to-End model gives results with a resolution in mass ~22 and in energy better than 0.1 eV as well as a resolution in temperature and velocity better than 50K and 20 m/s respectively.

The development of the ion source based on the concept of electron extraction by field effect on carbon nanotubes has been carried out. The principle of extracting electrons between a carbon nanotube tip and a grid can be used to define an ion source with low power consumption, while avoiding the space charge effect thanks to the large emitting area. The work on the ion source initially focused on numerical simulations, which helped to design a prototype of the source. Following the numerical simulations, the mechanical model of the ion source was fabricated, assembled and tested. The results of the experimental tests have led to the submission of a publication outlining the main features and performance of the ion source. Further progresses on the ion source could be reached by better understanding what controls the angular dispersion of the electrons emitted from the CNT. A better characterisation (by simulation or experiment) of the spatial and angular distribution of the primary electrons at the exit of the electron source assembly could lead to an improved design of the electrostatic lens placed between the electron emitter and the ionisation volume. Such an improvement could maximise the flux of electrons reaching the ionisation volume, with consequences for the ionisation rate, and ultimately improve the sensitivity of the source. Another important improvement of the ion source lies in the design of the ion lens. During this thesis the optimisation of this optic has been put aside and a consistent work of simulation and testing is still to be achieved. Improvements in the ion lens optics could greatly enhance the performance of the ion source, especially its sensitivity.

In addition to the work on the ion source, a design of an imaging detector was carried out. Numerical modelling was used to determine the geometry of the detector so as to minimise the effect of the necessary polarisation of the MCP front face. Moreover, the electronics, consisting of a pixelized detector linked to an ASIC, were developed. This design represents the nominal version of the INEA detector. The advantage of this type of detector lies in its relatively simple electronic design. Since each pixel is independent, the electronics required to register the counts

of the incoming particles do not need to be fast. Other electronic architectures of the detector will be discussed. For example, the use of delay lines and associated electronics rather than a set of pixels is another viable option. Such a technology would allow to simultaneously measure the time of flight and the impact position along the detector axis with the same electronics.

Finally, a complete prototype of INEA, including the ion source, energy analyser, detector and all the associated electronics, has been assembled. This prototype is currently being tested and we hope to have the first experimental results by the end of 2023 or beginning 2024.

Thanks to the work carried out during this thesis, it has been able to propose INEA in a space mission dedicated to multi-point measurements of the Martian thermosphere and ionosphere. The Mars - Magnetosphere Atmosphere Ionosphere and Space Weather Science (M - MATISSE) mission (Fig. A), currently proposed to the European Space Agency in the M7 call for projects, will provide, for the first time, continuous and simultaneous observations of the Martian system. Two orbiters, one mainly in the magnetosphere and the other mainly in the solar wind, will provide simultaneous coverage of the upper and lower ionosphere and of the neutral atmosphere with INEA (Fig. A). Our instrument is proposed in the context of M-MATISSE as a suite of three instruments, including an electron analyser and a solar particle detector, sharing a common DPU. the ESA recently selected the mission for a phase A study up to mid-2026. This is an important milestone in the development of the instrument, as it would significantly increase the maturity of INEA.

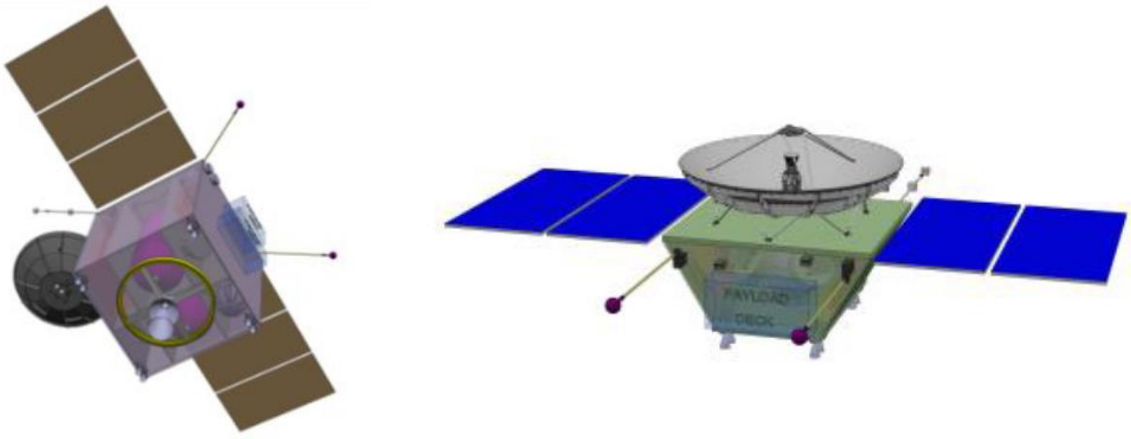

***Figure A**: The Henri fathership and Marguerite daughtership of the M-MATISSE mission.*

In addition to the M-MATISSE mission, progress on the electron emitter has made it possible to propose a satellite potential control system for a Japanese microsatellite, PRELUDE SAT. Shizuako - Ken University and Nihon University are building a 6U CubeSat to characterise disturbances in the ionospheric electric field, potential precursors to earthquakes. Due to the small total area of the spacecraft, the collection of ions from the environment is much less efficient than the collection of electrons during instrument operation. As a result, the spacecraft potential would be driven to large and variable negative values. The solution we have proposed is to ensure the global balance of the spacecraft by emitting an electron current into space to compensate the one collected by the electric field instrument. This device, called the Prelude Sat Electron Emitter (PSEE), relies on the use of carbon nanotube field emission cathode, similar to the INEA ion source. PSEE is an improved version of the prototyped

electron emitter used in this thesis. It consists of a circular CNT array and two grids, which allow electron extraction and potential shielding respectively. At the end of my thesis I had the opportunity to work on the design and first experiments on the system (Fig. B).

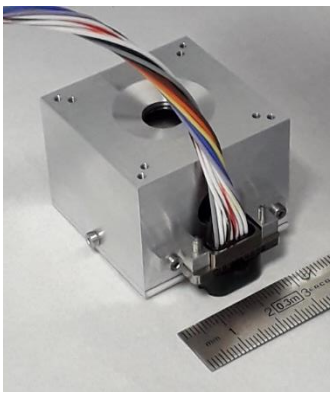

***Figure B**: Engineering model of PSEE*

With the launch of the PRELUDE SAT scheduled for mid-2025, this will be the first opportunity to qualify, in flight, the electron emitter developed at LATMOS. This first operation, under space conditions, will provide subsequent key information about the behaviour of the carbon nanotubes in this environment. Furthermore, PSEE sits as an excellent basis for the future improvements of INEA's ion source.

REFERENCES

Abe, T., Kurihara, J., Iwagami, N., Nozawa, S., Ogawa, Y., Fujii, R., Hayakawa, H., & Oyama, K. (2006). Dynamics and Energetics of the Lower Thermosphere in Aurora (DELTA)—Japanese sounding rocket campaign—. *Earth, Planets and Space*, *58*(9), 1165-1171. https://doi.org/10.1186/BF03352006

Acuna, M. H., Connerney, J. E., Ness, N. F., Lin, R. P., Mitchell, D., Carlson, C. W., McFadden, J., Anderson, K. A., Reme, H., Mazelle, C., Vignes, D., Wasilewski, P., & Cloutier, P. (1999). Global distribution of crustal magnetization discovered by the mars global surveyor MAG/ER experiment. *Science (New York, N.Y.)*, *284*(5415), 790-793. https://doi.org/10.1126/science.284.5415.790

Alken, P., & Maus, S. (2010). Electric fields in the equatorial ionosphere derived from CHAMP satellite magnetic field measurements. *Journal of Atmospheric and Solar-Terrestrial Physics*, *72*(4), 319-326. https://doi.org/10.1016/j.jastp.2009.02.006

Andrews, D. G., Leovy, C. B., & Holton, J. R. (1987). *Middle Atmosphere Dynamics, Volume 40—1st Edition*. https://shop.elsevier.com/books/middle-atmosphere-dynamics/andrews/978-0-12-058575-5

Arevalo Jr, R., Ni, Z., & Danell, R. M. (2020). Mass spectrometry and planetary exploration : A brief review and future projection. *Journal of Mass Spectrometry*, *55*(1), e4454. https://doi.org/10.1002/jms.4454

Baloukidis, D., Sarris, T., Tourgaidis, S., Pirnaris, P., Aikio, A., Virtanen, I., Buchert, S., & Papadakis, K. (2023). *A comparative assessment of the distribution of Joule heating in altitude as estimated in TIE-GCM and EISCAT over one solar cycle*. https://doi.org/10.22541/essoar.168056818.80893950/v1

Balsiger, H., Altwegg, K., Bochsler, P., Eberhardt, P., Fischer, J., Graf, S., Jäckel, A., Kopp, E., Langer, U., Mildner, M., Müller, J., Riesen, T., Rubin, M., Scherer, S., Wurz, P., Wüthrich, S., Arijs, E., Delanoye, S., Keyser, J. D., … Wollnik, H. (2007). Rosina – Rosetta Orbiter Spectrometer for Ion and Neutral Analysis. *Space Science Reviews*, *128*(1-4), 745-801. https://doi.org/10.1007/s11214-006-8335-3

Barabash, S., Bhardwaj, A., Wieser, M., Sridharan, R., Kurian, T., Varier, S., Vijayakumar, E., Abhirami, V., Raghavendra, K. V., Mohankumar, S. V., Dhanya, M. B., Thampi, S., Kazushi, A., Andersson, H., Yoshifumi, F., Holmström, M., Lundin, R., Svensson, J., Karlsson, S., … Wurz, P. (2009). Investigation of the solar wind–Moon interaction onboard Chandrayaan-1 mission with the SARA experiment. *Current Science*, *96*(4), 526-532.

Becker, E. (2004). Direct heating rates associated with gravity wave saturation. *Journal of Atmospheric and Solar-Terrestrial Physics*, *66*(6), 683-696. https://doi.org/10.1016/j.jastp.2004.01.019

Benkhoff, J., van Casteren, J., Hayakawa, H., Fujimoto, M., Laakso, H., Novara, M., Ferri, P., Middleton, H. R., & Ziethe, R. (2010). BepiColombo—Comprehensive exploration of

Mercury : Mission overview and science goals. *Planetary and Space Science*, *58*(1), 2-20. https://doi.org/10.1016/j.pss.2009.09.020

Benna, M., Mahaffy, P. R., Grebowsky, J. M., Fox, J. L., Yelle, R. V., & Jakosky, B. M. (2015). First measurements of composition and dynamics of the Martian ionosphere by MAVEN's Neutral Gas and Ion Mass Spectrometer. *Geophysical Research Letters*, *42*(21), 8958-8965. https://doi.org/10.1002/2015GL066146

Berthelier, J. J., Godefroy, M., Leblanc, F., Malingre, M., Menvielle, M., Lagoutte, D., Brochot, J. Y., Colin, F., Elie, F., Legendre, C., Zamora, P., Benoist, D., Chapuis, Y., Artru, J., & Pfaff, R. (2006). ICE, the electric field experiment on DEMETER. *Planetary and Space Science*, *54*(5), 456-471. https://doi.org/10.1016/j.pss.2005.10.016

Berthelier, J. J., Godefroy, M., Leblanc, F., Seran, E., Peschard, D., Gilbert, P., & Artru, J. (2006). IAP, the thermal plasma analyzer on DEMETER. *Planetary and Space Science*, *54*(5), 487-501. https://doi.org/10.1016/j.pss.2005.10.018

Berthelier, J.-J., Illiano, J. M., Hodges, R. R., Covinhes, J., Godefroy, M., Gogly, G., Guillou, J., Le Goff, F., Leblanc, F., Racic, Z., Rouchette, P., Krankowsky, D., Dorflinger, D., Vaisberg, O., Smimov, V., & Kolesova, N. (1998). The Dymio Ion Mass Spectrometer of the Mars 96 Mission. In *Measurement Techniques in Space Plasmas : Particles* (p. 215-220). American Geophysical Union (AGU). https://doi.org/10.1029/GM102p0215

Bonard, J.-M., Kind, H., Stöckli, T., & Nilsson, L.-O. (2001). Field emission from carbon nanotubes : The first five years. *Solid-State Electronics*, *45*(6), 893-914. https://doi.org/10.1016/s0038-1101(00)00213-6

Brain, D. A., McFadden, J. P., Halekas, J. S., Connerney, J. E. P., Bougher, S. W., Curry, S., Dong, C. F., Dong, Y., Eparvier, F., Fang, X., Fortier, K., Hara, T., Harada, Y., Jakosky, B. M., Lillis, R. J., Livi, R., Luhmann, J. G., Ma, Y., Modolo, R., & Seki, K. (2015). The spatial distribution of planetary ion fluxes near Mars observed by MAVEN. *Geophysical Research Letters*, *42*(21), 9142-9148. https://doi.org/10.1002/2015GL065293

Briois, C., Thissen, R., Thirkell, L., Aradj, K., Bouabdellah, A., Boukrara, A., Carrasco, N., Chalumeau, G., Chapelon, O., Colin, F., Coll, P., Cottin, H., Engrand, C., Grand, N., Lebreton, J.-P., Orthous-Daunay, F.-R., Pennanech, C., Szopa, C., Vuitton, V., … Makarov, A. (2016). Orbitrap mass analyser for in situ characterisation of planetary environments : Performance evaluation of a laboratory prototype. *Planetary and Space Science*, *131*, 33-45. https://doi.org/10.1016/j.pss.2016.06.012

Brockwell, T. G., Meech, K. J., Pickens, K., Waite, J. H., Miller, G., Roberts, J., Lunine, J. I., & Wilson, P. (2016). The mass spectrometer for planetary exploration (MASPEX). *2016 IEEE Aerospace Conference*, 1-17. https://doi.org/10.1109/AERO.2016.7500777

Carr, M. H. (2007). The surface of Mars. *Meteoritics &amp\mathsemicolon Planetary Science*, *42*(12), 2181-2182. https://doi.org/10.1111/j.1945-5100.2007.tb01018.x

Chaffin, M. S., Chaufray, J. Y., Deighan, J., Schneider, N. M., McClintock, W. E., Stewart, A. I. F., Thiemann, E., Clarke, J. T., Holsclaw, G. M., Jain, S. K., Crismani, M. M. J., Stiepen,

A., Montmessin, F., Eparvier, F. G., Chamberlain, P. C., & Jakosky, B. M. (2015). Three-dimensional structure in the Mars H corona revealed by IUVS on MAVEN. *Geophysical Research Letters*, *42*(21), 9001-9008. https://doi.org/10.1002/2015GL065287

Chaffin, M. S., Deighan, J., Jain, S., Holsclaw, G., AlMazmi, H., Chirakkil, K., Correira, J., England, S., Evans, J. S., Fillingim, M., Lillis, R., Lootah, F., Raghuram, S., Eparvier, F., Thiemann, E., Curry, S., & AlMatroushi, H. (2022). Combined Analysis of Hydrogen and Oxygen 102.6 nm Emission at Mars. *Geophysical Research Letters*, *49*(16), e2022GL099851. https://doi.org/10.1029/2022GL099851

Chamberlain, J. W. (1963). Planetary coronae and atmospheric evaporation. *Planetary and Space Science*, *11*(8), 901-960. https://doi.org/10.1016/0032-0633(63)90122-3

Chao, C. K., Su, S.-Y., & Yeh, H. C. (2003). Grid effects on the derived ion temperature and ram velocity from the simulated results of the retarding potential analyzer data. *Advances in Space Research*, *32*(11), 2361-2366. https://doi.org/10.1016/S0273-1177(03)90566-7

Chaufray, J. Y., Modolo, R., Leblanc, F., Chanteur, G., Johnson, R. E., & Luhmann, J. G. (2007). Mars solar wind interaction : Formation of the Martian corona and atmospheric loss to space. *Journal of Geophysical Research: Planets*, *112*(E9). https://doi.org/10.1029/2007JE002915

Chen, Y., & Chu, X. (2023). Lidar Observations of Predawn Thermosphere-Ionosphere Na (TINa) Layers Over Boulder (40.13°N, 105.24°W) : Annual Phase Variations and Correlation With Sunrise and Tidal Winds. *Geophysical Research Letters*, *50*(18), e2023GL105626. https://doi.org/10.1029/2023GL105626

Ching, B. K., & Rugge, H. R. (1975). Atmospheric density at 169 km from accelerometer measurements and orbital decay of a low altitude satellite. *Planetary and Space Science*, *23*, 1301-1308. https://doi.org/10.1016/0032-0633(75)90153-1

Cipriani, F., Leblanc, F., & Berthelier, J. J. (2007). Martian corona : Nonthermal sources of hot heavy species. *Journal of Geophysical Research*, *112*(E7). https://doi.org/10.1029/2006je002818

Codrescu, M. V., Fuller-Rowell, T. J., & Foster, J. C. (1995). On the importance of E-field variability for Joule heating in the high-latitude thermosphere. *Geophysical Research Letters*, *22*(17), 2393-2396. https://doi.org/10.1029/95GL01909

Cohen, I. J., Anderson, B. J., Bonnell, J. W., Lysak, R. L., Lessard, M. R., Michell, R. G., & Varney, R. H. (2020). Rocket Investigation of Current Closure in the Ionosphere (RICCI) : A novel application of CubeSats from a sounding rocket platform. *Advances in Space Research*, *66*(1), 98-106. https://doi.org/10.1016/j.asr.2019.04.036

Collinson, G., Halekas, J., Grebowsky, J., Connerney, J., Mitchell, D., Espley, J., DiBraccio, G., Mazelle, C., Sauvaud, J.-A., Fedorov, A., & Jakosky, B. (2015). A hot flow anomaly at Mars. *Geophysical Research Letters*, *42*(21), 9121-9127. https://doi.org/10.1002/2015GL065079

Cravens, T. E., Rahmati, A., Fox, J. L., Lillis, R., Bougher, S., Luhmann, J., Sakai, S., Deighan, J., Lee, Y., Combi, M., & Jakosky, B. (2017). Hot oxygen escape from Mars : Simple scaling with solar EUV irradiance. *Journal of Geophysical Research: Space Physics*, *122*(1), 1102-1116. https://doi.org/10.1002/2016JA023461

Dahl, D. A. (2000). Simion for the personal computer in reflection. *International Journal of Mass Spectrometry*, *200*(1-3), 3-25. https://doi.org/10.1016/s1387-3806(00)00305-5

Davidson, R. L., Earle, G. D., Klenzing, J. H., & Heelis, R. A. (2010). A numerical study of geometry dependent errors in velocity, temperature, and density measurements from single grid planar retarding potential analyzers. *Physics of Plasmas*, *17*(8), 082901. https://doi.org/10.1063/1.3457931

Delcourt, D., Saito, Y., Leblanc, F., Verdeil, C., Yokota, S., Fraenz, M., Fischer, H., Fiethe, B., Katra, B., Fontaine, D., Illiano, J.-M., Berthelier, J.-J., Krupp, N., Buhrke, U., Bubenhagen, F., & Michalik, H. (2016). The Mass Spectrum Analyzer (MSA) on board the BepiColombo MMO. *Journal of Geophysical Research: Space Physics*, *121*(7), 6749-6761. https://doi.org/10.1002/2016JA022380

Denisov, E., Damoc, E., Lange, O., & Makarov, A. (2012). Orbitrap mass spectrometry with resolving powers above 1,000,000. *International Journal of Mass Spectrometry*, *325-327*, 80-85. https://doi.org/10.1016/j.ijms.2012.06.009

Dong, Y., Fang, X., Brain, D. A., McFadden, J. P., Halekas, J. S., Connerney, J. E., Curry, S. M., Harada, Y., Luhmann, J. G., & Jakosky, B. M. (2015). Strong plume fluxes at Mars observed by MAVEN : An important planetary ion escape channel. *Geophysical Research Letters*, *42*(21), 8942-8950. https://doi.org/10.1002/2015GL065346

Dubinin, E., Fraenz, M., Pätzold, M., Tellmann, S., Modolo, R., DiBraccio, G., McFadden, J., & Espley, J. (2023). Magnetic Fields and Plasma Motions in a Hybrid Martian Magnetosphere. *Journal of Geophysical Research: Space Physics*, *128*(1), e2022JA030575. https://doi.org/10.1029/2022JA030575

Dubinin, E., Modolo, R., Fraenz, M., Woch, J., Duru, F., Akalin, F., Gurnett, D., Lundin, R., Barabash, S., Plaut, J. J., & Picardi, G. (2008). Structure and dynamics of the solar wind/ionosphere interface on Mars : MEX-ASPERA-3 and MEX-MARSIS observations. *Geophysical Research Letters*, *35*(11). https://doi.org/10.1029/2008GL033730

Earle, G. D., Davidson, R. L., Heelis, R. A., Coley, W. R., Weimer, D. R., Makela, J. J., Fisher, D. J., Gerrard, A. J., & Meriwether, J. (2013). Low latitude thermospheric responses to magnetic storms. *Journal of Geophysical Research: Space Physics*, *118*(6), 3866-3876. https://doi.org/10.1002/jgra.50212

Earle, G. D., Klenzing, J. H., Roddy, P. A., Macaulay, W. A., Perdue, M. D., & Patrick, E. L. (2007). A new satellite-borne neutral wind instrument for thermospheric diagnostics. *Review of Scientific Instruments*, *78*(11), 114501. https://doi.org/10.1063/1.2813343

Edwards, C. S., & Ehlmann, B. L. (2015). Carbon sequestration on Mars. *Geology*, *43*(10), 863-866. https://doi.org/10.1130/G36983.1

England, S. L., Englert, C. R., Harding, B. J., Triplett, C. C., Marr, K., Harlander, J. M., Swenson, G. R., Maute, A., & Immel, T. J. (2022). Vertical Shears of Horizontal Winds in the Lower Thermosphere Observed by ICON. *Geophysical Research Letters*, *49*(11), e2022GL098337. https://doi.org/10.1029/2022GL098337

Ergun, R. E., Andersson, L. A., Fowler, C. M., Woodson, A. K., Weber, T. D., Delory, G. T., Andrews, D. J., Eriksson, A. I., McEnulty, T., Morooka, M. W., Stewart, A. I. F., Mahaffy, P. r., & Jakosky, B. M. (2016). Enhanced O2+ loss at Mars due to an ambipolar electric field from electron heating. *Journal of Geophysical Research: Space Physics*, *121*(5), 4668-4678. https://doi.org/10.1002/2016JA022349

Fejer, B. G., Tracy, B. D., & Pfaff, R. F. (2013). Equatorial zonal plasma drifts measured by the C/NOFS satellite during the 2008–2011 solar minimum. *Journal of Geophysical Research: Space Physics*, *118*(6), 3891-3897. https://doi.org/10.1002/jgra.50382

Filippov, S. V., Popov, E. O., & Kolosko, A. G. (2021). Numerical simulations of field emission characteristics of open CNT. *Ultramicroscopy*, *230*, 113362. https://doi.org/10.1016/j.ultramic.2021.113362

Forme, F., Fontaine, D., & Persson, M. a. L. (1998). Large perpendicular velocity fluctuations observed in the topside ionosphere. *Journal of Geophysical Research: Space Physics*, *103*(A3), 4001-4009. https://doi.org/10.1029/97JA01990

Fowler, R. H., & Nordheim, L. (1997). Electron emission in intense electric fields. *Proceedings of the Royal Society of London. Series A, Containing Papers of a Mathematical and Physical Character*, *119*(781), 173-181. https://doi.org/10.1098/rspa.1928.0091

Fox, J. L., & Hać, A. (2010). Isotope fractionation in the photochemical escape of O from Mars. *Icarus*, *208*(1), 176-191. https://doi.org/10.1016/j.icarus.2010.01.019

Fraser, G. W., Pearson, J. F., & Lees, J. E. (1987). Dark noise in microchannel plate X-ray detectors. *Nuclear Instruments and Methods in Physics Research Section A: Accelerators, Spectrometers, Detectors and Associated Equipment*, *254*(2), 447-462. https://doi.org/10.1016/0168-9002(87)90699-1

Fritts, D. C., & Alexander, M. J. (2003). Gravity wave dynamics and effects in the middle atmosphere. *Reviews of Geophysics*, *41*(1). https://doi.org/10.1029/2001RG000106

Futaana, Y., Barabash, S., Wieser, M., Holmström, M., Lue, C., Wurz, P., Schaufelberger, A., Bhardwaj, A., Dhanya, M. B., & Asamura, K. (2012). Empirical energy spectra of neutralized solar wind protons from the lunar regolith. *Journal of Geophysical Research: Planets*, *117*(E5). https://doi.org/10.1029/2011JE004019

Gallois, A. (2018) Internship report.

Green, T. S., & Proca, G. A. (1970). A Parallel Plate Electrostatic Spectrograph. *Review of Scientific Instruments*, *41*(10), 1409-1414. https://doi.org/10.1063/1.1684294

Günzkofer, F., Pokhotelov, D., Stober, G., Liu, H., Liu, H.-L., Mitchell, N. J., Tjulin, A., & Borries, C. (2022). Determining the Origin of Tidal Oscillations in the Ionospheric Transition Region With EISCAT Radar and Global Simulation Data. *Journal of Geophysical Research: Space Physics*, *127*(10), e2022JA030861. https://doi.org/10.1029/2022JA030861

Hagan, M., Forbes, J., & Richmond, A. (2003). ATMOSPHERIC TIDES. In J. R. Holton (Éd.), *Encyclopedia of Atmospheric Sciences* (p. 159-165). Academic Press. https://doi.org/10.1016/B0-12-227090-8/00409-7

Halekas, J. S., Taylor, E. R., Dalton, G., Johnson, G., Curtis, D. W., McFadden, J. P., Mitchell, D. L., Lin, R. P., & Jakosky, B. M. (2015). The Solar Wind Ion Analyzer for MAVEN. *Space Science Reviews*, *195*(1), 125-151. https://doi.org/10.1007/s11214-013-0029-z

Hysell, D. L., & Kudeki, E. (2004). Collisional shear instability in the equatorial F region ionosphere. *Journal of Geophysical Research: Space Physics*, *109*(A11). https://doi.org/10.1029/2004JA010636

Izquierdo-Reyes, J., Bigelow, Z., Lubinsky, N. K., & Velásquez-García, L. F. (2022). Compact retarding potential analyzers enabled by glass-ceramic vat polymerization for CubeSat and laboratory plasma diagnostics. *Additive Manufacturing*, *58*, 103034. https://doi.org/10.1016/j.addma.2022.103034

Jakosky, B. M., Brain, D., Chaffin, M., Curry, S., Deighan, J., Grebowsky, J., Halekas, J., Leblanc, F., Lillis, R., Luhmann, J. G., Andersson, L., Andre, N., Andrews, D., Baird, D., Baker, D., Bell, J., Benna, M., Bhattacharyya, D., Bougher, S., … Zurek, R. (2018). Loss of the Martian atmosphere to space : Present-day loss rates determined from MAVEN observations and integrated loss through time. *Icarus*, *315*, 146-157. https://doi.org/10.1016/j.icarus.2018.05.030

Jakosky, B. M., Grebowsky, J. M., Luhmann, J. G., Connerney, J., Eparvier, F., Ergun, R., Halekas, J., Larson, D., Mahaffy, P., McFadden, J., Mitchell, D. L., Schneider, N., Zurek, R., Bougher, S., Brain, D., Ma, Y. J., Mazelle, C., Andersson, L., Andrews, D., … Yelle, R. (2015). MAVEN observations of the response of Mars to an interplanetary coronal mass ejection. *Science*, *350*(6261). https://doi.org/10.1126/science.aad0210

Jakosky, B. M., & Jones, J. H. (1997). The history of Martian volatiles. *Reviews of Geophysics*, *35*(1), 1-16. https://doi.org/10.1029/96RG02903

Jakosky, B. M., Slipski, M., Benna, M., Mahaffy, P., Elrod, M., Yelle, R., Stone, S., & Alsaeed, N. (2017). Mars' atmospheric history derived from upper-atmosphere measurements of 38Ar/36Ar. *Science*, *355*(6332), 1408-1410. https://doi.org/10.1126/science.aai7721

Jakosky, B., Pepin, R., Johnson, R., & Fox, J. (1994). Mars Atmospheric Loss and Isotopic Fractionation by Solar-Wind-Induced Sputtering and Photochemical Escape. *Icarus*, *111*(2), 271-288. https://doi.org/10.1006/icar.1994.1145

Johnson, R. E. (1990). *Energetic Charged-Particle Interactions with Atmospheres and Surfaces*. Springer. https://doi.org/10.1007/978-3-642-48375-2

Johnson, R. E. (1994). Plasma-induced sputtering of an atmosphere. *Space Science Reviews*, *69*(3), 215-253. https://doi.org/10.1007/BF02101697

Yoichi Kazama, Stas Barabash, Martin Wieser, Kazushi Asamura, Peter Wurz (2007). Development of an LENA instrument for planetary missions by numerical simulations, Planetary and Space Science, Volume 55, Issue 11, Pages 1518-1529, ISSN 0032-0633, https://doi.org/10.1016/j.pss.2006.11.027.

Kelley, M. C. (1989). Chapter 4—Equatorial Plasma Instabilities. In M. C. Kelley (Éd.), *The Earth's Ionosphere* (p. 113-185). Academic Press. https://doi.org/10.1016/B978-0-12-404013-7.50009-5

Klenzing, J. H., Earle, G. D., & Heelis, R. A. (2008). Errors in ram velocity and temperature measurements inferred from satellite-borne retarding potential analyzers. *Physics of Plasmas*, *15*(6), 062905. https://doi.org/10.1063/1.2936270

Klenzing, J. H., Earle, G. D., Heelis, R. A., & Coley, W. R. (2009). A statistical analysis of systematic errors in temperature and ram velocity estimates from satellite-borne retarding potential analyzers. *Physics of Plasmas*, *16*(5), 052901. https://doi.org/10.1063/1.3125311

Langlais, B., Thébault, E., Houliez, A., Purucker, M. E., & Lillis, R. J. (2019). A New Model of the Crustal Magnetic Field of Mars Using MGS and MAVEN. *Journal of Geophysical Research: Planets*, *124*(6), 1542-1569. https://doi.org/10.1029/2018JE005854

Leblanc, F., Benna, M., Chaufray, J. Y., Martinez, A., Lillis, R., Curry, S., Elrod, M. K., Mahaffy, P., Modolo, R., Luhmann, J. G., & Jakosky, B. (2019). First In Situ Evidence of Mars Nonthermal Exosphere. *Geophysical Research Letters*, *46*(8), 4144-4150. https://doi.org/10.1029/2019gl082192

Leblanc, F., Chaufray, J. Y., Modolo, R., Leclercq, L., Curry, S., Luhmann, J., Lillis, R., Hara, T., McFadden, J., Halekas, J., Schneider, N., Deighan, J., Mahaffy, P. R., Benna, M., Johnson, R. E., Gonzalez-Galindo, F., Forget, F., Lopez-Valverde, M. A., Eparvier, F. G., & Jakosky, B. (2017). On the Origins of Mars' Exospheric Nonthermal Oxygen Component as Observed by MAVEN and Modeled by HELIOSARES. *Journal of Geophysical Research: Planets*, *122*(12), 2401-2428. https://doi.org/10.1002/2017JE005336

Leblanc, F., Martinez, A., Chaufray, J. Y., Modolo, R., Hara, T., Luhmann, J., Lillis, R., Curry, S., McFadden, J., Halekas, J., & Jakosky, B. (2018). On Mars's Atmospheric Sputtering After MAVEN's First Martian Year of Measurements. *Geophysical Research Letters*, *45*(10), 4685-4691. https://doi.org/10.1002/2018gl077199

Leblanc, F., Modolo, R., Curry, S., Luhmann, J., Lillis, R., Chaufray, J.-Y., Hara, T., Mcfadden, J., Halekas, J., Eparvier, F., Larson, D., Connerney, J., & Jakosky, B. (2015). Mars heavy ion precipitating flux as measured by Mars Atmosphere and Volatile EvolutioN. *Geophysical Research Letters*, *42*(21), 9135. https://doi.org/10.1002/2015GL066170

Lee, C. O., Hara, T., Halekas, J. S., Thiemann, E., Chamberlin, P., Eparvier, F., Lillis, R. J., Larson, D. E., Dunn, P. A., Espley, J. R., Gruesbeck, J., Curry, S. M., Luhmann, J. G., & Jakosky, B. M. (2017). MAVEN observations of the solar cycle 24 space weather conditions at

Mars. *Journal of Geophysical Research: Space Physics*, *122*(3), 2768-2794. https://doi.org/10.1002/2016JA023495

Lillis, R. J., Brain, D. A., Bougher, S. W., Leblanc, F., Luhmann, J. G., Jakosky, B. M., Modolo, R., Fox, J., Deighan, J., Fang, X., Wang, Y. C., Lee, Y., Dong, C., Ma, Y., Cravens, T., Andersson, L., Curry, S. M., Schneider, N., Combi, M., … Lin, R. P. (2015). Characterizing Atmospheric Escape from Mars Today and Through Time, with MAVEN. *Space Science Reviews*, *195*(1-4), 357-422. https://doi.org/10.1007/s11214-015-0165-8

Lillis, R. J., Deighan, J., Fox, J. L., Bougher, S. W., Lee, Y., Combi, M. R., Cravens, T. E., Rahmati, A., Mahaffy, P. R., Benna, M., Elrod, M. K., McFadden, J. P., Ergun, Robert. E., Andersson, L., Fowler, C. M., Jakosky, B. M., Thiemann, E., Eparvier, F., Halekas, J. S., … Chaufray, J.-Y. (2017). Photochemical escape of oxygen from Mars : First results from MAVEN in situ data. *Journal of Geophysical Research: Space Physics*, *122*(3), 3815-3836. https://doi.org/10.1002/2016JA023525

Liu, H.-L. (2007). On the large wind shear and fast meridional transport above the mesopause. *Geophysical Research Letters*, *34*(8). https://doi.org/10.1029/2006GL028789

Lu, G. (2016). Energetic and Dynamic Coupling of the Magnetosphere-Ionosphere-Thermosphere System. In *Magnetosphere-Ionosphere Coupling in the Solar System* (p. 61-77). American Geophysical Union (AGU). https://doi.org/10.1002/9781119066880.ch5

Lu, G., Richmond, A. D., & Emery, B. A. (1995). Magnetosphere-ionosphere-thermosphere coupling : Effect of neutral winds on energy transfer and field-aligned current. *Journal of Geophysical Research*, *100*(A10). https://doi.org/10.1029/95JA00766

Luhmann, J. G., Johnson, R. E., & Zhang, M. H. G. (1992). Evolutionary impact of sputtering of the Martian atmosphere by O+ pickup ions. *Geophysical Research Letters*, *19*(21), 2151-2154. https://doi.org/10.1029/92GL02485

Luhmann, J. G., & Kozyra, J. U. (1991). Dayside pickup oxygen ion precipitation at Venus and Mars : Spatial distributions, energy deposition and consequences. *Journal of Geophysical Research*, *96*(A4), 5457. https://doi.org/10.1029/90ja01753

Ma, Y., Russell, C. T., Toth, G., Chen, Y., Nagy, A. F., Harada, Y., McFadden, J., Halekas, J. S., Lillis, R., Connerney, J. E. P., Espley, J., DiBraccio, G. A., Markidis, S., Peng, I. B., Fang, X., & Jakosky, B. M. (2018). Reconnection in the Martian Magnetotail : Hall-MHD With Embedded Particle-in-Cell Simulations. *Journal of Geophysical Research: Space Physics*, *123*(5), 3742-3763. https://doi.org/10.1029/2017JA024729

Mahaffy, P. R., Benna, M., Elrod, M., Yelle, R. V., Bougher, S. W., Stone, S. W., & Jakosky, B. M. (2015). Structure and composition of the neutral upper atmosphere of Mars from the MAVEN NGIMS investigation. *Geophysical Research Letters*, *42*(21), 8951-8957. https://doi.org/10.1002/2015gl065329

Mahaffy, P. R., Benna, M., King, T., Harpold, D. N., Arvey, R., Barciniak, M., Bendt, M., Carrigan, D., Errigo, T., Holmes, V., Johnson, C. S., Kellogg, J., Kimvilakani, P., Lefavor, M., Hengemihle, J., Jaeger, F., Lyness, E., Maurer, J., Melak, A., … Nolan, J. T. (2014). The

Neutral Gas and Ion Mass Spectrometer on the Mars Atmosphere and Volatile Evolution Mission. *Space Science Reviews*, *195*(1-4), 49-73. https://doi.org/10.1007/s11214-014-0091-1

Mahaffy, P. R., Richard Hodges, R., Benna, M., King, T., Arvey, R., Barciniak, M., Bendt, M., Carigan, D., Errigo, T., Harpold, D. N., Holmes, V., Johnson, C. S., Kellogg, J., Kimvilakani, P., Lefavor, M., Hengemihle, J., Jaeger, F., Lyness, E., Maurer, J., … Edmonson, C. (2014). The Neutral Mass Spectrometer on the Lunar Atmosphere and Dust Environment Explorer Mission. *Space Science Reviews*, *185*(1), 27-61. https://doi.org/10.1007/s11214-014-0043-9

March, R. E. (1997). An Introduction to Quadrupole Ion Trap Mass Spectrometry. *Journal of Mass Spectrometry*, *32*(4), 351-369. https://doi.org/10.1002/(SICI)1096-9888(199704)32:4<351::AID-JMS512>3.0.CO;2-Y

McFadden, J. P., Kortmann, O., Curtis, D., Dalton, G., Johnson, G., Abiad, R., Sterling, R., Hatch, K., Berg, P., Tiu, C., Gordon, D., Heavner, S., Robinson, M., Marckwordt, M., Lin, R., & Jakosky, B. (2015). MAVEN SupraThermal and Thermal Ion Compostion (STATIC) Instrument. *Space Science Reviews*, *195*(1), 199-256. https://doi.org/10.1007/s11214-015-0175-6

Mlynczak, M. G., Knipp, D. J., Hunt, L. A., Gaebler, J., Matsuo, T., Kilcommons, L. M., & Young, C. L. (2018). Space-Based Sentinels for Measurement of Infrared Cooling in the Thermosphere for Space Weather Nowcasting and Forecasting. *Space Weather*, *16*(4), 363-375. https://doi.org/10.1002/2017SW001757

Nakamura, Y., Shiokawa, K., Otsuka, Y., Oyama, S., Nozawa, S., Komolmis, T., Komonjida, S., Neudegg, D., Yuile, C., Meriwether, J., Shinagawa, H., & Jin, H. (2017). Measurement of thermospheric temperatures using OMTI Fabry–Perot interferometers with 70-mm etalon. *Earth, Planets and Space*, *69*(1), 57. https://doi.org/10.1186/s40623-017-0643-1

Orsini, S., Livi, S. A., Lichtenegger, H., Barabash, S., Milillo, A., De Angelis, E., Phillips, M., Laky, G., Wieser, M., Olivieri, A., Plainaki, C., Ho, G., Killen, R. M., Slavin, J. A., Wurz, P., Berthelier, J.-J., Dandouras, I., Kallio, E., McKenna-Lawlor, S., … Zampieri, S. (2021). SERENA : Particle Instrument Suite for Determining the Sun-Mercury Interaction from BepiColombo. *Space Science Reviews*, *217*(1), 11. https://doi.org/10.1007/s11214-020-00787-3

Palmroth, M., Grandin, M., Sarris, T., Doornbos, E., Tourgaidis, S., Aikio, A., Buchert, S., Clilverd, M. A., Dandouras, I., Heelis, R., Hoffmann, A., Ivchenko, N., Kervalishvili, G., Knudsen, D. J., Kotova, A., Liu, H.-L., Malaspina, D. M., March, G., Marchaudon, A., … Yamauchi, M. (2021). Lower-thermosphere–ionosphere (LTI) quantities : Current status of measuring techniques and models. *Annales Geophysicae*, *39*(1), 189-237. https://doi.org/10.5194/angeo-39-189-2021

Rahmati, A., Larson, D. E., Cravens, T. E., Lillis, R. J., Halekas, J. S., McFadden, J. P., Dunn, P. A., Mitchell, D. L., Thiemann, E. M. B., Eparvier, F. G., DiBraccio, G. A., Espley, J. R., Mazelle, C., & Jakosky, B. M. (2017). MAVEN measured oxygen and hydrogen pickup

ions : Probing the Martian exosphere and neutral escape. *Journal of Geophysical Research: Space Physics*, *122*(3), 3689-3706. https://doi.org/10.1002/2016JA023371

Richmond, A. D. (1979). Ionospheric Wind Dynamo Theory : A Review. *Journal of geomagnetism and geoelectricity*, *31*(3), 287-310. https://doi.org/10.5636/jgg.31.287

Ramstad, R., Barabash, S. (2021) Do Intrinsic Magnetic Fields Protect Planetary Atmospheres from Stellar Winds? *Space Sci Rev* **217**, 36. https://doi.org/10.1007/s11214-021-00791-1

Richmond, A. D., & Lu, G. (2000). Upper-atmospheric effects of magnetic storms : A brief tutorial. *Journal of Atmospheric and Solar-Terrestrial Physics*, *62*(12), 1115-1127. https://doi.org/10.1016/S1364-6826(00)00094-8

Riousset, J. A., Paty, C. S., Lillis, R. J., Fillingim, M. O., L. England, S., Withers, P. G., & M. Hale, J. P. (2013). Three-dimensional multifluid modeling of atmospheric electrodynamics in Mars' dynamo region. *Journal of Geophysical Research: Space Physics*, *118*(6), 3647-3659. https://doi.org/10.1002/jgra.50328

Rispoli, R., Angelis, E. D., Colasanti, L., Vertolli, N., Orsini, S., Scheer, J. A., Mura, A., Milillo, A., Wurz, P., Selci, S., Lellis, A. M. D., Leoni, R., D'Alessandro, M., Mattioli, F., & Cibella, S. (2012). ELENA MCP detector : Absolute detection efficiency for low-energy neutral atoms. In R. Navarro, C. R. Cunningham, & E. Prieto (Éds.), *SPIE Proceedings*. SPIE. https://doi.org/10.1117/12.926185

Roeten, K. J., Bougher, S. W., Benna, M., Mahaffy, P. R., Lee, Y., Pawlowski, D., González-Galindo, F., & López-Valverde, M. Á. (2019). MAVEN/NGIMS Thermospheric Neutral Wind Observations : Interpretation Using the M-GITM General Circulation Model. *Journal of Geophysical Research: Planets*, *124*(12), 3283-3303. https://doi.org/10.1029/2019JE005957

Sanchez-Cano, B. (2023). *The M-MATISSE mission: Mars Magnetosphere ATmosphere Ionosphere and Space weather SciencEAn ESA Medium class (M7) candidate* (EGU23-13687). EGU23. Copernicus Meetings. https://doi.org/10.5194/egusphere-egu23-13687

Sanchez-Cano, B., Witasse, O., Knutsen, E. W., Meggi, D., Lester, M., & Wimmer-Schweingruber, R. F. (2022). *Space Weather detections with housekeeping sensors onboard Mars Express, Rosetta, BepiColombo and Solar Orbiter* (EGU22-4289). EGU22. Copernicus Meetings. https://doi.org/10.5194/egusphere-egu22-4289

Sangalli, L., Knudsen, D. J., Larsen, M. F., Zhan, T., Pfaff, R. F., & Rowland, D. (2009). Rocket-based measurements of ion velocity, neutral wind, and electric field in the collisional transition region of the auroral ionosphere. *Journal of Geophysical Research: Space Physics*, *114*(A4). https://doi.org/10.1029/2008JA013757

Sarris, T. E., Talaat, E. R., Palmroth, M., Dandouras, I., Armandillo, E., Kervalishvili, G., Buchert, S., Tourgaidis, S., Malaspina, D. M., Jaynes, A. N., Paschalidis, N., Sample, J., Halekas, J., Doornbos, E., Lappas, V., Moretto Jørgensen, T., Stolle, C., Clilverd, M., Wu, Q.,

… Aikio, A. (2020). Daedalus : A low-flying spacecraft for in situ exploration of the lower thermosphere–ionosphere. *Geoscientific Instrumentation, Methods and Data Systems*, *9*(1), 153-191. https://doi.org/10.5194/gi-9-153-2020

Sarris, T., Palmroth, M., Aikio, A., Buchert, S. C., Clemmons, J., Clilverd, M., Dandouras, I., Doornbos, E., Goodwin, L. V., Grandin, M., Heelis, R., Ivchenko, N., Moretto-Jørgensen, T., Kervalishvili, G., Knudsen, D., Liu, H.-L., Lu, G., Malaspina, D. M., Marghitu, O., … Yamauchi, M. (2023). Plasma-neutral interactions in the lower thermosphere-ionosphere : The need for in situ measurements to address focused questions. *Frontiers in Astronomy and Space Sciences*, *9*. https://www.frontiersin.org/articles/10.3389/fspas.2022.1063190

Satoh, T., Tsuno, H., Iwanaga, M., & Kammei, Y. (2005). The Design and Characteristic Features of a New Time-of-Flight Mass Spectrometer with a Spiral Ion Trajectory. *Journal of the American Society for Mass Spectrometry*, *16*(12), 1969-1975. https://doi.org/10.1016/j.jasms.2005.08.005

S. Scherer, K. Altwegg, H. Balsiger, J. Fischer, A. Jäckel, A. Korth, M. Mildner, D. Piazza, H. Reme, P. Wurz, (2006). A novel principle for an ion mirror design in time-of-flight mass spectrometry, *International Journal of Mass Spectrometry*, Volume 251, Issue 1, 2006, Pages 73-81, ISSN 1387-3806, https://doi.org/10.1016/j.ijms.2006.01.025.

Schläppi, B., Altwegg, K., Balsiger, H., Hässig, M., Jäckel, A., Wurz, P., Fiethe, B., Rubin, M., Fuselier, S. A., Berthelier, J. J., Keyser, J. D., Rème, H., & Mall, U. (2010). Influence of spacecraft outgassing on the exploration of tenuous atmospheres with in situ mass spectrometry. *Journal of Geophysical Research: Space Physics*, *115*(A12). https://doi.org/10.1029/2010ja015734

Seppälä, A., Verronen, P. T., Clilverd, M. A., Randall, C. E., Tamminen, J., Sofieva, V., Backman, L., & Kyrölä, E. (2007). Arctic and Antarctic polar winter NOx and energetic particle precipitation in 2002–2006. *Geophysical Research Letters*, *34*(12). https://doi.org/10.1029/2007GL029733

Sinnhuber, M., Nieder, H., & Wieters, N. (2012). Energetic Particle Precipitation and the Chemistry of the Mesosphere/Lower Thermosphere. *Surveys in Geophysics*, *33*(6), 1281-1334. https://doi.org/10.1007/s10712-012-9201-3

Spencer, N. W., Brace, L. H., & Grimes, D. W. (1973). The Atmosphere Explorer spacecraft system. *Radio Science*, *8*(4), 267-269. https://doi.org/10.1029/RS008i004p00267

Spencer, N. W., & Carignan, G. R. (1988). In situ measurements of thermospheric composition, temperature and winds by mass spectrometry. *Advances in Space Research*, *8*(5), 107-117. https://doi.org/10.1016/0273-1177(88)90040-3

Steichen V., Leblanc, F. (2019). Caractérisation d'une source d'ionisation pour spectromètre de masse à haute résolution, Internship report.

Stone, S. W., Yelle, R. V., Benna, M., Elrod, M. K., & Mahaffy, P. R. (2018). Thermal Structure of the Martian Upper Atmosphere From MAVEN NGIMS. *Journal of Geophysical Research: Planets*, *123*(11), 2842-2867. https://doi.org/10.1029/2018JE005559

Tapley, B., Ries, J., Bettadpur, S., & Cheng, M. (2006). Neutral Density Measurements from the GRACE Accelerometers. In *AIAA/AAS Astrodynamics Specialist Conference and Exhibit*. American Institute of Aeronautics and Astronautics. https://doi.org/10.2514/6.2006-6171

Taylor, M. G. G. T., Altobelli, N., Buratti, B. J., & Choukroun, M. (2017). The Rosetta mission orbiter science overview : The comet phase. *Philosophical Transactions of the Royal Society A: Mathematical, Physical and Engineering Sciences*, *375*(2097), 20160262. https://doi.org/10.1098/rsta.2016.0262

Tesema, F., Partamies, N., Whiter, D. K., & Ogawa, Y. (2022). Types of pulsating aurora : Comparison of model and EISCAT electron density observations. *Annales Geophysicae*, *40*(1), 1-10. https://doi.org/10.5194/angeo-40-1-2022

Thayer, J. P., & Semeter, J. (2004). The convergence of magnetospheric energy flux in the polar atmosphere. *Journal of Atmospheric and Solar-Terrestrial Physics*, *66*(10), 807-824. https://doi.org/10.1016/j.jastp.2004.01.035

Victor, A. L., Zurbuchen, T. H., & Gallimore, A. D. (2006). Top hat electrostatic analyzer for far-field electric propulsion plume diagnostics. *Review of Scientific Instruments*, *77*(1), 013505. https://doi.org/10.1063/1.2165549

Waite, J. H., Lewis, W. S., Kasprzak, W. T., Anicich, V. G., Block, B. P., Cravens, T. E., Fletcher, G. G., Ip, W.-H., Luhmann, J. G., Mcnutt, R. L., Niemann, H. B., Parejko, J. K., Richards, J. E., Thorpe, R. L., Walter, E. M., & Yelle, R. V. (2004). The Cassini Ion and Neutral Mass Spectrometer (INMS) Investigation. *Space Science Reviews*, *114*(1), 113-231. https://doi.org/10.1007/s11214-004-1408-2

Wordsworth, R., Kalugina, Y., Lokshtanov, S., Vigasin, A., Ehlmann, B., Head, J., Sanders, C., & Wang, H. (2017). Transient reducing greenhouse warming on early Mars. *Geophysical Research Letters*, *44*(2), 665-671. https://doi.org/10.1002/2016GL071766

Yamazaki, Y., & Maute, A. (2017). Sq and EEJ—A Review on the Daily Variation of the Geomagnetic Field Caused by Ionospheric Dynamo Currents. *Space Science Reviews*, *206*(1), 299-405. https://doi.org/10.1007/s11214-016-0282-z

Young, D. T., Berthelier, J. J., Blanc, M., Burch, J. L., Coates, A. J., Goldstein, R., Grande, M., Hill, T. W., Johnson, R. E., Kelha, V., McComas, D. J., Sittler, E. C., Svenes, K. R., Szegö, K., Tanskanen, P., Ahola, K., Anderson, D., Bakshi, S., Baragiola, R. A., … Zinsmeyer, C. (2004). Cassini Plasma Spectrometer Investigation. In C. T. Russell (Éd.), *The Cassini-Huygens Mission: Orbiter in Situ Investigations Volume 2* (p. 1-112). Springer Netherlands. https://doi.org/10.1007/978-1-4020-2774-1_1